The electrification of industrial process heat

Implementation of thermal energy storage and the potential of novel high-temperature heat pump technologies

Master Thesis ME-EFPT

Koen Verloop

Delft University of Technology

TU Delft

TEIJIN

The electrification of industrial process heat

Implementation of thermal energy storage and the potential of novel high-temperature heat pump technologies

by

Koen Verloop

to obtain the degree of Master of Science
at the Delft University of Technology,
to be defended publicly on Friday December 8, 2023 at 13:00.

Student number:	4559053	
Project duration:	February 13, 2023 – December 8, 2023	
Thesis committee:	Prof. dr. ir. K. Hooman,	TU Delft, supervisor
	Prof. dr. ir. S.A. Klein,	TU Delft
	Dr. ir. E. Zanetti,	TU Delft
	Dr. ir. C. Scholtens,	Teijin Aramid, supervisor

TU Delft

Preface

This thesis project was conducted in close collaboration with the company Teijin Aramid. Teijin Aramid's interest and motivation to potentially decarbonize their production through this project serves as an admirable example for other industrial players. Decarbonization, being a common global objective, requires collective efforts and the industry sector lags behind compared to other sectors. In special, I would like to thank my supervisors from Teijin Aramid, Chris Scholtens and Hans Meerman, for initiating the project and the considerable time and effort they dedicated to this project. The constructive discussions we have had over the past 9 months and their assistance to acquire the necessary internal and external data formed the foundation to make this project a success. Additionally, I express my gratitude to my TU Delft supervisor, Professor Kamel Hooman, for his unwavering support, insightful suggestions, and the time he dedicated to assist me throughout the project. His consistent guidance and critical reflections were a crucial factor in the project's success. I would also like to express a word of gratitude to Professor Sikke Klein. Though not directly involved in the project, he generously made time to meet and provide support whenever I sought it. This project has provided me with valuable insights into the potential future of electrifying industrial process heat as well as the involved challenges. I hope that through this thesis project, I have contributed my share to further advance and speed up the energy transition.

Koen Verloop
Delft, November 2023

Abstract

Electrification and decarbonization of industrial process heat is an important next step in the energy transition to reduce greenhouse gas (GHG) emissions. This study provides an in-depth analysis of how in the current industrial landscape the combination of commercially available electric heating technologies with the implementation of thermal energy storage (TES) can realize the electrification of medium-temperature industrial process heat on the short-term. Moreover, it explores what potential novel high-temperature heat pump (HTHP) technologies, specifically the supercritical CO_2 (sCO_2) reversed Brayton HTHP, have to realize this electrification even more efficient in terms of electricity demand in the future. Thereby, it also briefly highlights the opportunities and challenges to combine HTHP technology and TES in the future to realize an optimal electrification.

Through a case study for the company Teijin Aramid the feasibility for the electrification of medium-temperature industrial process heat in the current industrial landscape was studied. It was found that electric heating in combination with sensible TES is currently the most viable option to electrify medium-temperature industrial process heat for industrial players like Teijin Aramid. These systems are commercially available and from a technical point of view successful electrification of the process heat demand proved to be very feasible. However, the economics prove to be more of a challenge, especially if 100% electrification is desired. Therefore, 75% electrification is currently a more realistic number. Additional incorporation of demand-side response shows potential to reach closer to 100% electrification. Nonetheless, the business-case remains quite poor compared to fossil-fuel alternatives. Therefore, it will mainly have to be driven by a willingness to decarbonize. Furthermore, to assess the feasibility of a novel sCO_2 reversed Brayton HTHP a numerical thermodynamic model was constructed. Through an optimization based on a parametric analysis it was concluded that continuously supply and waste heat availability at sufficiently high temperatures the sCO_2 reversed Brayton HTHP would be able to continuously supply 3 MW of process heat at 280 °C with a COP of between 2.5 and 3. However, for more realistic design operations the COP that could be achieved was around 2. On the other hand, it was shown that these limitations were mainly caused by equipment limitations and that the cycle itself offers interesting potential to reach both higher output temperatures as well as higher COP in the future. To improve the HTHP cycle the addition of an ejector was studied. The ejector-assisted sCO_2reversed Brayton HTHP showed promising results in COP and even for more realistic design operations resulted in a COP of between 2.5 and 3. In both cases the full system equipment cost were estimated at around 4 million euros. To combine novel HTHP technologies like the sCO_2reversed Brayton HTHP with TES in the future still poses significant challenges. However, development of novel TES technologies based on latent- and thermochemical thermal energy storage could help to realize this.

Recommendations for further research are also given. These are mainly related to further investigation of ejector technology for the presented HTHP design and to execute more practical realisation of the sCO_2 reversed Brayton HTHP. This to find out what COP could be achieved in real-life operation and to validate this study, and comparable numerical studies, with experimental data. Regarding the electric heating and thermal energy storage the recommendations are mainly related to practical implementation of the proposed system.

Contents

Nomenclature

Abbreviations

Abbreviation	Definition
APEA	Aspen process economic analyzer
CAPEX	Capital expenditure
COP	Coefficient of Performance
CSP	Concentrated solar power
CST	Concentrated solar thermal
DSR	Demand-side response
EDR	Exchanger Design and Rating
E-heater	Electric heater
EJ	Ejector
EOS	Equation of state
ETES	Electric thermal energy storage
GHG	Greenhouse gasses
GWP	Global warming potential
HEX	Heat exchanger
HTHP	High-temperature heat pump
HTF	Heat transfer fluid
IHX	Internal heat exchanger
LHS	Latent heat storage
NTU	Number of transfer units
O&M	Operation and maintenance
OPEX	Operating expenditure
PCHE	Printed circuit heat exchanger
PCM	Phase change material
PTES	Pumped thermal energy storage
P2H	Power-to-heat
sCO_2	Supercritical CO_2
SHS	Sensible heat storage
TCS	Thermochemical storage
TES	Thermal energy storage
TRL	Technology readiness level
VRE	Variable renewable energy
VRES	Variable renewable energy sources

Symbols

Symbol	Definition	Unit
A	Area	$[m^2]$
C	Heat capacity flow rate	$[W/K]$
c	Local speed of sound	$[m/s]$
c_p	Specific heat capacity at constant pressure	$[J/kg.K]$
h	Specific enthalpy	$[J/kg]$
I	Current	$[A]$
M	Mach number	$[-]$
m	Mass	$[kg]$
$\dot{m}$	Mass flow	$[kg/s]$
P	Pressure	$[Pa]$
Q/$\dot{Q}$	Thermal energy/power	$[J]$/$[J/s]$
q	Heat transfer rate	$[J/s]$
R	Resistance	$[\Omega]$
s	Specific entropy	$[J/kgK]$
T	Temperature	$[K]$
t	Time	$[s]$
U	Overall heat transfer coefficient	$[W/m^2K]$
V or u	Velocity	$[m/s]$
W	Work	$[J/s]$
ϵ	Effectiveness	$[-]$
η	Efficiency	[%]
γ	Heat capacity ratio	$[-]$
ω	Entrainment ratio	$[-]$
ρ	Density	$[kg/m^3]$

Subscripts

Subscript	Definition
C or c	Cold
$compr$	Compressor
cs	Cold stream
d	Diffuser (section)
H or h	Hot
hs	Hot stream
i	Inlet
id	Ideal (cycle)
in	Into system
lm	Logarithmic mean
m	Mixing (section)
n	Nozzle (section)
max	Maximum
min	Minimum
o	Outlet
out	Out of system
p	Primary (flow)
$turb$	Turbine
re	Real (cycle)
s	Secondary (flow)
$,s$	Constant entropy

1 Introduction

1.1. Background

Since the industrial revolution, the global economy has been built on the energy derived from the extensive utilization of fossil fuels, resulting in the emission of greenhouse gases (GHG), and contributing to global warming. Entities like the European Commission have stated their ambition to achieve climate neutrality by 2050 and to reduce European GHG emissions to zero in accordance with the Paris Agreement (EC, n.d.). Considering the increased economic dependence on technology, expanding globalization, and the growing world population, it is foreseeable that the demand for energy will likely increase rather than decrease. Consequently, to reduce GHG emissions and mitigate global warming the decarbonization of the supply of this energy is crucial. Variable renewable energy sources (VRES), primarily in the form of solar and wind, along with controllable renewable energy sources such as hydro power and biomass, have proven to present a viable and emission-free alternative to fossil fuels. However, the rapid implementation of VRES technologies and their successful integration into the global energy system emerge is a pressing issue. Generally, this swift implementation of VRES is already underway, as highlighted in 2020 by the International Energy Agency (IEA). The IEA projected that VRES will globally surpass both natural gas and coal in terms of total installed production capacity by 2024, as illustrated in Figure 1.1 (IEA, 2020).

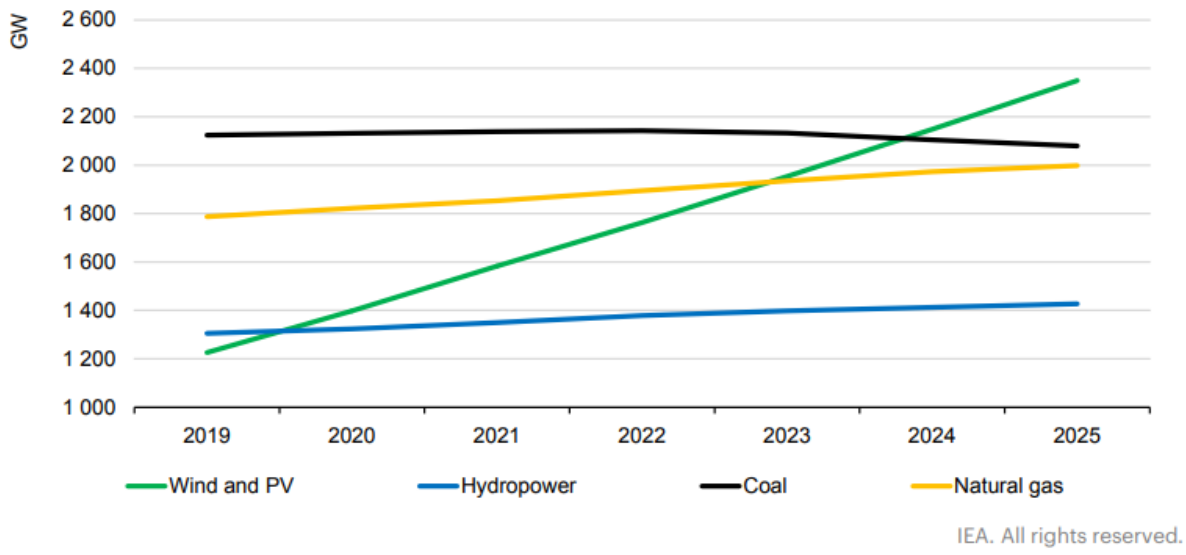

Figure 1.1: Total worldwide installed power capacity by fuel and technology from 2019-2025 as predicted by the IEA in 2020 (IEA, 2020).

The electrification of energy demand represents a crucial next step toward the successful integration of renewable energy production into the global energy system. The feasibility of this electrification is demonstrated by the widespread and swift electrification observed in the automotive industry. Utilizing data sourced from the IEA, Adamson et al. (2022) estimated the global final energy demand per sector for the year 2019, as depicted in Figure 1.2 (Adamson et al., 2022).

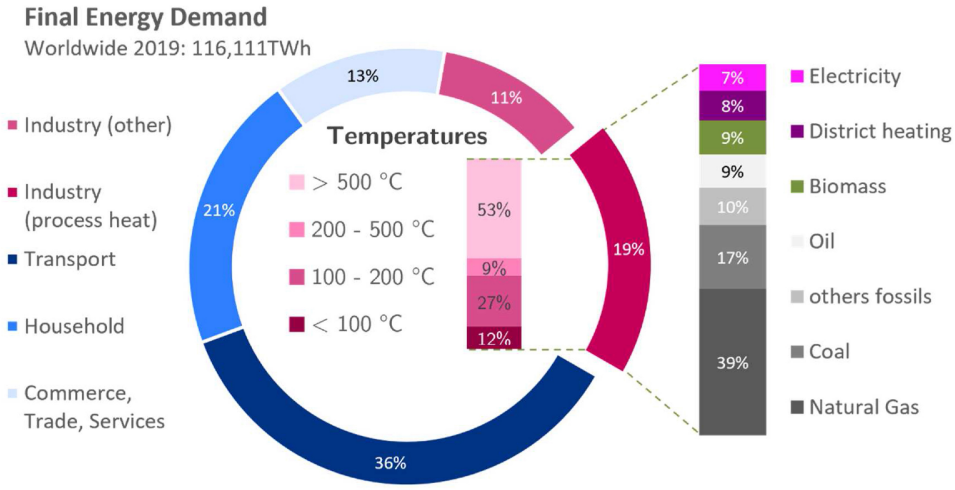

Figure 1.2: Global final energy demand in 2019 per sector including estimates for the source of production and temperature levels of process heat demand (Adamson et al., 2022).

Figure 1.2 illustrates that industrial process heat contributes significantly to the final energy demand. The IEA's latest report underscores that, on a global scale, heating in general remains the predominant end-use of energy, constituting nearly 50% of global final consumption. Within this context, industrial processes account for 53% of the final energy consumed for heat, with less than 25% of this heat production being derived from non-fossil sources. Moreover, biomass currently represents half of this non-fossil heat production (IEA, 2022). Furthermore, Adamson et al. (2022) note that although process heat for industry constitutes approximately 19% of the global final energy demand, it is responsible for 36.8% of total emissions. This high emission rate is primarily attributed to the extensive reliance on fossil fuels for this sector, particularly natural gas, as illustrated in Figure 1.2. Moreover, it was found that approximately 74% of the total energy consumption in the industrial sector is attributed to on-site process heat production (IRENA, 2020). Despite the notable growth in global heat pump sales, with a reported 11% increase in 2022 according to the IEA, the majority of these sales refer to domestic heat pumps, facilitating the electrification of household energy consumption (IEA, 2023). In contrast, the electrification of the industrial sector, particularly related to industrial process heat, appears to be progressing at a significant slower pace. The data presented in Figure 1.2 illustrates that the electrification of process heat production has the potential to significantly diminish the reliance on fossil fuels and mitigate GHG emissions in the industrial sector. However, it is important to note that approximately 88% of the demand for process heating pertains to temperatures exceeding 100 °C, with around 61% necessitating temperatures surpassing 200 °C.

The carbon-neutral alternatives for addressing this process heat demand include the combustion of hydrogen and Power-to-Heat (P2H), which involves the direct conversion of electrical energy into thermal energy. The current viability of hydrogen combustion is hindered by the low overall energetic efficiency and substantial costs associated with (green) hydrogen production. Thus, it is currently considered a realistic option only for applications that require very high temperatures, such as those exceeding 1000 °C, where the options for P2H are more limited. Given these limitations this study does not further explore the combustion of hydrogen as a viable solution. Among the P2H technologies, three technologies show particular promise for converting electricity into process heat: heat pumps, electric boilers, and electric resistance heaters (Maruf et al., 2022). In the context of this report, the term "E-heating technologies" will be employed to collectively refer to electric boilers and electric resistance heaters. Specifically, the term "E-heater" will be utilized to denote electric resistance heaters.

It is useful to note that in general process heat can be categorized into three segments (IRENA, 2020):

- Low-temperature process heat: < 150 °C
- Medium-temperature process heat: 150-400 °C
- High-temperature process heat: > 400 °C

The distribution of process heat demand based on temperature levels, as illustrated in Figure 1.2, reveals that approximately 12-39% of the demand falls within the category of low-temperature process heat, while 27-36% qualifies as medium-temperature process heat demand, and around 53-62% is considered high-temperature process heat demand. Consequently, the combination of medium-temperature and high-temperature process heat demand constitutes approximately 62-88% of the total process heat demand. Low-temperature process heat can be realized through the use of commercially available heat pumps, E-boilers, and E-heaters. Additionally, commercially available E-boilers and E-heaters possess the capability to provide medium-temperature, and potentially also high-temperature, process heat. However, the operation of E-boilers and E-heaters requires a substantial amount of electricity, leading to a substantial increase in electricity demand and significant costs for industries, particularly given the high cost of electricity compared to natural gas. The intermittent nature of VRES results in surpluses and deficits in the available supply of renewable energy, leading to substantial variations in electricity prices. Consequently, electricity supply remains heavily influenced by the (expensive) production of fossil-fuel-based electricity due to the intermittency of VRES production and the installed capacity of fossil-fuel-based power, as depicted in Figure 1.1. This situation poses challenges both in terms of the financial feasibility of electrification and the reduction of carbon emissions. In this study it was chosen to focus on only medium-temperature process heat in relation to the scope of the research.

Heat pump technology has demonstrated its success in domestic applications and for low-temperature industrial applications. It also appears as a compelling alternative to E-boilers and E-heaters for medium-temperature process heat. This is primarily attributed to its significantly lower electrical energy consumption and the capacity to effectively reuse available waste heat. Unfortunately, presently available industrial heat pump technologies are constrained to output temperatures ranging from approximately 90 to 160 degrees Celsius, rendering them unsuitable for supplying medium-temperature process heat (Arpagaus et al., 2018). Additionally, the standalone adoption of heat pump technologies does not address the challenge associated with the intermittency of supply from VRES. Consequently, there is a need, both from an economic and environmental perspective, as well as in terms of overall energy efficiency, to explore technologies that can enhance the operation of E-boilers and E-heaters or incorporate inherently more energy-efficient heat pump technologies. As emphasized by Adamson et al. (2022), integrating (thermal) storage and optimizing systems to enable highly efficient operation and minimize required capital investment could position industrial heat pumps at the forefront of the electrification of industry (Adamson et al., 2022). The incorporation of (thermal) energy storage could also be effectively applied to currently available E-boiler and E-heater technologies for mid-temperature process heat. This to better cope with the intermittency of supply from VRES, thereby enhancing financial feasibility and further reducing carbon emissions.

This study will go into more detail what the electrification of medium-temperature industrial process heat could look like through implementation of (thermal) energy storage and novel high-temperature heat pump (HTHP) technologies. The focus of this thesis is centered on a case study involving the company Teijin Aramid. Within the production process of Teijin Aramid there is a medium-temperature thermal oil process heat demand of approximately 2-4 MW at a temperature of around 280 degrees Celsius. Teijin Aramid serves as an exemplary industrial entity with on-site process heat production. Currently, like for many industrial applications, this process heat is generated through the combustion of natural gas. However, there is a desire to electrify and decarbonize this process to achieve a more sustainable mode of production.

1.2. Research objectives

The objective of this thesis project included two primary aspects:

1. Identify what is based on commercially available technologies currently the most viable way to electrify the production of medium-temperature process heat for industrial players like Teijin Aramid. Thereby considering optimal use of energy storage technologies to deal with intermittency of electricity production through VRE sources. Additionally, explore the potential role that demand-side response could play to increase the feasibility of the electrification.
2. Explore the potential for novel high-temperature heat pump technologies that could serve as an alternative means of providing medium-temperature process heat in the future. Particularly focused on the viability and potential of a sCO_2reversed Brayton HTHP. Additionally, consider the integration of this novel HTHP technology with the explored energy storage technologies to address the intermittency in electricity production associated with VRES.

To fulfill the first objective of the thesis report, in-depth research on commercially available E-heating and energy storage technologies was required. This research aimed at identifying the most viable E-heating and energy storage technology for medium-temperature process heat. Subsequently, the chosen technology necessitated the collection of detailed technical and financial data. This involved an extensive review of literature, own analysis, and, when feasible, direct interviews with suppliers of these technologies.
To apply these findings to the Teijin Aramid case study, an examination of the production process was essential to evaluate the technical feasibility of the electrification solution and explore potential DSR opportunities. Furthermore, an own analysis was required to project a future estimation of fluctuations in natural gas prices and grid electricity prices in the Netherlands. By consolidating all this information, a techno-economic analysis could be conducted to assess the feasibility of electrifying the production of medium-temperature process heat for Teijin Aramid in the near future.

To accomplish the second project objective, an initial literature review was conducted to identify the constraints associated with currently available HTHP technologies. The goal was to pinpoint a promising combination of thermodynamic cycle, working medium, and equipment for more in-depth research. The literature study, coupled with discussions with Professor Hooman, led to the determination that the combination of the reversed Brayton cycle and sCO_2 as refrigerant presented itself as an interesting option for more in-depth research. Further supported by the identified knowledge gaps in research associated with the sCO_2 reversed Brayton HTHP technology. Following the selection of this HTHP technology, the subsequent step involved the development of a numerical model for the HTHP design. This model was designed to simulate its operation, offering insights into the potential performance when delivering medium-temperature process heat. Moreover, the investigation sought to explore the integration of additional equipment, such as the use of an ejector as a ”pre-compression” step, to further enhance overall performance. The final phase of the process encompassed a cost estimation of the full HTHP design to indicate the practical feasibility of implementing the technology and to ascertain the associated costs.

As highlighted, an additional point of interest was to briefly consider the potential synergies arising from combining the newly proposed HTHP design with energy storage solutions, either the ones explored for the case study of Teijin Aramid or, if more applicable, other storage technologies. This exploration was rooted in the understanding that, from both an emission reduction perspective and a financial viewpoint, the operation of a HTHP system could substantially benefit from surpluses of VRES supply in terms of reducing carbon emissions, and financially benefit from leveraging low electricity prices, facilitated by energy storage technology.

1.3. Literature review

1.3.1. Commercially available industrial E-heating methods

As discussed in Section 1.1, the existing technologies for delivering process heat via electrical heating, commonly referred to as P2H, encompass heat pumps, E-boilers, and E-heaters. However, upon examination of the technology readiness level (TRL) of these methods, as depicted in Figure 1.3, it becomes apparent that the viable alternatives are limited to E-boilers and E-heaters. At least, in the context of commercially available technologies to supply medium-temperature process heat. Consequently, only E-boilers and E-heaters are being considered as commercially available industrial electric heating methods. Given the focus of this research on providing process heat through thermal oil, the E-boiler technology, which is exclusively utilized for generating (high-pressure) steam, has not been further examined. As E-heater technology has reached full maturity and is readily available in the market, this section will only offer a brief overview of the existing variations and the operational principles of this technology.

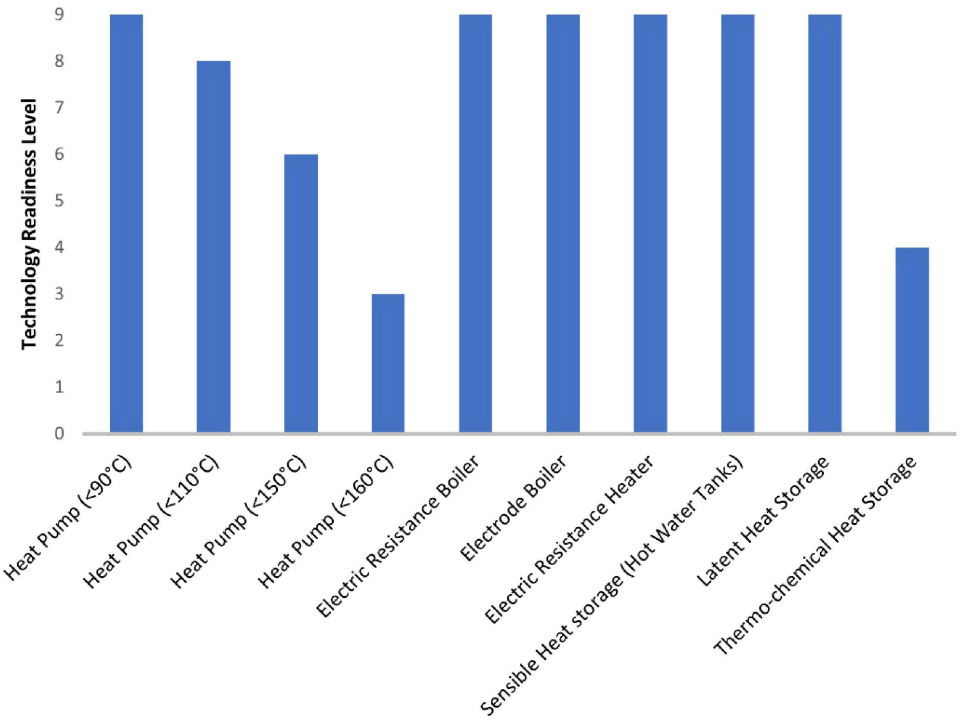

Figure 1.3: Technology readiness levels of P2H and TES technologies (Maruf et al., 2022).

The TRL for heat pump technologies presented in Figure 1.3 were based on relatively dated information from 2018. Recent data and commercial applications by MAN Energy and Siemens Energy, further discussed in Section 1.3.3, indicate a TRL of 9 for heat pump technologies designed to supply process heat up to 150 °C. Nevertheless, this remains below the spectrum required for medium-temperature process heat. As discussed in Section 1.1, heat pump technology can therefore currently not be regarded as a commercially available industrial electric heating method for providing medium-temperature process heat. Within E-heater technology, various methods are utilized to realize the electrical heating. These methods include conductive-, inductive-, high-frequency-, and infrared heating. In industrial processes, however, electric process heaters predominantly employ conductive heating to provide the necessary process heat (Maruf et al., 2022). Conductive heating, exemplified by electric arc furnaces or resistive heaters, represents a fully matured technology well-suited for applications involving high temperatures and pressures, particularly for heating fluids like thermal oil. The other aforementioned technologies find application in more specific heating scenarios, such as heating metals, plastic processing, drying, and are utilized in specific industries such as in the production of textiles, paper, and plastics (Maruf et al., 2022). Thermal fluid process electric heaters are commonly known as electric resistance heaters or circulation heaters. They generally have the capacity to provide heat up to approximately 5 MW. An example of such an E-heater is presented in Figure 1.4.

Figure 1.4: Example of an industrial thermal fluid circulation E-heater (Heating group, 2023).

Electric heaters operate through the direct conversion of electric energy (current) into thermal energy (heat), utilizing the inherent resistance of the wire through which the current passes. This phenomenon is commonly known as the Joule effect (Maruf et al., 2022) and is described in Equation 1.1. Wherein 'Q' denotes the heat generated within the wire, 'I" represents the current flowing through the wire, 'R' signifies the resistance of the wire, and 't' denotes the duration of time. The thermal energy is subsequently absorbed by the heat transfer fluid, e.g. thermal oil, as it passes through the electric heater. This absorption leads to an increase of the internal energy of the heat transfer fluid, consequently elevating its temperature.

$$Q = I^2 * R * t \tag{1.1}$$

This results in the creation of relatively straightforward systems that exhibit rapid start-up capabilities, occupy minimal space, and incur modest investment costs. Output temperatures of up to 1000 °C are not uncommon and are mainly dependent on the thermal constraints imposed by the materials and subcomponents employed in the E-heater technology. Despite achieving an efficiency approaching 100%, the direct conversion of electricity into heat through the Joule effect necessitates a substantial amount of electricity. This results in significant costs compared to alternative technologies such as heat pump technology, known for its lower electricity consumption. Certain characteristics of the E-heater technology, such as the very fast response time and turndown ratio are on the other hand very advantageous compared to heat pump technology. Moreover, the significantly lower CAPEX costs compared to heat pump technology also supports the use of E-heater technology for the electrification of industrial process heat.E-heater technologies are frequently discussed in combination with thermal energy storage, as illustrated by Maruf et al. (2022), to deal with the intermittency of supply from VRES. This approach enables the production of heat using surplus renewable electricity, thereby reducing overall costs and reduce carbon emissions. As currently heat pump technology cannot be combined with TES solutions for medium-temperature process heat demand this gives E-heater technology a significant advantage to reduce carbon emissions and profit financially from low electricity prices. Thermal energy storage will be further discussed and explored in Section 1.3.2.
Maruf et al. (2022) also highlight the possibility of hybrid heating systems, which involve the combination of a heat pump with an electric resistance heater. This configuration allows for either ”pre-heating” of the heat pump's source temperature or to further increase the heat pump's sink (output) temperature to the desired level. Thereby lowering the required temperature lift and enhancing overall performance. This concept will be revisited in Section 3.1.1.

All in all, considering commercially available industrial E-heating technologies designed for the conversion of electrical energy into thermal energy, the utilization of resistive fluid E-heater technology emerges as the most advisable choice. Its efficacy lies in its seamless integration with established thermal oil systems traditionally heated by natural gas, coupled with the technology's TRL, rendering it the presently most feasible solution. This is particularly due to its flexible nature concerning output power and temperature, as well as its excellent compatibility with thermal energy storage systems.

1.3.2. (Thermal) energy storage technologies

As mentioned in Section 1.1 the global increase of VRES to replace fossil-fuels looks very promising but the intermittency of these renewable sources poses a challenge. To deal with this intermittency on different time scales energy storage technologies offer a realistic and effective choice with great potential to optimise energy management and control energy spillage (Mitali et al., 2022). Energy storage could aid in the decoupling of the supply of electricity from heat demand, and help to successfully integrate the higher shares of renewables (IRENA, 2020). Pumped hydro storage has always dominated the energy storage market. However, due to the growth of new storage technologies it's global market share is in decline, and fell for example with 4.1% to 86.2% by the end of 2021 compared to 2020 (CNESA, 2021). The division of the global energy storage market in 2021 per storage technique is shown in Figure 1.5, where "new" energy storage techniques like (molten-salt) thermal storage and (lithium-ion) battery storage show most dominance next to pumped hydro storage.

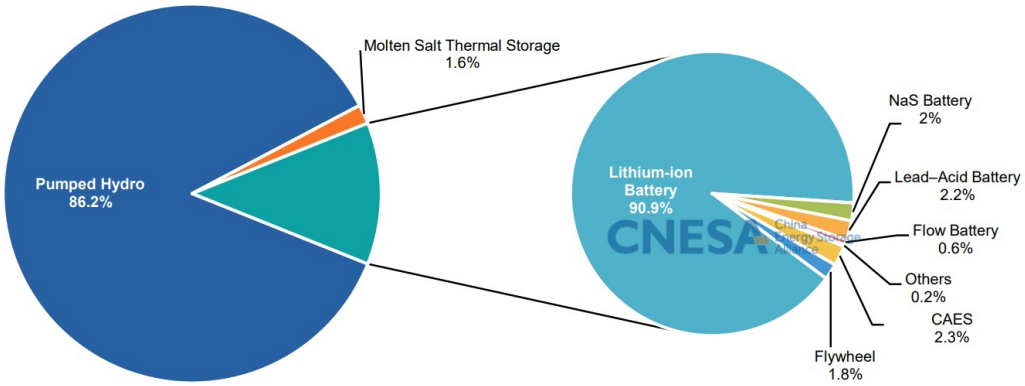

Figure 1.5: Global energy storage market capacity by the end of 2021 in MW% (CNESA, 2021).

This growth is expected to continue and the "new" energy storage market, so excluding pumped hydro storage, is projected by BloombergNEF (2022) to reach a total global size of around 411 GW/1194 GWh by the end of 2030. This is 15 times the size of the global "new" energy storage capacity of 27 GW/56 GWh at the end of 2021. BloombergNEF based this projected growth mainly on the expected developments in battery technologies.They state that new developments in other technologies like compressed air and thermal storage may result in even larger growth (BloombergNEF, 2022). This combined with the fact that these numbers are without the currently dominating pumped hydro storage clearly shows the need and potential of energy storage in our global energy system.

Furthermore, is it useful to make a division between energy storage based on the time energy can effectively be stored. The storage time scales relevant for industry can be divided in four categories (Eggers et al., 2022):

1. Intraday storage - up to 24 hours
2. Multiday storage - from 24 hours up to one week
3. Multiweek storage - from one week up to several weeks
4. Seasonal storage - from several weeks up to multiple months

Intraday storage can be used to cover the daily variations found in in VRES production over the course of a day. Multiday storage is able to cover consecutive days of low VRES production often seen in winter. This is caused by a constantly low solar PV yield combined with periods of low wind yield. Technologies focused on this kind of storage are generally characterized by smaller storage capacities, and fast charging and discharging is required as the stored energy is needed on a regular basis. Losses of energy over time are a factor but to a lesser extent due to relative short storage times.
Multiweek and seasonal storage is applied to deal with longer periods of low VRES yield and to shift

surpluses in yield observed in the spring and the summer to cover deficits in the fall and winter. Characteristics of these kind of technologies are: large storage capacities with systems that have large spacial requirements but no need for fast charging and discharging as the energy is not often required. Opposed to intraday and multiday storage the losses of energy over time play a significant role to enable effective energy storage.
The base load process heat demand is substantial for most industrial processes and generally requires rapid charge and discharge of the energy stored. Multiweek and seasonal storage would therefore require large storage capacities which was not deemed realistic for on-site process heat production like in the case of Teijin Aramid. Therefore, intraday and multiday storage was considered to be most realistic and therefore only technologies suitable for this timescale were further considered.

Energy storage technologies

The different industrial energy storage technologies currently available or under development can be classified based on the way the energy is stored, this is depicted in Figure 1.6.

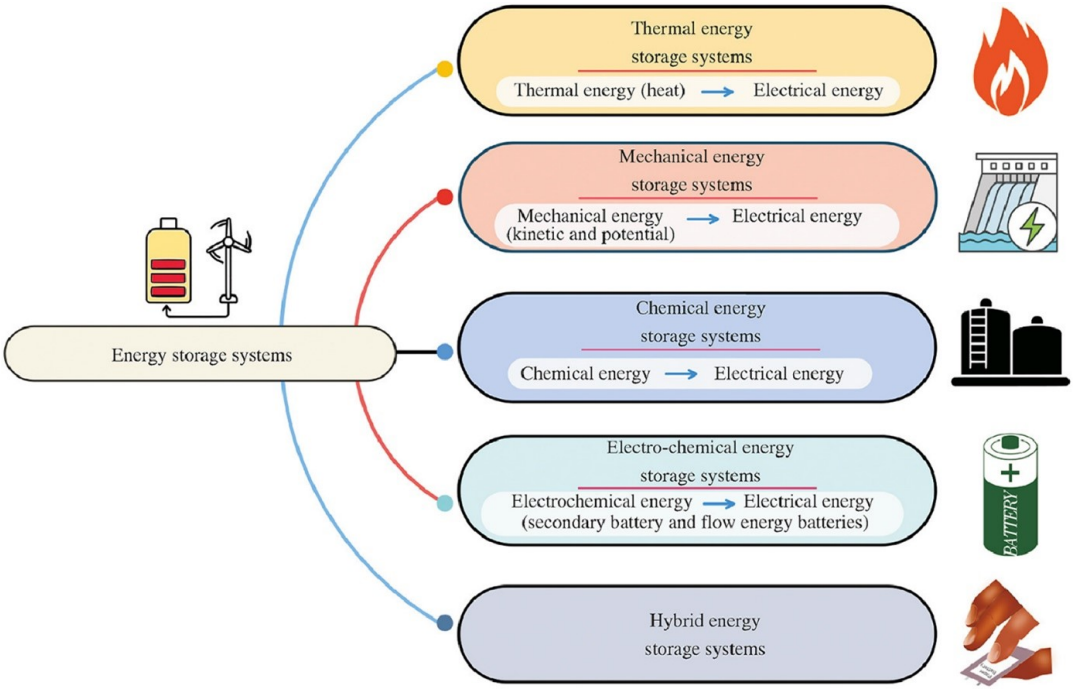

Figure 1.6: Overview and categorisation of the different energy storage technologies available (Mitali et al., 2022).

The different energy storage systems all have their own advantages and disadvantages. Nonetheless, to aid the electrification of industrial process heat most storage technologies are not suited due to either spacial and geological requirements or the focus on multiweek and seasonal storage. As the the energy is generated in the form of electrical energy and is needed in the form of heat supplied by a P2H system, thermal energy storage is an obvious choice. Where it should be noted that hot water TES is not included as it is limited by the boiling point of water at 100 °C.

Battery energy storage, or electro-chemical energy storage, could alternatively be combined well with the P2H system but is of lesser interest due to the relatively low costs and footprint of TES compared to battery storage. According to Professor Sikke Klein of Delft University of Technology TES is about a factor 10 cheaper than conventional (lithium-ion) battery storage. This is supported by other studies where example lithium-ion battery storage is estimated at 308-419 $/kWh while TES is estimated at 15-70 €/kWh (excluding hot water storage), which results in a comparable factor (Energy.at-site.be, 2023). Based on this it was concluded that TES was the most promising technology for this application and was further explored.

Thermal energy storage

Thermal storage can be defined as ”a system designed to store heat energy by cooling, heating, melting, condensing, or vaporising a material” (Mitali et al., 2022). This can either be at low- or high temperature but in either case the systems needs to be well insulated to minimize losses of the stored heat energy back into the surroundings (Mitali et al., 2022). Depending on the kind of TES system and temperature range it can be used for various applications from space heating up to delivering industrial process heat. The combination of TES with CSP systems in the form of concentrated solar thermal (CST) has also been extensively researched in studies like by Powell et al. (2017) and Pelay et al. (2017) and shows the promise and potential of effectively utilizing TES technology (Powell et al., 2017)(Pelay et al., 2017). In general TES encompasses three methods of thermal storage dependent on the thermodynamic phenomena utilized for the energy storage: sensible heat storage (SHS), latent heat storage (LHS) and thermochemical storage (TCS). This is illustrated in Figure 1.7.

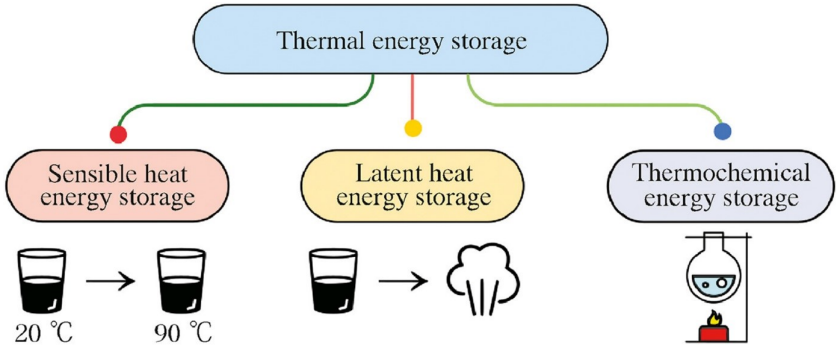

Figure 1.7: General overview and categorisation of the different TES technologies available (Mitali et al., 2022).

Figure 1.8 gives a good overview of the differences between the three methods of thermal energy storage.

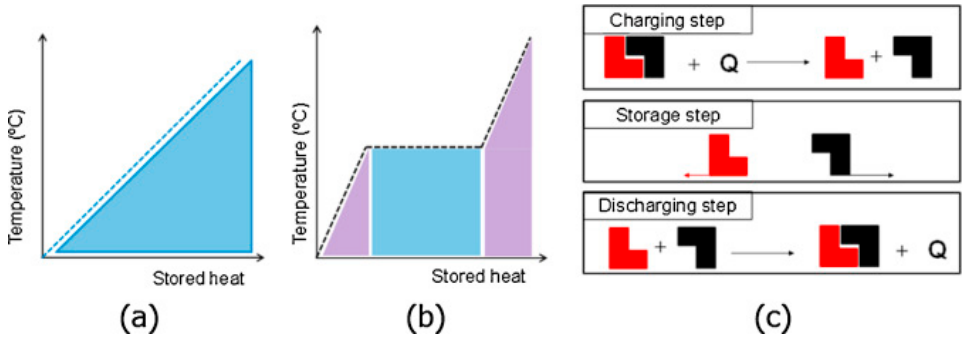

Figure 1.8: Overview of the methods of thermal energy storage: (a) Sensible heat, (b) latent heat, (c) thermochemical reactions (de Gracia and Cabeza, 2015).

It can be seen that SHS and LHS are very similar as both storage methods rely on the direct thermodynamic relation between temperature and stored heat within the storage material. The amount of thermal energy stored is calculated based on the amount of storage material (mass), the specific heat capacity, and the change in temperature as illustrated in Equation 1.2. The higher the temperature the more heat is stored. In principle any material can be used for this but low-cost materials with a high specific heat capacity able to withstand high temperatures are most suitable. Examples of materials applied in SHS technologies are metals like steel, volcanic rocks, bricks or molten-salt.

$$Q = m * c_p * \Delta T \tag{1.2}$$

However, LCS additionally utilizes the heat of fusion of the storage material when it changes phase. In this process, indicated by the blue area in the Figure 1.8(b) energy is stored while the temperature does not increase further. This results in higher energy densities and hence more energy that can

be stored in a smaller storage if the storage is operated in the temperature range around the phase-change (Sarbu and Sebarchievici, 2018). Materials suitable for LCS are generally referred to as a phase change materials (PCM) and are characterized by a high latent heat of fusion which allows a high energy storage density. However, these PCMs also have a low thermal conductivity resulting in slow charging and discharging. Moreover, do most of these materials exhibit a significant volume change in the phase-change process and involve more complex systems compared to SHS. This poses a significant challenge for implementation in TES technologies and LCS has therefore not been implemented on an industrial scale at this point in time.

TCS is a more indirect way of storing heat as it uses the thermochemical phenomena that heat is absorbed and released during dissociation/association of molecular bonds in a reversible chemical reaction (Mitali et al., 2022). It utilizes the enthalpy of reaction to store heat during charging and release heat during discharging. Through this enthalpy of reaction essentially thermal energy is indirectly ”captured” in the material as shown in Figure 1.8(c). This gives TCS a large advantage compared to SHS and LHS as it enables a relative high energy density and long storage capabilities without the need for insulation due to no heat leakage (Mitali et al., 2022). Nonetheless, there are still a lot of challenges to overcome especially with regard to the identification of materials that are most suited for TCS and the complex storage process.

Although LHS and especially TCS are very promising TES technologies both technologies are for industrial applications not yet developed into commercial applications. This was described in a recent report of the International Renewable Energy Agency (IRENA) and illustrated in Figure 1.9. It should be noted that this was based on data from 2018 and that solid-state sensible storage is currently commercially available.

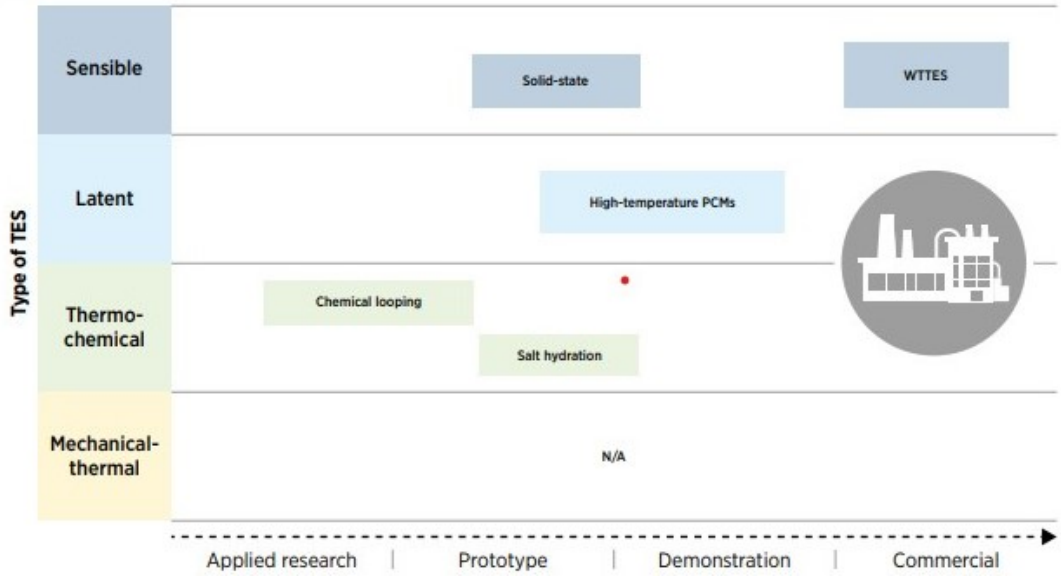

Figure 1.9: TRL of thermal storage methods for industrial applications (IRENA, 2020).

A future outlook on TES technologies for industry was also given by IRENA. This also included predictions for technical specifications and very rough expected cost ranges. The application of solid-state TES technology was named as a promising technology for the short/medium term of 5-10 years. It is expected to serve as a relative low-cost form of (thermal) energy storage with possible improvements to higher energy density materials like HT-cPCMs and salt hydration in a later stage (IRENA, 2020). For the long term most promise was dedicated to thermochemical storage which could have large benefits compared to SHS and LHS as explained earlier. However, it also mentioned that with currently a very low TRL this technology still requires large breakthroughs in research and development activities (IRENA, 2020).

As the focus of this project was on the short/medium term electrification of industrial process heat through the use of (thermal) energy storage only SHS was further considered. For medium-temperature process heat this is limited to solid-state SHS and molten-salt SHS which refers to the state of the storage material. Generally the system consists of insulated containers or tanks for the storage medium and external equipment used for charge and discharge of the thermal storage (Mitali et al., 2022).
For solid-state SHS a wide variety of solid materials can be used such as (volcanic) rocks, concrete, steel or ceramic bricks. These materials can be heated over a wide temperature range and are generally able to withstand temperatures up to 1000 °C (IRENA, 2020). In terms of molten-salts special compositions of inorganic salts are used which are heated above the melting point and kept in liquid phase. This generally results in an operating range of between 100 °C and 500 °C but with a large storage capacity due to the high energy density of the molten salt (Mitali et al., 2022).
Both solid-state and molten-salt SHS is used in commercially available TES systems suited for medium-temperature process heat storage. A further comparison between technologies applying them will be given in Section 2.1.

On a final note it is interesting to briefly mention pumped thermal energy storage (PTES), often also denoted as electric thermal energy storage (ETES). This is considered more of a hybrid storage system and is actually a combination of a heat pump cycle and TES technology based on the Carnot Battery principle. It is a relative new technology and is currently being tested in pilot plants mainly aimed at at low-temperature process heat but has potential for medium-temperature as well. The heat pump cycle is placed between two reservoirs, a cold and hot reservoir, and is used to convert electricity into thermal energy. The heat pump cycle can be reversed, acting as a heat engine, to convert the thermal energy back into electricity.
PTES offers potential due to high energy densities and large storage capacities. However, it is also limited by a round-trip efficiency of 40-50 % when discharging the energy as electricity. The temperature limitations of the heat pump cycle are also similar to that of HTHP as mentioned in Section 1.1 (Mitali et al., 2022). Moreover, the large footprint of these systems makes it more difficult to incorporate in industrial plants for on-site process heat production. The current focus of the technology is also not to deliver process heat but rather to be used in grid-scale applications to store and deliver electrical energy. Commercial applications of PTES/ETES by companies like MAN Energy and Siemens Energy are present but due the above mentioned reasons at this point PTES/ETES was currently not considered as viable option within the scope of this research.

Conclusion

The studied literature with regard to energy storage technologies provided both more in-depth information as well as enabled a balanced trade-off between the different available (thermal) storage technologies. Thermal energy storage in general provided the most advantages from a techno-economic point of view compared to other energy storage technologies to supply industrial process heat. It was furthermore concluded that sensible thermal energy storage in the form of solid-state or molten-salt was most interesting for this application. This was mainly due to the commercial availability of this technology to supply medium-temperature process heat for industrial players like Teijin Aramid. Moreover, the characteristics of this technology enabled a good combination with electric heating technologies required to generate the process heat itself. In the future other (thermal) energy storage technology are expected to emerge as viable alternatives but this still requires further research and technological developments. A more in-depth of how the electric heating and thermal energy storage could be combined in practise to realise the desired electrification of the process heat demand will be given in Section 2.1.

1.3.3. High-temperature heat pump technologies

To introduce (high-temperature) heat pump technology it was useful to start at the basic heat pump principle as illustrated in Figure 1.10. The main goal of a heat pump system is to elevate a heat source from a certain temperature to a higher temperature due to utilization of external work, generally in the form of electrical energy (Moen and Heggset, 2021).

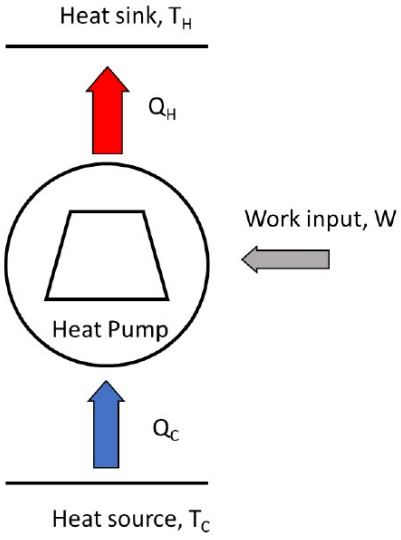

Figure 1.10: Basic heat pump principle (Moen and Heggset, 2021).

Thermodynamically every heat pump system is based on the first- and second law of thermodynamics. The first law expresses that the system's internal energy has to be constant over the whole cycle, hence the change of the internal energy has to be zero. This is expressed through Equation 1.3 wherein 'ΔU' denotes the change in internal energy, 'Q_C' represents the thermal energy supplied by the heat (cold) source, 'Q_H' signifies the thermal energy delivered to the heat (hot) sink, and 'W' denotes the work input. This law states that to comply with the law of conservation of energy the amount of heat delivered to the heat sink should be equal to the amount of heat energy taken from the heat source plus the performed work. According to the second law, as shown in Equation 1.4, heat transfer only spontaneously occurs from higher to lower temperatures. This is due to entropy always being equal or larger than 0. Therefore, external work is required to realize the reverse flow of heat and deliver heat to the heat sink at elevated temperatures.

$$\Delta U = Q_C + W + Q_H = 0 \tag{1.3}$$

$$\Delta S \geq 0 \tag{1.4}$$

Efficiency is generally characterized as the ratio between the energy required that is required by the system and the energy that is delivered by the system.. This ratio can never exceed 1 due to the principle of conservation of energy. However, as shown in Figure 1.10 and Equation 1.3 for a heat pump the energy put into the system consists of both work "W" and heat energy "Q_C" extracted from a heat source. As the heat source is generally either waste heat or coming from the surroundings "for free" it is more useful to express the efficiency of a heat pump through the Coefficient of Performance (COP). The COP is the ratio between the produced heat energy that can be used "Q_H" and the amount of electrical energy or external work "W" needed to produce this heat as shown in Equation 1.5.

$$COP = \frac{Q_H}{W} \tag{1.5}$$

The required external work is always smaller than the produced heat energy, due to the additional heat extracted from the heat source. Therefor, the COP is always larger than 1. The COP generally takes values between 2 and 5 depending on the temperature difference between the heat source and sink (Moen and Heggset, 2021). This means an "efficiency" of 100-500% which clearly shows the benefit

of a heat pump versus standard electric heating with a maximum efficiency of 100%, or COP of 1.
In terms of thermodynamics the reverse Carnot cycle is the most efficient, due to consisting of only reversible processes ($\Delta S = 0$). The Carnot cycle is therefore generally called the ideal heat pump cycle. Hence the ideal COP is referred to as the Carnot COP, the maximum COP that can be theoretically achieved. Based on this combined with the first and second law the ideal COP can be written as shown in Equation 1.6 (Hołyst and Poniewierski, 2012).

$$COP_{Carnot} = \frac{Q_H}{W} = \frac{Q_H}{Q_H - Q_C} = \frac{T_H}{T_H - T_C} = \frac{1}{1 - \frac{T_C}{T_H}} \tag{1.6}$$

The final form of Equation 1.6 explains why the larger the temperature difference between the heat source Q_C and heat sink Q_H or the required "temperature lift", the lower the COP of the heat pump. Therefore is it for a heat pump always desirable to have a heat source at the highest possible temperature to decrease the required external work. It is important to note that the Carnot COP assumes isothermal heat exchange between the refrigerant and the heat source and sink. However, often heat is exchanged at gliding temperatures where the temperature changes during the heat exchange with the heat source and sink. In this case it is more accurate to make use of the Lorenz COP and is especially suited for heat pump cycles where purely sensible heat transfer occurs. This is for example the case in the reversed Brayton cycle which will be further discussed later (Moen and Heggset, 2021). The Lorenz COP can be defined as shown in Equation 1.7.

$$COP_{Lorenz} = \frac{T_H}{T_H - T_C} \tag{1.7}$$

Where:

$$T_H = \frac{T_{H,out} - T_{H,in}}{\ln(\frac{T_{H,out}}{T_{H,in}})}$$

$$T_C = \frac{T_{C,in} - T_{C,out}}{\ln(\frac{T_{C,in}}{T_{C,out}})}$$

In practise the real COP is dependent on the required temperature lift and negatively impacted by thermodynamic losses and irreversibilities in the cycle (Moen and Heggset, 2021). Therefore, it is often useful to compare the real COP to the Carnot/Lorenz COP through the Carnot/Lorenz efficiency as described in Equation 1.8. This efficiency is for effective industrial heat pumps generally between the 40-60% (Moen and Heggset, 2021).

$$\eta_{Carnot} = \frac{COP}{COP_{Carnot}} \tag{1.8}$$

$$\eta_{Lorenz} = \frac{COP}{COP_{Lorenz}} \tag{1.9}$$

From a thermodynamic perspective there are multiple thermodynamic cycles in existence that could realize this heat pump cycle, something which will be further discussed later. Currently the most dominant cycle is the vapour compression heat pump cycle, often referred to as the standard heat pump cycle. The above-described reverse Carnot cycle is only a theoretical cycle and not realisable in practise. Therefore, the standard heat pump cycle is based on the reverse Rankine cycle with isenthalpic expansion instead of isentropic expansion. The P-h and T-s diagram of the reverse Rankine cycle are shown in Figure 1.11. Other identified cycles suitable for heat pump technology are the reversed Stirling cycle, reversed Ericsson cycle and reversed Brayton cycle.

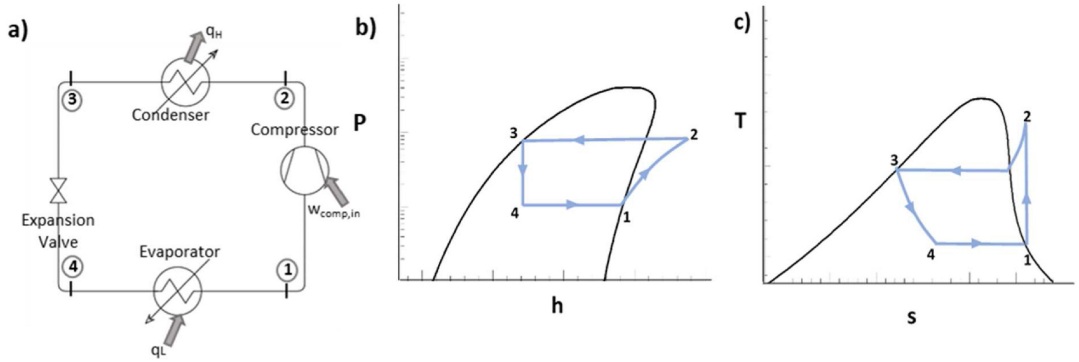

Figure 1.11: Schematic overview of reverse Rankine cycle including P-h and T-s diagrams (Adamson et al., 2022).

For industrial applications the practical working principle of the standard heat pump cycle can be illustrated with a simplified overview as given in Figure 1.12. The Figure shows the different components and flows of energy through the heat pump system. The cycle starts at the evaporator where heat energy is extracted from the (waste) heat source and absorbed by the refrigerant which causes the refrigerant to evaporate and become low-temperature vapour. The refrigerant is compressed in the electrically driven compressor to a high-temperature vapour. In the condenser heat energy is rejected by the refrigerant condensing it again from vapour to liquid, and this heat is transferred to the (process) heat sink. After this process the refrigerant is expanded through an expansion valve to a liquid/vapour phase at lower temperature and pressure to complete the cycle.

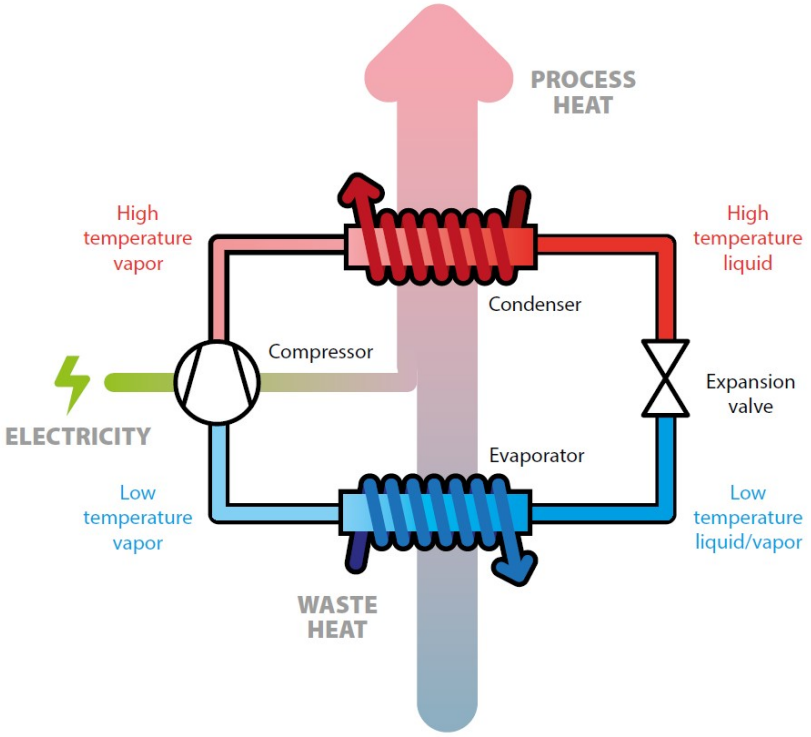

Figure 1.12: Simplified overview of the basic heat pump cycle for industrial applications (de Boer et al., 2020).

Within heat pump cycles a distinction can be made between subcritical, transcritical and supercritical cycles. Most of the heat pumps, including the standard heat pump cycle, work based on a subcritical cycle. In this subcritical cycle the full thermodynamic cycle is completed at temperatures and pressures below the critical point of the working medium or refrigerant. Important for the subcritical heat pump cycle are the critical temperature and pressure of the used refrigerant. As this limits the output temperatures and pressures of the heat pump to ensure subcritical operation throughout the cycle. However,

these lower pressures also generally result in less challenges regarding operation conditions and equipment.
Some more recently developed cycles work based on a transcritical heat pump cycle. In this cycle heat is absorbed from the heat source at temperatures and pressures below the critical point, but the heat is rejected to the heat sink in the supercritical region of the refrigerant. This is done through sensible cooling of the refrigerant in its supercritical phase with a gas cooler instead of a condenser (Adamson et al., 2022). The fact that the transcritical cycle rejects heat in the supercritical region has certain advantages. The outlet temperature and pressure are for example no longer interdependent and the gas cooler enables a larger temperature glide of the refrigerant. This enables optimization of the temperature glide to the heat sink temperature profile. This is desirable as the temperature glide is often substantial when working with process streams, and enables reduction of entropy generation and power consumption (Adamson et al., 2022).
Lastly, the supercritical heat pump cycle operates fully in the supercritical domain of the refrigerant, where the refrigerant does not change phase during the cycle. Heat pump cycles based on this concept have not been developed and commercialized yet but could offer interesting benefits as will be further discussed later.

Current state-of-the-art industrial heat pump technologies

To describe the current state-of-the-art industrial (high-temperature) heat pump technologies it is useful to first define what is considered a high-temperature heat pump. In the course of the literature study multiple definitions were found all related to the heat sink temperature levels. As the exact definition is not of specific importance it was chosen to define a high-temperature heat pump as any heat pump able to reach heat sink temperatures of above 100 °C.
In terms of (industrial) heat pump technologies a lot of different systems are available. This ranges from open to closed systems, and from mechanical compression heat pumps to absorption and adsorption heat pumps each with their own advantages and disadvantages. Nevertheless, all these systems are bounded in terms of the output temperature that can be reached. In 2018 the maximum output temperature of HTHP technology was defined in the range of 90-160 °C (Arpagaus et al., 2018). Technologies able to reach these output temperature include different kind of compression systems and hybrid heat pump technologies. An overview of these state-of-the-art technologies including their heating capacity and maximum heat sink temperatures is shown in Figure 1.13.

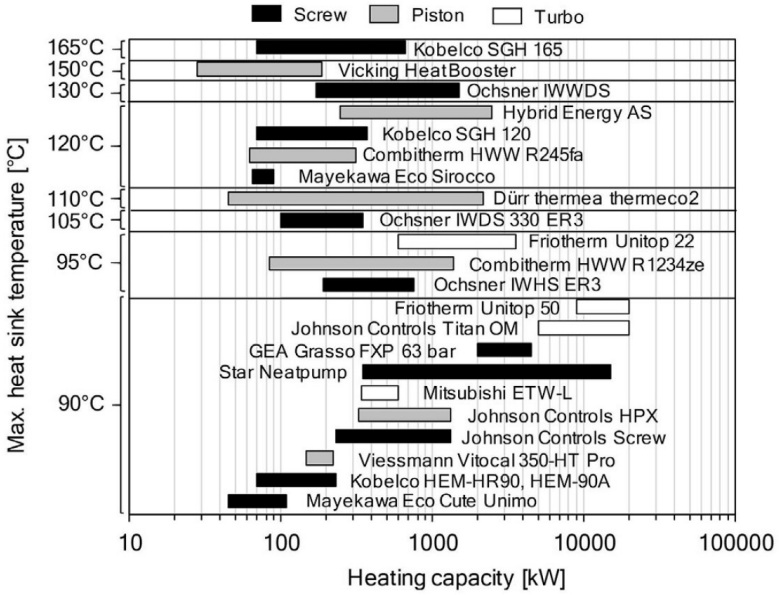

Figure 1.13: Overview of commercially available industrial HTHPs with maximum sink temperature and heating capacity and color-coded based on the compressor type used (Arpagaus et al., 2018).

Since the publication of the paper of Arpagaus et al. (2018) further development and commercialization has occurred. It was found that this is tracked by the Heat Pumping Technologies division of the

International Energy Agency (IEA HPT) in their ”Annex 58: Technologies – State of the art and ongoing developments for systems and components”. In this Annex 58 examples are shown of hybrid heat pumps, developed by e.g. Hybrid Energy, different kinds of compression system heat pumps like a turbo compressor system developed by e.g. Siemens, and a transcritical CO2 system heat pumps developed by e.g. MAN Energy Solutions. Also novel designs are included like a helium reversed Stirling cycle heat pump developed by Olvondo. These HTHP technologies show output temperatures ranging from 120-200 °C and a TRL of 8-9, implicating full commercialization (IEA HPT, n.d.). Furthermore, Adamson et al. (2022) mention a range of 49 heat pump cycle configurations currently in existence that could potentially reach output temperatures of towards 200 °C. Moreover, did Adamson et al. (2022) develop a new concept for a transcritical cascade heat pump cycle which shows promise of reaching a 200 °C output temperature with reasonable COP.

The Annex 58 from the IEA HPT also highlights technologies still under development or in the demonstration/pilot phase with a lower TRL of 4-8. These technologies show promise of reaching output temperatures of up to 250 °C. Other interesting progress in the development of new HTHP technologies is the research by the Deutsches Zentrum für Luft- und Raumfahrt (DLR), who ambitiously aim to deliver heat up to 650 °and on industrial scale in the MW range (Finger and Khass, 2021). Currently, DLR has developed two systems which show promise to reach output temperatures up to 300 °C. First of all, the CoBra system which operates based on a closed reversed Brayton cycle using dried air as working medium. An operational 200-250kW CoBra prototype was constructed in 2022 and is able to reach an output temperature of 300 °C using the surrounding air as heat source. A picture of the prototype can be seen in Figure 1.14. However, with a simulated COP of below 1.5 the performance is expected to be quite poor (Oehler et al., 2021). The other system is the ZiRa system which operates based on a closed reversed Rankine cycle using steam as working medium. A simulated COP of 4 is claimed for the ZiRa system for an output temperature of around 300 °C. However, this has not yet been validated through the construction of prototype of the ZiRa system (Finger and Khass, 2021). The above-mentioned technologies currently under development could potentially be viable to supply process heat at multiple hundreds of degrees. However, it remains to be seen how they will perform in real operation, e.g. what output power can be realized and if a reasonable COP can be achieved for high output temperatures.

Figure 1.14: Prototype of the CoBra heat pump system build in Cottbus, Germany (DLR, n.d.).

An important factor that limits higher output temperatures are the commonly used refrigerants. These refrigerants can only be operated in their subcritical domain due to stability issues in the supercritical phase. It was found that especially for the reversed Rankine or standard vapour compression cycle, based on the phase change of the refrigerant during the cycle, the temperature range is limited by physical properties of the used refrigerant (Oehler et al., 2021). This cycle therefore seems of lesser

interest for new HTHP applications where the refrigerant stays in either a single (supercritical) phase during the cycle or makes use of transcritical operation. It has been illustrated that in more recent developments different refrigerants are combined with alternative kinds of thermodynamic cycles to overcome these limitations. Examples of this are the helium reversed Stirling cycle heat pump or the dried air reversed Brayton cycle heat pump.

$sCO2$ as refrigerant

Currently applied refrigerants are like chlorofluorocarbons (CFCs), hydrochlorofluorocarbons (HCFCs) and more recently hydrofluorocarbons (HFCs). The stability issues for higher pressures and temperatures are the main factor to make them unsuitable for application in new HTHP technologies. It was identified during the literature study that natural refrigerants could prove to be an interesting alternative to enable high-temperature operation. Moreover, most natural refrigerants have low global warming potential (GWP) and low toxicity compared to currently applied refrigerants. This makes natural refrigerants a safer and more climate friendly option. It was concluded that sCO_2, steam and helium are interesting natural refrigerants suited for high temperature applications (Dostal et al., 2006). Specifically, sCO_2 has recently gained attention for use in power and heat pump cycles due to some favourable properties compared to the other natural refrigerants. Moreover, as steam and helium can already be found in recent HTHP developments only the use of $sCO2$ as refrigerant was further investigated in this study.

In subcritical conditions CO_2 shows relative poor performance in terms of theoretical COP and heat transfer characteristics for high-temperature applications compared to other refrigerants like ammonia (Sarkar et al., 2007). However, in supercritical conditions the properties of CO_2 change significantly. In Figure 1.15 the phase diagram of CO_2 is shown, where it should be noted that the pressure axis uses a logarithmic scale. Its triple point is located at about 216.6 K and 5.2 bar, and its critical point at 304.1 K and 73.8 bar (The Engineering Toolbox, n.d.). In practise this results in the fact that in regular conditions CO_2 is always in gaseous phase as can be seen in the phase diagram. Nevertheless, compared to other working media the low critical temperature and reasonable critical pressure makes it possible to compress CO_2 in the supercritical phase within a heat pump cycle.

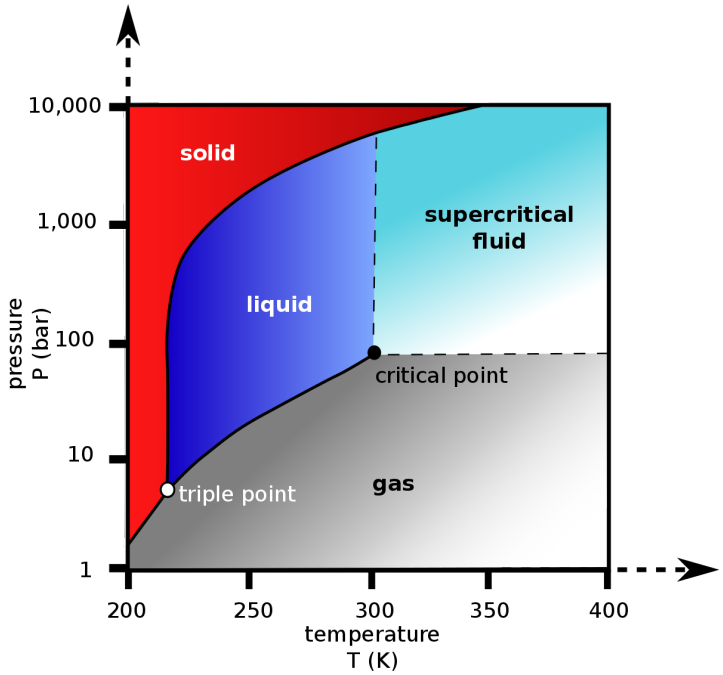

Figure 1.15: P-T phase diagram of CO_2 (Finney and Jacobs, 2010).

The history of sCO_2 cycles is sufficiently long dating back as far as the 1950s and 1960s as a part of research into supercritical thermodynamic power cycles (Karakurt et al., 2020). Additionally, the use

of sCO_2 in nuclear power and power cycles was deemed very promising for high cycle temperatures of above 550 °C compared to the Rankine (steam) cycle (Dostal et al., 2006). Karakurt et al. (2020) mention that CO_2 has a high heat capacity, high heat transfer coefficient, low viscosity, and good mass transfer properties. Furthermore, it has a low surface tension combined with low viscosity which results in low required pumping power. It is non-corrosive in dry environments and non-flammable, explosive, toxic or harmful to the environment (Karakurt et al., 2020). Additionally, in supercritical conditions CO_2 acts like a gas but with the density of a fluid (Cabeza et al., 2017). This relative high density combined with the high heat capacity results in a high volumetric heating capacity (VHC) and energy density for sCO_2 compared to other working media. Practically, this results in the fact that the compression work can be greatly reduced. The thermophysical properties that generally control the heat transfer of CO_2 as working medium are the constant pressure specific heat, the thermal conductivity, the dynamic viscosity and the density (UNILAB SRL, 2019). What happens with these properties around the critical point of CO_2 is illustrated in Figure 1.16, where especially the decrease in density aids the properties of sCO_2 as refrigerant.

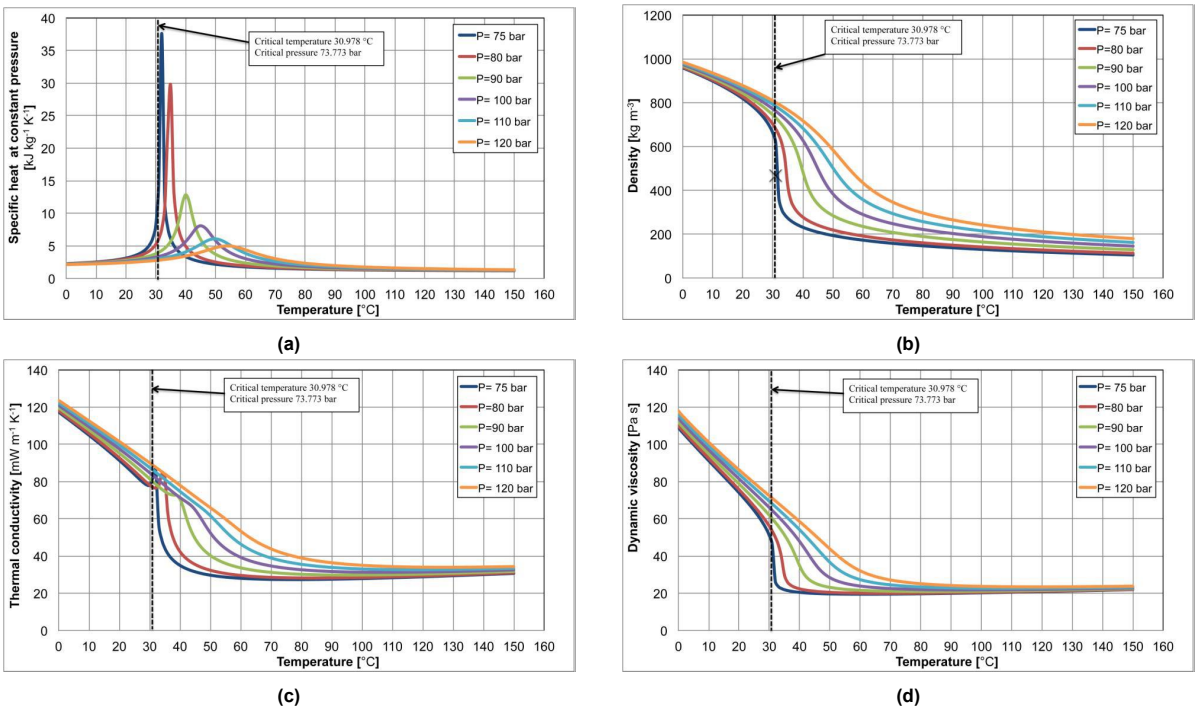

Figure 1.16: Thermophyiscal properties of CO_2 around its critical point presented for a range of temperatures and pressures around the critical point (UNILAB SRL, 2019).

Moreover, in supercritical conditions CO_2 is for example nearly twice as dense as steam significantly reducing the required sCO_2 volumes (Patel, n.d.). Most components such as the compressor, turbine and heat exchangers can therefore be largely reduced in size enabling compact turbomachinery design compared to for example steam cycle equipment as illustrated in Figure 1.17 (Persichilli et al., 2012). This more compact equipment enables the system to have a lower footprint in terms of required space and reduces overall costs. The single-phase nature is also advantageous for the use of turbomachinery as this needs to deal with just one phase during compression and expansion. The high pressures the sCO_2 cycle would operate at also make the effect of the pressure drop over the heat exchangers less significant. The trade-off that normally must be considered in heat exchangers between the heat transfer and pressure drop becomes less of an issue. This enables higher heat transfer between the sCO_2 and the process streams.

Finally, sCO_2 cycles are able to operate efficiently at a wide range of temperatures and $sCO_2$is still stable at high temperature-pressure combinations. This is of interest as this indicates that if the equipment can deal with the required temperature- and pressure levels sCO_2 heat pumps can in theory be

used for high-temperature process heat. Additionally, sCO_2 is able to effectively exchange heat when the process streams have a more or less constant heat capacity. This is due to the character of its heat capacity which prevents pinch points in the exchange of heat (Persichilli et al., 2012). However, it should be noted that due to the required high operating pressures special kind of equipment and careful system design is required. This could result in significant system complexity and high cost compared to systems using alternative refrigerants.

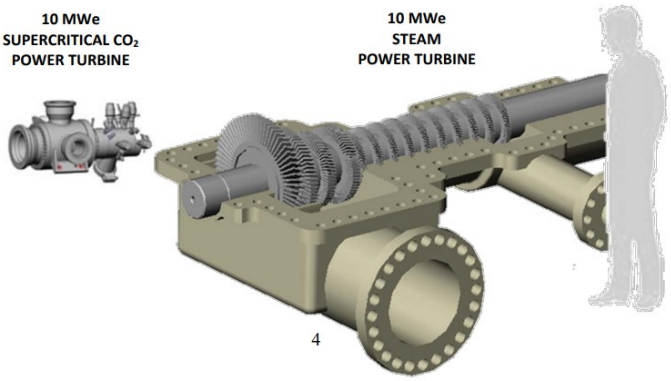

Figure 1.17: An example of the size of a 10 MW sCO_2 power turbine compared to a 10 MW steam turbine (Persichilli et al., 2012).

Due to the interesting properties of sCO_2 interest has grown to apply it in new technologies such as transcritical heat pumps. The transcritical CO_2 heat pump operates partly above and partly below the critical point of CO_2. The special properties of CO_2 around the critical point makes operation close to this critical region interesting. Its advantages include a higher temperature lift in the gas cooler and a higher efficiency, but requires operation with high refrigerant pressures of over 100 bar (De Kleijn Energy Consultants & Engineers, n.d.). The mentioned example of a transcritical CO_2heat pump developed by MAN Energy, the MAN HPU, shows the potential of using sCO_2 as refrigerant for high-temperature operation.

Reversed Brayton cycle

In the literature study a few alternative thermodynamic cycles suitable for HTHP technology were identified: the reversed Stirling cycle, the reversed Ericsson cycle, and the reversed Brayton cycle.
The reversed Stirling cycle has been extensively researched and already found its way into commercialized HTHP technologies with the combination of helium as working medium, such as in the Olvondo HighLift. The reversed Ericsson cycle could also theoretically be used as an alternative heat pump cycle. However, it showed less interesting properties compared to the other cycles and no recent studies or commercial developments around a power cycle or heat pump cycle based on the reversed Ericsson cycle were identified in literature. Therefore, it was decided to dedicate further research to the reversed Brayton cycle.

The reversed Brayton cycle, also known as the gas refrigeration cycle, Joule cycle or most commonly the Bell-Coleman cycle, was briefly mentioned as part of the CoBra system. It is the reversed (closed) version of the well-known regular open Brayton power cycle used in for example gas turbines and jet engines of airplanes. The reversed Brayton cycle is relative more unknown cycle with fewer applications. However, the idea to look at reversed Brayton cycle for heat pumps is not entirely new as it was for example already investigated in 1995 by Angelino & Invernizzi. They mentioned that the fact that the reversed Brayton heat pump cycle operates in vapour phase without phase change means there is solely sensible heat exchange. Under subcritical operating conditions this causes larger turbomachinery losses and worse performance compared to the reverse Rankine cycle heat pump (Angelino and Invernizzi, 1995). However, their most important finding was that expansion close to the critical point and high maximum cycle pressures of towards 100 bar showed potential for acceptable efficiencies. According to Angelino & Invernizzi (1995) the reversed Brayton cycle heat pump was most promising for large-scale and high-temperature non-isothermal applications where conventional cycles would need to become overly complicated and able to deal with high pressure ratios. More recently, interest

in the thermodynamic cycle has sparked as a power/heat pump cycle in applications like PTES/ETES and shows promise as an alternative heat pump cycle for new HTHP technologies. In Figure 1.18 below the P-V and T-S diagram of the (ideal) reversed Brayton cycle are depicted. The cycle consists of two isentropic processes, isentropic compression and expansion, and two isobaric processes, isobaric heat rejection and heat absorption.

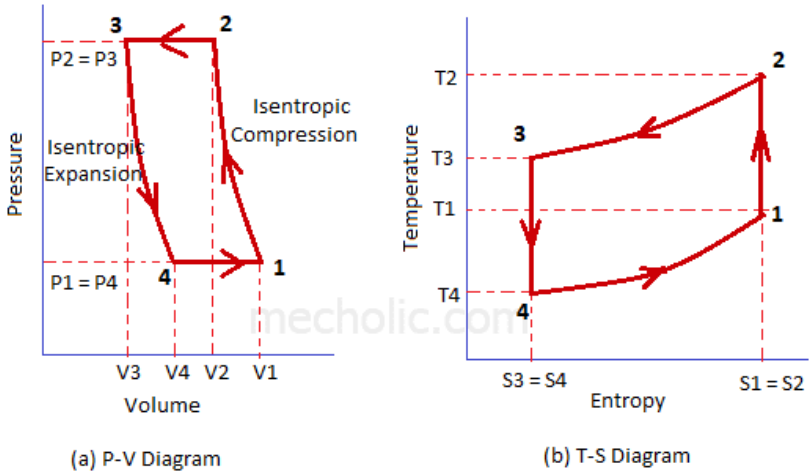

Figure 1.18: P-V and T-S diagram of the reversed Brayton cycle (Mecholic, n.d.).

In a more practical sense, the reversed Brayton heat pump cycle works as shown by the simplified cycle overview in Figure 1.19. Generally, the system shows large similarities with the standard heat pump cycle as shown in Figure 1.12, but there are two main differences. Firstly, the expansion valve is replaced with a turbine where the expansion takes place and which is connected directly to the compressor. Secondly, the evaporator and condenser are replaced by two heat exchangers to exchange heat with the heat source and heat sink. The heat source heat exchanger is also commonly referred to as the gas heater and the heat sink heat exchanger as the gas cooler. The main advantage of the reversed Brayton cycle is that during the isentropic expansion energy is re-generated by the turbine. This opposed to the use of an expansion valve that just expands the refrigerant without re-generating energy. As the turbine is connected to the compressor, work is done by the turbine on the compressor which reduces the external compression work required. In other words, the overall amount of work needed is decreased and the COP increases. This is most advantageous in heat pump cycles that involve high pressure ratio's and that involve expansion solely in the gas/supercritical (single) phase. The reason for this is that with high pressure ratio's an expansion valve creates significant irreversibilities and that turbines are more suited for single phase operation. The use of $(s)CO_2$ therefore gives the reversed Brayton cycle the potential to be advantageous over the standard vapour compression heat pump cycle.

The application of the reversed Brayton cycle also comes with some disadvantages. However, as little research was present on the combination of the cycle with sCO_2 as refrigerant most of this disadvantages were not directly applicable. Nevertheless, a notable disadvantage is the that the reversed Brayton cycle consists of the refrigerant purely in the (supercritical) gas phase. This results in the fact that the reversed Brayton cycle does not benefit from a phase change and only sensible heat is exchanged. Something that results in for example larger required mass flows of the refrigerant inside the heat pump cycle. Additionally, the heat transfer takes place within a certain temperature range and requires high compression. Turbomachinery efficiencies also strongly limit the COP of the reversed Brayton cycle especially at lower temperature levels (Wang, 2018). More recently the (reversed) Brayton cycle with different kinds of working media has gained attention. One example that was briefly mentioned is the CoBra system which makes use of a reversed Brayton cycle with dried air as working medium. With a working 200 kW prototype able to reach output temperatures towards 300 °C it shows the potential for reversed Brayton cycle-based heat pumps.

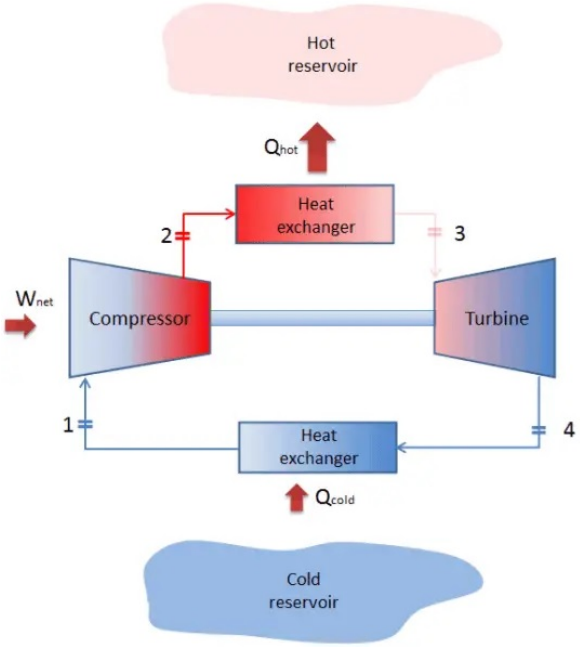

Figure 1.19: Simplified overview of the reversed Brayton cycle (Nuclear Power, n.d.-a).

Furthermore, the combination of sCO_2 and (reversed) Brayton cycles was strongly present in literature. It was observed that most studies were focused on power cycles and applications such as nuclear power generation. This makes sense as it was shown that at high temperatures (>450 °C) the cycle outperforms other power cycles in terms of (thermal) efficiency (Dostal et al., 2006)(Ahn et al., 2015). On the other hand, also concentrated solar power (CSP) and PTES have already been named as interesting applications of the sCO_2 reversed Brayton cycle (Garg et al., 2013)(Zühlsdorf et al., 2019). Some studies related to PTES were of interest and are largely similar to how a sCO_2 reversed Brayton HTHP for industrial applications could operate. As briefly mentioned the Carnot battery concept was reiterated for these concepts, with the use of a heat pump inside the system that operates based on the reversed Brayton cycle. Designs proposed by GE make use of large-scale and off-the-shelf compressors and turbines from oil and gas applications. With a COP of just 1.3 the performance was relatively poor. Nonetheless, for these storage application in combination with solar power a reasonable round-trip efficiency and cost competitiveness with other storage technologies could be achieved (Aga et al., 2016). In comparable studies from Tafur-Escanta et al., 2022 and Linares et al., 2023 a techno-economic analysis was done of a sCO_2 reversed Brayton cycle PTES system based on the Carnot battery concept. The studies reported promising results in terms of heat pump COP and round-trip efficiencies.

Moreover, promising findings were obtained from the study done by Zühlsdorf et al. (2019). In this study they analysed a HTHP concept based on the reversed Brayton cycle with sCO_2 as refrigerant able to reach output temperatures up to 280 °C. The numerical model of the cycle was operated with pressures between 40.7 and 140 bar resulting in a compressor outlet temperature of 290 °C and a COP of 1.72 (Zühlsdorf et al., 2019). In addition, interesting research was conducted by Moen and Heggset (2021), largely similar to the study done by Zühlsdorf et al., 2019. In this study they designed a concept for a reversed Brayton heat pump based on sCO_2 for output temperatures up to 250 °operating with pressures between 150 and 356 bar and obtaining a COP of 2.44 for a heat source inlet temperature of 160 °C (Moen and Heggset, 2021). Finally, was a paper from Huang et al. (2022) identified that included an investigation into the thermodynamic-economic potential of a two-stage sCO_2 heat pump based on the reversed Brayton cycle. The cycle made use of refrigerant injection and an internal heat exchanger and operates fully in the supercritical domain. Using the numerical model of the cycle they investigated the performance with heat sources ranging between 45 and 75 °C and resulting in output temperatures ranging between 121.5 and 157.1 °C while reporting a COP ranging between 2.34 and

3.05.

Conclusion
Based on what was found in literature the combination of sCO_2 and the reversed Brayton cycle presented an interesting direction for further research. The unique properties of sCO_2 combined with the performance of the reversed Brayton cycle at high-temperature operation has the potential to lead to a break-through in the development of HTHP technology. Recent implementations of the reversed Brayton cycle in the Cobra HTHP prototype and PTES systems show the feasibility of applying this concept to an industrial sCO_2 reversed Brayton HTHP. Moreover, did the MAN HPU indicate the potential of sCO_2 heat pump cycles. However, the studied literature also showed that the practical potential and feasibility of an industrial sCO_2 reversed Brayton HTHP had not yet been successfully mapped.

The PTES systems that involved the sCO_2 reversed Brayton cycle are on multiple aspects fundamentally different than how an industrial sCO_2 reversed Brayton HTHP would operate. The studies from Zühlsdorf et al. (2019), Moen and Heggset (2021) and Huang et al. (2022) present a numerical model of an industrial sCO_2 reversed Brayton HTHP. However, for their modelling of the equipment Zühlsdorf et al. (2019) mention that they make use of large-scale equipment from the oil and gas industry and use conservative estimates for the isentropic efficiencies based on the discussed paper from Angelino & Invernizzi (1995). To estimate the costs Zühlsdorf et al. (2019) mention that Turton cost estimations are used. It was observed that was done purely based on the output powers of the turbomachinery and no detailed cost estimations were done. Moreover, the used equipment was not modelled in detail and it was not discussed what equipment would be required to realize the mentioned 50 MW output power. In the study by Moen and Heggset (2021) no cost estimations were given although the design was in terms of equipment more detailed and extensive. The equipment efficiencies were in the studies Moen and Heggset (2021) and Huang et al. (2022) also roughly estimated and adapted from the study by Zühlsdorf et al., 2019. While this enables a straightforward basis for the modelling it are rough and conservative estimates that prevents a realistic design. The design from Moen and Heggset (2021) also required pressures of beyond 345 bar which is currently considered as the maximum operating pressure for sCO_2 compressor. Furthermore, the choice of equipment like the use of a printed circuit heat exchanger (PCHE) was not fully justified, and no mention was done of for example the use of an ejector or other potentially interesting equipment to improve performance. The discussed studies and (numerical) designs of sCO_2 reversed Brayton HTHP technologies seemed a bit superficial. Nonetheless, the generated outputs could be useful for the validation of the HTHP design proposed in this study.

All in all, the studied literature showed that a sCO_2 reversed Brayton cycle could be viable. However, there a knowledge gap was identified in combining sCO_2 with a reversed Brayton cycle to investigate the potential for an implementable industrial HTHP technology. Mainly at the component level a lot of different approaches were identified and there was room to investigate how the basis cycle could be improved through for example ejector technology. It has not yet been clearly defined what kind of equipment would be needed to actually realize a sCO_2 reversed Brayton HTHP and what costs could be realistically expected. Therefore, it was decided to research this in more detail to be able to give a good assessment of the potential and feasibility of sCO_2 reversed Brayton HTHP technology.

1.4. Structure

This thesis report is organized as follows. Chapter 2 provides an overview of the investigation into E-heating combined with thermal energy storage. The focus of this investigation is on the case study of Teijin Aramid, and a techno-economic analysis was conducted to assess the feasibility of electrifying their process in the near future. In Chapter 3, a detailed description of the numerical investigation into the sCO_2 reversed Brayton HTHP is presented. This includes an explanation of the thermodynamic models constructed in Python, and a parametric analysis to determine the optimal HTHP design. The chapter concludes with proposed HTHP designs, along with detailed cost estimations obtained through Aspen Plus. Chapter 4 briefly discusses the potential combination of HTHP technology and (alternative) TES solutions in the future. Chapter 5 discusses what uncertainties had to be considered in the research and what relevance the obtained results have. The report concludes with Chapter 6, where final conclusions are provided, along with recommendations for future work.

2

Electric heating with thermal energy storage

2.1. Electric heating and thermal energy storage

Based on the reviewed literature as discussed in Section 1.3.1 & Section 1.3.2 two main conclusions were done. First of all, it was concluded that currently the most promising solution to electrify medium-temperature process heat for industrial applications is the use of electric heating. In relation to the case study for Teijin Aramid the electric heating method would have to be an E-heater to heat the thermal oil loop. Secondly, this electric heating should preferably be combined with a commercially available TES system to to deal with the intermittency of supply through VRE production. The optimal storage time to be able to deal with longer periods of deficits in VRE production still had to be further investigated. This would also be largely affected by the techno-economic feasibility of the proposed system. The proposed system of an E-heater combined with TES will from here on be referred to as the E-heater + TES system. This combination was deemed most promising as it was already found to be commercially available. Multiple manufacturers of such a combined E-heater + TES system were identified. The most notable manufacturers identified were:

- Kraftblock
- EnergyNest
- Kyoto
- Rondo Energy
- Magaldi
- Lumenion GmbH
- Brenmiller
- MGA Thermal*

It should be noted that the MGA Thermal TES system is currently not yet commercially available hence the '*'. MGA Thermal is currently constructing its first pilot plant and their solution is expected to become commercially available in the near future. All solutions make use of sensible TES with either solid-state materials or molten-salt. However, Magaldi uses a slightly more complex system with fluidized sand. Moreover, MGA Thermal combines a solid-state material with a miscibility gap alloy (MGA) that acts as a PCM and is contained inside the brick (MGA Thermal, n.d.). This results in some of the advantages connected to LHS as explained in Section 1.3.2, especially regarding the combined energy density of the storage material. Their solution can therefore be seen as a combination of sensible- and latent TES. A more in-depth analysis of the differences between the TES solutions from the above mentioned suppliers will be given in Section 2.2.3.

The operating principle of a continuously operating E-heater + TES can be explained through the schematic in Figure 2.1 below.

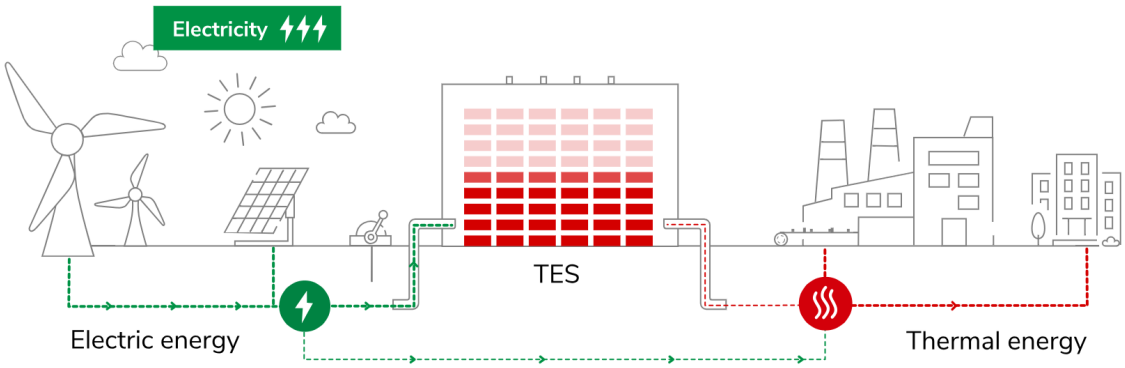

Figure 2.1: Example of a combined E-heater and TES system to supply process heat (Lumenion, 2023).

In the figure it can be seen that the system generally consist of three sections:

1. Charge with electrical energy (electricity)
2. Storage (TES)
3. Discharge of thermal energy (process heat)

The process undergoes a transformation from electrical energy, preferably coming purely from VRE sources like solar and wind, to thermal, or heat, energy. This conversion is in TES systems practically realized with the use of resistive heating, through the E-heater, to convert electrical energy into thermal energy. The storage part of the system is not necessarily a part in this energy conversion but serves as the a way to decouple the charge and discharge process. As mentioned that largest challenge with VRE production is the intermittency with intraday and multiday variations resulting in surpluses and deficits of renewable energy over time. To therefore maximize the use of purely renewable energy the TES can be charged during surpluses of renewable energy, and discharged during deficits.

It can be seen in Figure 2.1 that in order to realize the required continuous 24/7 (base load) supply of process heat to the industrial process there are two streams of electrical energy. The conversion of electrical energy to thermal energy to charge the TES is not separately shown. Generally, an external E-heater is used to charge the TES as well as directly deliver thermal energy to the industrial process through a ”bypass ”in times of surpluses of VRE production as illustrated in the Figure. This is important as most commercially available TES systems are not able to charge and discharge simultaneously. In times of deficit of renewable energy the electrical energy to thermal energy conversion stops and the process heat is provided purely by the TES. An additional advantage of this setup is that the required size of the TES can be reduced. This as only thermal energy needs to be stored to supply the process heat when there is a deficit of renewable energy. Moreover, if something happens with the TES system heat can still be provided directly to the process. Some E-heater + TES systems do not require this bypass as they are able to simultaneously charge and discharge the TES and continuously supply the process heat to the industrial process. This however requires a more complex system compared to the system illustrated in Figure 2.1.

Depending on the size of the TES and the amount of thermal energy required continuously for the process the storage time can be varied. This directly affects its ability to properly cover the deficits in renewable energy production. As discussed an inherent challenge in the electrification of industrial process heat is the mismatch between a continuous demand and an intermittent supply. Therefore, the concept of demand-side response also plays a role. In practise DSR means that during deficits of renewable energy the thermal energy demand from the process can be reduced, while during surpluses

the thermal energy demand demand from the process can be increased. In other words, decrease demand during times of low supply and increase demand during times of high supply to better deal with the intermittency from VRE sources. The E-heater + TES system itself does not have a direct role in this but the combination of the storage and DSR enables longer storage times. This either results in a reduction of the required size of the storage or enables a better match with the intermittency of renewable energy supply. An important question regarding energy storage was therefore the storage times that are desired. This in order to properly cover the intermittency in VRE supply. This is something which will be further discussed in Section 2.2.4.

The electrification of industrial process heat through the application of electric heating combined with thermal energy storage has two other important considerations: the technical feasibility for the process and the cost-competitiveness compared to fossil fuel heating systems.
In terms of technical feasibility it is mainly the question if the current process can be adapted to receive the required process heat through the E-heater + TES solution as opposed to a heater using fossil fuels. The main considerations here are the required power and temperature levels as well as factors like spatial- and safety requirements and response times. The required data to asses the technical feasibility was gathered through a combination of own research and interviews with four of the TES manufacturers mentioned above. A more in-depth analysis of the technical requirements will be discussed in Section 2.2.2 for the case study process of Teijin Aramid. In terms of cost-competitiveness compared to fossil fuel heating systems this is two-fold. There are initial system investment costs measured through the capital expenditure (CAPEX) costs. As well as ongoing expenses measured through the operation and maintenance (O&M) costs of the equipment and operating expenditure (OPEX) costs of the required energy. For most industrial players like Teijin Aramid the OPEX costs are a trade-off between the electricity price versus the natural gas price that is paid.

The CAPEX and O&M costs of an E-heater + TES system depend mainly on the characteristics of the system and the operating conditions as well as the required additional equipment. A lot of technical parameters like the required temperature levels, charge and discharge power and used storage material come into play here. These CAPEX and O&M costs could be predicted based on literature but it was quickly observed these predictions vary greatly with large uncertainty ranges. This hindered an accurate prediction of what costs could be expected. Moreover, these initial investments cost were expected to be considerable for an E-heater + TES system compared to a simple natural gas heater. It was therefore deemed of interest to get accurate data on this. Through meetings with four of the TES manufacturers mentioned earlier, detailed data with regard to the CAPEX and O&M costs was obtained. The economic parameters involved with this will be discussed in more detail in Section 2.2.2 for the case study process of Teijin Aramid.

To make accurate predictions in terms of OPEX costs proved to be very difficult as there are so many factors involved in the development of the global energy system. Therefore, the future developments in the prices of electricity and natural gas are always rough estimates at best. However, based on historical data and predictions from reports by for example Klimaat- en Energieverkenning (KEV) and Netbeheer Nederland it was possible to get an idea on this. Thereby, analyzing how the prices of electricity and natural gas currently compare to each other and how this is expected to change in the (near) future. To get an idea for what could be expected in terms of OPEX costs for such an E-heater + TES system compared to a natural gas heater an own analysis was executed which will be discussed in Section 2.2.5.

2.2. Techno-economic analysis for Teijin Aramid's process

In this section the research done for Teijin Aramid with regard to the electrification of the final part of the the sulphuric acid recovery system of the Emmen plant will be described. This research was done through a techno-economic analysis of the process and the electrification of this process through the application of an E-heater + TES system. First a description and analysis of the current process will be given including the possibilities for DSR in Section 2.2.1. After this will in Section 2.2.2 an overview be given of the technical and economical parameters that needed to be considered in the design of an appropriate E-heater + TES system. In Section 2.2.3 a general overview will be given of the commercially available E-heater + TES solutions with their advantages and disadvantages compared to each other. Then in Section 2.2.4 the own global analysis on the current surpluses and deficits in VRE production in the Netherlands will be given. This is accompanied by a future outlook based on the II3050-scenario's from Netbeheer Nederland. This will be followed by an own analysis on historical electricity- and gas price data in the Netherlands and predictions based on the KEV 2022 report in Section 2.2.5. Finally, will the setup of the techno-economic analysis for Teijin Aramid be briefly discussed in Section 2.2.6.

2.2.1. Process description and analysis

Teijin Aramid is world-leader in the production of a wide range of aramid based fibers. Aramid based fibers are recognized for their strength and are used in high-performance materials. These materials are suited for products ranging from bullet-proof vests and fire-proof clothing up to racing cars and airplanes which require the ability to withstand high forces and temperatures. Due to confidentiality restrictions it is not possible to go into extensive detail of how Teijin Aramid's process operates. However, a general description will be given. The focus of the description is on the part of the process that was analyzed for the case study to electrify the process heat demand. The production of aramid yarn sold under the name Twaron is done within two plants in the Netherlands, the Delfzijl plant and the Emmen plant. The aramid polymer is produced in Deflzijl. The aramid polymer is then transported to the Emmen plant where the Twaron fibre is "spinned" from this aramid polymer. Sulfuric acid at an concentration of 99.8% is used to dissolve the aramid polymer which is then processed into aramid yarn in the spinning plant. In the process involving the sulfuric acid it is diluted with water to a concentration of 15%. In the sulfuric acid recovery plant this concentration is reprocessed back to a concentration of 96%. The final step to get to 99.8% is done with the help of Oleum.

The focus of this research was on the sulfuric acid recovery plant which consists of a few stages to go from a 15% concentration to a 96% concentration of sulfuric acid. The stages and concentrations before and after every stage are shown in Figure 2.2. The recovery consists of a two stage mechanical vapour recompression (MVR), a three stage multiple effect and a single effect in the "Bertrams" and two stage single effect in the "Plinke". In Figure 2.2 all the energy streams in the sulfuric acid recovery are also depicted. The red arrows indicate energy that flows into the different systems either in the form of electricity, low-pressure (LP) or medium-pressure (MP) steam, or natural gas as indicated in the Figure. The blue arrows indicate (waste) energy that is released in the form of condensate. In theory these outgoing streams of condensate could potentially be used as a source of heat energy for heat pump technology. In terms of heat energy the condensate streams contain multiple MW of energy but unfortunately at a temperature level of around 30-40 °C. These low temperature levels make the condensate streams not directly useful for the HTHP designs investigated in this study.

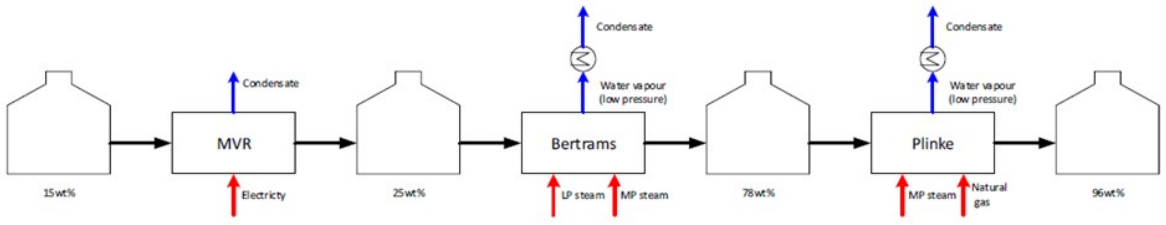

Figure 2.2: Simplified overview of the full sulfuric acid recovery process

This sulfuric acid recovery process is very energy-intensive due to the high soluble heat of sulfuric acid

in water and the heat of vaporization of water. As can be seen in Figure 2.2 the MVR and Betrams are powered with electricity and steam but the Plinke is partly powered with natural gas, which was therefore selected as the focus for the research. In Figure 2.3 below the full process that occurs within the Plinke is shown. The process consists in terms of equipment of a mid-pressure (MD) steam heater, a scrubber, a condenser, a hot oil (HO) heater, a flashdrum and a circulation pump. The feed of 78% sulfuric acid enters the process through the steam heater, the first stage, where it is heated and sent to the scrubber. The second stage of the process is used to maximize the sulfuric acid concentration in the product. This is done by flashing the sulfuric acid in the flash drum and sending the (water) vapour through the scrubber to recover heat. To get the sulfuric acid at the required temperature for the flash process, the sulfuric acid stream is heated in the HO heater and with the help of the circulation pump transported through the system. After the flash drum the 96% sulfuric acid leaves the process as product stream. The remaining water vapour is disposed as condensate through the condenser, which requires some cooling water (KW).

As mentioned, for the second stage thermal/hot oil, is used to heat deliver the required process heat through the ”HO heater”. This is done at a temperature level of around 280 °C delivering on average about 2-4 MW of thermal energy. In the current operation of the plant this thermal oil is heated through the combustion of natural gas in a separate natural gas heater. Therefore, this final stage of the sulfuric acid recovery in the Plinke was chosen to investigate the techno-economic feasibility to electrify this process heat demand.

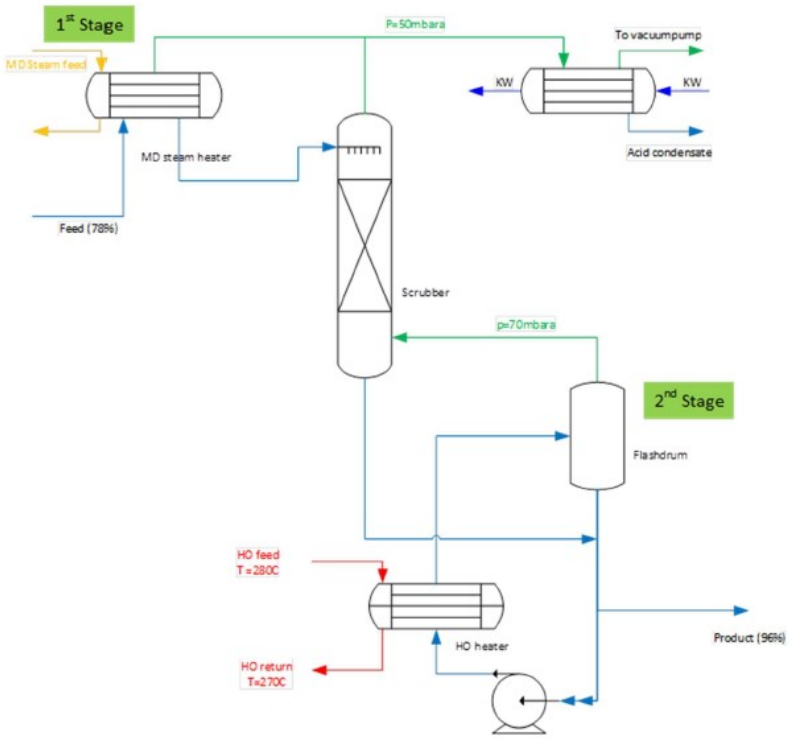

Figure 2.3: Simplified overview of the analyzed step inside the sulfuric acid recovery referred to as the ”Plinke”.

The required temperature and power level are not constant and depend on the operation of the process. First of all, the Plinke consists of two identical installations that, if in operation, always need to operate between a certain minimum and maximum output. This translates into a certain required power level in terms of process heat with a long-term average requirement of around the mentioned 2-4 MW. The E-heater + TES system should therefore be able to directly and continuously deliver between 0 and 5 MW of process heat. The same holds for the delivered temperature level which should be somewhere between 250 and 290 °C. The thermal oil is recirculated back to the heating system at a temperature

of about 5- 20 °C lower.

What was interesting regarding the possibilities for DSR is that in the current process not all feed of 78% that comes from the Bertrams is processed to 96% in the Plinke. Moreover, not all product of 96% produced with the Plinke is worked up to 99.8% to be used again in the spinning plant. This results in that a part of both 78% and 96% is stored in storage tanks and sold to customers that require the sulfuric acid at these concentrations. Opposed to using everything to dissolve the aramid polymer. Moreover, the presence of two Plinke installations and the ability to vary the throughput of sulfuric acid means that the required amount of process heat can be varied within a certain range. This combined, results in the fact that there is room for some DSR. If there is a deficit in renewable energy available and the electricity prices increases the production of 96% can temporarily be reduced to decrease the thermal energy demand and the TES can deliver heat for a longer time without charging. Later, when there is again a surplus of renewable energy the production of 96% can be ramped up with the available overcapacity from the Plinke's to compensate for the lower production earlier. It should however be noted that this overcapacity is limited in comparison the the amount of product of 78% that comes from the Bertrams. Thus, in order to keep the levels of feed and product within the capacities of the storage tanks a part of the 78% and 96% would probably have to be sold. Moreover, would it help to purchase some extra storage tanks to create more storage capacity available for DSR. Nevertheless, it was concluded that some form of DSR was possible. This would make the process more suited to match the intermittency of VRE sources and decrease the OPEX of the E-heater + TES system.

2.2.2. Technical and economical parameters

In order to be able to execute a good techno-economic analysis on the E-heater + TES solution it was important to identify what technical and economical parameters played a role. To replace a natural gas heater with an (resistive) E-heater was from a technical viewpoint not very challenging and also the cost related to this are straightforward. Therefore, most of these parameters were connected to the TES as this was the more complex part of the system. Generally, the most important things to consider were first of all the energy density that could be realized within the TES as this had a large impact on the size and the CAPEX cost of the system. Moreover, the round-trip efficiency and energy loss over time were important as this also had a significant impact on the costs. The OPEX that could be expected by effectively utilizing the TES to profit from the dips in the electricity price due the surpluses of VRE production was another important parameter to assess the economic feasibility. Finally, the compatibility of the E-heater + TES system with the current process and possible operating and safety constraints were of significant importance from a technical point of view. A more detailed description of the technical and economical parameters considered will be given below.

As mentioned in Section 2.1 this data was obtained through a combination of publicly available data from internet as well as through interviews with Kraftblock, EnergyNest, Kyoto and Magaldi for detailed information on their systems. It would have been interesting to have gathered more detailed data from the other TES suppliers. However, this was constrained by a combination of time limitations and not being able to establish contact with some suppliers. As the goal of the study was to get a general idea on the techno-economic feasibility of the E-heater + TES solution for Teijin Aramid the detailed data from the four mentioned TES suppliers was deemed sufficient.

The quantitative technical parameters that were considered to asses the techno-economic feasibility of the E-heater + TES solution were:

- Operating range of output power/discharge rate in MW_{th}
- Operating range of input power/charge rate in MW_{el}
- Required input voltage in V and current in A
- Operating temperature range in °C
- Maximum possible storage duration in days
- Energy losses per day in % of the storage capacity
- Energy density in MWh/m3
- Maximum storage capacity in MWh

- Standard system size (LxWxH) in meters
- Full round-trip efficiency of the E-heater + TES system in %
- Efficiency of just the E-heater in %
- Lifetime in number of cycles and years
- Response time of the system in seconds

As mentioned in addition to these quantitative technical parameters it was also important to asses the compatibility of the E-heater + TES system with the current process and possible operating and safety constraints. Therefore also more general technical specifications were formulated related to this:

- Compatibility with thermal oil at around 300 °C
- Presence of an internal control system able to control operation based on the current/predicted electricity price to maximize peak-shaving
- The possibility to supply process heat continuously either by simultaneous charge and discharge of the TES system or through a bypass of the TES
- Potential safety risks/considerations and additional system requirements related to safety and operation
- Effects of going to higher temperatures in terms of losses
- Operating constraints like the dependency on certain operating conditions such as temperature levels, stored energy, etc.
- Relation between the system size and the storage capacity and if there are any economies of scale involved or that the system is entirely modular
- General system/material compatibility e.g. what surroundings should be created around the storage system (closed containers/concrete walls/open space, distance to other structures, etc.)
- Required thermodynamic/chemical/mechanical conditions for the system to operate properly
- Possibility to modify the system in the future to supply the heat through an alternative electric heating method like a HTHP

The combination of the quantitative technical data as well as the more general data allowed to make a good assessment of the technical feasibility of the E-heater + TES solution for this application. In terms of the economical parameters that were required for the techno-economic analysis this was more straightforward. The economical parameters considered were:

- Average CAPEX costs per storage capacity in €/MWh
- Full system CAPEX costs for a specific system size in €
- Levelized cost of storage (LCOS) in €/MWh
- Levelized cost of energy (LCOE) in €/MWh
- Levelized cost of heating (LCOH) in €/MWh
- O&M costs in % of the full system CAPEX costs
- OPEX costs in €/MWh
- Additional costs (not included in the full system CAPEX) like infrastructure adaption costs or transportation

2.2.3. TES manufacturers

In this section a brief description will be given of the most notable manufacturers for TES systems and what general advantages and disadvantages their TES systems have compared to each other.

First of all, was the German company Kraftblock identified as a manufacturer that had a large potential to be able to supply a TES system for medium-temperature process heat. Global information on their system was obtained through a direct interview. Unfortunately, for more detailed information and a proposal for the application from Teijin Aramid a fee needed to be paid which limited the level of detail of information. However, the technical data provided made it clear that in terms of technical feasibility their TES solution would fit the application well. Based on the cost estimate given it also seemed like a cost-competitive solution. Their TES system makes use of recycled steel slags as storage medium

and has a relative straightforward and safe storage design due to the use of a solid storage medium. It can be operated from temperature of about 350 °C up to temperatures up to 1000 °C. Moreover, it can be designed for large charge and discharge powers ranging from 0-25 MW which is more than enough for the Plinke process. Within the system hot air is used as heat transfer medium but through a hot air-thermal oil HEX the system can be made fully compatible with a thermal oil system. External (resistive) E-heaters to heat the hot air for the TES system are delivered with the TES solution. Through a bypass heat can either be delivered directly to the hot air-thermal oil HEX, while simultaneously the TES is charged, or heat can be delivered by the TES only. In terms of size and storage capacity the design is most suited for intraday charge but with energy losses of about 2% a day the heat can be stored for a few days if required. Kraftblock also already has multiple projects in the Netherlands, like for PepsiCo in collaboration with Eneco.

The solution from the the Norwegian company EnergyNest, the ThermalBattery, was largely similar to the TES solution offered by Kraftblock. Here high-performance thermal concrete (solid-state) is used as storage material instead of the steel slags but the rest of the storage system was comparable. However, for this solution a lot more detailed data was obtained through multiple direct interviews. A rough design and cost estimate from their side was provided for a system with a +-50 MWh storage capacity which allowed full intraday storage with about 6 hours of charging per 24 hours. This system would be able to fully fit the Plinke process in terms of technical specifications as well as enabling continuous operation of the thermal oil system. The proposed system would in terms of dimensions also fit well in the area available at the Emmen plant. A larger system was also possible but due to the cost number for the 50 MWh system it was immediately confirmed that multiday storage would not be economically feasible. Most other specifications like the round-trip efficiency and energy losses were comparable to the Kraftblock solution and with a response time of seconds the system was highly flexible. Currently there is not yet an EnergyNest TES system present in the Netherlands but they have build TES systems in other European countries.

Moreover, does the Norwegian company Kyoto offer an interesting TES solution with molten-salt as storage medium, the HeatCube. The molten-salt is stored in multiple tanks and transported between these tanks. As opposed to the solid-state storage this enables simultaneous charge and discharge of the TES. Therefore, there is no need for a bypass from the external (resistive) E-heaters and operation can be more flexible adapted to optimize the system. The higher energy density of the molten salt compared to the solid-state storage materials is advantageous in terms of storage size. However, the operating temperatures are also more limited as the molten salt could only be heated between 190 and 415 °C. As the minimum temperature of the thermal oil was above this value of 190 °C, as explained in Section 2.2.1, this means that the storage capacity of the molten-salt could not be utilized entirely. This would reduce the effective storage capacity of the storage tanks by about 35%. This low-temperature heat could be used for other applications in the process such as steam for the first step of the Plinke but this would require extra adaptions. For the HeatCube solution also detailed data was obtained through multiple direct interviews. A design and cost estimate was provided from their side for a system with a +-51 MWh storage capacity which allowed full intraday storage with about 8 hours of charging per 24 hours. The reason for the 8 hours charge was due to lower E-heater capacities, but larger E-heater capacities were also possible. This system also met all required technical specifications of the Plinke process where the thermal oil would be heated through a molten-salt-thermal oil HEX. There is no HeatCube TES system currently present in the Netherlands but they have TES systems present in Scandinavia.

The Italian company Magaldi offered a very different TES solution compared to the manufactures described above, the MGTES. Their system makes use of a fluidized sand bed to store the heat of which the most notable advantage is that this enables very high heat transfer. When the fluidization is stopped during storage the heat transfer is decreased significantly and the energy losses become almost zero. Through a direct interview more information was obtained on the technical operation of the system and also a system design and rough cost estimate was done by Magaldi for a +-51 MWh system. However, as there is no commercial system in place yet this cost estimate was less accurate compared to the other TES suppliers. Nevertheless, from a technical viewpoint the MGTES system was suitable for the Plinke process. Due to the fluidization the (resistive) electric heaters were fully integrated in the design.

This allows for high charging powers which would enable a charge time of less than 6 hours per day and profit more from the electricity price fluctuations discussed later in this Chapter. It also enabled simultaneous charge and discharge. The largest disadvantage was that currently no commercial installations was in place. Therefore, a MGTES system can not be realized in the same time window as the other discussed solutions and the actual system cost are more uncertain.

For the other mentioned manufacturers Rondo Energy, Lumenion GmbH, Brenmiller and MGA Thermal no detailed technical and economical could be obtained through interviews. Therefore, these manufacturers were not considered for the techno-economic analysis. Nevertheless, in the next step for Teijin Aramid to select a TES manufacturer it would definitely be interesting to also consider these suppliers. Rondo Energy, an American company partly founded by Bill Gates, for example makes ambitious claims on the system sizes that they can realize at low costs. If they are actually able to meet these numbers it would be a very cost-competitive TES solution. The earlier mentioned solution of MGA Thermal is theoretically able to reach very high energy densities through the combination of sTES and LHS which could make this also a very interesting solution. However, due to the low TRL of this solution it is not expected that this TES solution will be commercially available soon.

2.2.4. Surpluses and deficits in VRE production

The availability of renewable energy in the form of electricity from VRE sources, mainly solar and wind, has a large impact on the practical feasibility of a E-heater + TES system to replace a natural gas heater. In an early stage of the research Professor Sikke Klein shared that based on his experience a storage time of about 3-4 days was required to successfully cover most of the fluctuations in VRE production. To confirm this number it was decided to look at the variations of solar and wind supply in the Netherlands from January 2022 to July 2023 as well as variations in the day-ahead price of electricity. This as a simultaneous increase/decrease in VRE production and a decrease/increase in the electricity price generally was expected to serve as a good indication of a surplus/deficit of VRE production. The data for the VRE production was obtained from ”energieopwek.nl” and the data for the day-ahead electricity price from ”nieuwestroom.nl/epex-apx-handelsbeurs/”. An example of the data used for the analysis is shown in Figure 2.4 and Figure 2.5. The circles were added to indicate clear examples of surplus and deficits in VRE production and the effect on the electricity price.

More detailed data for the day-ahead electricity price could be obtained from the ENTSO-E platform, which was done for the more detailed price analysis in Section 2.2.5. However, the graphical representation from nieuwestroom.nl enabled more straight-forward comparison with the VRE production data.

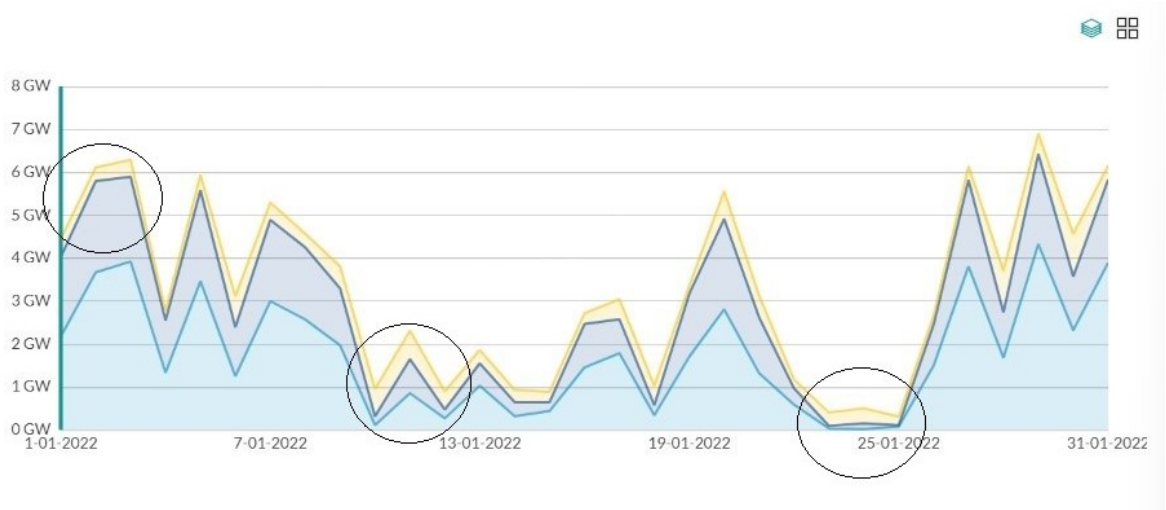

Figure 2.4: The cumulative daily production from solar PV (yellow), onshore wind (light blue) and offshore wind (dark blue) in the Netherlands for January 2022.

Figure 2.5: The day-ahead electricity price in the Netherlands for January 2022.

To be able to analyze a longer period of time it was chosen to first look at multiday variations with two objectives. Firstly, to observe if there was indeed a clear relation between a surplus/deficit in VRE production and a decrease/increase in the daily electricity price. Secondly, in case there was a surplus/deficit in VRE production or a decrease/increase in the daily electricity price for how many days this lasted. In this analysis a surplus/increase was denoted as a peak and a deficit/decrease as a dip. A VRE production a peak/dip was counted if there was a relative large increase/decrease compared to the surrounding days and the value in GW was not close to the average VRE production over the month. It was quickly observed that a large enough peak/dip in the VRE production almost always resulted in a dip/peak in the electricity price. As a peak/dip was more clearly seen in the daily electricity price a price peak/dip was defined as at least a 10% deviation from the average monthly price. Where it was noticed that price dips could often also be caused by other factors like the price of natural gas. The natural gas price fluctuated significantly in 2022 due to the difficulties in supply in the EU. This approach resulted in a rather rough estimate of the general duration of peaks/dips. However, this was deemed accurate enough to get an idea of what storage times would be desired to cover most of the fluctuations in VRE production. The results of this analysis are displayed in Figure 2.6 and Figure 2.7.

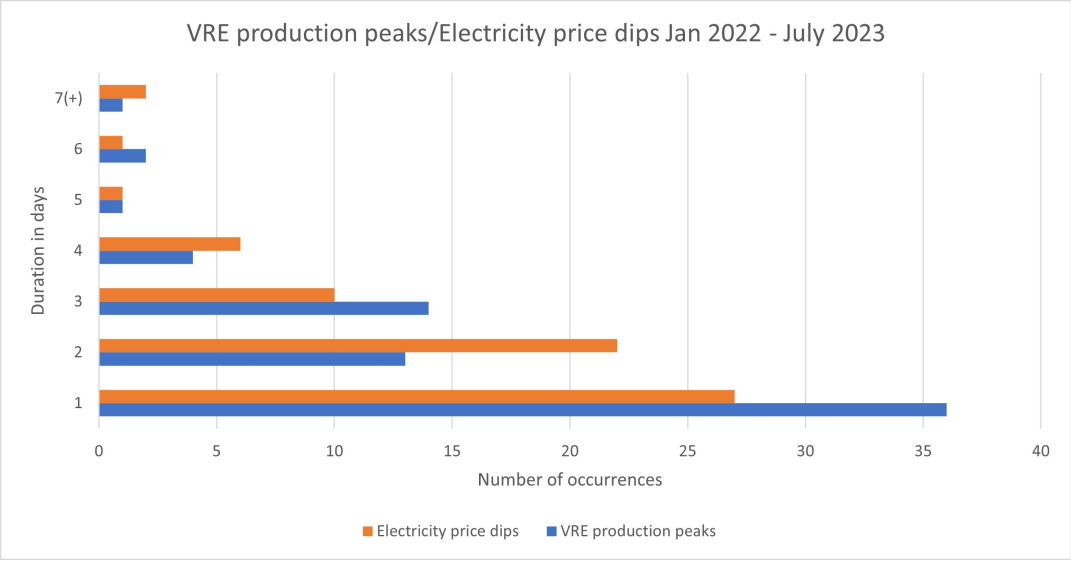

Figure 2.6: Estimate of the daily VRE production peaks and electricity price dips in the period January 2022 to July 2023.

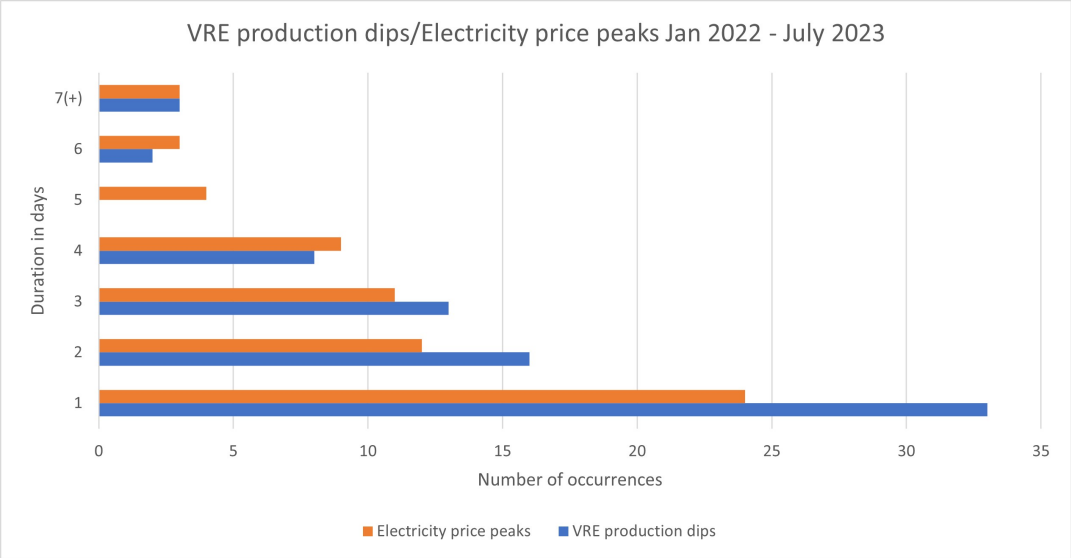

Figure 2.7: Estimate of the the VRE production dips and electricity price peaks in the period January 2022 to July 2023.

A few interesting observations were done in the obtained results. First of all, it was observed that by far most dips in VRE production/peaks in electricity price had a duration of 1 day. As Professor Klein already predicted only a very small share of the peaks/dips had a duration of more than 4 days. Storage times of more than 3-4 days would therefore be required to fully cover the fluctuations in VRE production. However, this would further increase the storage size and costs for only a few occurrences per year. On the other hand a storage time of just 1-2 days could already cover most of the VRE production dips. Moreover, it was observed that there was indeed a relation between peaks/dips in VRE production and dips/peaks in the electricity price. This was concluded as the occurrences of the peaks/dips for both the VRE production and the electricity price were close together. However, it was not always the case that a peak in VRE production resulted in an equally-long dip in the electricity price or the other way around. This can for example be seen in Figure 2.6 where it seems like a few electricity price dips last 2 days while the VRE production dip that caused this only lasted 1 day. This could be explained by the fact that the electricity price is also largely impacted by electricity demand and other external factors. Nevertheless, the results gave a good indication that a storage time of between 1 and 3-4 days would be ideal to cover most fluctuations in VRE production and could greatly reduce the OPEX of the E-heater + TES solution compared to the average electricity price.

After this analysis also a brief analysis was executed of the intraday variations of VRE production which also showed interesting, and more extreme, variations especially during summer time. In Figure 2.8 and Figure 2.9 it is illustrated that the large surpluses of solar PV can even cause the electricity price to become negative for multiple hours during the day. Logically, this only happens occasionally, but intraday variations in the hourly day-ahead electricity price were always present to some degree. The E-heater + TES system could already benefit significantly from these variations without the need for a very large storage capacity compared to if storage for multiday variations was desired. It was found in this analysis that if a charge time of around 6 hours per period of 24 hours could be realized the E-heater + TES system could successfully benefit from most intraday variations. This charge time of 6 hours number was also mentioned by most of the TES manufacturers during the interviews. It is based on the fact that during summer time the sun is at its strongest from around 11:00 to 17:00 and that the demand for electricity is also lowest during these hours. In winter time this pattern shifts more to between 12:00 and 15:00. Nonetheless, it was observed that in winter there is little energy demand during the night while often there is still wind generation. This causes the electricity prices to drop for around 3 hours which combined also results in the 6 hours.

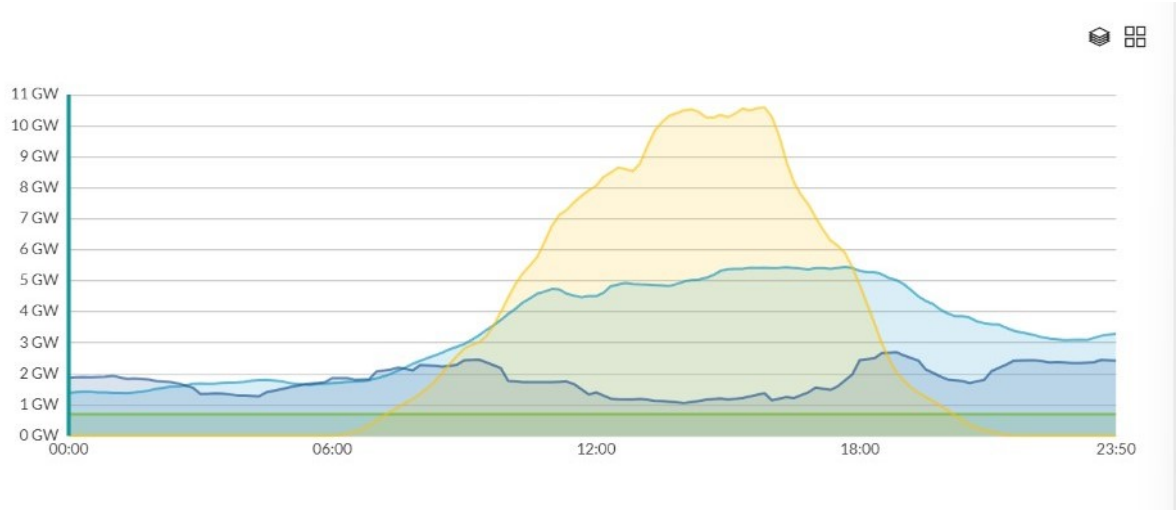

Figure 2.8: Intraday variations in solar PV and wind production in the Netherlands on 31-07-2022.

Figure 2.9: The hourly day-ahead electricity price in the Netherlands on 31-07-2022.

A future outlook on the expected VRE production and the surpluses and deficits of electricity also showed some promising signs. In the KEV 2022 report the Dutch Planbureau voor de Leefomgeving (PBL) give a prediction of the increase in solar PV and wind production in the Netherlands up to 2030. This is depicted in Figure 2.10 below. It can observed that recently a large surge has been observed in the production through solar. Moreover, in the coming years especially wind energy is expected to rise rapidly and generate almost five times more electricity in 2030 than solar.

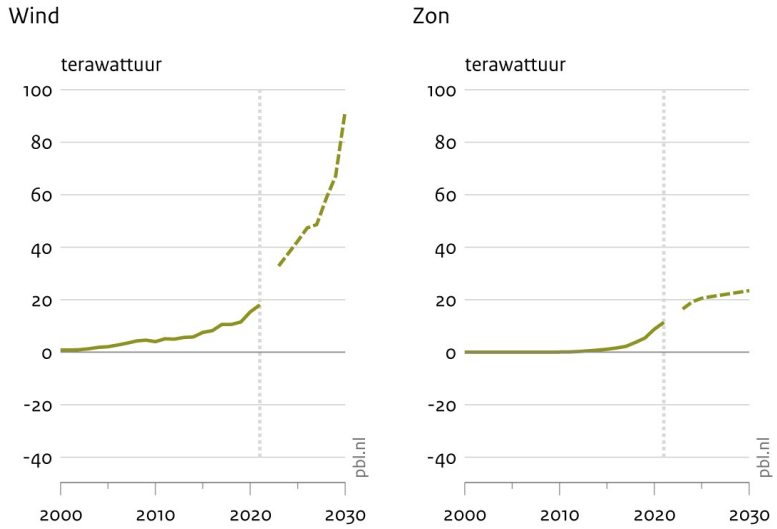

Figure 2.10: Electrical energy production from solar and wind from 2000 to 2020 including a prediction towards 2030 (PBL, 2022.

To put the expected increase in solar PV and wind production in perspective to the expected total supply of electricity to cover demand, the predictions of total installed electrical capacity from the KEV 2022 were also of interest. This is depicted in Figure 2.11.

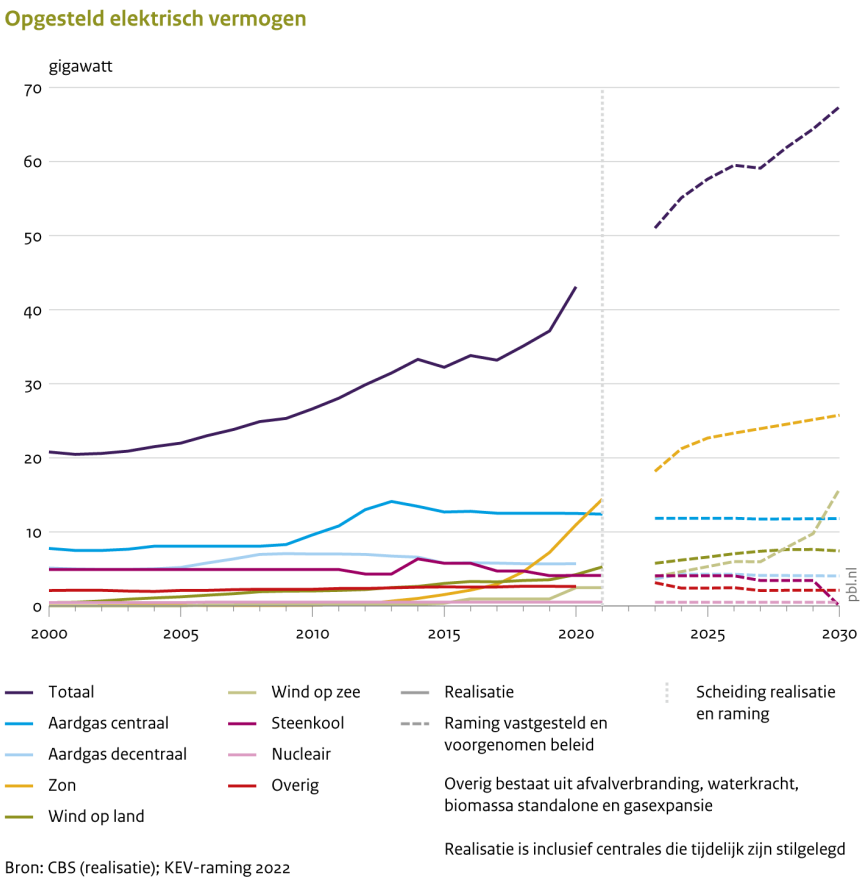

Figure 2.11: Installed electrical capacity specified per source from 2000 to 2020 including a prediction towards 2030 (PBL, 2022.

It can be observed that the installed capacity of solar PV already surpassed natural gas, and that offshore wind is also expected to do so before 2030. With the other fossil-fuel alternatives decreasing in installed capacity up to 2030 the share of solar PV and wind is expected to increase significantly until 2030 compared to the other sources. It is therefore also expected that the surpluses and deficits are more likely to increase than decrease. This results in that larger electricity price differences are to be expected until enough energy storage capacity is installed to properly deal with these variations. However, the cost of wind and solar energy is also decreasing rapidly. An interesting study from 2018 by Ecofys already predicted a levelized cost of electricity from wind and solar PV of 30-60 €/MWh in 2030 which could become competitive with natural gas.

Unfortunately, the KEV 2022 report gave no predictions of the situation after 2035 but a report from Netbeheer Nederland did. In this report they present the results of a few scenario's in terms of the expected future energy supply and demand up to 2050. The expected supply and demand of renewable energy for 2019, 2030, 2040, and 2050 is shown in Figure 2.12. As can be seen the demand is expected to become somewhat more flexible, mainly due to DSR and energy storage. The supply on the other hand is expected to become significantly more volatile which results in more extreme surpluses and deficits.

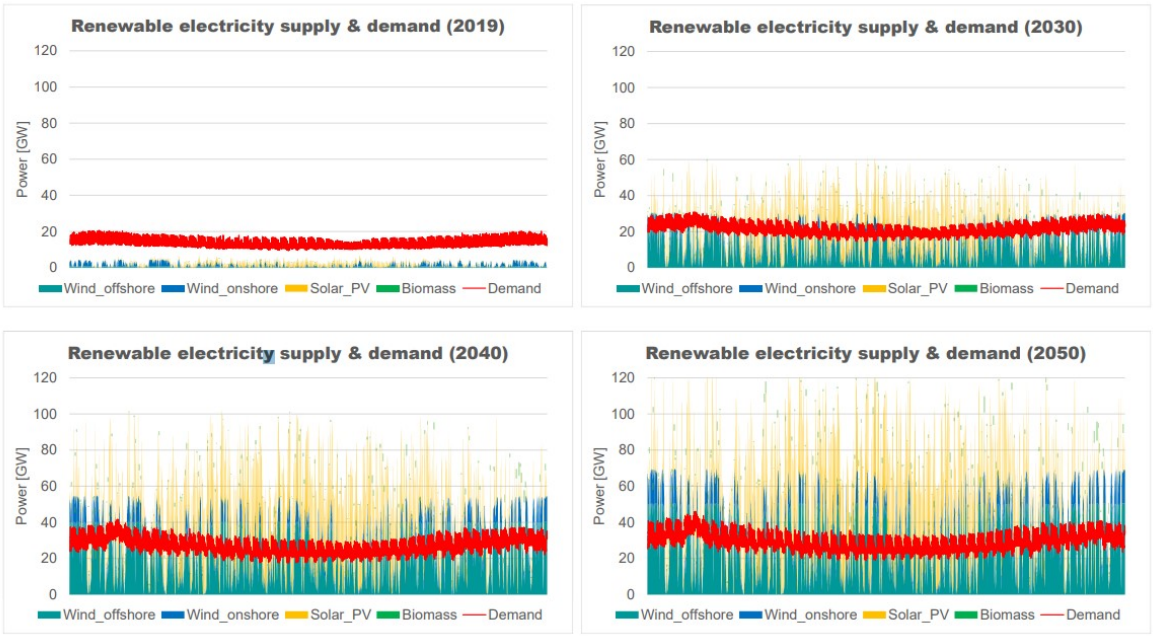

Figure 2.12: Predicted developments in renewable electricity supply and demand up to 2050 (Netbeheer Nederland, 2023).

This was also studied in more detail in the report as illustrated in Figure 2.13 & 2.14. In these predictions up to 2050 it can be seen that both the surpluses and deficits are expected to become significantly larger especially during summer time. Already in 2030 the peaks in renewable energy supply are expected to regularly exceed the demand by a considerable factor. This can result in even negative prices, something that was already incidentally observed in 2023 and illustrated in Figure 2.9. In Figure 2.14 it can be seen that especially the surpluses are expected to significantly increase in 2040 and 2050 compared to the deficits. It can be expected that because of this the electricity price becomes more decoupled from the price of fossil-fuel electricity production which would result in significantly lower prices. These predictions also stress the need for flexibility through DSR and energy storage to be able to utilize these surpluses effectively and cover the periods of deficits.

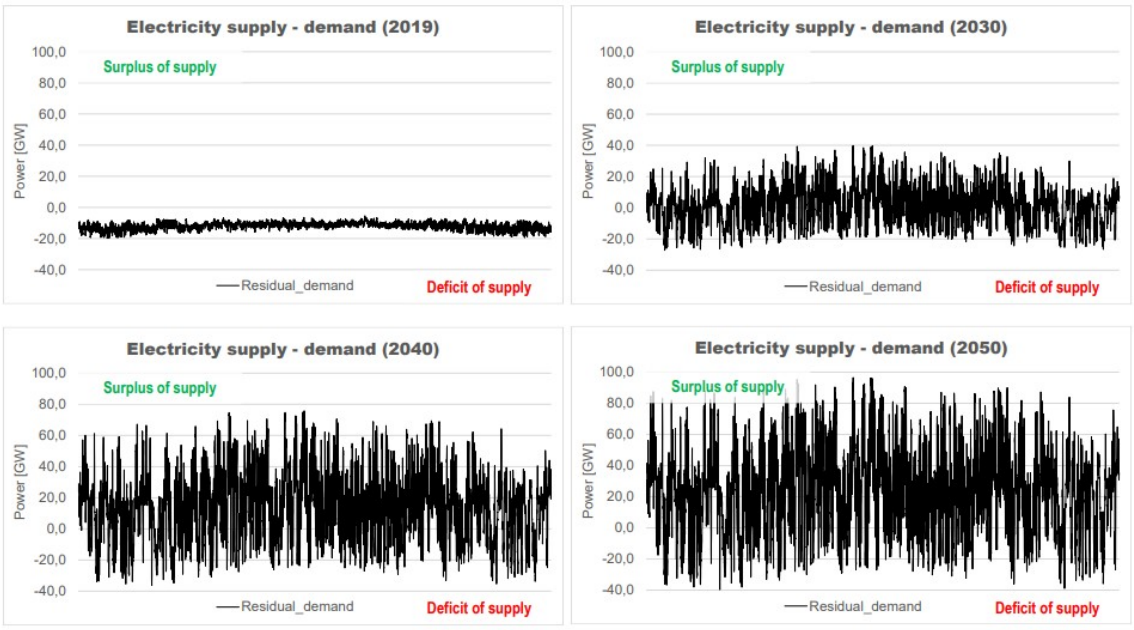

Figure 2.13: Predicted developments in mismatch between supply and demand of electricity up to 2050 (Netbeheer Nederland, 2023).

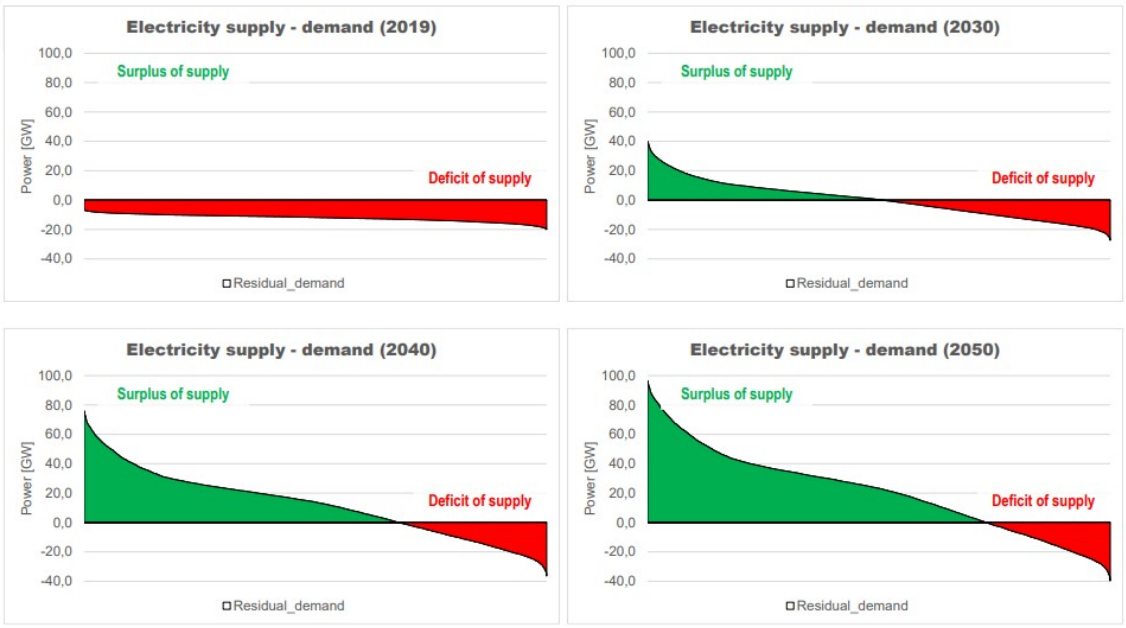

Figure 2.14: Predicted developments in the need for flexibility on the demand-side up to 2050 (Netbeheer Nederland, 2023).

A few things could be concluded from the presented future outlook on the expected VRE production and the predicted developments regarding the surpluses and deficits of electricity. It is evident that the need for the flexibility in demand through DSR and energy storage is considerable. Moreover, it is expected to also have an impact on the differences between peak and off-peak electricity prices which would further increase the economical feasibility of the E-heater + TES solution. However, it should also be noted that only the predicted trends in 2040 and 2050 show that considerable and stable surpluses will be present throughout the year and not only during summer. This raised the question if it is realistic to fully decarbonize the process heat supply already in the near future or that a back-up with natural gas for

longer periods of deficits is required. This would be supported by the fact that during periods of deficits the electricity supplied from the grid will also be governed by natural gas power plants. Taking into account the efficiency of these power plants it would in terms of GHG emissions actually be beneficial to produce the process heat directly through the combustion of natural gas during these times.

2.2.5. Electricity- and natural gas price analysis and prediction

The analysis on to the surpluses and deficits presented in Section 2.2.4 was done in an earlier stage of the research and was focused mainly on the variations in VRE production. This to get an idea what storage times would be desired and at what frequency these surpluses and deficits occurred. When it became more evident that from a technical viewpoint the E-heater + TES solution was expected to be feasible the economics started to become a more significant factor. Through the data obtained from internet as well as directly from the TES manufacturers the CAPEX and O& M costs that could be expected became quite accurately known. However, on the OPEX cost side there was a lot more uncertainty and it was more difficult to make accurate predictions on what costs should be expected in the operation of the E-heater + TES system.

The findings from the analysis on to the surpluses and deficits and early conversations with the TES manufacturers showed that multiday storage was not viable to further investigate for this application for multiple reasons. It became clear that although storage times of up to 3-4 days would enable to operate almost entirely on renewable energy this would require a substantial storage to meet the required process heat demand. From a technical viewpoint this was not feasible as there was not enough space available at the Emmen plant to construct such a system. However, also the extra savings on GHG emissions became disproportional to the substantial extra investments costs to realize such as multiday storage. The TES manufacturers interviewed were also purely focused on intraday storage themselves and that is where they designed and build their systems for. Finally, from the analysis on to the surpluses and deficits it was already concluded that most observed peaks/dips had a duration of just one day. The intraday variations already showed a lot of potential to significantly reduce emissions and OPEX costs especially if charge times of around 6 hours or less per 24 hours could be realized.

As historical day-ahead electricity price data was readily available through the ENTSO-E platform it was decided to analyse this data to observe what fluctuations were seen. Thereby the focus was on what effect it would have to make use of the identified intraday variations by charging the TES for only 6 hours every 24 hours and discharge the remaining 18 hours. This analysis was done for the years 2019-2023. For every day the daily average day-ahead electricity price was calculated as well as the daily average day-ahead electricity price if only the cheapest 6 hours were considered. This was compared to the yearly average day-ahead electricity price as well as the average monthly natural gas price, which was reasonably stable over the duration of a month. As an example the results of the analysis for 2019 and 2022 are shown in Figure 2.15 and Figure 2.16 respectively.

The unusual large fluctuations in the electricity price caused by external factors, like the Russia-Ukraine war, made it more difficult to provide fully accurate estimates. However, as the goal of this part of the study was to use historical data to make an estimation for the future electricity price that could be expected the exact values were not of significant interest. What was most notable to observe was that in 2019 a small difference between the daily average price and the average price during the cheapest 6 hours of the day was present. Moreover, the average price in €/MWh during the cheapest 6 hours only became lower than the natural gas price on incidental occasions and never negative. However, in 2022 the difference between the price during the cheapest 6 hours was significantly lower than the daily average price. The average price during the cheapest 6 hours of the day in €/MWh was actually more than 25% of the time below the monthly average gas price and even negative multiple times. This can easily be explained by the fact that over this period of time also the installed capacity of solar PV and wind increased rapidly creating larger surpluses and deficits and hence larger price fluctuations. On average was in 2019 the day-ahead price during the cheapest 6 hours of the day about 20% lower than the yearly average day-ahead price, while in 2022 this number had increased to about 31%. In the months April-June these number was even around 45%.

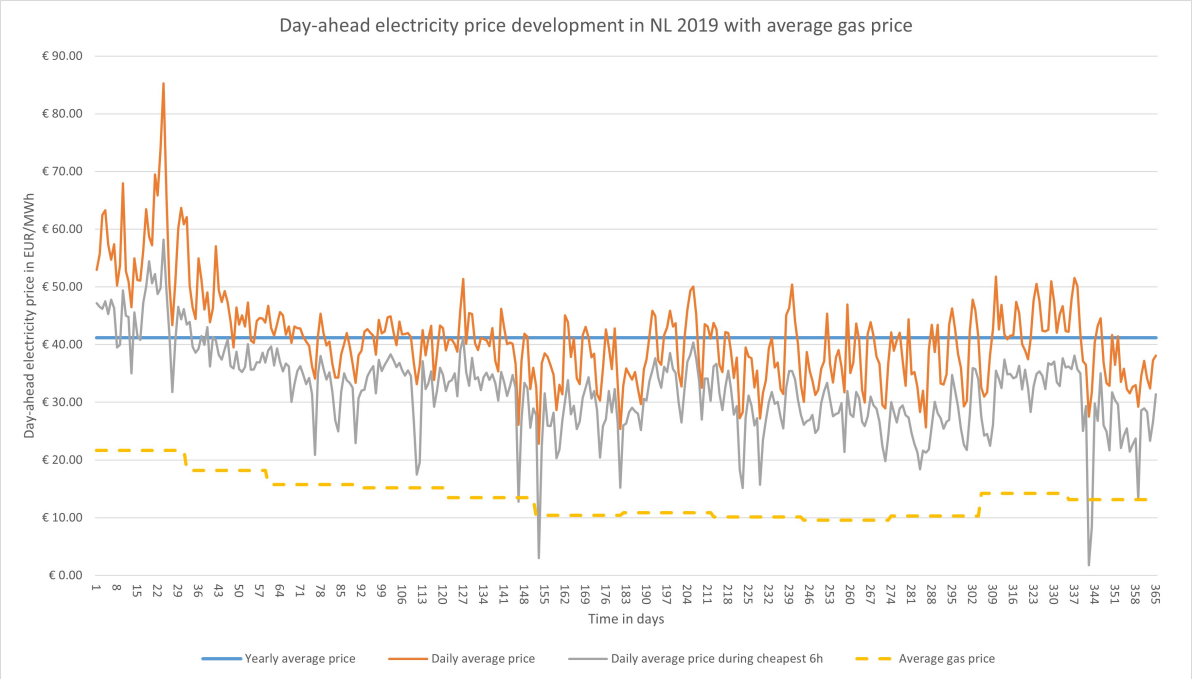

Figure 2.15: Developments in day-ahead electricity- and gas prices for 2019 including the day-ahead electricity price during the cheapest 6 hours per day of 24 hours.

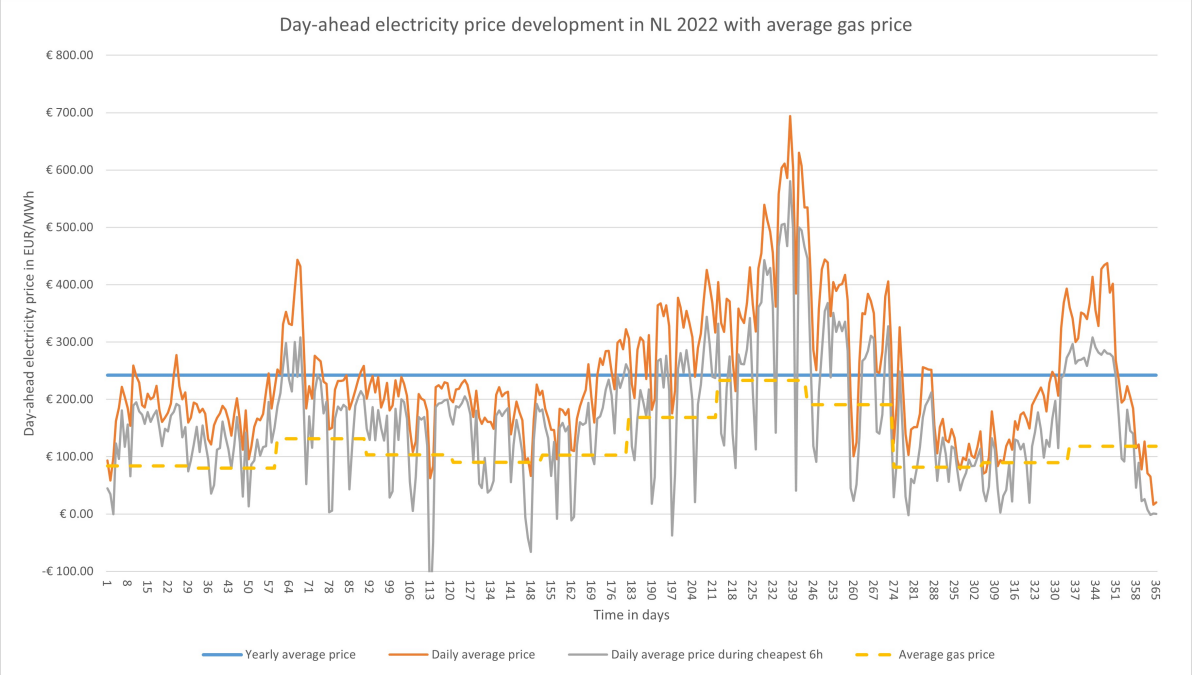

Figure 2.16: Developments in day-ahead electricity- and gas prices for 2022 including the day-ahead electricity price during the cheapest 6 hours per day of 24 hours.

The described developments continued in 2023 but this analysis could not yet been done over the whole year. Therefore, the results from 2023 were analyzed separately. Nonetheless in the data from 2023 until the end of September, shown in Figure 2.17, even larger fluctuations in the electricity price were observed. In the summer there was even a full day that the electricity price was negative. In the period from January to September 2023 the day-ahead price during the cheapest 6 hours of the day (59.27 €/MWh) was 40% lower than the yearly average price (98.99 €/MWh) and almost 30% of the time below

the monthly average day-ahead natural gas price. In the scenario that only 75% decarbonization was realized, meaning that at the 25% most expensive days natural gas was used instead of electricity, the average combined day-ahead price that would be paid for energy was calculated to be 41.77 €/MWh. This number of 75% decarbonization was based on the studied data and the observed surpluses and deficits throughout the year and deemed the most viable based on the current energy system in the Netherlands. As the average day-ahead natural gas price until the end of September 2023 was 40.74 €/MWh the number of 41.77 €/MWh was an interesting observation in the potential feasibility of the E-heater + TES solution compared to natural gas.

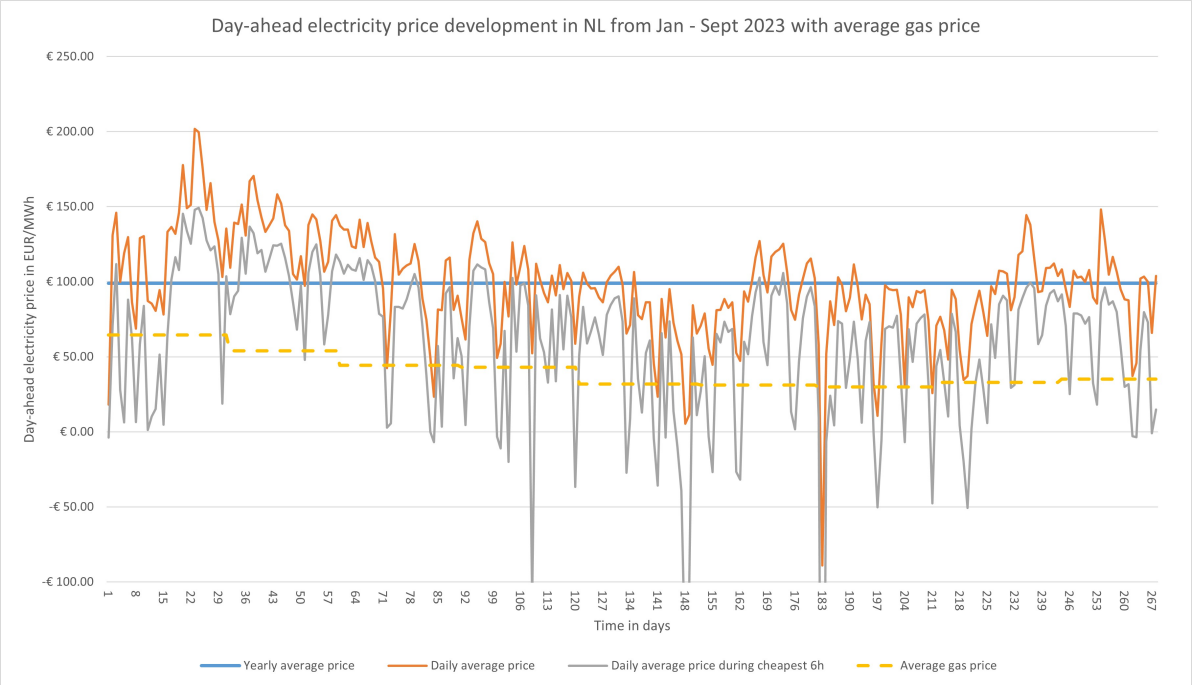

Figure 2.17: Developments in day-ahead electricity- and gas prices from Jan 2023 to Sept 2023 including the day-ahead electricity price during the cheapest 6 hours per day of 24 hours.

As the data from 2023 was not complete it was chosen to use a conservative estimate for the expected OPEX it the E-heater + TES system was charged during 6 hours per day. Moreover, it was not certain that this reduction would increase with a similar trend as observed for the from 2019 due to increasing DSR and other energy storage solutions. Therefore, it was chosen to use the estimate that only charging during 6 hours per day would result in a day-ahead electricity price that would be 35% lower than the predicted yearly average day-ahead electricity price. Nonetheless, based on the predictions by Netbeheer Nederland it is not unrealistic that this difference will increase in the future. Due to a design proposed by Kyoto where charging of about 8 hours was required it was also briefly investigated what difference this would give compared to the 6 hours charging. It was observed that this made little difference for the analysis of 2019 but for 2022 and 2023 this already resulted in respectively 27% and 34% compared to the mentioned 31% and 40% decrease in average electricity price with 6 hours of charging per day. It was therefore concluded that if possible a maximum charge time of 6 hours per day should be realized if this was possible in terms of E-heater capacity.

The trends observed in the historical data from 2019-2023 could be combined with the existing predictions for the electricity- and natural gas prices until 2030 from the KEV 2022 report to estimate what prices could be expected in 2030. The predicted day-ahead electricity prices until 2030 are shown graphically in Figure 2.18. In Figure 2.19 the predicted day-ahead natural gas prices were depicted. For the techno-economic analysis these predicted natural gas prices were converted to €/MWh.

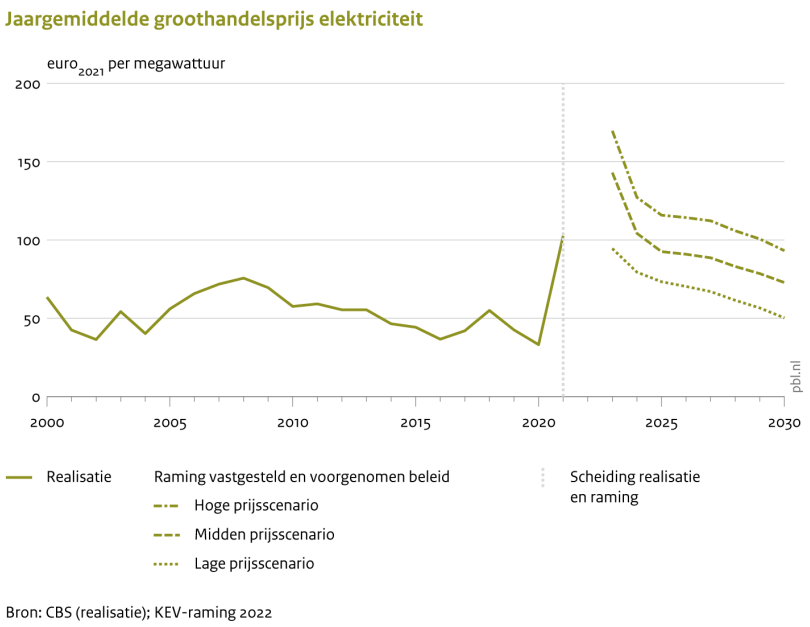

Figure 2.18: Predictions of the average day-ahead electricity price with a low, medium and high price scenario until 2030 (PBL, 2022).

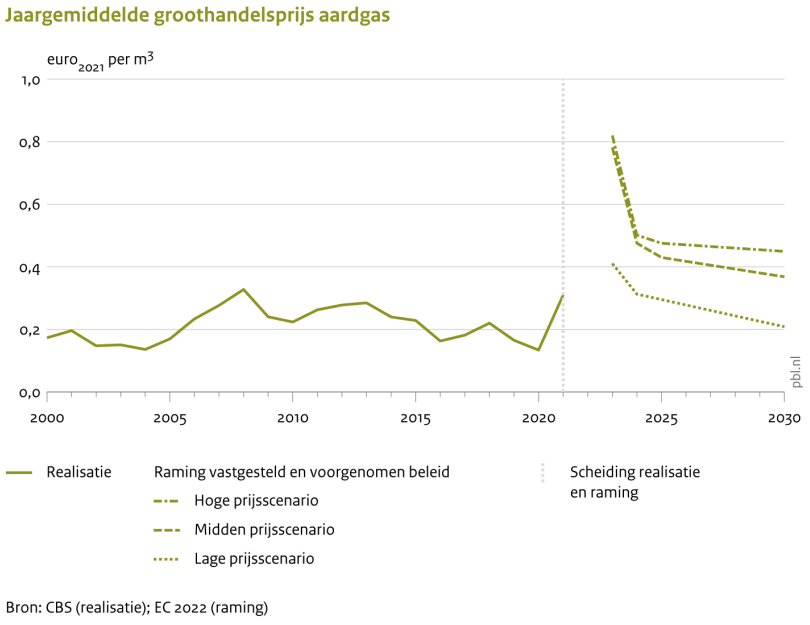

Figure 2.19: Predictions of the average day-ahead natural gas price with a low, medium and high price scenario until 2030 (PBL, 2022).

The KEV 2022 report also presented some predictions for the development of the carbon emission pricing within the EU ETS system, which is graphically shown in Figure 2.20. This numbers could be translated into a carbon tax in €/MWh for the use of natural gas to see what effect this increase in natural gas price would have on the economical feasibility of the E-heater + TES solution.

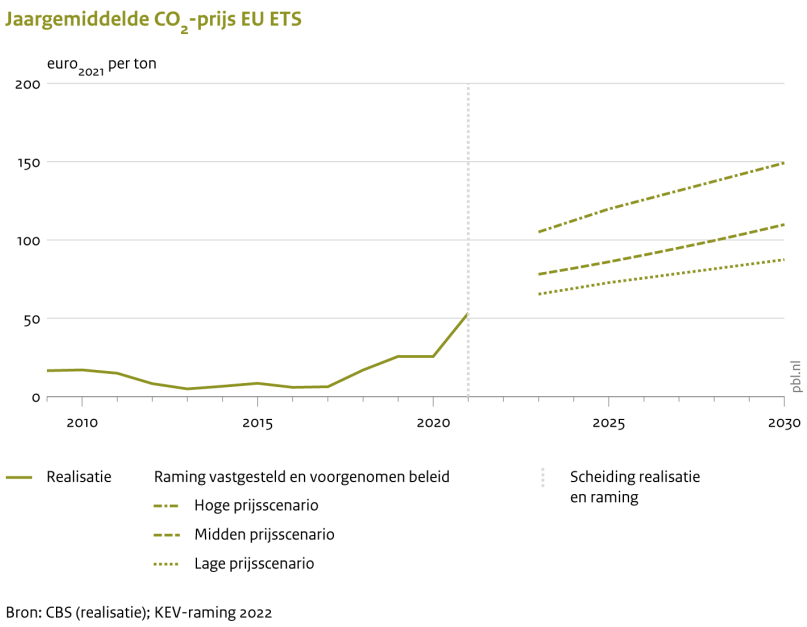

Figure 2.20: Predictions of the average carbon emission pricing in the EU ETS system with a low, medium and high price scenario until 2030 (PBL, 2022).

Moreover, it was learned from the interviews with the TES manufacturers that next to the carbon tax the Dutch government is working on a kind of reversed carbon tax. This would entail that for every ton of reduced carbon emissions a financial compensation would be granted. This could also be translated in a reduction of the electricity price paid when using the E-heater + TES solution instead of natural gas.

All the obtained information from the analysis and predictions of the electricity and natural gas price was combined within different scenario's in the techno-economic analysis to estimate the OPEX costs that could be expected. A final note should be made that in practise not the day-ahead price is paid for both electricity and natural gas but that extra fees are paid such as energy tax which are quite comparable for electricity and natural gas. However, also fees related to the transportation and connection and transmission costs. The exact predictions for the expected fees came from confidential numbers within Teijin Aramid but it can be said that in the current Dutch system these fees are significantly higher for electricity than for natural gas in €/MWh. This unfortunately makes it even more difficult to realize a comparable OPEX for the E-heater + TES compared to natural gas.

2.2.6. Setup of techno-economic analysis

The techno-economic analysis was executed in Excel and in the analysis the technical and economical parameters as described in Section 2.1 were specified. This was done based on the data obtained from the TES manufacturers regarding the technical specifications of the E-heater + TES system and the CAPEX and O&M costs. CAPEX and O&M cost data of the gas heater currently used for the system was supplied by Teijin Aramid. This was combined with the predictions for the OPEX costs of both electricity and natural gas. With al this information multiple scenario's were calculated to asses the techno-economic feasibility of the E-heater + TES system versus the current system with the natural gas heater.

2.3. Results

As the data obtained from the TES manufacturers was protected by a NDA and a lot of confidential internal data from Teijin Aramid was required for the techno-economic analysis the final results of the analysis cannot be shared in this report. However, global results of the techno-economic feasibility could be presented to illustrate the potential and challenges related to this solution, also for cases similar to the case study for Teijin Aramid.

First of all, it was found that in terms of technical feasibility the discussed TES systems from suppliers like Kraftblock, EnergyNest and Kyoto were all suited for the electrification of the Plinke process in the Emmen plant. It would require some modifications to the current thermal oil system but no major changes would be needed. The fact that the E-heater was an external subsystem for nearly all TES solutions was also of interest. This would mean that in the future the E-heater could in theory be replaced by a HTHP. However, even for the Kyoto system this would require heat sink inlet temperatures of above 415 °C to be able to successfully charge the TES. This was therefore not further considered in the design or in the identification of the most interesting TES supplier. In order to realize partial electrification/decarbonization more efficiently the current gas heater should also be kept and combined with the E-heater + TES system. This to be able to switch between natural gas and electricity based on the availability of renewable energy to cover longer periods of deficits in VRE production. The main technical challenge was identified in the charge capacity that can be realized to profit optimally from the intraday variations in VRE production and realize a charge time of 6 hours or lower per day. The charge capacity is related the grid connection available and it is difficult to obtain a new grid connection for the multi-MW capacity that would be required for the E-heater + TES solution. Teijin Aramid might be able to realize this through Getec, the local steam and natural gas supplier, but this is something that would have to be further investigated.

The economical feasibility was unfortunately a different story. The full CAPEX costs including installation and expected infrastructure adaptions are significant. Due to the NDA restrictions no exact data can be given but for the 24 hours storage system this is in the ball-park of 5-10 million euros. On the other hand, the O&M costs of an E-heater + TES system were found to be generally a factor 4 or more lower than for a natural gas heater. However, it was found that the OPEX costs were the main issue to make the electrification economically feasible compared to natural gas heating. This was illustrated well with the data from the analysis in Section 2.2.5. On average the day-ahead natural gas price is about 2.5 times lower than the electricity price. This factor of 2.5 was assumed to be related to the efficiency of around 40 % of gas-fired power plants, which determine the electricity price for the majority of the year. When also taking the additional fees paid on top of the day-ahead price into consideration this difference becomes even larger. Especially during multiday deficits of VRE production this creates high electricity prices throughout the day. On the other hand, charging during only 6 hours per 24 hours already results in a large improvement in terms of OPEX costs as well as actually reducing emissions by using renewable electricity from solar PV and wind. Moreover, it was shown in Section 2.2.4 that it is expected the fluctuations in VRE production will increase further. This could in the future potentially enable emission-free electrical energy and for a price comparable to natural gas.

Nevertheless, for the near future it was observed that to strive for full decarbonization making use of intraday variations with the E-heater + TES system still resulted in significantly higher OPEX costs than natural gas heating. This makes the business-case for industrial players like Teijin Aramid very difficult. On the other hand, it was observed that partial electrification/decarbonization of up to 75 % was already expected to further reduce the OPEX costs. Where it should be noted that in the current Dutch energy system during deficits in VRE production the grid electricity is also produced with natural-gas fired power plants as mentioned before. This creates substantially more emissions than direct on-site combustion of natural gas to produce the required process heat. So, although partial decarbonization by keeping the natural gas heater as back-up is in the long-term not desired, it is in terms of emissions a good solution for the near future. As the Dutch energy system becomes more renewable in the future the shift can be made to full decarbonization.

Moreover, can considerable government grants/taxes for both the CAPEX and OPEX costs significantly improve the economic feasibility. With all this combined the economic feasibility of the E-heater + TES solution could become realistic. Nonetheless, it should be mentioned that every calculated scenario that made use of realistic assumption showed that if the E-heater + TES system would be implemented this would result in significant extra costs compared to the current natural gas system. Therefore, it also becomes a matter of what price an industrial player like Teijin Aramid is willing to pay to decarbonize.

Finally, as mentioned the available flexibility in the production process enables some room for DSR. It had to be concluded that based on the economic feasibility and the maximum storage capacities of the TES solutions currently multiday storage is not practically realizable. However, through smart application of DSR some of the multiday deficits in VRE production could be covered which would enable to increase this number of 75% more towards the 100%. Hence combine the E-heater + TES intraday storage with the DSR flexibility of the process to in some cases realize multiday storage. The main considerations here would be that in order to effectively apply DSR it might be necessary to do some additional investments in extra 78% feed and 96% product storage capacity to make sure the Twaron production process is not exposed to risks in shortages of sulfuric acid. Additionally, should in case the excess 78% feed cannot all be processed into 96% in time there be ways to sell this 78% sulfuric acid without having too much negative financial consequences.

3

sCO2 reversed Brayton cycle high-temperature heat pump

3.1. Thermodynamic model

To present the potential of a HTHP based on the reversed Brayton cycle and with sCO_2 as refrigerant thermodynamic modelling was done of two configurations. First, a basic sCO_2 reversed Brayton cycle HTHP configuration was modelled, further referred to as the HTHP configuration. After this, also a configuration of an ejector-assisted sCO_2 reversed Brayton cycle HTHP was modelled, further referred to as the HTHP-EJ configuration.
In general a (closed) heat pump cycle is purely based on an equation of state (EOS) that describes the thermodynamic properties of the refrigerant used inside the cycle. It provides the properties of the refrigerant under the different operating conditions throughout the cycle. To accurately simulate this in the model CoolProp 6.5.0 was used (Bell et al., 2014). For CO_2 CoolProp is based on the EOS as described by Span and Wagner (1996). This EOS is given in the form of a fundamental equation explicit in the Helmholtz free energy from which all required thermodynamic properties are automatically derived by CoolProp (Span and Wagner, 1996).

To simulate the heat pump operation, both configurations were based on the interaction with external process streams serving as heat source and heat sink respectively. The heat pump cycle was therefore designed around these external process streams. The thermodynamic properties for the external process streams where also obtained through CoolProp. The medium used for the external streams was a free choice. Therminol-66 was chosen as this is a commonly used heat transfer fluid in process heating for industrial applications. Moreover, with a temperature range of 273 to 618 Kelvin (liquid phase) it was suitable to be used for both external streams.
The thermodynamic HTHP and HTHP-EJ model were constructed in Python 3.8.10 (Python Core Team, 2019). In both models mass- and energy balances were performed on all different components of the configuration as will be discussed in more detail below. To model the ejector energy- and momentum balances as well as the continuity equation were used. The theoretical ejector model was directly incorporated in the HTHP-EJ model as will be explained in more detail below.

3.1.1. sCO_2 reversed Brayton cycle

General operation

The HTHP and HTHP-EJ configurations were based directly on the schematic of the reversed Brayton cycle discussed in Section 1.3.3 and illustrated in Figure 1.18. The components present in the configuration were therefore: two heat exchangers to exchange heat with the external process streams, a compressor and a turbine. The HTHP-EJ configuration additionally included the ejector. It will be discussed in more detail below how these components were exactly modelled. However, it is good to mention that the flow direction and numbering of the states used in Figure 1.18 was adapted in the model:

1. The compressor inlet
2. The compressor outlet or heat sink HEX inlet
3. The turbine inlet
4. The turbine outlet or heat source HEX inlet

In practical operation, and indicated in Figure 1.18, the connecting rod between the compressor and turbine enables the work regenerated in the turbine to directly power the compressor and reduce the required external work. This was incorporated in the COP calculations of the configurations as will be discussed below. At each state the thermodynamic properties of the sCO_2 were computed to realize the desired thermodynamic cycle. In between the states isentropic compression and expansion was applied in the turbomachinery. Isobaric heat addition and heat rejection was modelled through the heat source HEX and heat sink HEX respectively. The ideal reversed Brayton cycle assumes perfect isentropic compression and perfect isentropic expansion. However, in real life the turbomachinery operates with an isentropic efficiency. This results in energy losses and hence a decrease in COP. To create a ”real” cycle which also accounts for the isentropic efficiencies of the turbomachinery the thermodynamic model consists of two loops. First a loop based on the ideal reversed Brayton cycle is run, without losses in the turbomachinery are considered ($s_1 = s_2$ & $s_3 = s_4$). This was required to quantify the effect of the isentropic efficiencies as will be explained in more detail in the description of the compressor and turbine modelling. In the second ”real” loop the isentropic efficiencies were taken into account to create a realistic HTHP cycle. The exact relations used within the different components of the HTHP system are explained per component below. As a final note, it is good to mention that the definitions of the symbols and subscripts used in the equations can be found in the Nomenclature at the beginning of the report.

Heat exchangers

The heat exchangers were both modelled as counter-current HEX through the logarithmic mean temperature difference (LMTD) model as described by Bergman et al. (Bergman et al., 2011). Firstly, the following basic relation was used to obtain the heat exchanged inside the HEX :

$$\dot{Q}_{in} = U * A * \Delta T_{lm} \tag{3.1}$$

To find the log mean temperature difference the following relation was used that included the terminal temperature differences:

$$\Delta T_{lm} = \frac{\Delta T_1 - \Delta T_2}{\ln(\frac{\Delta T_1}{\Delta T_2})} \tag{3.2}$$

As shown in Figure 3.1 the terminal temperature difference is defined as the temperature difference between the inlet of the hot stream and the outlet of the cold stream (ΔT_1); or the temperature difference between the outlet of the hot stream and the inlet of the cold stream (ΔT_2).

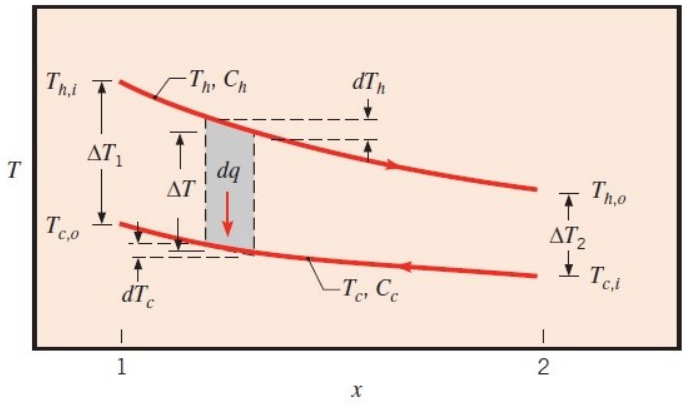

Figure 3.1: Temperature distribution inside a counter-current HEX indicating the terminal temperature differences ΔT_1 and ΔT_2 (Bergman et al., 2011).

To be able to solve the LMTD method in the thermodynamic model one of the two terminal temperature differences had to be chosen. The other terminal temperature difference could be calculated through Equations 3.1 & 3.2 where it was important to make sure the temperature difference in the HEX always stayed above the pinch temperature to prevent nonphysical behaviour. The terminal temperature differences could then be used to compute the inlet- and outlet temperature of the unknown stream.
To model the heat exchangers accurately and allow for heat transfer optimization, also the NTU-effectiveness method from Bergman et al. (2011) was applied to check the number of transfer units (NTU) and effectiveness (ε) of the HEX (Bergman et al., 2011). This entailed the following equations:

$$C_h = \dot{m}_h * c_{p,h} \tag{3.3}$$

$$C_c = \dot{m}_c * c_{p,c} \tag{3.4}$$

$$C_{min} = min(C_c, C_h) \tag{3.5}$$

$$C_{max} = min(C_c, C_h) \tag{3.6}$$

$$q = C_h * (T_{h,i} - T_{h,o}) \tag{3.7}$$

$$q_{max} = C_{min} * (T_{h,i} - T_{c,i}) \tag{3.8}$$

$$\varepsilon = \frac{q}{q_{max}} \tag{3.9}$$

$$NTU = \frac{UA}{C_{min}} \tag{3.10}$$

It should be noted that as c_p is not constant through the HEX due to the change of the temperature and pressure of the streams the average value of c_p between the inlet and outlet was used for both streams.
The HTHP model operation started from the external which delivers heat to the sCO_2 stream inside the heat source HEX. Initially the mass flow and the thermodynamic properties of this heat source stream at the in- and outlet of the HEX were chosen to realize a certain input of heat energy:

$$\dot{Q}_{in} = \dot{m}_{cs} * \Delta h = \dot{m}_{cs} * (h_{cs,i} - h_{cs,o}) \tag{3.11}$$

The change in enthalpy Δhcould alternatively be replaced by $c_p * \Delta T$. However, the c_p changes with temperature so it was more convenient and accurate to work with the specific enthalpy. This was mainly because CoolProp automatically incorporated this in its calculation of the specific enthalpy.
Through the Equations 3.1 & 3.2 the thermodynamic properties of the sCO_2 stream at the inlet of the HEX (state 4) and outlet of the HEX (state 1) are then be computed. The mass flow of the sCO_2 stream was then computed through:

$$\dot{m}_{sCO2} = \frac{\dot{Q}_{in}}{(h_1 - h_4)} \tag{3.12}$$

Here it is assumed that the sCO_2 mass flow remains constant throughout the HTHP cycle. As explained, in the second loop of the model the isentropic efficiencies of the turbomachinery are taken into account. Therefore, the thermodynamic properties at state 4 changes, and Equations 3.1,3.2 & 3.11 are used to calculate the final mass flow and the thermodynamic properties of the heat source stream at the inlet and outlet of the HEX.

The heat sink HEX was used to reject heat from the sCO_2 to the external heat sink stream in a similar fashion as the heat source HEX. The heat rejected to the heat sink stream could be computed with Equations 3.1 & 3.2 and the thermodynamic properties of the sCO_2 stream at the in- and outlet of the HEX. Moreover, the thermodynamic properties of the heat sink stream at the in- and outlet of the heat sink HEX could calculated. As a final step also the mass flow of the external stream could be computed:

$$\dot{m}_{hs} = \frac{\dot{Q}_{out}}{(h_{hs,o} - h_{hs,i})} \tag{3.13}$$

Compressor
As explained the ideal isentropic compression is modelled first. In this ideal case the specific entropy at the compressor outlet is equal to the specific entropy at the compressor inlet ($s_1 = s_2$). The compressor inlet pressure (state 1) and pressure ratio are chosen and together determine the pressure at the compressor outlet (state 2). With the known specific entropy and pressure all thermodynamic properties at the compressor outlet could be computed through CoolProp.

In the second loop the isentropic efficiency of the compressor needed to be taken into account to simulate real operation of the HTHP. The isentropic compression relations based on the changes in specific enthalpy as described in Equation 3.14 were used to calculate the ”real” thermodynamic properties at the compressor outlet (Nuclear Power, n.d.-b):

$$h_{2,re} = h_1 + \frac{h_{2,id} - h_1}{\eta_{compr}} \tag{3.14}$$

The required compressor work (W_{compr}) could then subsequently be calculated based on the specific enthalpy difference between the in- and outlet of the compressor and the mass flow of the sCO_2 through the relation:

$$W_{compr} = \dot{m}_{sCO2} * (h_{2,re} - h_1) \tag{3.15}$$

Turbine
The ideal turbine was modelled in a similar fashion as the compressor making use of CoolProp. However, now with the specific entropy at the turbine inlet equal to the specific entropy at the turbine outlet (($s_3 = s_4$). Moreover, due to the assumption of isobaric heat addition/rejection in the heat exchangers the turbine inlet pressure was assumed to be equal to the compressor outlet pressure; and the turbine outlet pressure equal to the compressor inlet pressure. This resulted in an identical pressure ratio over the turbine as for the compressor. The real turbine makes use of the isentropic expansion relations based on the changes in specific enthalpy. This is described in Equation 3.14 to calculate the ”real” thermodynamic properties at the turbine outlet (Nuclear Power, n.d.-b).

$$h_{4,re} = h_3 - \eta_T * (h_3 - h_{4,id}) \tag{3.16}$$

The incorporation of the isentropic efficiency of the turbine caused a change in the turbine outlet (state 4), hence a change in the heat source HEX. As explained earlier, to maintain a correct interaction with the heat source the heat addition from the heat source was re-calculated while the sCO_2 mass flow was unchanged to keep the heat pump cycle the same. The regenerated work in the turbine (W_{turb}) used to power the compressor was subsequently calculated based on the specific enthalpy difference between the in- and outlet of the turbine and the mass flow of the sCO_2 using the relation:

$$W_{turb} = \dot{m}_{sCO2} * (h_3 - h_{4,re}) \tag{3.17}$$

3.1.2. Ejector

The idea behind the ejector model was to obtain a first estimation if it could be beneficial to add an ejector parallel to the turbine to “pre-compress” the sCO_2 before it is fed to the compressor. It was observed from the T-s diagram of the basic HTHP cycle that the required compression work is larger than the generated turbine work due to the isobaric lines that diverge. Therefore it was expected that it might benefit the overall performance to find a way to decrease the compressor work, even at the cost to sacrifice some turbine work. The idea to add an ejector to (combined) power cycles to improve performance has been studied and proposed as explained by Padilla et al. (2016) in their paper on the addition of an ejector to a supercritical CO_2 Brayton cycle (Padilla et al., 2016). Additionally, do the IEA mention in their Annex 58 Task 1 report the potential of the addition of an ejector to the standard heat pump cycle to reduce the irreversibilities caused by the use of the expansion valve. This is of interest especially for HTHPs which often need to operate with high compression ratio’s for high temperature lift applications (IEA HPT TCP, 2023). They also indicate some studies on (advanced) ejector assisted HTHPs that reported significant COP improvements of up to 36 % for output temperatures up to 140 °C (IEA HPT TCP, 2023).

Moreover, there are also CO_2 ejectors on the market from companies like Danfoss (Danfoss, 2018). However, these are designed for refrigeration systems and for flows and pressures significantly smaller than the HTHP model makes use of. Therefore, it was concluded that currently no ejector technology exists that is suitable for this application.
In terms of numerical modelling of ejectors it was found that this is generally quite complex. In order to accurately model/design an ejector also the precise geometry of the ejector has to be (accurately) defined. It is very much dependent on the working fluid and operating conditions used, and in the literature no ejector models were identified that where directly applicable to this application of sCO_2.

However, in the literature the ejector model from the earlier mentioned study from Padilla et al. (2016) was identified as the most suitable option. This to obtain a good estimate on how the addition of an ejector could enhance the sCO_2 reversed Brayton HTHP cycle. In the study they look into different Brayton power cycle configurations using sCO_2 as working medium assisted by an ejector. Thereby, having the ejector operating solely with sCO_2 around temperatures of 800 K and pressures up to 250 bar indicating that the ejector model is suitable for high-temperature and high-pressure operation.
The ejector model was based on the work of Aly et al. (1991) and Eames et al. (1995) that propose simplified models for steam jet ejectors (Aly et al., 1999)(Eames et al., 1995). Padilla et al. (2016) adapted this to the use of sCO_2 instead of steam. They also present a validation of their ejector model with experimental data for the working medium R141b which showed reasonable agreement with the experimental data within an error margin of 15 %. It is mentioned with the validation that the fact that the ejector is modelled purely based on thermodynamic relations and does not take geometrical parameters into account leads to some discrepancies with the experimental data (Padilla et al., 2016). However, as explained earlier the inclusion of geometrical parameters also makes it more difficult to apply the ejector model to a different application. The fact this model was somewhat more general made it easier to adapt it to the sCO_2 reversed Brayton HTHP cycle.
The operational principle of the ejector can best be described supported by the schematic overview of an ejector and the variation of the pressure and velocity through the ejector as shown in Figure 3.2. The ejector consists of 4 sections:

1. Nozzle section
2. Mixing section
3. Constant area section
4. Diffuser section

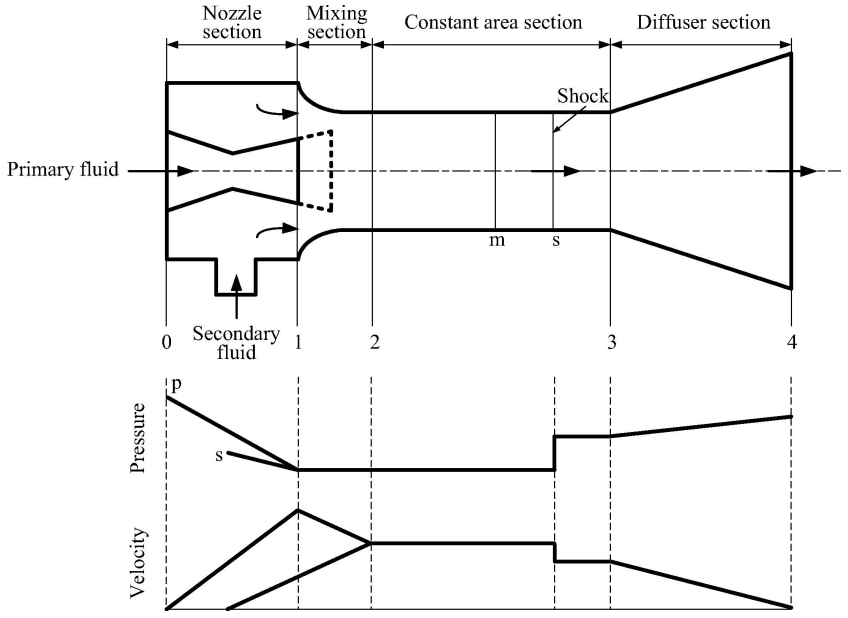

Figure 3.2: Schematic overview of an ejector including the variation of the pressure and velocity through the ejector (Padilla et al., 2016).

The numbering used in Figure 3.2 was also adopted in the ejector model described below. It can be seen in Figure 3.2 that the idea behind the ejector is that the high-pressure primary flow is used to increase the pressure of the low-pressure secondary flow. This to obtain a combined flow with a pressure as close as possible to the pressure of the high-pressure flow. During this process the pressure and velocity undergo variations as well as the occurrence of a shock inside the constant area section due to supersonic velocities. Something that will be described in more detail below in the thermodynamic relations describing the ejector operation. It was found that in the model from Padilla et al. (2016) a slightly different approach is adopted than in some of the studies mentioned in the paper. In these studies they calculate the velocities and pressures through the Mach number. Therefore, next to the approach used by Padilla et al. (2016) also a (combined) Mach number approach from Aly et al. (1991), Eames et al. (1995) and El-Dessouky et al. (2002) was added to check what outcomes would be obtained (Aly et al., 1999)(Eames et al., 1995) (El-Dessouky et al., 2002).

Although Padilla et al. (2016) mention that the model was build in Python and REFPROP was used to calculate the properties of CO_2 the model itself was not included. Based on their model description and aforementioned papers the ejector was modelled using Python 3.8.10 (Python Core Team, 2019 and CoolProp 6.5.0 (Bell et al., 2014).
The thermodynamic operation principle of the ejector model is based on energy- and mass balances and the continuity equation and assumes adiabatic processes and steady state conditions (Padilla et al., 2016).

Energy balance for adiabatic process:

$$\sum \dot{m}_i(h_i + \frac{u_i^2}{2}) = \sum \dot{m}_o(h_o + \frac{u_o^2}{2}) \tag{3.18}$$

Momentum balance:

$$P_i A_i + \Sigma \dot{m}_i u_i = P_o A_o + \sum \dot{m}_o u_{out} \tag{3.19}$$

Continuity equation:

$$\sum \rho_i u_i A_i = \sum \rho_o u_o A_o \tag{3.20}$$

As a final note a few simplifying assumptions, obtained from the papers, were used in the ejector model:

1. The entire process is adiabatic.
2. The model is generalized in such a way that geometrical parameters of the ejector were not needed but are therefore also not taken into account.
3. As indicated in Figure 3.2 the velocities of the primary and secondary flow upon entering the ejector as well as the velocity of the combined flow exiting the ejector were assumed to be negligible.
4. Losses in the ejector, like wall friction or boundary layer separation, were included through the introduction of isentropic efficiencies in every section.
5. The mixing of the primary and secondary flow occurs at an uniform and constant pressure using the constant pressure approach.

Nozzle section

In the nozzle section the primary (high-pressure) flow is accelerated inside the nozzle decreasing its pressure and increasing its velocity as can be seen in Figure 3.2 in accordance with the mass and energy balances. The pressure of the flow at the exit of the nozzle section is denoted as P_1 and the exit velocity of the primary flow (u_{p1}) at the end of the nozzle is described with:

$$u_{p1} = \sqrt{2 * \eta_n * (h_p - h_{p1,s})} \tag{3.21}$$

Where the required thermodynamic properties were calculated using CoolProp based on the known properties and through the relations $h_p = h\,(T_p, P_p)$, $s_p = s\,(T_p, P_p)$ and $h_{s1,s} = h\,(P_1, s_p)$.

The properties of the secondary flow were calculated in a similar fashion but as the secondary flow is not accelerated in the nozzle no nozzle efficiency is taken into account. The velocity of the secondary flow at the entrance of the mixing section was described with:

$$u_{s1} = \sqrt{2 * (h_s - h_{s1,s})} \tag{3.22}$$

Where again the required thermodynamic properties are calculated using CoolProp based on the known properties and through the relations $h_s = h\left(T_s, P_s\right)$, $s_s = s\left(T_s, P_s\right)$ and $h_{s1,s} = h\left(P_1, s_s\right)$.

As described earlier the ejector can also be described through the Mach number approach where the velocities inside the ejector are modelled through the local Mach number in every section. For the mixing process this approach also requires the definition of the critical Mach number M^*, which is defined as the ratio of the local flow velocity over the speed of sound at critical conditions ($M = 1$) at every point (El-Dessouky et al., 2002). The relationship between the Mach number and the critical Mach number is described through the equation:

$$M^* = \sqrt{\frac{M^2(\gamma + 1)}{M^2(\gamma - 1) + 2}} \tag{3.23}$$

Next to the Mach number the critical Mach number was also calculated at every section, for the Nozzle section this results in the following equations:

$$M_{p1} = \sqrt{\eta_n * \frac{2}{\gamma_p - 1} * \left(\frac{P_p}{P_1}\right)^{\frac{\gamma_p - 1}{\gamma_p}} - 1} \tag{3.24}$$

$$M_{s1} = \sqrt{\frac{2}{\gamma_s - 1} * \left(\frac{P_s}{P_1}\right)^{\frac{\gamma_s - 1}{\gamma_s}} - 1} \tag{3.25}$$

$$M^*_{p1} = \sqrt{\frac{M^2_{p1}(\gamma_p + 1)}{M^2_{p1}(\gamma_p - 1) + 2}} \tag{3.26}$$

$$M^*_{s1} = \sqrt{\frac{M^2_{s1}(\gamma_s + 1)}{M^2_{s1}(\gamma_s - 1) + 2}} \tag{3.27}$$

γ_p and γ_s were calculated through the specific heat capacities at constant pressure and volume as described in Equations 3.28 & 3.29:

$$\gamma_p = \frac{c_{p,p1}}{c_{v,p1}} \tag{3.28}$$

$$\gamma_s = \frac{c_{p,s1}}{c_{v,s1}} \tag{3.29}$$

Where $c_{p,i} = c_p\left(P_i, T_i\right)$ and $c_{v,i} = c_v\left(P_i, T_i\right)$ are calculated through CoolProp.

Mixing section

In the mixing section the primary flow that exits the nozzle has a high velocity and a pressure lower than the pressure of the secondary flow which is therefore ”sucked” into the mixing chamber. Due to the converging channel through which the secondary flow is led it is accelerated thereby decreasing its pressure until it reaches the pressure P_1.
In the mixing section the momentum balance as described in Equation 3.19 is applied where as mentioned in the assumptions the pressure is assumed to stay constant ($P_1 = P_2$) resulting in the following momentum balance:

$$\left(\dot{m}_p + \dot{m}_s\right) u_2 = \dot{m}_p u_{p1} - \dot{m}_\varepsilon u_{s1} \tag{3.30}$$

By rewriting the momentum balance u_2 could be calculated with:

$$u_2 = \eta_m \left(\frac{u_{p1} + \omega u_{s1}}{1 + \omega}\right) \tag{3.31}$$

The entrainment ratio ω is a variable commonly used in ejector analysis and is defined as the ratio of the mass flow of the secondary flow and the primary flow:

$$\omega = \frac{\dot{m}_s}{\dot{m}_p} \tag{3.32}$$

With the mass flows and velocities known the energy balance as described in Equation 3.18 can now be rewritten to find the specific enthalpy at the end of the mixing section:

$$h_2 = \frac{\omega h_s + h_p}{1+\omega} - \frac{u_2^2}{2} \tag{3.33}$$

With the pressure P_2 known ($P_1 = P_2$) and the calculated specific enthalpy h_2 all other thermodynamic properties of the flow at the end of the mixing section could be calculated using CoolProp.

For the Mach number approach the Mach number M_2 at the end of the mixing section (or start of the constant area section) was calculated through first calculating the critical Mach number M_2^* as described in Equation 3.34:

$$M_2^* = \frac{M_{p_1}^* + \omega M_{s_1}^* \sqrt{T_s/T_p}}{\sqrt{(1+\omega)\,(1+\omega T_s/T_p)}} \tag{3.34}$$

The Python code was used to solve Equation 3.23 for the Mach number M_2 as described in the papers. M_2 was then calculated in a similar way to Equation 3.28 based on the known thermodynamic properties and using the heat capacity ratio at the end of the mixing chamber.

Constant area section

In the constant area section the mixed flow reached supersonic speeds which results in a shock wave as indicated in Figure 3.2, where there is a sudden drop in velocity and sudden increase in pressure. To determine the velocity downstream of the shock (u_3) the following equation was used as proposed by Padilla et al. (2016):

$$u_3 = c_3 \sqrt{\left(M_2^2 + \frac{2}{\gamma_c - 1}\right) / \left(M_2^2 \frac{2\gamma_c}{\gamma_c - 1} - 1\right)} \tag{3.35}$$

However, the problem with Equation 3.35 was that in order to determine the local speed of sound c_3 downstream of the shock using CoolProp the thermodynamic properties after the shock needed to be known. These could only be calculated after u_3 was calculated.
This was overcome in the Python code by first solving Equation 3.35 with the local speed of sound at the end of the mixing section c_2 where all thermodynamic properties were known. Then use this "inaccurate" value of u_3 to calculate the thermodynamic properties after the shock and hence calculate c_3. Then recalculate Equation 3.35 with this value of c_3, compare it with the previously calculated value of u_3 and iterate until a constant, and assumed correct, value of u_3 was obtained. See the Python code in the Appendix for more detailed information on this approach.
With this correct value of u_3 and using the energy balance from Equation 3.18 the specific enthalpy downstream of the shock was calculated through:

$$h_3 = h_2 + \frac{u_2^2}{2} - \frac{u_3^2}{2} \tag{3.36}$$

The continuity equation as described in Equation 3.20, assuming a constant area at the location where the shock occurs, was then used to calculate the density of the mixed flow downstream of the shock with:

$$\rho_3 = \rho_2 \left(\frac{u_2}{u_3}\right) \tag{3.37}$$

With u_2 and u_3 from Equations 3.31 and 3.35 respectively and the density of the mixture at the end of the mixing section ρ_2 calculated with Coolprop using the known thermodynamic properties.
The pressure downstream of the shock was then calculated with Coolprop based on the known specific enthalpy and density downstream of the shock with $P_3 = P\,(h_3, \rho_3)$.
For the Mach number approach the Mach number downstream of the shock could be calculated with:

$$M_3 = \frac{M_2^2 + \frac{2}{(\gamma_c - 1)}}{M_2^2 \frac{2\gamma_c}{(\gamma_c - 1)} - 1} \tag{3.38}$$

With M_2 and γ_c as calculated earlier and the pressure downstream of the shock could then be calculated with:

$$P_3 = P_2 \left(\frac{1 + \gamma_c M_2^2}{1 + \gamma_c M_3^2} \right) \tag{3.39}$$

Diffuser section

In the last part of the ejector, the Diffuser section, the mixed flow is expanded which results in a decrease of the velocity back to negligible values. This caused an increase of the pressure as illustrated in Figure 3.2 to create a flow with a pressure as high as possible that exits the ejector.
Through the use of the momentum balance as described in Equation 3.19 the specific enthalpy of the flow at the ejector exit h_4 was calculated as well as the specific enthalpy of the flow at the ejector exit assuming constant specific entropy $h_4 s$ with:

$$h_{4s} = h_3 + \frac{u_3^2}{2\eta_d} \tag{3.40}$$

$$h_4 = h_3 + \frac{u_3^2}{2} \tag{3.41}$$

With h_3 and u_3 from Equation 3.36 & 3.35 respectively.
Now the ejector exit pressure P_4 and temperature T_4 were calculated with:

$$P_4 = P\left(h_{4s}, s_4\right) \tag{3.42}$$

$$T_4 = P\left(h_{4s}, P_4\right) \tag{3.43}$$

Where $s_3 = s\left(h_3, \rho_3\right)$ and $s_4 = s_3$ due to the assumption of constant specific entropy in the diffuser. The value of the ejector exit pressure P_4 was maximized by adjusting the pressure of the mixed flow at the exit of the nozzle section P_1. This could in theory be done up until just below the pressure of the secondary flow P_s to still generate enough suction in the mixing section.

For the final step of the Mach number approach the ejector exit pressure P_4 is calculated with:

$$P_4 = P_3 \left[\left(\eta_d \frac{\gamma_d - 1}{2} M_3^2 + 1 \right)^{\frac{\gamma_d}{\gamma_d - 1}} \right] \tag{3.44}$$

Where P_3 and M_3 were adopted from Equation 3.39 & 3.38 respectively.

Incorporation of ejector in HTHP model

The designed sCO_2 reversed Brayton HTHP cycle as described in Section 3.1.1 needed to be adapted to be able to incorporate the ejector as a ”pre-compression” step before the compressor. Firstly, to realize a primary (high-pressure) flow and a secondary (low-pressure) flow the sCO_2 stream is split into two streams before entering the turbine. The first stream is send directly to the ejector to serve as primary flow. The second stream is first expanded in the turbine, then send through the heat source HEX to exchange heat with the external process stream and then send to the ejector to serve as the secondary flow. The mixed flow that exits the ejector is then send to the compressor to complete the HTHP cycle again. This resulted in new inlet conditions for the compressor but no other adjustments to the compressor modelling were needed.

In this configuration only the second stream is able to exchange heat with the heat source. In order to have enough input power the sCO_2 mass flow of the combined stream in the HTHP-EJ configuration had to be higher than for the HTHP configuration. This is calculated after the ejector is modelled as this value is determined by the entrainment ratio chosen for the ejector. The higher the entrainment ratio the lower the required combined sCO_2 mass flow needed to be.

3.1.3. Aspen Plus

In order to obtain a more realistic HTHP design it was in consultation with Prof. Hooman chosen to also simulate the HTHP in Aspen Plus V12, a Process Simulation Software (SPS) program. Aspen Plus is powerful tool that utilizes a combination of data from real-life equipment combined with available correlations in literature to simulate a process as accurately as possible based on the given input parameters. The described Aspen Plus models in this section were also implemented in the final HTHP and HTHP-EJ designs. This also provided an extra means of validation of the thermodynamic model by simulating the HTHP and HTHP-EJ with the actual components that would be used. Something which will be further discussed in Section 3.1.4.

The use of Aspen Plus provided the additional advantage of access to the build-in Aspen Exchanger and Design Rating (EDR) and the Aspen Process Economic Analyzer (APEA) software. The EDR software could be used to find a realistic and optimal heat exchanger design for both the heat source HEX and heat sink HEX based on the input parameters. At the same time it could be used also verify the results from the thermodynamic model, including for example vibration and heat transfer checks of the heat exchangers. Thereby, also provide the right numbers regarding for example the overall heat transfer coefficient 'U'. The APEA software was most useful to evaluate the expected costs of the different components of the HTHP within certain operating conditions, using a combination of data from existing equipment that it has stored in its database and cost scaling based on the proper correlations.

As explained earlier Aspen Plus enables the digital construction of the HTHP with the actual components that would be used. Moreover, it accurately predicts the (real-life) performance based on the most recent data on existing equipment it has in its database. If information is missing or e.g. the operating conditions are slightly different it uses correlations for further estimations to simulate real-life performance as accurately as possible.
The use of Aspen Plus first required a more detailed design to be specified, mainly regarding the heat exchangers used. It was chosen to go for the use of TEMA shell-and-tube heat exchangers because of three main reasons. First of all, shell-and-tube heat exchangers are well-known for their robustness and ability to deal with high temperature-pressure combinations. This was convenient for the required operating conditions of the sCO_2 at pressures of up to 345 bar and temperatures exceeding 300 °C inside the HTHP cycle. Secondly, the only realistic alternative for this application would be the use of a printed-circuit-heat-exchanger (PCHE) as mentioned in other studies. Although PCHE's might serve as an compact and effective solution in terms of heat transfer they are significantly more expensive than shell-and-tube heat exchangers and are not commercially available for this application. Something which was also illustrated in the design proposed by Moen and Heggset (2021) where the PCHE modelling was based on other theoretical studies rather than an actual PCHE designs. Finally, shell-and-tube heat exchangers could be computed in detail by Aspen EDR while for example PCHE could not. Hence it would be very difficult to accurately validate the HTHP and HTHP-EJ model with PCHE's and get an accurate equipment cost estimation. This arguments combined resulted in the choice for TEMA shell-and-tube heat exchangers.

The full HTHP cycle could be constructed in the general Aspen Plus program which was then able to calculate the operation of the turbomachinery and heat exchangers in a comparable way to the HTHP model. For the design of the heat exchangers this is categorized in Aspen Plus through the "model fidelity". This is related to the accuracy compared to real designs and is standard set at "Shortcut". which is comparable to the way the HEX are modelled in the HTHP model without e.g. pressure drops or correction factors. This setting therefore always resulted in exactly similar outputs to the HTHP model. When "Shell & Tube" was chosen as model fidelity Aspen EDR could be launched within to Aspen Plus. This to do some calculations based on the input data and operating conditions and propose an optimal HEX design. In the next simulation this HEX design was then automatically implemented to generate a more realistic HTHP design. A note should be made that the introduction of the detailed (shell-and-tube) heat exchangers introduced for example pressure drops in the streams. As described in Section 3.1 the heat exchangers in the HTHP model were modelled quite general and simplified through the LMTD and NTU-effectiveness model. This was done as there was a high level of uncertainty in how the HEX would actually perform. The goal was to get a general idea of what (optimally) the HTHP cycle should look like and the detail that Aspen EDR designs the HEX with was a level of

detail that could never be reached within the own Python model. Thereby Aspen EDR also enabled to provide a detailed value of the overall heat transfer coefficient 'U' inside the HEX. As this value was difficult to estimate at first a value from internet was used of 200-400 $\frac{W}{m^2K}$ for high pressure gas in the tubes and liquid outside the tubes Engineers Edge, n.d. It was already expected the actual value could be significantly different due to the use of sCO_2 and Therminol-66. The use of Aspen EDR therefore allowed to obtain the actual heat transfer surface area required for the shell-and-tube heat exchangers. This initially caused some deviations between the HEX design from the HTHP model and Aspen EDR. This was solved by also introducing the pressure drops from the Aspen Plus model in the HTHP model. After a few iterations it was possible to obtain a nearly identical cycle in terms of pressure, temperature and energy and hence obtain a HTHP model which better resembled real operation.

The design of the sCO_2 reversed Brayton HTHP in Aspen Plus is shown in Figure 3.3 below.

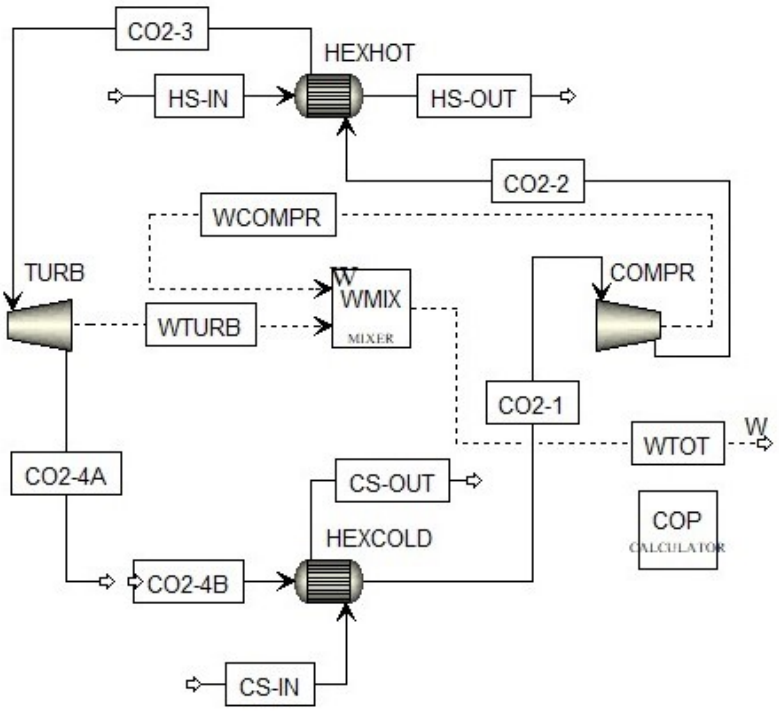

Figure 3.3: Design of the sCO_2 reversed Brayton cycle HTHP (HTHP) in Aspen Plus V12.

To explain the different kind of lines observed in Figure 3.3: in Aspen Plus solid lines are used to indicate streams of material (matter) and dotted lines are used for energy (work) streams. The external streams are abbreviated with "CS" and "HS" for the source (cold) stream and sink (hot) stream respectively. The streams interact with the HTHP cycle through the heat source HEX ("HEXCOLD") and heat sink HEX ("HEXHOT"), modelled as TEMA shell-and-tube heat exchangers as mentioned. The sCO_2 stream is indicated with "CO2" and the numbering matches the numbers in the HTHP model for every state in the cycle. It was learned that Aspen Plus cannot deal well with fully closed cycles so the sCO_2 cycle needed to be split. This split only works well if the properties of the stream are identical before and after the split (Adams II, 2022). It was chosen to have the split just before the heat source HEX, indicated with a "CO2-4A" and a "CO2-4B" stream. This was done as the stream properties needed to be given at this point anyway before the sCO_2 entered the heat source HEX. An additional advantage of this was that if there is was something not right in the cycle the properties before and after the split would not be identical. This indicated an error in the modelling. The compressor ("COMPR") and turbine ("TURB") were both set as isentropic and were modelled as a motor-driven (centrifugal) gas turbocompressor and an isentropic (radial) turboexpander respectively.

The (work) streams ”WCOMPR” and ”WTURB” indicate the net work required for the compressor and generated by the turbine respectively. They are combined in a so-called ”Work mixer” to simulate the direct connection between the turbine and compressor. This enabled the regenerated work from the turbine to partly power the compressor. The output ”WTOT” was the (net) external work required to power the compressor.
Finally, was a ”Calculator” added which uses Fortran syntax and where mathematical expressions can be written. It was used to calculate the COP of the HTHP according to Equation 1.5 using ”WCOMPR”, ”WTURB”, and the output heat power delivered in the heat sink HEX ”QOUT”.

The construction of the HTHP model was done in a few steps. Firstly, the properties of $(s)CO_2$ and Therminol-66 were fetched from the Aspen Plus database. The REFPROP property method was selected, which is nearly identical to CoolProp, for CO_2. Unfortunately, Therminol-66 was not suitable for REFPROP hence the advised NRTL property method was adopted for the heat source and heat sink streams. Secondly, in the turbomachinery the required outlet pressures could be set as well as the isentropic efficiencies. Thirdly, as already briefly mentioned above, Aspen Plus required every stream entering the heat exchangers to be fully defined in terms of pressure, temperature, mass flow and composition. Therefore the properties of the sCO_2 stream at state 4 (”CO2-4B”), the heat source inlet stream (”CS-IN”) and the heat sink inlet stream (”HS-IN”) were supplied to the Aspen Plus model. Finally, the HEX could be modelled using Aspen EDR based on some input parameters regarding the desired terminal temperature differences and pinch. After this the model could be run to generate the outputs of the Aspen Plus HTHP design.

The construction of the HTHP-EJ configuration in Aspen Plus posed more of a problem. Unfortunately, the ejector technology for applications like these is not developed or used in other applications so it was not available to add an ejector in Aspen Plus. It was found online that the ”Mixer” component might work alternatively but after constructing the cycle with the addition of this component it was concluded that this was not the case.
However, through the relocation of the the earlier described split in the sCO_2 stream to just behind the ”Mixer” it was possible to fully simulate the rest of the equipment used in the HTHP-EJ model in Aspen Plus. This did cause a temperature mismatch before and after the split which, as explained earlier, was not desirable to enable good validation of the HTHP model. Moreover, it showed that the Mixer block was not able to simulate the performance of the ejector. However, this ”trick” made it possible to simulate the turbomachinery and heat exchangers with the correct mass flows, temperatures and pressures from the HTHP-EJ model which was still of use.
The design of the sCO_2 reversed Brayton ejector-assisted HTHP in Aspen Plus is shown in Figure 3.4. The cycle is similar to the HTHP cycle as described above apart from the addition of the ”Mixer” component as ejector and the addition of a ”Splitter” component. This component is placed between the heat sink HEX and the turbine to realize the required primary (high-pressure) stream (”CO2-HP”) and secondary (low-pressure) stream (”CO2-LP”) for the ejector. As explained earlier the ratio of the mass flows of these two streams is determined through the chosen entrainment ratio in the HTHP-EJ model. The split in the sCO_2 stream is indicated with ”CO2-EA” and ”CO2-EB”. All other components and mass/energy flows are similar to the Aspen Plus design for the HTHP model.

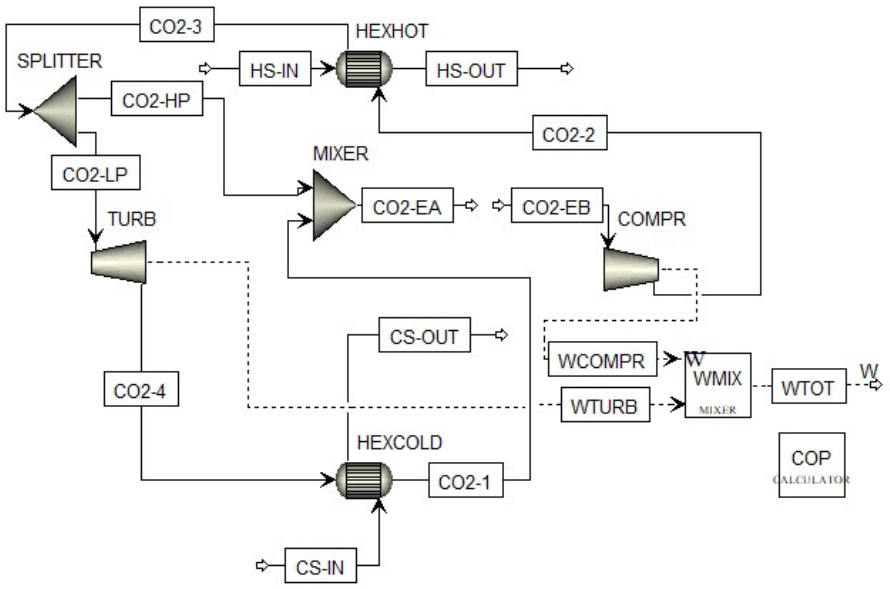

Figure 3.4: Design of the ejector-assisted sCO_2 reversed Brayton cycle HTHP (HTHP-EJ) in Aspen Plus V12.

3.1.4. Model validation

It became evident during the literature review and research into HTHP technologies that no real HTHP or prototype of a sCO_2 reversed Brayton HTHP exists. Therefore it was not possible to validate the models with experimental results or real-life (operational) data. However, the existence of the MAN HPU transcritical CO_2 HTHP and the CoBra air reversed Brayton HTHP prototype as described in Section 1.3.3 showed that the idea to design a HTHP operating based on the reversed Brayton cycle and a HTHP with sCO_2 as working medium could very well prove to be successful.

Although only theoretical, the studies by Zuhlsdorf et al. (2019) and Moen and Heggset (2021) as discussed in Section 1.3.3 could be used to validate the model. This to check if the thermodynamic background of the model as described in Section 3.1 would provide similar results when using the inputs from these papers. Moreover, the validation through the Aspen Plus models as described above provided a more detailed and stronger (numerical) validation. The detailed result of the validation of the HTHP model with the papers from Zuhlsdorf et al. (2019), Moen and Heggset (2021) and Aspen Plus can be found in Appendix-a: Model validation results.

Moreover, also the results from the validation of the HTHP-EJ model with Aspen Plus are included in Appendix-a. Despite the mentioned challenges to create the HTHP-EJ configuration in Aspen Plus. In general it was observed that for the same model inputs the HTHP model outputs matched well with the results presented in the two papers and Aspen Plus. Satisfactory results were obtained with only very minor differences in terms of output parameters. On the other hand, it had to be concluded that for the validation of the HTHP-EJ model Aspen Plus was less useful. This was mainly due to not being able to validate the ejector, being the most important component of the HTHP-EJ cycle. It could still be used to validate the other components in the cycle but as these were largely similar to the components used in the HTHP cycle did not provide a lot of additional information.

3.2. Parametric analysis

After the successful validation of the HTHP model it was interesting to further investigate the influence of different model parameters on the performance, size and costs of the HTHP system. It was also of interest to investigate the optimal design for the HTHP-EJ cycle to see what performance enhancement could potentially be obtained through the addition of an ejector to the HTHP cycle. Since the HTHP-EJ model was aimed to investigate if the HTHP performance would improve through the addition of an ejector the parametric analysis was first done for the basic HTHP model. The knowledge obtained during this analysis was then used to also execute a parametric analysis on the HTHP-EJ model focused on the parameters specifically related to the ejector.

3.2.1. HTHP model

Before the parametric analysis could be done it was important to set the boundary conditions on the operation of the HTHP. This to make sure the effect of changing certain model parameters produced comparable results to create a realistic design. The main boundary conditions where:

- The output power should be above 3.0 MW and as close to 3.0 MW as possible
- The output temperature should be above 280.0 °C and as close to 280.0 °C as possible
- For the heat source HEX: ΔT_1 should be 10 K, and ΔT_2 should be above 10 K to make sure ΔT_1 was the pinch
- For the heat sink HEX: a ΔT_1 of minimal 15 K was required to have a pinch of at least 10 K inside the HEX, ΔT_2 should be (slightly) larger than ΔT_1
- The inlet temperature of the heat sink stream should be above the inlet temperature of the heat source stream
- The CO_2 should either by in gas-phase or supercritical-phase throughout the cycle to stay outside the two-phase region
- The outlet pressure of the compressor should be 345 bar at maximum as this is the limitation for existing sCO_2 turbomachinery technology

The model parameters that influenced the performance, size and cost of the HTHP design could be categorized based on the interaction between the working medium and the external process streams, through the heat exchangers, and based on the turbomachinery. The chosen categories where therefore: the heat source HEX, the turbomachinery, and the heat sink HEX. It was chosen to evaluate the parametric analysis for three isentropic turbomachinery efficiency scenario's that indicated the worst and best turbomachinery efficiency that could be expected in a real life design. A realistic range to be expected was 60-80% for the compressor and 70-90% for the turbine. As a mid scenario it was chosen to adapt the proposed efficiencies by Aspen Plus of 72 % for both the turbine and compressor. It is not entirely clear how Aspen calculates these efficiency values, just that it uses somewhat complex default efficiency correlations (Adams II, 2022). The turbomachinery efficiency scenario's were:

- Low efficiency scenario: η_{compr} of 60% and η_{turb} of 70%
- Mid efficiency scenario: η_{compr} of 72% and η_{turb} of 72%
- High efficiency scenario: η_{compr} of 80% and η_{turb} of 90%

Moreover the equipment cost estimations used in the parametric analysis were computed with the help of Aspen EDR, for the heat exchangers, and APEA, for the turbomachinery. The calculation of the costs of the heat exchangers through Aspen EDR was very straightforward as this was done automatically when the heat exchangers were designed according to the method described in Section 3.1.3. However, as APEA was partly restricted in the cost calculations for the turbomachinery these cost calculations proved to be more challenging. The compressor inlet temperature could not exceed 93 °C, so if the actual inlet temperature was higher than that it had to be set to 93 °C. The other parameters like the inlet- and outlet pressure and the isentropic efficiency could be set to any desired values. The only limitation present was that the compressor outlet pressure could not exceed 345 bar as mentioned. The mass flow of the sCO_2 stream was then varied to obtain the correct output power. This resulted in a cost estimation of the exact same design in terms of pressure, isentropic efficiency and power but for slightly lower temperatures.
The turbine (turboexpander) was limited by the fact that the input temperature could not exceed 320

°C, the inlet pressure could not exceed 205 bar, and the power was limited at 1.5 MW. In the cost data obtained the temperature and power limitation were not exceeded but the maximum pressure was an unfortunate limitation. As the compressor was able to go to pressure up to 345 bar it was assumed that in real-life operation the turbine would also be able to handle this. Therefore, a pressure cost scaling was introduced for the turbine for inlet pressure above 205 bar. This was done by analyzing the % increase of the cost for the compressor in terms of the total costs when the output power and pressure ratio were kept constant and the compressor inlet pressure increased from 25 to 85 bar. The pressure scaling was executed for the power levels 0.5 MW, 1 MW and 1.5 MW and for the three efficiency scenario's. This to be able to use the value that was in terms of operating conditions most similar to the turbine. Figure 3.5 shows the result for the 1 MW case to give an idea on how the costs increased with pressure, where it can be seen that this increase is quite stable. It was found that based on the power level and the compressor efficiency the compressor costs increased with 0.228-0.286 %/bar.

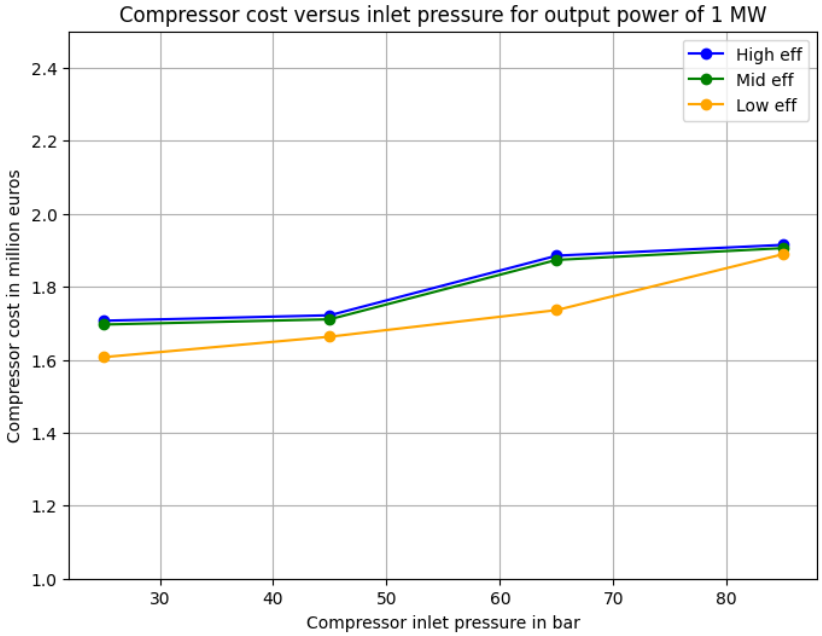

Figure 3.5: Compressor costs versus the compressor inlet pressure for a constant output power of 1 MW.

To estimate the turbine costs first the operation with a pressure up to 205 bar was calculated for the correct inlet temperature, pressure ratio and turbine power. Based on the actual inlet pressure this number was then scaled using the appropriate pressure cost scaling number based on the compressor cost scaling as described above. This method introduced a significant uncertainty compared to the way the other equipment costs were estimated. Nevertheless, it provided a significant more detailed number compared to how for example Zühlsdorf et al. (2019) estimated the turbine costs, which was done purely on the output power as explained in Section 1.3.3.

Heat source HEX

The cycle starts from the external process stream serving as heat source. Therefore, the interaction between the sCO_2 stream and the external process stream through the heat source HEX had a significant impact on the setup of the HTHP cycle. The way the parameters of the heat source HEX are chosen determines how the two streams interact. This further determines model parameters like the mass flows and temperature/enthalpy change of the sCO_2 stream during the heat absorption. Especially the mass flow of the sCO_2 stream is an important parameter as this remained constant throughout the cycle.

The model parameters connected to the heat source HEX investigated during the parametric analysis were:

- The properties of the sCO_2 stream in the form of the temperature difference between in- and outlet and the mass flow
- The properties of the external heat source stream in the form of the temperature difference between inlet and outlet and the mass flow
- The HEX pinch temperature
- Size of the HEX measured through the UA value
- Estimated equipment costs of the HEX

It should be noted that the overall heat transfer coefficient is not a variable that could be chosen. However, as that value was estimated in the HTHP model and depended on the operating conditions it was deemed better to estimate the required size of the HEX through the combined UA value rather than through just the heat exchanger surface area. Moreover, does the size of the HEX also serve as a direct indication of the costs of the heat exchanger if the operating temperatures and pressures stay more or less the same. However, the cost of the heat source HEX were also separately investigated for different operating temperature-pressure combinations to see how strong the influence of the operating conditions were on the costs.

First of all, it was already observed before the execution of the parametric analysis that the properties of the external heat source stream did not have a direct impact on the COP. This was due to the way the model was constructed where first an ideal heat source HEX was used to generate the ideal sCO_2 reversed Brayton cycle. This determined the mass flow of sCO_2 stream and the temperature/enthalpy difference in the heat source HEX. The actual external heat source stream was then constructed to match the sCO_2 cycle which was updated with the isentropic turbomachinery efficiencies to obtain a realistic HTHP design. Therefore, adapting the properties of the external heat source stream could be done quite freely without impacting the sCO_2 cycle. This was something that in practise would be very welcome as it allowed a lot of flexibility for the heat source stream in terms of suitable temperature glide and mass flow depending on how the heat source stream would be provided. Generally a low NTU results in a smaller, and hence less expensive, HEX. However, also less efficient heat transfer. For a high NTU value this is the other way around. A NTU value of between 3 and 4 is generally considered as a good optimal between efficient heat transfer and size/cost and was advised by Professor Hooman as a target value. As this value was well-attainable for the heat source HEX design it was therefore decided to make sure the NTU was kept between 3 and 4 as well as realizing an effectiveness of at least 80%. This was realized by adapting the UA value of the heat source HEX.

Next, the impact of the properties of the sCO_2 stream inside the heat source HEX were analyzed. The temperature/enthalpy difference of the sCO_2 stream between the in- and outlet of the heat source HEX was a model parameter that could be adapted most conveniently. Through adapting this value the effect of this on the COP of the HTHP cycle could be evaluated. Similar as for the external heat source stream the temperature/enthalpy difference of the sCO_2 stream and its mass flow are linked through Equation 3.12 and are inversely proportional. It was found during the parametric analysis that changing the temperature/enthalpy difference of the sCO_2 stream not only changed the mass flow but had a significant impact on the COP. This is illustrated in Figure 3.6 for a heat source temperature of 150 °C and sCO_2 compressor inlet pressure of 85 bar, evaluated for the three turbomachinery efficiency scenario's. These graphs also clearly show the inversely proportional relation between the temperature/enthalpy difference and the mass flow of the sCO_2 stream.

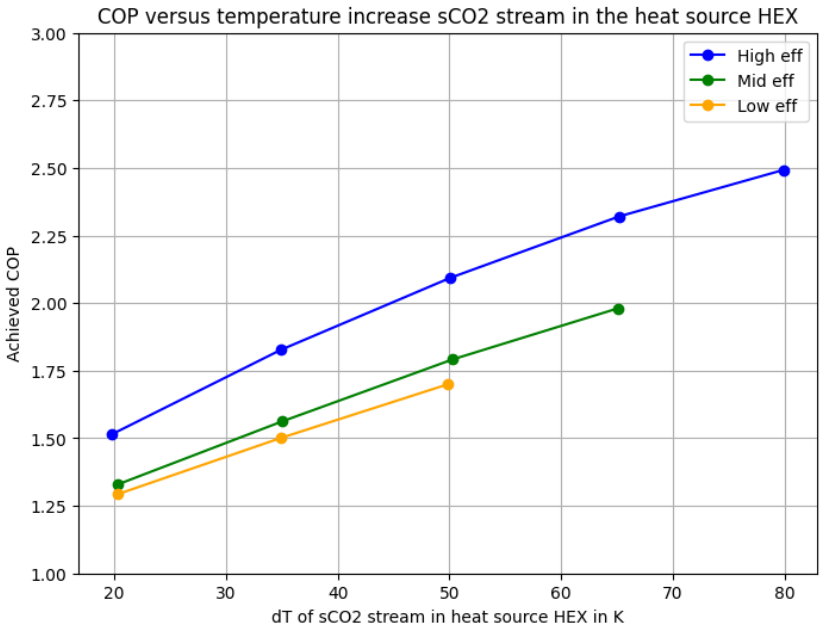

(a)

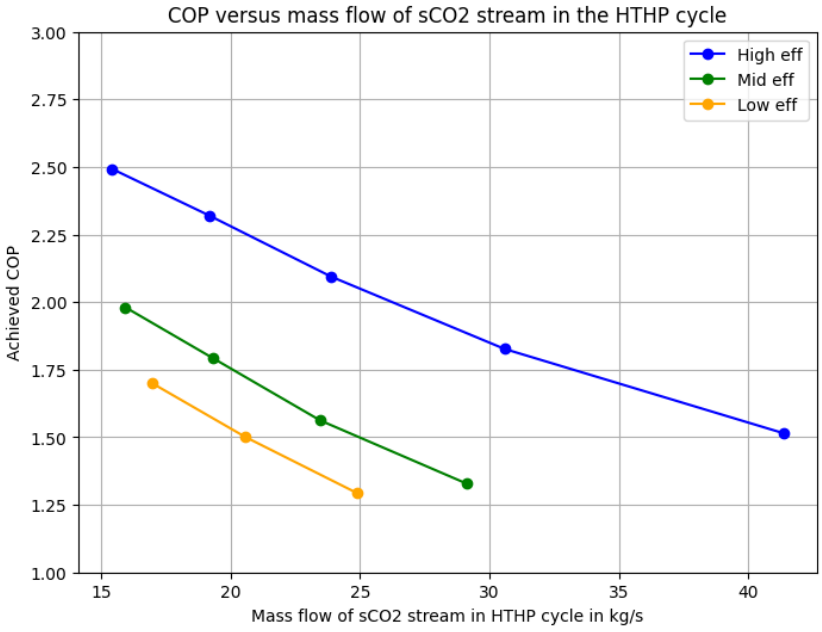

(b)

Figure 3.6: The COP of the HTHP design for different temperature differences (a) and mass flows (b) of the sCO_2 stream inside the heat source HEX

Due to the set boundary conditions the temperature differences of the sCO_2 stream were limited for the low- and mid efficiency scenario's. Nevertheless, the scenario's all clearly showed that the larger the temperature differences of the sCO_2 stream, or lower the mass flow, the higher the achieved COP. The explanation for this was found when observing what happened with the equipment requirements of the cycle. The required compressor ratio increased slightly, which required a larger compressor outlet pressure to reach the desired output temperature, and therefore the specific enthalpy also increased. However, the mass flow decreased significantly due to the increase in the temperature/enthalpy difference of the sCO_2 stream. As the required compressor power is the multiplication of the mass flow and the specific enthalpy difference (Equation 3.17) this resulted in a decline of compressor power. The same phenomena occurred within the turbine but as the decrease in compressor power was larger

the net power required decreased resulting in the improvement in COP. It was therefore concluded that a trade-off was present between the temperature/enthalpy difference over the compressor, based on the required pressure ratio, and the temperature/enthalpy difference inside the heat source HEX. However, due to the significant impact of a change in the temperature/enthalpy difference inside the heat source HEX on the COP this was generally more important to focus on. The observed effect with regard to the turbomachinery power is illustrated in Figure 3.7 based on the same model parameters. It was observed that due to the lower isentropic efficiencies the cycle in the low- and mid scenario is very different from the high isentropic efficiency scenario. Although the same effect was seen, the COP improvement was significantly less.

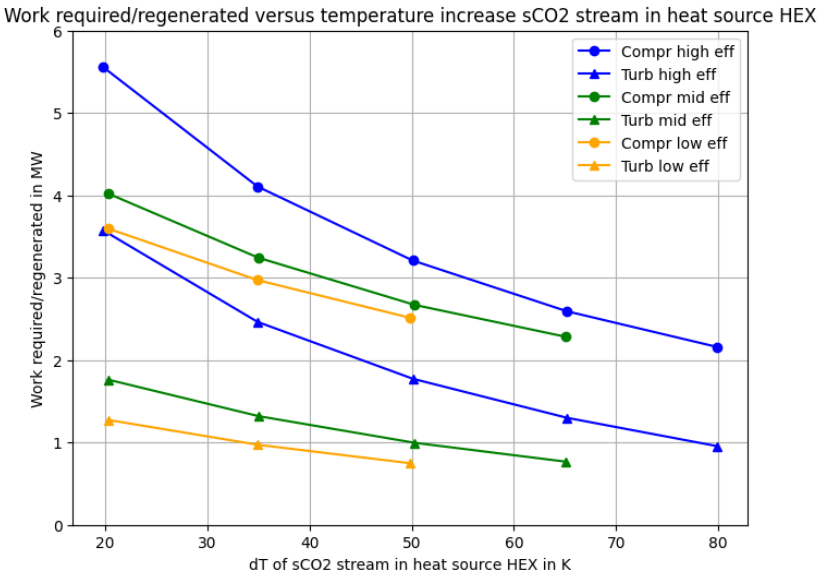

(a)

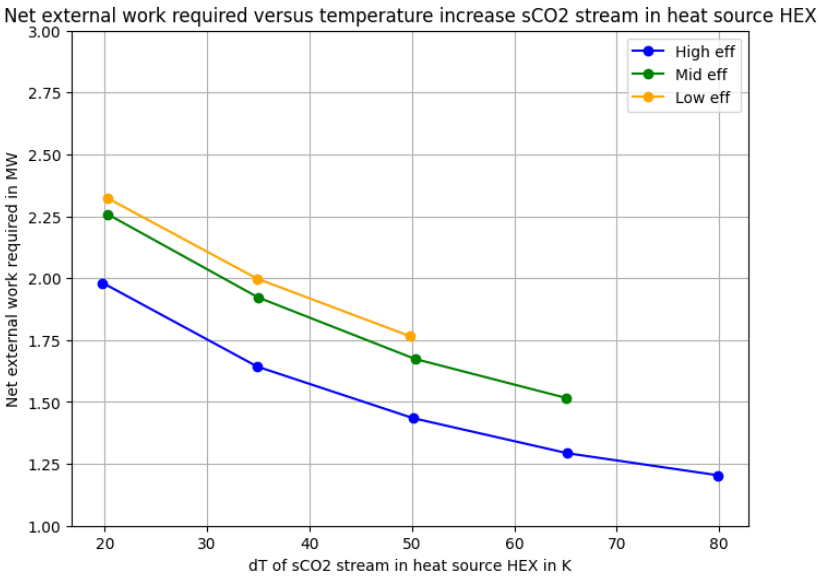

(b)

Figure 3.7: The required work for the compressor, regenerated work from the turbine and net required work of the HTHP design for different temperature differences of the sCO_2 stream inside the heat source HEX.

It can be observed in the presented figures that the increase in COP is a little higher for lower values of dT and the graphs show a parabolic profile. This is explained through the fact that as the dT value is increased the cycle moves more towards the critical point. Closer to the critical point the slope

of the isobar decreases which resulted in two things. First of all, it becomes more difficult to match the sCO_2 stream to the external streams as the slope of the sCO_2 stream changes significantly. On the other hand, the slope of the external streams stays nearly constant. This is also the reason that there is maximum value of the dT as otherwise the boundary condition that the inlet temperature of the heat sink stream should be above the inlet temperature of the heat source stream is not met any longer. Secondly, due to the isobars being closer together near the critical point the turbine work starts to decrease relatively more than the compressor work when the mass flow decreases. This causes the COP increase to stagnate. What is however also important to note from a cost perspective is that due to required compressor power and turbine power the size of the turbomachinery also decreased significantly. As the required power is the main factor in the equipment costs also the HTHP system costs could be greatly reduced due to this. A more detailed analysis of this was done in the parametric analysis of the turbomachinery and will be discussed later.

It was observed that the cycle became slightly transcritical for lower heat source inlet temperatures in order to realize the required output temperature. In these cases the two-phase region limited this maximum value for dT even more, hence limited the COP that could be obtained. Due to this observation heat source inlet temperatures of below 100 °C where not further considered. As in that case a transcritical cycle is required to realize the required output temperature it is better to make use of a transcritical CO_2 HTHP like the one from MAN HPU. The above described behaviour was observed for all temperature and pressure levels considered for the HTHP design and within the boundary conditions. It was therefore concluded that the temperature differences of the sCO_2 stream inside the heat source HEX should be taken as large as possible within the set boundary conditions. An additional observed advantage was that also the required UA value of the heat source HEX decreased when the dT was increased reducing the size and costs of the heat sink HEX.

The final model parameter that could be analyzed for the heat source HEX was the impact of the chosen pinch. To minimize the required temperature lift it it was desired to have the external streams as close as possible to the sCO_2 stream in terms of temperature. However, as illustrated in Figure 3.8 there is an optimum in the trade-off between the energy costs, or the efficiency/effectiveness, and the capital costs, or the size, of the heat exchanger. If the pinch is chosen too large the size can be decreased which results in lower capital costs, but the heat transfer is less effective resulting in higher energy costs. If the pinch is chosen too small this is the other way around where the heat transfer becomes more effective, but the size of the heat exchangers increases hence the total costs also increase.

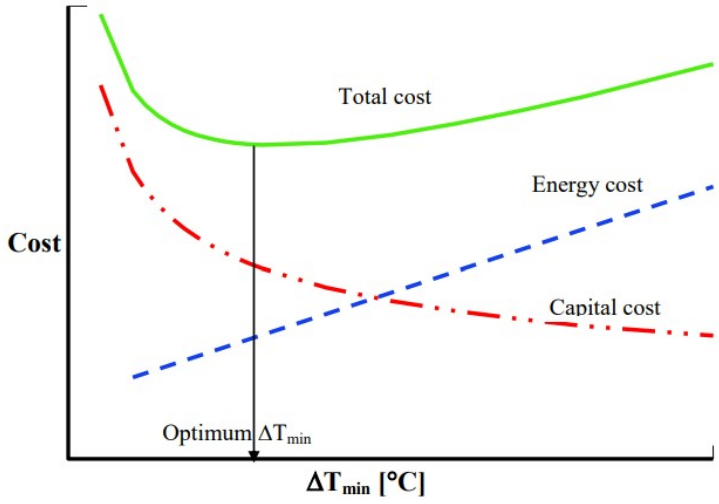

Figure 3.8: Heat exchanger cost as a function of the average temperature difference inside the heat exchanger (Rokni, 2016).

Based on literature and discussions with Professor Hooman it was concluded that the pinch for an application like these should ideally be around 10 K. This to have a good trade-off in terms of HEX size and heat transfer. As for the heat source HEX the properties of the heat source stream could be

chosen quite freely an increase to 15-20 K did not significantly benefit the size/cost. It only resulted in a larger required temperature lift and pressure ratio hence a COP decrease. A reduction of the pinch to 5 K resulted in a slight COP improvement due to a smaller required temperature lift. However, also an increase in the size/cost of the heat exchanger and made it more difficult to match the two streams well.

For the heat sink HEX the effects of increasing/decreasing the pinch were more significant. Reducing the pinch to 5 K resulted in a slight increase in the COP as the temperature lift decreased and the required pressure ratio could be reduced. However, it came at the cost of a much larger UA value so at the cost of a larger value of the heat exchange surface area A and a more expensive HEX. It was thereby assumed that for similar pressure and temperatures the U value would stay more or less the same. Similar as for the heat source HEX this also made it more difficult to match the two streams well inside the HEX. Increasing the pinch to 15-20 K resulted in decrease in the UA value of the heat source HEX and hence the size of the HEX but also significantly decreased the COP. This is as next to a larger required pressure lift also the outlet temperature of the sCO_2 stream decreased which meant a reduction of the temperature difference of the sCO_2 stream inside the HEX which caused a decrease in COP as explained earlier. It was therefore decided to just work with a pinch of 10 K. Where it should be noted that due to the diverging nature of the two streams inside the heat source HEX, as can be seen in Figure 6.3, the pinch was set at the inlet of the heat source stream/outlet of the sCO_2 stream. For the heat sink HEX the pinch of 10 K was chosen in the middle of the HEX due to the shape of the sCO_2 isobar as can also be seen in Figure 6.3.

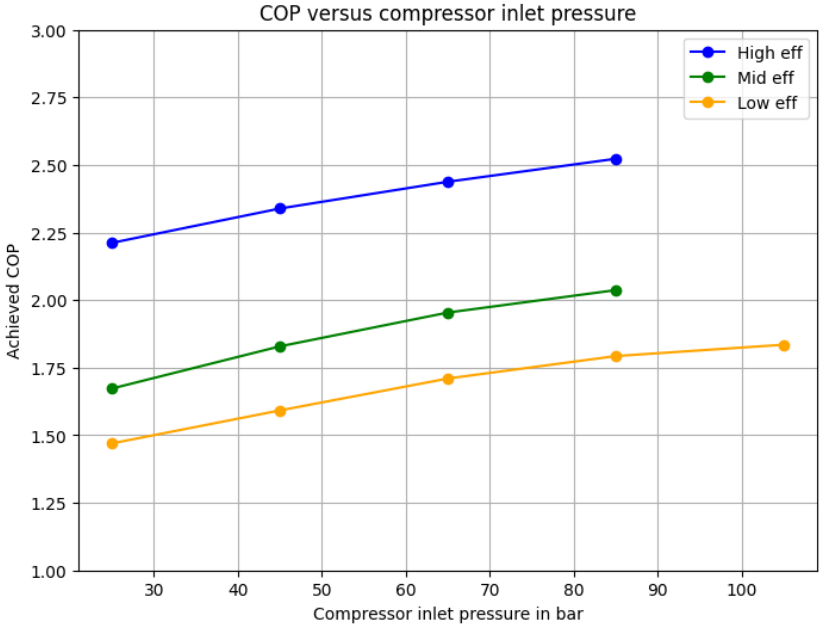

Figure 3.9: The COP of the HTHP design for different compressor inlet pressures

Turbomachinery

For the turbomachinery the model parameters of interest where the isentropic efficiencies, the compressor in- and outlet pressure and the resulting pressure ratio. Also the required power was of interest as this mainly determines the size and cost of the turbomachinery. As described in Section 3.1 the turbine in- and outlet pressures were similar for the HTHP model and were not varied independently as isobaric heat addition/rejection was assumed. The isentropic efficiency of the turbomachinery was a standard model parameter throughout the analysis and was therefore already included in the analyses this was not separately analyzed. Moreover, it was observed that the turbine outlet pressure and pressure ratio could also not be chosen freely if a heat source inlet temperature and compressor inlet pressure were chosen. To create the required output conditions of 3 MW output power and an output temperature of 280 °C a specific turbine outlet pressure ratio was needed. For the power this was also the case as this was a result of how the cycle was designed in the heat source HEX. Therefore, next

tot the isentropic efficiencies the only model parameter connected to the turbomachinery that could be varied to analyze the effect was the compressor inlet pressure. Nevertheless, the outputs of the other mentioned model parameters could be analyzed based on different compressor inlet pressures to potentially further optimize the HTHP design.

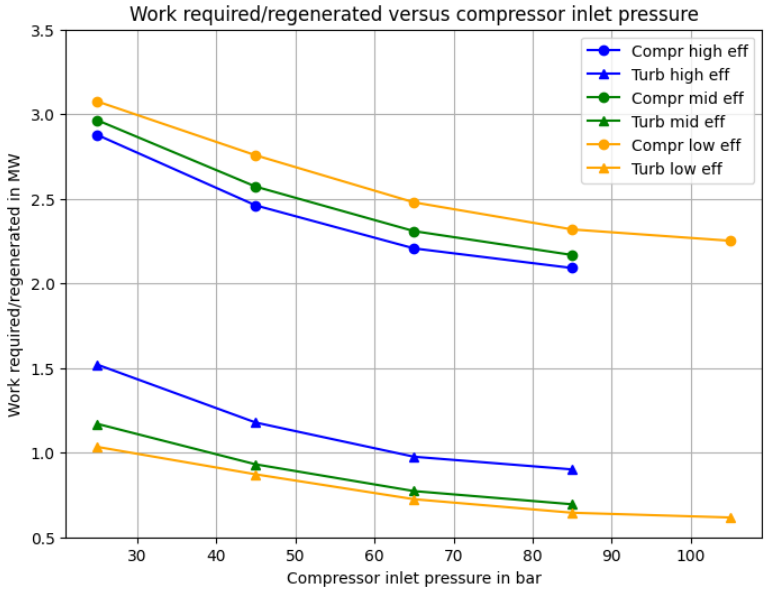

(a)

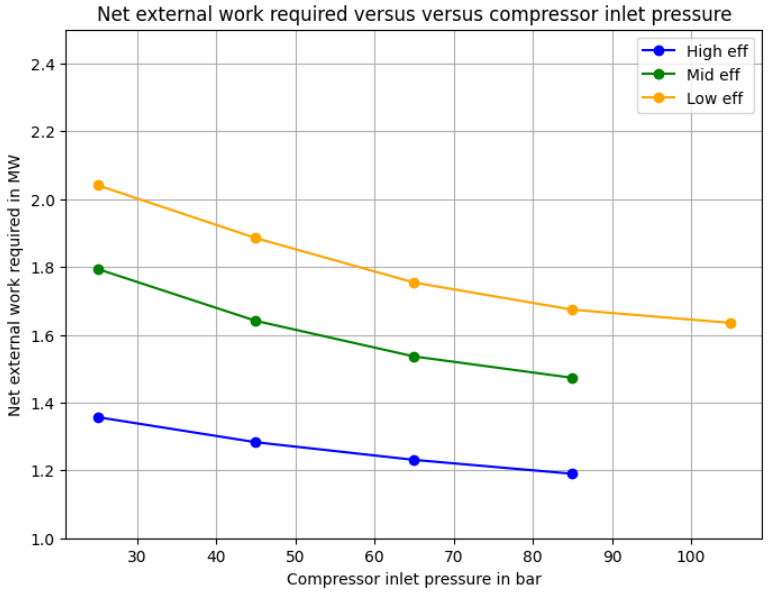

(b)

Figure 3.10: The required work for the compressor, regenerated work from the turbine and net required work of the HTHP design for different compressor inlet pressures.

It was observed that increasing the compressor inlet pressure had a slight positive effect on the achieved COP. Where it should be noted that the window to vary this pressure was limited if a fully supercritical cycle was desired. This was mainly because of the boundary condition that the compressor outlet pressure could not be higher than 345 bar due to equipment constraints. Therefore, also subcritical compressor inlet pressures were evaluated to get a better view on the impact of the compressor inlet pressure. For these subcritical compressor inlet temperatures the earlier described limitation of two-phase region came into play. It was therefore tried to keep the shape of the T-s diagram more or less

the same for all compressor inlet pressures to create a comparable situation. The results of this analysis are shown in Figure 3.9 for a range from 20 to 85-105 bar, depending on the efficiency scenario, for a heat source inlet temperature of 150 °C.

It was observed that the increase in achieved COP was caused by the compressor power which was reduced relatively more than the turbine power, This caused a reduction of the net external work required, illustrated in Figure 3.10. This was again mainly caused by a decrease in the sCO_2 mass flow. The shape of the T-s diagram was kept more or less constant, and for example the pressure ratio and temperature difference of the sCO_2 stream inside the heat source HEX remained more or less constant. However, the properties of the sCO_2 inside the heat source HEX changed significantly due to the different pressures used hence the mass flow changed. Therefore, it was difficult to establish what exact role the compressor inlet pressure had on the achieved COP as it seemed related more due to changing properties of the sCO_2 as a result of a higher pressure. Nevertheless, as the goal of this research was to realize optimal performance it was still desired to go for the highest possible compressor inlet temperature as a COP increase as small as 0.1 can already have a significant impact on the financial feasibility of the HTHP. Higher pressures generally causes higher stresses in the equipment and requires stronger (more expensive) equipment to practically realize the HTHP cycle. Therefore, doubts arose if in that case it would be beneficial to go for the highest possible compressor inlet temperature in terms of costs. As already shown in Figure 3.5 the turbomachinery cost indeed increased for higher pressures. However, this was for constant power levels while it was observed from Figure 3.10 that for higher pressure levels the required power levels decrease which could result in a reduction of the costs. With the cost estimation method described earlier the turbomachinery costs were computed for the designs presented in Figure 3.9. The results of this can be found in Figure 3.11. Here it can be seen that for the compressor the reduction in required power indeed (largely) compensates for the cost increase due to the higher pressures. Moreover, for the turbine it even seemed that the costs go down for higher compressor inlet pressures.

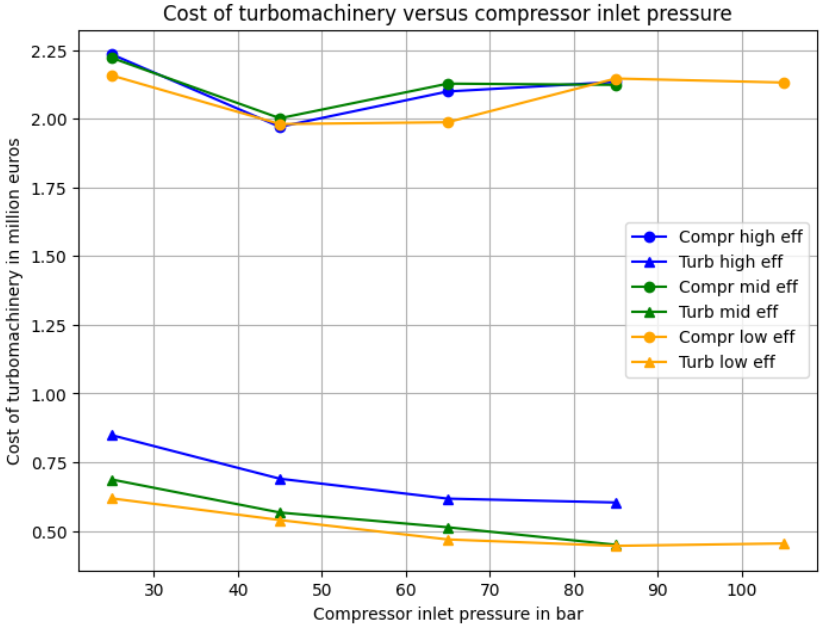

Figure 3.11: Cost of the turbomachinery for the HTHP designs with different compressor inlet pressures.

The cost increase of the heat sink HEX when going to higher pressures was briefly reviewed for the HTHP designs as presented in Figure 3.9. As illustrated in Figure 3.12 the cost of the heat sink HEX increased for higher pressures but no steady increase was observed like for the turbomachinery. This was mainly due to the fact that the properties of the HEX also changed significantly for different pressures. Nevertheless, the cost increase due to higher pressures was of more relevance here. To put the observed cost increase in perspective to the increase in COP a quick and rough calculation was

done. If an average electricity price of 80 €/MWh was assumed and the HTHP was expected to have a lifetime of 20 years. Thereby, producing 3 MW of heat continuously with either a COP of 2.4 or 2.5, meaning an electricity consumption of 1.25 MW and 1.20 MW respectively. Over 20 years this would result in energy savings of 219,000 MWh - 210,240 MWh = 9,240 MWh. This multiplied with the average average electricity price of 80 €/MWh would already result in a cost saving of about 0.7 million euros. So, although this is a very rough calculation, it indicates that a small increase in COP would in this case already be worth the more expensive equipment. Moreover, it was observed that a lower compressor inlet pressure resulted in a shift of the T-s diagram towards higher specific entropy values and away from the two-phase region. The steeper isobars made it more difficult to properly match the streams which would prevent optimal design and increases the costs.

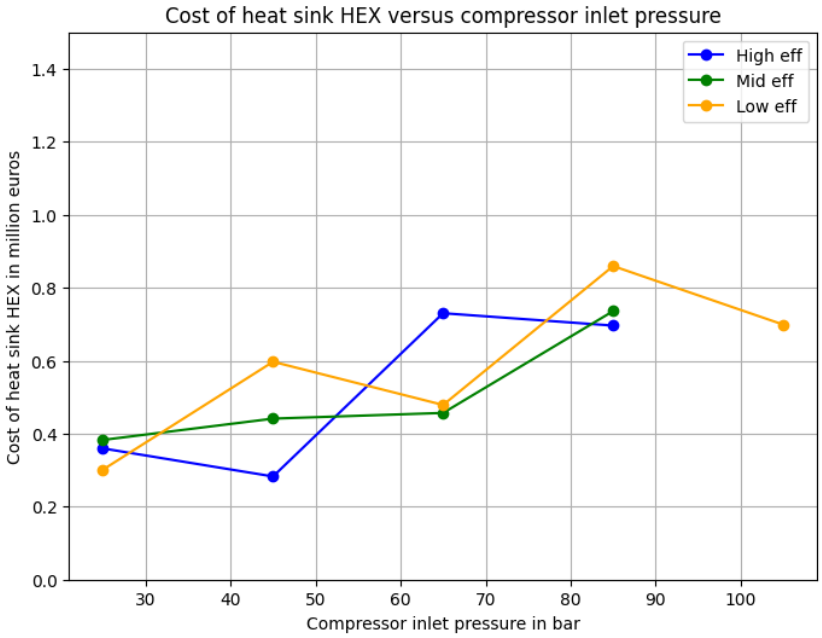

Figure 3.12: Cost of the heat source HEX for the HTHP designs with different compressor inlet pressures.

Based on the parametric analysis of the turbomachinery it was concluded that compressor inlet pressure should be as large as possible to maximize the achieved COP. From a cost perspective the higher pressures seemed to (partly) result in higher equipment cost especially for the heat sink HEX. Nonetheless, as the HTHP design was aimed to be fully supercritical to profit optimally from the properties of sCO_2 the compressor inlet pressures below the critical pressure were of less relevance. For the higher compressor inlet pressures the cost increases were less significant while the COP increase was more steady so it was decided to still go for an as large as possible compressor inlet pressure.

Heat sink HEX

It was observed that the model parameters of the heat sink HEX were almost entirely depended on other parameters already discussed in the parametric analysis. The effect of the chosen pinch temperature was already discussed earlier. It was just desired to match the heat sink stream as good as possible with the sCO_2 stream by adjusting the terminal difference temperatures within the boundary conditions. Moreover, was the UA value of the heat sink HEX purely depended on how the cycle was constructed in terms of compressor outlet pressure, mass flow of sCO_2 and the dT of the sCO_2 stream inside the heat sink HEX which was determined by other model parameters and already investigated.
The only thing that could be varied to see what impact it would have on the COP was the output (heat) power. However, it was quickly observed that if the output power was increased the HTHP cycle stayed exactly the same while only the mass flows of all streams increased as the design was focused on an output of 3 MW. This resulted in a linear scaling of the mass flows and turbomachinery powers with the output power. Next to this, output powers different from 3 MW were not the focus of this research and therefore it was decided to not further pursue the investigation into other output powers than 3 MW.

3.2.2. HTHP-EJ model

As the HTHP-EJ model was largely similar to the HTHP model it was observed that the conclusions from the parametric analysis of the HTHP model described in Section 3.2.1 were also valid for the HTHP-EJ model. It was observed that to the HTHP-EJ model just required a somewhat larger pressure ratio due to extra pressure losses due to the ejector and that the final design of the cycle was different as will be discussed in Section 3.3. The optimization of the model parameters directly involved with the ejector was limited. The nozzle, mixing and diffuser efficiency were based on the paper by Padilla et al. (2016) and the other parameters like the pressures were directly connected to the rest of the HTHP cycle. However, the entrainment ratio was a model parameter that could be varied to study its impact on the performance. It was unfortunately not specifically mentioned in the paper by Padilla et al. (2016) for what range of operating conditions their sCO_2 ejector model should be deemed valid. Based on the information and graphs identified in the paper it was estimated that for the entrainment ratio's values of 1 up to 5 the model was valid. To clearly show the effect a higher entrainment ratio had it was decided to evaluate the model for entrainment ratio's from 1 to 9. The results of this analysis for the different efficiency scenario's is illustrated in Figure 3.13 for a heat source inlet temperature of 150 °C and turbine outlet pressure of 75 bar.

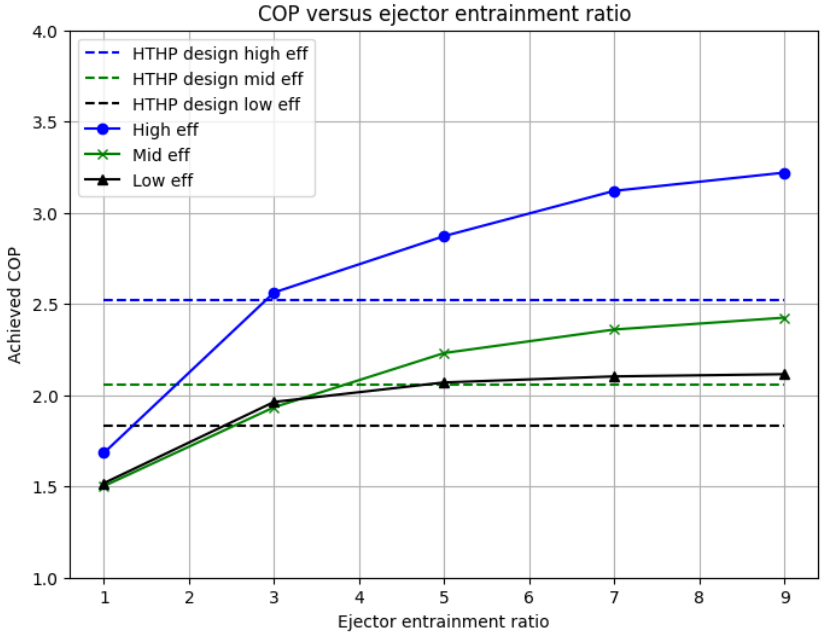

Figure 3.13: Achieved COP with the HTHP-EJ design for different ejector entrainment ratio's for a heat source inlet temperature of 150 °C and turbine outlet pressure of 75 bar.

It was interesting to observe that for entrainment ratio's of below 3-4 the achieved COP actually decreased due to the addition of the ejector. This could be explained by the fact that the is ejector operated in parallel to the turbine. Thus, a lower entrainment ratio, which meant relatively less flow through the turbine, caused a large decrease in the turbine work. For entrainment ratio's below 3-4 it appeared to be the case that the "pre-compression" done to reduce the compressor work did not outweigh the reduction in turbine work. This makes sense as the turbine and ejector are both aimed at reducing the required compressor work. However, either through supplying a part of the required compressor work or decreasing the required pressure ratio and in that way reduce the required compressor work. For larger entrainment ratio's, where the turbine was used more, it showed that the COP improvement was larger. This growth started to stagnate for larger entrainment ratio's. It was found that this was at least partly caused by the fact the as the secondary (low-pressure) stream became relatively larger then the primary (high-pressure) stream, due to a higher entrainment ratio. Therefore, the primary stream had more difficulty to lift the low secondary stream which resulted in a lower ejector outlet pressure. This in turn caused less "pre-compression" for the compressor increasing the required compressor work. The lower ejector outlet pressure was caused by a lower suction pressure as illustrated in Figure 3.14 for

lower entrainment ratio's. This behaviour was observed similarly for all efficiency scenario and also for other heat source inlet temperatures and pressure levels.

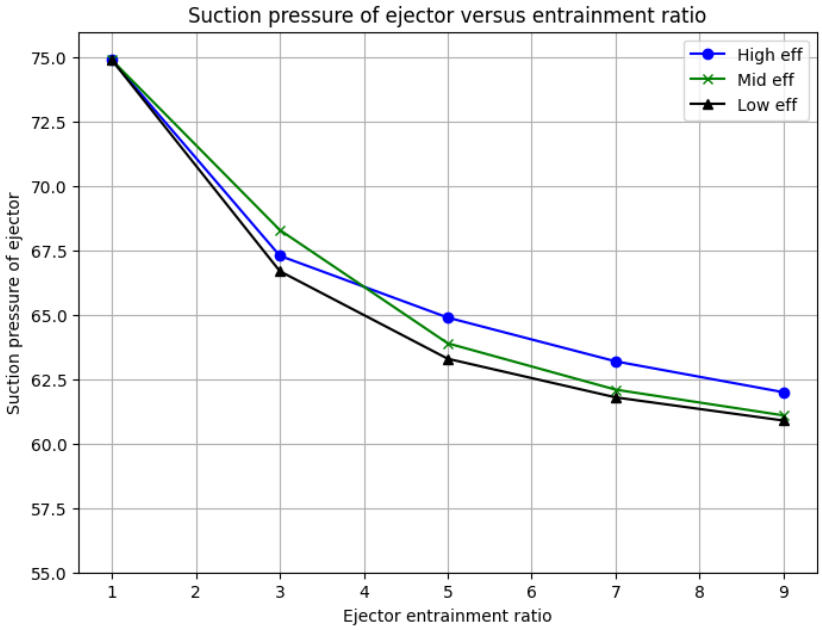

Figure 3.14: The maximum attainable suction pressure in the ejector for different ejector entrainment ratio's.

It was therefore concluded that a larger entrainment ratio was most beneficial to realize a potential COP improvement for all HTHP-EJ designs. However, to be careful in overestimating the positive effect the addition could have on the performance of the HTHP cycle the maximum value for the entrainment ratio was set at the maximum value identified in the paper by Padilla et al. (2016). As mentioned this was an entrainment ratio of 5 and in the final HTHP-EJ designs the entrainment ratio was therefore set at 5.

A final note that should be made that already during the parametric analysis it was observed that the two methods to model the ejector did not always produced similar results. This resulted for the Mach number method in differences up to 100 % compared to the value from the other method. No pattern could be observed in the difference in ejector output pressure. Consequently, as the Mach number approach could not provide any other outputs in terms of temperature, specific entropy, or specific enthalpy it was decided to only use the fully specified ejector outlet conditions from the other model. Also supported by the fact that the Mach number model was based on general ejector theory, partly focused on liquid-liquid and liquid-gas ejectors. While the other model was directly adapted from the paper by Padilla et al. (2016) specifically for a comparable application in a sCO_2 Brayton cycle at comparable operating conditions.

3.3. Results

After the successful completion of the parametric analysis for both the HTHP and HTHP-EJ cycle the most optimal designs could be constructed for different heat source inlet temperatures. The reason to do this was that it was interesting to see what effect the heat source inlet temperature had on the performance. Moreover, in practise the availability of waste heat can be at a wide range of temperature levels so this enabled a selection of an optimal design based on this. It was also investigated what the feasibility would be of "cascading" the designed HTHP with a regular HP/alternative HTHP currently commercially available and able to deliver heat up to temperatures of 150-200 °C as discussed in Section 1.3.
First the general results for the HTHP designs will be shown and discussed after which a more detailed description of the practical design and costs of the HTHP designs will be given. After this the same will be down for the HTHP-EJ designs.

3.3.1. HTHP design results

All HTHP designs were constructed for an output temperature of 280 °C and an output power of 3 MW. The results from the parametric analysis in Section 3.2.1 were adapted to realize the most optimal HTHP designs. This included a compressor outlet pressure of close to 345 bar, an as low as possible mass flow of sCO_2], pinch of 10 K and of 15-20 K in the heat source HEX and heat sink HEX respectively. The other parameters, such as the compressor inlet pressure, differed based on what parameters provided the highest possible COP. All designs were also modelled in Aspen Plus according to the method described in Section 3.1.3 to obtain designs that were as detailed as possible. In Figure 3.15 the achieved COP is shown for all optimized HTHP designs based on the heat source inlet temperature and within the design boundary conditions as the beginning of Section 3.2. As discussed in the parametric analysis it was chosen to take 100 °C as minimum heat source inlet temperature as below that temperature the HTHP cycle became transcritical for all efficiency scenario's. The heat source inlet temperature of 180 °was taken as maximum as the most recent HTHP technology available on the market is able to deliver heat at this temperature at a reasonable COP as described in Section 1.3. Moreover, it was not deemed useful to have a heat source temperature less than 100 °C below the desired outlet temperature.

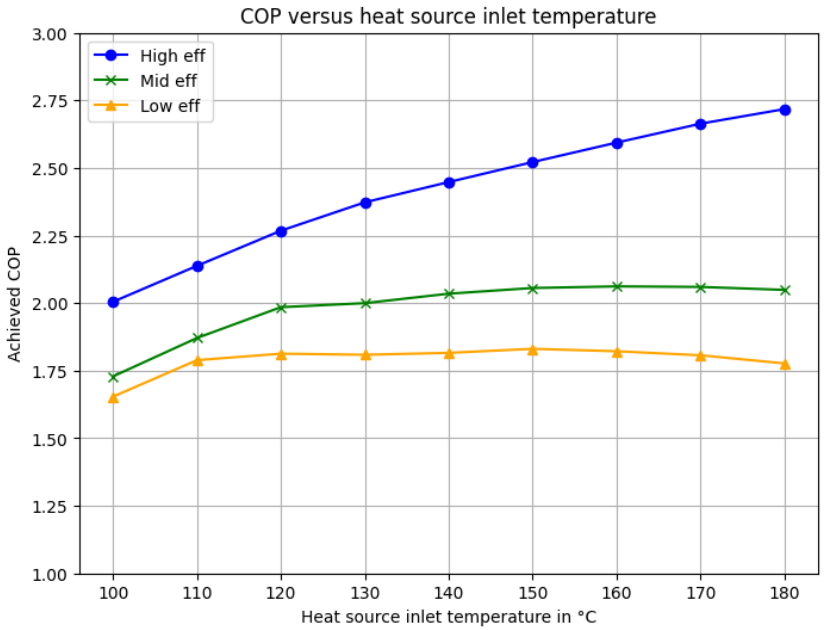

Figure 3.15: Achieved COP of the HTHP cycle for the different HTHP designs based on heat source inlet temperatures.

Logically, the lowest COP was obtained for the 100 °C heat source inlet temperature for all efficiency scenario's, varying between 1.65 and 2.00 based on the isentropic efficiency scenario. This was on the low side but the value for the high efficiency scenario was already in a range that could be of interest. However, it was interesting to observe that, except for the high eff scenario, the maximum obtained COP was not reached for the maximum heat source inlet temperature. For the high efficiency scenario the maximum obtained COP was 2.72 for a heat source inlet temperature of 180 °C, while for the mid efficiency scenario this was 2.06 obtained at 160 °C and for the low efficiency scenario 1.83 obtained at 150 °C. This was not expected as a lower required temperature lift generally results in a higher COP for heat pump technology as explained in Section 1.3. To explain this the effect of the isentropic turbomachinery efficiency on the cycle was illustrated in Figure 3.16 for a heat source inlet temperature of 150 °C. This shows how the HTHP cycle changed for the three efficiency scenario's. The heat source stream (blue) and heat sink stream (red) were also indicated for the low eff scenario to show their temperature profile inside the HTHP cycle. As all designs were required to deliver 3 MW of heat and a heat sink stream outlet temperature of 280 °C with the highest possible COP, hence a compressor outlet pressure as close to 345 bar as possible, the high pressure part of the cycles were observed to be fairly similar. Therefore, the differences were observed in the lower pressure part.

The most notable difference was in the optimal compressor inlet pressure and the temperature change of the sCO_2 stream inside the heat source HEX. The lower the isentropic efficiencies the lower the required pressure ratio hence the compressor inlet pressure increased. However, most importantly, the temperature change of the sCO_2 stream inside the heat source HEX decreased which also brought the temperature of the heat source inlet temperature closer to heat sink stream inlet temperature as illustrated in Figure 3.16. The limitation that the heat source inlet temperature should be above the heat sink inlet temperature therefore limited optimal design of the HTHP cycle. This effect was also observed for the high efficiency scenario as can be seen in the decrease in the slope in Figure 3.15 for higher heat source inlet temperatures but was much stronger present for the low and mid efficiency scenario hence the stagnation in the increase in the COP for higher heat source inlet temperatures.

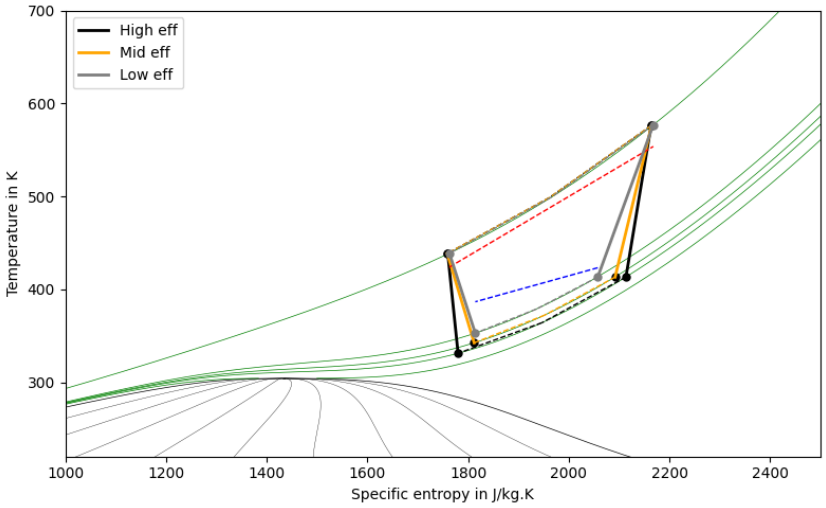

Figure 3.16: T-s diagram for the different efficiency scenario's for a heat source inlet temperature of 150 °C.

Due to this observation it was also briefly investigated what the effect on the COP would be if a higher output temperature was allowed for higher heat source inlet temperatures. This was realized by decreasing the compressor inlet pressure and actually resulted only in a slight decrease in COP while a significantly higher output temperature could be reached. This while still complying with the same boundary conditions as the other HTHP designs. As an example for the mid efficiency scenario case and a heat source inlet temperature of 180 °C the COP decreased from 2.05 to 1.97 but the output temperature increased from 280 °C to 312 °C. This shows that within the currently existing equipment limitations to reach an output temperature 280 °C it is not necessarily beneficial to have higher heat source inlet temperatures. However, if higher heat source inlet temperatures are available, or can be realized, the reachable output temperatures can be increased easily beyond 280 °C with similar HTHP performance. This shows the potential of this sCO_2 reversed Brayton HTHP also for higher output temperatures beyond 280 °C within the currently existing equipment limitations.

In addition to the analysis of the achieved COP of the different HTHP designs it was also deemed interesting to take a look at the Lorenz efficiencies that were obtained. As discussed in Section 1.3.3 the Lorenz efficiency is calculated through Equations 1.7 & 1.9 which were also included in the Python codes. In Figure 3.17 the Lorenz efficiency is depicted for every HTHP design based on the heat source inlet temperature and efficiency of the turbomachinery. It was observed that for for high efficiency scenario most of the HTHP designs where in the expected range for heat pumps of 40-60 % as mentioned in Section 1.3.3. However, for the lower efficiency scenario's the Lorenz efficiency was quite poor. This indicates relative poor heat pump performance which was also observed in the achieved COP values in Figure 3.15. The same limitations that restricted (significantly) higher COP values for smaller temperature differences between heat source and heat sink was also observed in the Lorenz efficiencies. The Lorenz efficiency even decreased for larger heat source inlet temperatures.

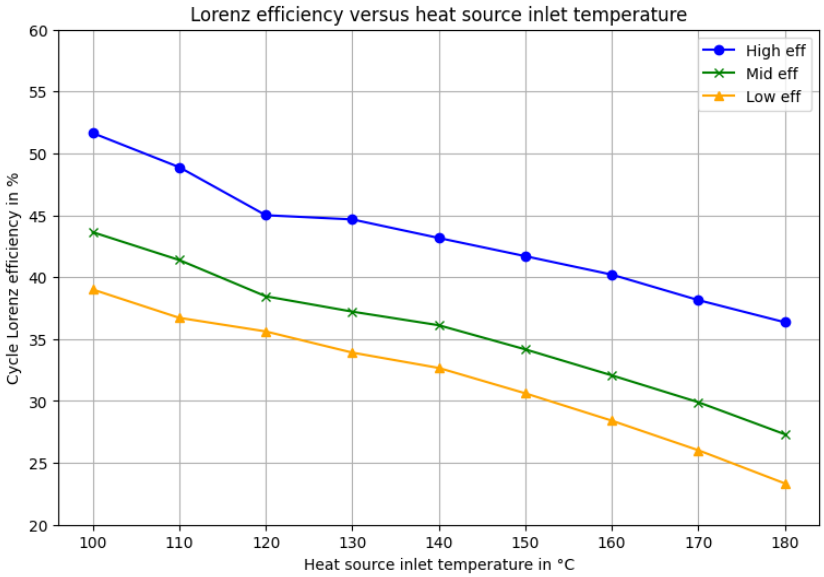

Figure 3.17: Cycle Lorenz efficiency for the different HTHP designs based on heat source inlet temperatures.

As mentioned, it was also briefly investigated what combined COP would be obtained if a separate heat pump would be used to create the required heat source stream in a kind of cascaded configuration. It was assumed that the heat needed from the heat source, Q_{in}, could be delivered by by another heat pump at a COP of 3. Suitable options with be an ammonia heat pump or a transcritical CO_2 heat pump like the one from MAN Energy. This resulted in the fact that the combined COP fluctuated somewhere between 1.36 in the worst case and 1.73 in the best case. Considering the fact that this would require two heat pumps in terms of CAPEX costs this number was not very promising. Nevertheless, at least this would make it technically feasible to realize the required output temperature if only (waste) heat at low temperatures was available. If waste heat at temperatures of 100 °C or higher would be available this could be directly used in the proposed HTHP design.

An alternative solution would be to combine the HTHP with an E-heater as briefly mentioned in Section 1.3.1. To create the required heat source stream at the required temperature levels through the use of an E-heater could be possible. However, as a considerable amount of heat needs to be delivered by the heat source this would result in a very low combined COP due to E-heater's COP of about 1. To increase the outlet temperature of the heat sink stream seems on the other hand like a more viable option. This could be realized relatively easy and depending on the desired output temperature could result in a decent combined COP. In the paper by Zühlsdorf et al. (2019) it was for example mentioned that the PTES design from GE made use of an E-heater to reach a slightly higher output temperature. However, the results of this study into the sCO_2 reversed Brayton HTHP showed that the main challenge was to have a heat source available at a high temperature level to obtain a reasonable COP. As opposed to limitations in output temperatures. Therefore, the addition of an E-heater could be of interest to further increase the output temperature but seemed disadvantageous due the decrease in COP and extra CAPEX costs associated with this solution.

It can be concluded that it proved to be difficult to achieve a reasonable COP with the basic sCO_2 reversed Brayton HTHP with the design choices as described. Only for the high efficiency scenario the achieved COP values showed promise. Therefore, if only turbomachinery with lower isentropic efficiency is available the achieved COP is on the low side in relation to the CAPEX costs of the HTHP which will be discussed in more detail in Section 3.3.1 below. As it was found that from a cost perspective natural gas is about 2.5 times cheaper than electricity from the grid a COP of 2.5 or higher could be cost competitive. Unfortunately, a COP of 2.5 was only attained for the high efficiency scenario and heat source inlet temperatures of 150 °C and higher. This nevertheless showed promise in the case efficient equipment could be realized.

What is also interesting to mention on a final note is that the transcritical CO_2 HTHP or standard subcritical HP is limited by the two-phase region where the heat source needs to be located. So, if a higher output temperature is desired a larger pressure ratio is required hence the COP decreases significantly. The sCO_2 reversed Brayton HTHP on the other hand can be used for any heat source and is not limited by this two-phase region. Thus, it can reach higher output temperatures without necessarily requiring a higher pressure ratio if a higher heat source temperature is supplied. This study also showed that sCO_2 could be heated and pressurized to high temperatures and pressures easily so the only limitation here is the maximum pressure and temperature that the equipment can deal with. Hence if sCO_2 equipment would be developed that could even go beyond the 350 bar the output temperatures can be further increased while still maintaining a decent COP. Moreover, is the possibility to cascade this HTHP with currently existing HTHPs present.

Final HTHP design and cost estimation analysis

As the goal of this study was to realize a HTHP design that could actually be build and to make an estimation of the costs of such a system this was done with the help of Aspen Plus, Aspen EDR and APEA. Thereby adopting the same method as described in Section 3.2. Figure 3.18 shows an overview of the suitable kind of turbomachinery depended on the power range. Based on this, Aspen Plus, and discussions with Prof. Hooman it was concluded that a radial turbine/turboexpander in combination with a motor-driven centrifugal gas turbocompressor was the most suited combination of turbomachinery for the HTHP. In case higher output powers were desired the turbine and compressor should be switched to an axial design as indicated in Figure 3.18. As explained in Section 3.1.3 the heat exchangers used were TEMA shell-and-tube heat exchangers.

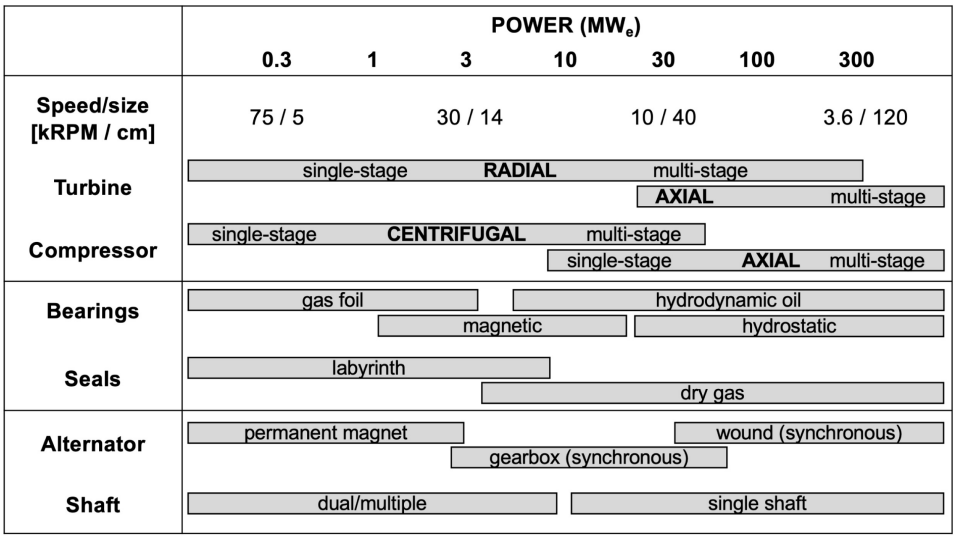

Figure 3.18: Overview of turbomachinery options for sCO_2 power cycles (White et al., 2021).

In addition, it is good to mention that turbo compressors are able to work with a pressure ratio of up to 5 per stage (IEA HPT TCP, 2023). This means that if a HTHP design requires a pressure ratio that exceeds 5, a multi-stage compressor needs to be incorporated in the design. It should be mentioned that this was the case for all designs with a heat source inlet temperature of 100 °C, and for the heat source inlet temperatures of 110 °C and 120 °C for the mid and high turbomachinery efficiency scenario. Aspen Plus did not seem to distinguish between single and multi-stage (turbo) compressors in its cost calculations so for the economics this was not further considered. Nevertheless, due to increased complexity of a multi-stage compressor it is important to verify if a multi-stage compressor is required for the HTHP design.

With all the right equipment selected the costs of the HTHP designs could be estimated through Aspen EDR and APEA. To compute the full system costs in terms of equipment costs were added for piping and instrumentation. Based on the cost estimation done by Aviles et al. (2021) a value of 10% of the main equipment cost was used (Aviles et al., 2021). It should be noted that although Aspen makes use

of data on real equipment and uses appropriate scaling for different operating conditions the costs are still estimates and could be very different in reality. Nonetheless, the use of Aspen Plus was considered the most accurate method to obtain an estimation of the costs.

The results of this analysis are shown combined for all heat source inlet temperatures and efficiency scenario's in Figure 3.19 where the costs per equipment part are also indicated. As can be seen there is some variation in the total HTHP costs but for all designs it fluctuates between just over 3.6 million euros and just under 4.5 million euros. In terms of the cost of every equipment type it was observed that compressor was by far the largest cost component which was not surprising as compressor technology is generally expensive. The fact that the turbine costs were significantly lower, while the operating conditions in terms of temperature and pressure where comparable, could be explained by the fact that the turbine power was also generally a factor 3 to 4 lower than the compressor power. It was on the other hand observed that in general the costs of the heat sink HEX were relatively high, especially compared to the cost of the heat sink HEX, and for some designs even exceeded the turbine costs. This could best be explained by the fact that the heat sink HEX operated under high pressures compared to the heat source HEX. Moreover it operated with smaller temperature differences between the streams and nearly twice as much heat was exchanged between the stream as was illustrated in Figure 6.4 resulting in a larger HEX and hence higher costs.

With regard to the differences between the efficiency scenario's it was generally observed that the costs for the HTHP design in the high efficiency scenario was higher than for the mid and low scenario which was mainly caused by higher turbomachinery costs and to some extent by the cost of the heat source HEX. The fact that the turbomachinery was more expensive for the high turbomachinery efficiencies was because both the compressor and turbine power were larger which increased the costs. For the turbine this effect was stronger hence a relative large cost increase. Nonetheless, this higher turbine power also results in a more regeneration and hence the much higher observed COP compared to the other efficiency scenario's as was illustrated in Figure 3.15. The increase in the costs of the heat source HEX was less evident. However, it seemed to be caused by the relatively lower compressor inlet pressure, as explained through Figure 3.16, which for most designs caused the pressure to be closer to the critical point which caused a more expensive HEX. The cost of the heat sink HEX fluctuated for most heat source inlet temperatures not significantly between the different efficiency scenario's which was to be expected based on what was shown in Figure 3.16. The small variations could best be explained by the fact that sometimes the compressor outlet pressure differed by a few bars and that the overall heat transfer coefficient was computed different for every HEX design causing deviations in the required surface heat exchanger area and hence the costs. Logically, the costs of the piping & instrumentation only showed minor fluctuations following the fluctuations in the total equipment costs as this was calculated as a small percentage of this total equipment cost.

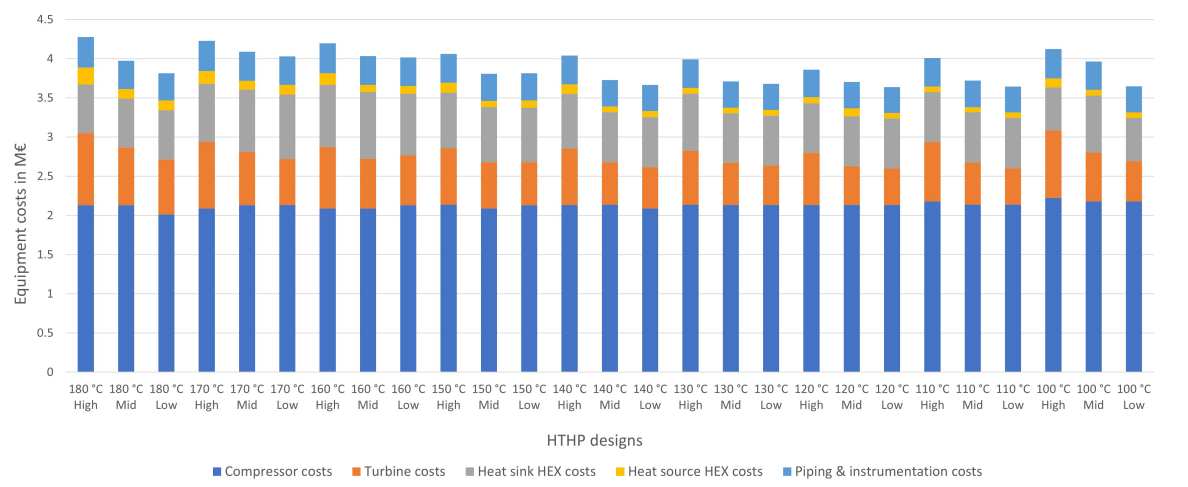

Figure 3.19: Equipment cost build-up for the HTHP designs for the different heat source inlet temperatures and efficiency scenario's.

It was also deemed interesting to briefly investigate if any effects were observed within the efficiency scenario's for the different heat source inlet temperatures. In Figure 3.20 the cost build-up for only the high efficiency scenario is given for the different heat source inlet temperatures. It can be seen that only the compressor cost stay more or less constant with some small variations. The turbine cost first decreased for lower heat source inlet temperatures and towards the lowest heat source inlet temperatures increased again. This was explained by the fact that the mass flow of sCO_2 in the cycle followed this same pattern so the turbine power as well hence the direct influence on the costs. For the compressor this was not the case as the enthalpy change over the compressor increased as the mass flow decreased which resulted in only minor variations. The heat source HEX costs also decreased for lower heat source inlet temperatures as the pressure of the sCO_2 stream inside the HEX decreased. The fluctuations in the cost of the heat sink HEX and the piping & instrumentation were already discussed earlier. In terms of the total HTHP cost the lowest costs were observed for the 120 °C design but from 110-150 °C the total costs remained quite stable.

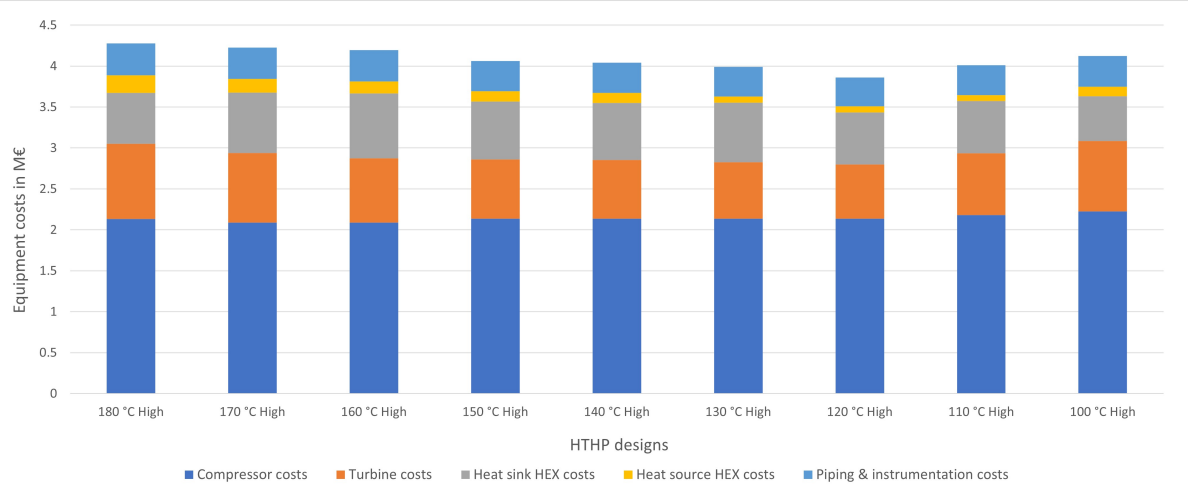

Figure 3.20: Equipment cost build-up for the HTHP designs for the different heat source inlet temperatures for the high efficiency scenario.

Moreover, in Figure 3.21 the cost build-up for only the mid efficiency scenario is given for the different heat source inlet temperatures. Here all equipment cost components follow more or less the same pattern as for the high efficiency scenario except for the fact that here the total costs of the 180 °C design are actually a little lower than for the 170 °C design. This is caused by relatively lower heat sink HEX costs, presumably caused by the stronger effect of the the boundary condition on the heat sink inlet temperature. In terms of the total HTHP cost the highest costs were observed for the 160-170 °C designs due to the operation at relatively higher pressures were the 180 °C design was an exception as discussed earlier. The lowest costs were observed for the 120-140 °C design but from 110-150 °C the total costs remained quite stable.

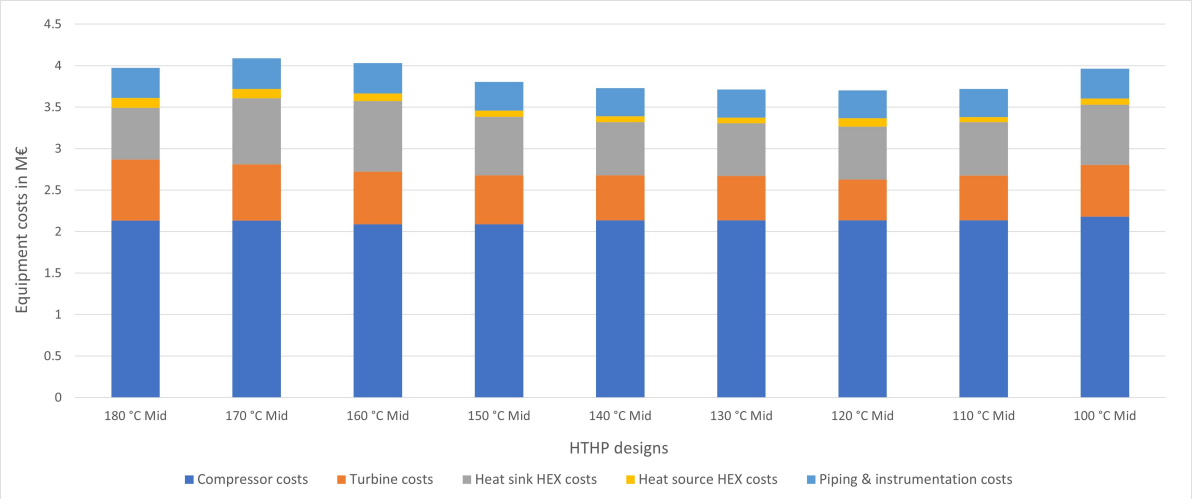

Figure 3.21: Equipment cost build-up for the HTHP designs for the different heat source inlet temperatures for the mid efficiency scenario.

Finally, in Figure 3.22 the cost build-up for only the low efficiency scenario is given for the different heat source inlet temperatures. Again all equipment cost components show similar trends for different heat source inlet temperatures to what was observed for the other efficiency scenario's. A similar effect as for the mid efficiency scenario was observed for the heat sink HEX costs of the 180 °C design. In terms of the total HTHP cost the highest costs were observed for the 150-170 °C designs due to the operation at relatively higher pressures were the 180 °C design was an exception as discussed earlier. The lowest costs were observed for the 140 °C design but from 100-140 °C the total costs remained quite stable.

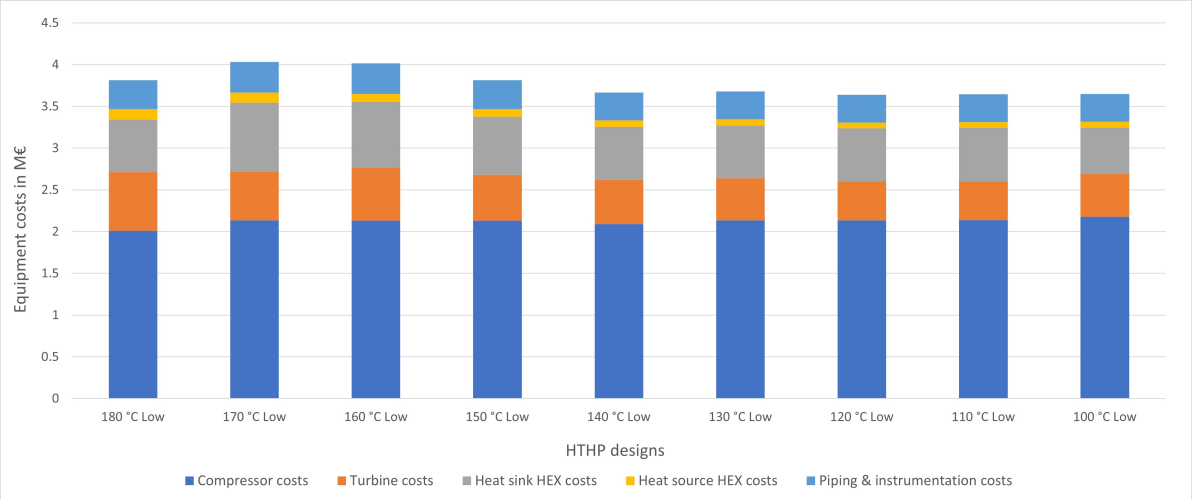

Figure 3.22: Equipment cost build-up for the HTHP designs for the different heat source inlet temperatures for the low efficiency scenario

To also reflect briefly on the relevance of the practical HTHP design for the Teijin Aramid case study. It can be observed in the results that in order to realize a COP with a reasonable performance a significant temperature slide is required in the heat sink stream. This to be able to match this stream well to the the sCO_2 stream inside the heat sink HEX. As the current process of Teijin Aramid only has a very small temperature glide in the thermal oil circuit this makes it not plausible to supply the process heat with a HTHP like the one proposed in this research. If the process could be adapted in the future to enable a larger temperature glide in the thermal oil stream this would improve the feasibility. However, as it was learned that the sulfuric acid is required at a temperature of about 230 °C the temperature glide that could be realized is limited.

3.3.2. HTHP-EJ design results

After the results from the HTHP design were obtained it was of interest to find out what improvements were obtained through the addition of the ejector to the HTHP cycle. All designs were constructed for an output temperature of 280 °C and an output power of 3 MW similar to the HTHP designs. Moreover, all designs applied a compressor outlet pressure of 345 bar and an ejector entrainment ratio of 5 based on the results from the parametric analysis. The other parameters differed based on what parameters provided the highest possible COP. For the different turbomachinery scenario's this resulted in a similar difference as was observed for the HTHP designs that the low- and mid efficiency scenario required a higher turbine outlet pressure. The results of the achieved COP of the HTHP-EJ compared to the HTHP designs for the same heat source inlet temperatures were shown in separate graphs to enable a more clear analysis and can be found in Figure 3.24. It should be noted that the addition of the ejector required a larger pressure ratio over the turbine. This resulted, in combination with the maximum allowable compressor outlet pressure of 345 bar, in the fact that a majority of the HTHP-EJ designs were not fully supercritical anymore. This happened around a heat source inlet temperature of 140-150 °C depending on the efficiency scenario. Something which for the HTHP designs only happened for heat source inlet temperature of around 120 °C.

First of all, for all three scenario's a similar trend was observed that for a heat source inlet temperature below 130 °C the HTHP-EJ cycle showed little to no improvement compared to the HTHP cycle. For heat source inlet temperature above 130 °C an improvement in the COP was observed where for larger temperatures also a larger increase in the COP was seen. For the high eff scenario this even seemed to follow a quadratic growth and resulted in a COP of above 4.5 for the 180 °C scenario. The HTHP-EJ designs for other efficiency scenario's seemed to show a more linear growth. Nevertheless, the COP improvement was significant for all scenario's. The reason for this behaviour was traced back to a few interesting observations. First of all, it was found that the increase in COP was not actually caused by a decrease in compressor power due to the "pre-compression" done with the ejector. The pressure ratio over the compressor was decreased due due to a higher compressor inlet pressure being equal to the ejector outlet pressure. Therefore, the ejector indeed realized mechanical "pre-compression". However, the mass flow of the sCO_2 stream was actually higher for the HTHP-EJ cycle compared to the HTHP cycle resulting in an overall increase in required compressor power. The increase in COP was actually caused by a, for some cases significant, increase in power regenerated through the turbine. This was caused by two phenomena. Firstly, the mentioned larger mass flow of the sCO_2 stream also caused the turbine power to increase. Although this increase in mass flow was relatively smaller than for the compressor, as a part of the sCO_2 stream was used as primary (high-pressure) stream in the ejector, the mass flow of sCO_2 through the turbine still increased.

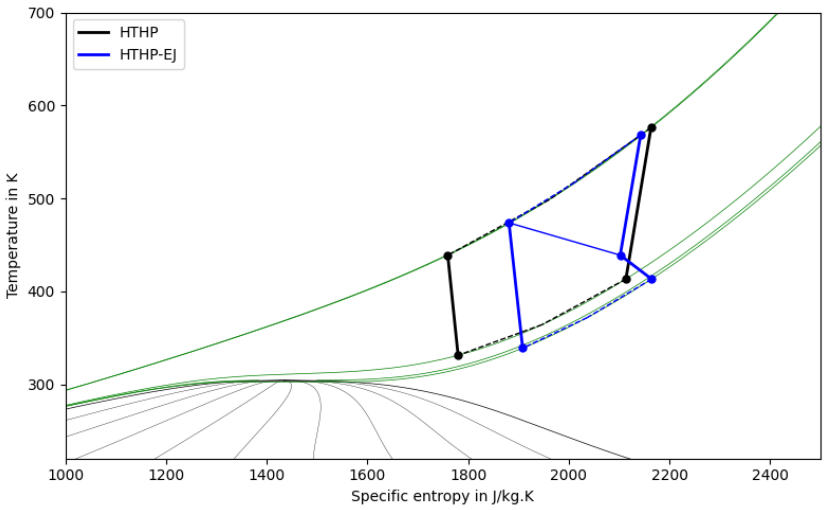

Figure 3.23: T-s diagram for the HTHP versus the HTHP-EJ cycle for the high efficiency scenario and a heat source inlet temperature of 150 °C.

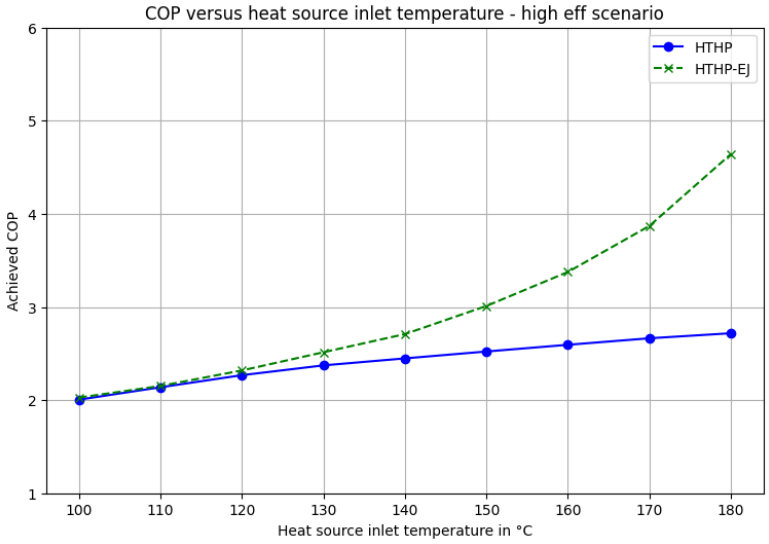

(a)

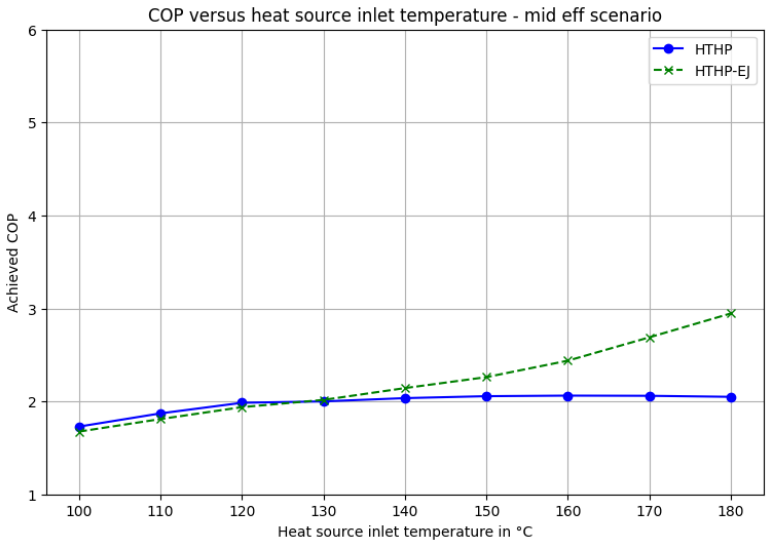

(b)

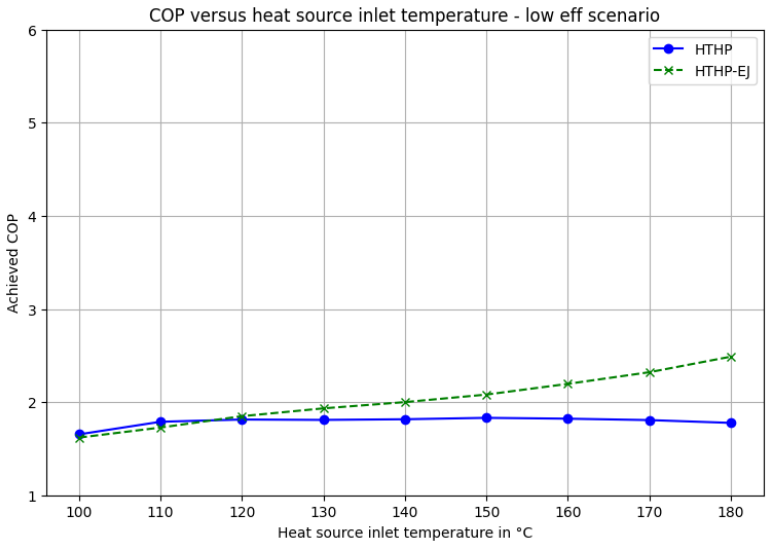

(c)

Figure 3.24: Comparison of the achieved COP of the HTHP and HTHP-EJ cycle for different heat source inlet temperatures for the high efficiency scenario (a), the mid efficiency scenario (b) and the low efficiency scenario(c).

Secondly, the addition of the ejector required a lower turbine outlet pressure while the turbine inlet pressure remained the same. This resulted in a larger pressure ratio over the turbine (not similar to the pressure ratio over the compressor anymore) hence an even larger increase in the power regenerated with the turbine. In Figure 3.23 this effect is clearly illustrated for the high efficiency scenario and a heat source inlet temperature of 150 °C. This observation also further explained why a smaller entrainment ratio, as investigated in Section 3.2.2, resulted in a smaller increase of the COP or even a decrease. As the entrainment ratio was decreased the flow through the turbine was reduced while the flow through the turbine was the main reason the COP increased. This also explains further why the positive effect on the COP becomes less for higher entrainment ratio's as the increase of flow through the turbine becomes smaller due to the majority of the flow already going through the turbine. This also meant that a design with a lower turbine efficiency was expected to profit less from the addition of the ejector as the regeneration effect of the turbine was limited by this efficiency. Something which was indeed observed when comparing the COP improvement for the different efficiency scenario's in Figure 3.24. For the lowest heat source inlet temperatures there could even be a decrease in the COP compared to the HTHP cycle as in those cases the turbine power was not able to increase much and the increase in compressor power outweighed the increase in turbine power.

However, for the HTHP designs with higher heat source inlet temperatures the boundary condition that the heat sink inlet temperature had to be above the heat source inlet temperature the ejector was partly took away due to the addition of the ejector as the overall pressure ratio of the cycle was increased. This also explains why the COP increase was larger for higher heat source inlet temperatures which were initially significantly limited by this natural boundary condition as explained in Section 3.3.
Finally, the observation that the positive effect of the ejector on the COP was more significant for higher turbomachinery efficiencies also could be explained with the fact that increase in COP was mainly caused through an increase of the turbine power. The increase of turbine power was simply more significant if the losses in the turbine were smaller, which was directly related to the turbine efficiency. This is also why the low and mid efficiency scenario, for which the turbine efficiency is nearly the same, show a more similar pattern than the high efficiency scenario.

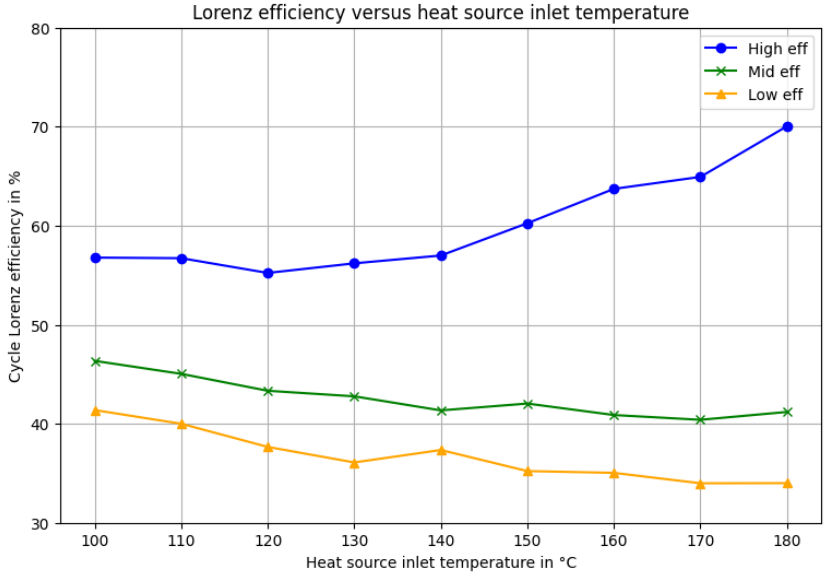

Figure 3.25: Cycle Lorenz efficiency for the different HTHP-EJ designs based on heat source inlet temperatures.

Similar to for the HTHP designs it was of interest to take a look at the Lorenz efficiencies that were obtained for the HTHP-EJ designs. The Lorenz efficiency for every HTHP-EJ design based on the heat source inlet temperature and the efficiency of the turbomachinery can be found in Figure 3.25. Similar to the trends observed for the improvement in achieved COP also the Lorenz efficiencies of the HTHP-EJ designs were higher compared to the HTHP designs for the same operating conditions. For the mid- and low efficiency scenario this resulted in a more or less constant Lorenz efficiency of

between 30-50% for all heat source inlet temperatures which was reasonable. In the HTHP-EJ designs with the highest turbomachinery efficiencies the Lorenz efficiency was between 50-60% for most cases and even increased towards 70% for higher heat source inlet temperatures. This indicated that the improvement of the HTHP cycle with the ejector would indeed result in a much more effective heat pump. This Lorenz efficiency improvement was explained by the same phenomena as mentioned earlier.

Final HTHP-EJ design and cost estimation analysis

The final HTHP-EJ design would in practise by largely similar to the HTHP design as described earlier due to similar operating conditions and required power range for the turbomachinery. The design would be composed of a radial turbine/turboexpander in combination with a motor-driven centrifugal gas turbocompressor. The required output power of the turbine and compressor would still be within the range of a radial/centrifugal design previously indicated in Figure 3.18. Moreover, due to the decreased pressure ratio over the compressor it was even observed that for all designs, except for the "100 °C - high efficiency" design, the compressor pressure ratio was below 5 and a single-stage compressor could be used. Also could TEMA shell-and-tube heat exchangers be used again.

Similar to the cost estimation done for the basic HTHP designs the cost of the HTHP-EJ designs could also be estimated through Aspen EDR and APEA. As the design of the ejector-assisted sCO_2 reversed Brayton HTHP in Aspen Plus was nearly identical to the sCO_2 reversed Brayton HTHP, except for the addition of the splitter and mixer component, the same method was applied as in Section 3.3.1 to estimate the costs of the HEX and turbomachinery. Where it should be noted that for some HTHP-EJ designs the turbine power exceeded the threshold of 1.5 MW output power from Aspen Plus. This meant that APEA could not compute the costs of the turbine anymore. As it it was still desired to estimate the costs for these larger turbines the earlier mentioned paper by Aviles et al. (2021) provided cost data for a turbine of just over 6 MW directly from a turbine manufacturer (Aviles et al., 2021). Hence, the turbine costs for HTHP-EJ designs that included turbines with output powers in the range 1.5-6 MW were scaled with the use of this cost data. This was done through linear interpolation between the turbine costs provided by APEA for a 1.5 MW turbine and the number provided in the paper for a 6.289 MW turbine, which was the maximum turbine output power provided.

APEA could not provide cost data for the splitter and mixer and as explained the ejector itself could not be modelled in Aspen Plus. Nevertheless, to realize a comprehensive estimation of the cost of the HTHP-EJ designs it was useful to apply another method to estimate the costs associated with the ejector. First of all, it was found online that the company Danfoss offers a CO_2 ejector for €11,804.94. This ejector is able to go up to temperatures of 50 °C, pressures of 140-200 bar and CO_2 mass flow of 1.076 kg/s (Invertwell, 2023). To base the costs of the ejector used in the HTHP design on this known cost number it was most important to scale the capacity of the ejector, measured through the total sCO_2 mass flow, and the operating pressure to the numbers in the HTHP-EJ designs. In terms of capacity scaling the method from Turton et al. (2018) could be applied, more specifically the six-tenths rule as explained in Chapter 7 (Turton et al., 2018). It was identified in literature that cost estimation methods for steam ejectors, such as applied in the study by EL-Sayed et al. (2001), were also based on scaling the mass flow was also and therefore seemed like a trustworthy scaling parameter (El-Sayed, 2001). To account for the (slightly) higher operating pressures a pressure factor of 1.2 was introduced, a factor that seemed realistic and that was for example also used by Zühlsdorf et al. (2019) to scale their $(s)CO_2$ heat exchanger designs to higher pressure operation (Zühlsdorf et al., 2019). This pressure factor of 1.2 was used for all HTHP-EJ designs as the pressure of the primary (high-pressure) flow was similar for all designs. This cost scaling was combined with the mentioned 2023 price of the Danfoss CO_2 ejector in Equation 3.45 to obtain an estimate for the ejector costs in the HTHP-EJ designs in euros. This resulted in ejector costs in the range of €63000 to €94000 for the different HTHP-EJ designs, which seemed like a reasonable estimate and the costs were incorporated in the equipment costs of the full HTHP-EJ designs.

$$Cost_{ej} = 11,804.94 * \left(\frac{\dot{m}_{sCO_2}}{1.076}\right)^{0.6} * 1.2 \tag{3.45}$$

In Figure 3.26 the cost estimations for all heat source inlet temperatures and efficiency scenario's are

shown similar to how this was done in Figure 3.19 for the HTHP designs. It can be observed that compared to the HTHP designs there is a stronger fluctuation in the total costs between the designs and that the total HTHP-EJ costs fluctuate between about 3.7 and 4.9 million euros. This is on average about 0.3 million euros higher than the basic HTHP designs, mainly caused by the increased turbine costs due to more regeneration as described above. In the high efficiency scenario, where relatively most regeneration takes place, this effect is seen most notably. For the mid and low scenario, where significantly less regeneration is realized, in most cases the turbine costs are similar or slightly below the costs of the heat sink HEX. Something that was also observed for the HTHP designs. The difference between the costs of the heat source HEX and heat sink HEX were similar as observed in the HTHP results. However, an interesting difference was observed in the costs of the heat sink HEX for different designs where for higher heat source inlet temperatures especially for the high scenario the costs were relatively low. This was caused by relative effective heat exchange with high U values due to a relatively higher sCO_2 mass flow caused by how the HTHP-EJ cycle was (optimally) designed. An effect which was only valid for the purely supercritical cycles and diminished from heat source inlet temperatures of about 150 °C showing again similar development to the costs of the HTHP designs. The costs of the heat source HEX showed similar behaviour as for the HTHP designs, although due to the relative lower pressure in the HEX for similar heat source inlet temperatures the heat source HEX was for every case slightly cheaper.

The ejector costs proved to have a relative insignificant effect on the total equipment costs of the designs. The relative small impact of the ejector on the total equipment costs did not come as a surprise due to the relative simple operation of the ejector as a mechanical compression device. Especially, in relation to the complex, and hence expensive, turbine and compressor technology comprising the largest part of the total equipment costs. It could therefore be concluded that the benefits realized through the addition of the ejector in terms of the increase in achieved COP for all HTHP-EJ designs outweigh the (equipment) costs of the ejector. It should be noted however that that for most HTHP-EJ designs the ejector costs were close to the costs of the heat source HEX. This was somewhat surprising as it would be expected that a heat exchanger would be relatively more expensive indicating that the estimated ejector costs might be a little high. As no actual sCO_2 ejector technology actually exists for these mass flow capacities and temperature-pressure combinations it would have to be verified in future research how accurate the ejector costs estimations are. The observed differences in the ejector costs were a direct cause of the sCO_2 mass flow as can be seen in Equation 3.45. As the sCO_2 mass flows were generally lower for the mid- and low scenario HTHP-EJ designs it was found that the ejector costs were the lowest for these designs. However, this were unfortunately also the HTHP-EJ designs which showed no or very little improvement compared to the HTHP designs for the same heat source inlet temperatures. Finally, the addition of the ejector hardly affected the required compressor power which can also be seen in the compressor costs for every HTHP-EJ design which are quite similar to the compressor costs as shown in Figure 3.19 with only small variations between the different designs.

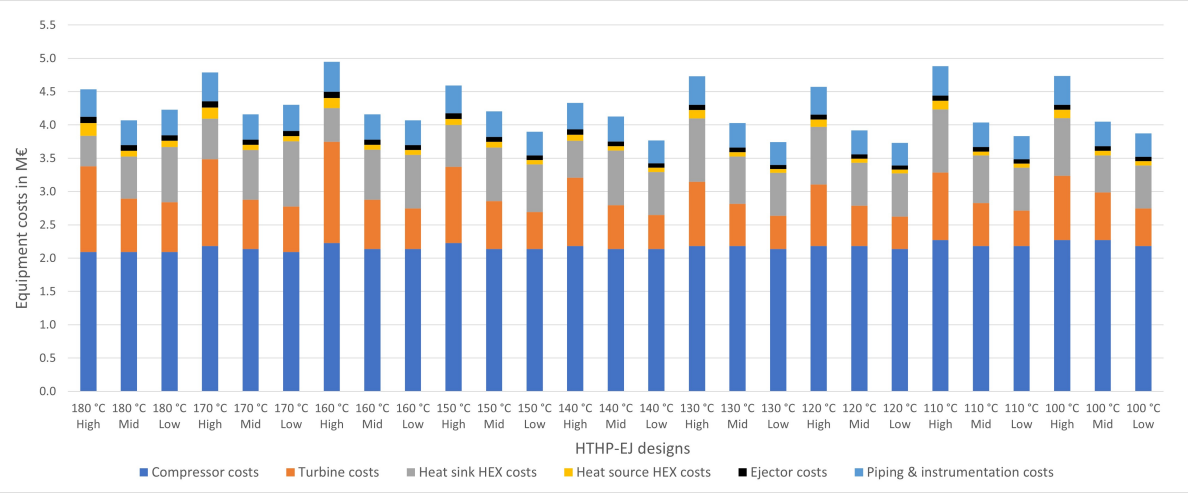

Figure 3.26: Equipment cost build-up for the HTHP-EJ designs for the different heat source inlet temperatures and efficiency scenario's.

In Figure 3.27 the full HTHP-EJ system costs are shown for only the high efficiency scenario to analyze the costs for the different heat source inlet temperatures. The most notable observation are the significant differences in the turbine costs which are a direct cause of larger turbine powers. As previously explained, the reason that the turbine powers are relatively large for heat source inlet temperature of 150 °C and above could be traced back to the basic HTHP designs. The higher heat source inlet temperatures were severely limited by the boundary condition that the heat sink inlet temperature had to be above the heat source inlet temperature. The addition of the ejector to the HTHP cycle partly diminished this limitation while simultaneously increasing the work regenerated through the turbine. This happened through a combination of a higher sCO_2 mass flow and a larger enthalpy difference in the turbine as illustrated in Figure 3.23. This increase in turbine power for some HTHP-EJ designs does come at a cost through significantly higher turbine costs compared to the HTHP design. For the 160 °C heat source inlet temperature for example the turbine costs increase from about 0.8 million euros to 1.5 million euros. However, in return the COP is predicted to increase from about 2.6 to almost 3.5 which would mean the benefits outweigh the additional costs. The decrease in cost of the heat source HEX for lower heat source inlet temperatures as well as the fluctuations in the piping & instrumentation costs are similar as for the HTHP designs. The relative low heat sink HEX costs for higher heat source inlet temperatures was mentioned earlier. In terms of the total HTHP-EJ costs the lowest costs were observed for the 140 °C design due to a combination of a relative average turbine power and hence costs and low heat sink HEX costs. Overall, the total equipment costs fluctuated more between the different designs due to balance between the increase/decrease in turbine costs and the decrease/increase in heat sink HEX costs.

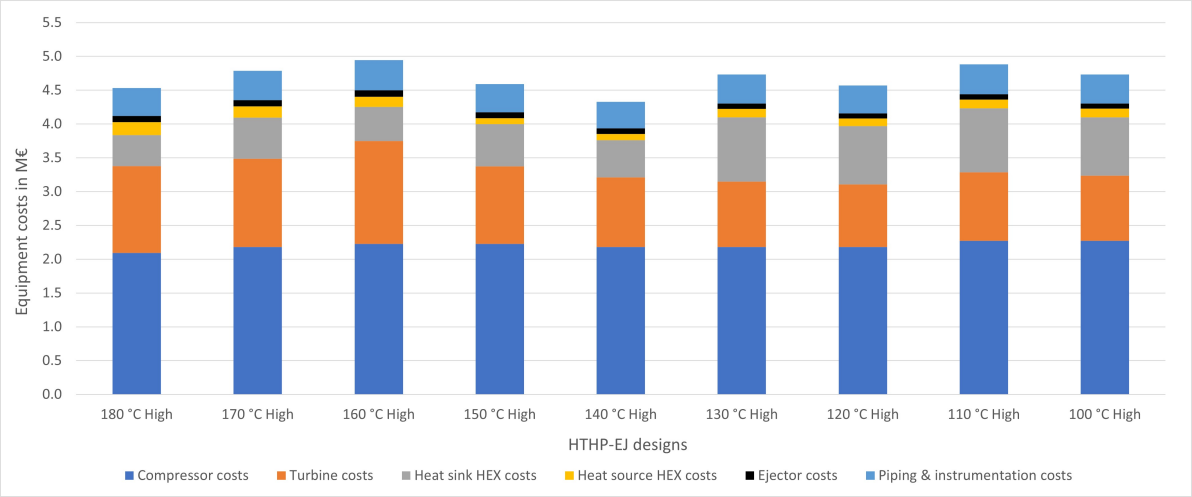

Figure 3.27: Equipment cost build-up for the HTHP-EJ designs for the different heat source inlet temperatures for the high efficiency scenario.

In Figure 3.28 the cost build-up for only the mid efficiency is illustrated for the different HTHP-EJ designs. It was observed that the differences in the costs of the components are less significant than for the high efficiency scenario and only minor fluctuations were observed. This was caused by the fact that the HTHP-EJ cycles were largely similar for the different heat source inlet temperatures. The same changes were seen as for the high efficiency scenario but to a lesser extent hence the smaller differences in for example the turbine costs. In terms of the total HTHP-EJ costs the lowest costs were observed for the 120 °C design due to the relative lowest turbine costs and relatively cheap heat sink HEX. Generally, the lowest costs were observed for the lower heat source inlet temperatures.

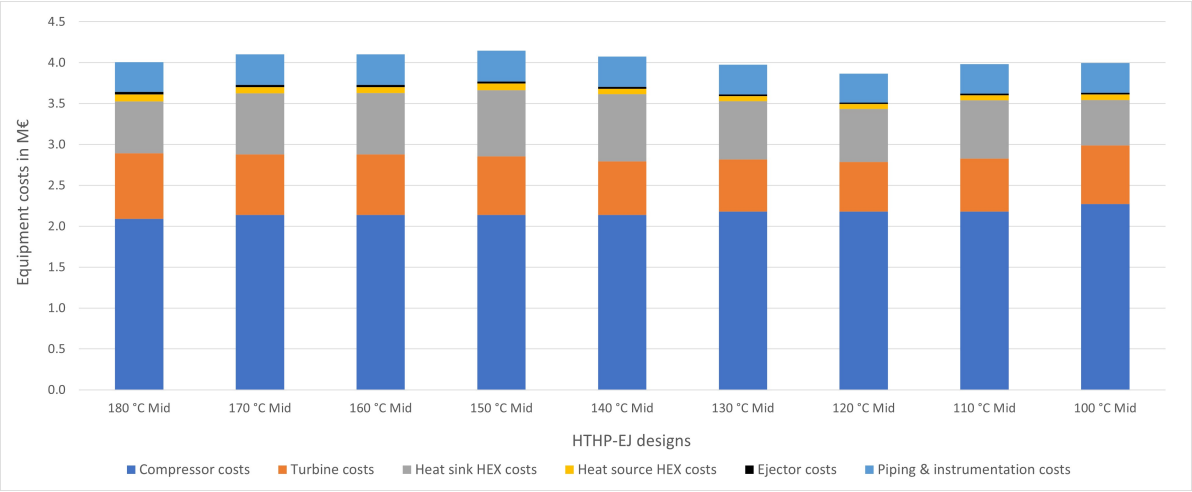

Figure 3.28: Equipment cost build-up for the HTHP-EJ designs for the different heat source inlet temperatures for the mid efficiency scenario.

In the low efficiency scenario larger fluctuations were seen between the costs of the HTHP-EJ designs as illustrated in Figure 3.27. This was mainly caused by higher heat sink HEX costs combined with larger turbine costs for the higher heat source inlet temperatures. Similar as for the HTHP designs these HTHP-EJ designs were still relatively limited by the boundary condition that the heat sink inlet temperature should be above the heat source inlet temperature. The addition of the ejector therefore improved the designs but due to a larger sCO_2 mass flow and difficulty to match the streams inside the HEX the heat sink HEX costs were still relatively high for the high heat source inlet temperatures. The highest total HTHP-EJ costs were therefore observed for the 170-180 °C designs. The lowest costs were observed for the 120 °C design but from 100-150 °C the costs proved to be relatively similar.

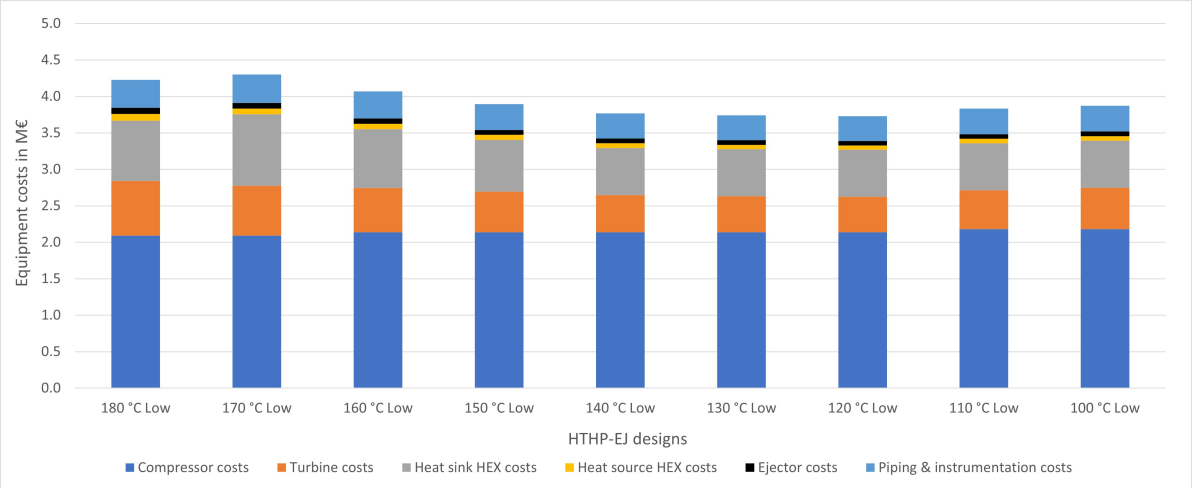

Figure 3.29: Equipment cost build-up for the HTHP-EJ designs for the different heat source inlet temperatures for the low efficiency scenario

4

High-temperature heat pump with thermal energy storage

In this chapter a brief discussion will be given what opportunities and challenges would arise if a HTHP, like the one proposed in Section 3.1.1, could be combined with a TES system, like the one proposed in Section 2.1. This is mainly focused on the future and what effect future developments are expected to have on this. Thereby, also presenting a future outlook for the electrification of medium-temperature industrial process heat. In any case, it would be desirable to combine future HTHP technologies with some form of energy storage to deal with the intermittency in VRE supply extensively discussed in Section 2.1.

4.1. Opportunities

As explained a HTHP generally has a COP of 3 compared to a COP of just below 1 for an E-heater. In terms of significant higher OPEX costs that result from this the E-heater had to be combined with the TES system to profit from electricity price fluctuations to give it a chance to be competitive with natural gas heaters. However, a HTHP could be competitive with natural gas without the need for storage if a COP of around 2.5 could be achieved. Although, it was observed that the predicted COP for the sCO_2 revered Brayton HTHP would realistically be more towards 2 this still meant that in terms of OPEX costs it might be able to compete with natural gas. Especially, if waste heat at high temperatures would be available and considering future government grants and carbon tax. Nonetheless, as not all this electricity is produced through VRE sources this would still result in significant emissions. The combination of a HTHP with TES could realize a truly sustainable system. While, at the same time realize significantly lower OPEX costs than if an E-heater was used and potentially offer a cheaper solution than natural gas heating. In practise the TES system as currently designed for the combination with the E-heater would also not require major adaptations as for most of the proposed design the E-heater is not directly integrated with the TES system. The means the E-heater could easily be replaced by a HTHP to heat the heat transfer fluid used in the TES system.

4.2. Challenges

The main challenge to combine the HTHP with the TES solution are the required temperature levels. The study on the sCO_2 revered Brayton HTHP showed that to reach an output temperature of 280 °C or even slightly higher is possible with a reasonable COP depending on the availability of waste heat. However, the commercially available TES systems discussed are all based on sensible heat storage and require significantly higher temperatures to charge the storage. Of these TES systems only the Kyoto HeatCube would come in the vicinity with a maximum required temperature of 415 °C which is still a lot higher than 280 °C. Moreover, makes the large temperature difference required in the HTF stream inside the HTHP to reach a good COP it even more challenging to match this with the TES as the heat sink stream inlet temperatures determines the maximum temperature that can then be realized inside the TES.

4.3. Future outlook

An important consideration that needs to be made is that the current TES systems analysed are designed to operate with an E-heater that has no output temperature limitations and does not become (significantly) less efficient when higher output temperatures are required. This makes sensible energy storage very suitable. However, as explained in Section 4.2 this is less suited for a HTHP which is considerably limited in terms of output temperatures and the COP is decreases rapidly for higher required temperature lifts. Therefore, TES in the form of SHS is not very suited to combine with HTHP technology. Nevertheless, as briefly discussed in Section 1.3, a lot of research is ongoing into LHS and TCS which would not necessarily require the high output temperatures to store large amounts of heat. The challenge that remains is the large temperature glide required in the HTF stream inside the HTHP if the output temperature is required at a constant level, which is for example generally the case for LHS. Nonetheless, if these TES technologies further develop and become commercially available on the same scale that SHS is currently available this would greatly improve the feasibility of combining HTHP technology with TES.

Alternatively, the briefly introduced technologies of PTES and ETES that are a direct integration of HTHP and TES technology through the Carnot battery concept could also become an option. As explained in Section 1.3.2 these systems are currently focused on grid-scale applications to convert electricity to heat and back to electricity based on supply and demand for electricity. Moreover, do they have a significant footprint which hinders application at individual industrial sites. Nevertheless, these technologies have the potential to also supply high-temperature process heat with a COP above 1 especially in combination with CSP technologies. Further research and improvements in this technology might make it a good alternative to supply medium-temperature industrial process heat in the future.

5

Discussion

To put the presented results in perspective, it was useful to look critically at the assumptions done to obtain these results and reflect briefly on the results themselves.
First of all, within the research executed on the E-heater + TES solution the main uncertainties lay in the obtained data for the techno-economic analysis. The exact technical specifications of the E-heater + TES solutions and economical parameters in the form of the CAPEX costs and O&M costs are very application specific. Only after an in-depth study is executed by the TES supplier the exact data is known. This study was also limited to the E-heater + TES system and did not consider additional requirements. Examples of this are the grid connection able to deliver the required electrical power levels or the necessary modifications to the current thermal oil loop to accommodate the E-heater + TES system. Assumptions were also made with regard to the process data of the process from Teijin Aramid to not overcomplicate the calculations, such as the required temperature levels and output power. In real-life operation these fluctuate substantially over time and are also submitted to required maintenance or equipment breakdowns. Nevertheless, the goal of this study was to assess the techno-economic feasibility of the electrification. If Teijin Aramid decides to continue with the project a detailed analysis should be executed on the implementation of the proposed system and what exact cost numbers are to be expected.

Moreover, the estimations on the OPEX costs and most importantly the expected future OPEX costs were purely based on historic data, assumptions and estimates found online such as the KEV 2022 report. History has shown that the prices of energy are very unpredictable and with all the ongoing global conflicts the scenarios can change quickly. Therefore, it should be noted that the provided estimates were the best that could currently be obtained and involve a large uncertainty factor. The predicted supply of electricity in the decades to come contains this same uncertainty based on both private and public investments as well as technological advancements. The sudden break-through of new (thermal) energy storage technologies could take over the (thermal) energy storage market and put the findings presented in this study in a different light. This could be both in the current field of sensible thermal storage but also in latent- or thermochemical storage or with regard to battery- or hydrogen storage. The similar uncertainty is present with (electric) heating technologies. Nonetheless, the most realistic alternative would be the combustion of hydrogen if green hydrogen production would show an explosive growth due to technological breakthroughs regarding its efficiency. However, based on the currently available information the proposed E-heater + TES solution to supply medium-temperature process heat is the best solution for industrial players like Teijin Aramid to electrify and decarbonize their process heat demand on the short-term.

With regard to the HTHP model it should be noted that due to the absence of experimental data the HTHP model could only be validated through comparable theoretical studies and Aspen Plus. It cannot therefore not be said with certainty that the results from the HTHP model are a good reflection of reality. However, as Aspen Plus is based on real-life equipment data and experimentally validated correlations for different operating conditions it is believed the results are trustworthy. All the equipment was modelled as detailed as possible and the HTHP model was purely based on thermodynamic rela-

tions and equations of state using CoolProp. Additionally, the most important goal of the HTHP model was to give an indication of the potential of the sCO_2 reversed Brayton HTHP. Further research and actual experimental results will have to validate the predicted operation and COP that can be achieved.

Regarding the HTHP-EJ model the main uncertainty was in the ejector model and its interaction with the rest of the HTHP model. First of all, was the ejector model based on the model proposed in the paper by Padilla et al. (2016). In this paper the ejector was incorporated in a sCO_2 Brayton cycle with multiple turbines and a very different layout. It was operated at temperatures of around 800 K and with pressures up to 250 bar. Despite, this being comparable to the operating conditions of the HTHP-EJ model this caused uncertainties. Notably, the substantial higher pressure used, and the mass flows the ejector was submitted to, in the HTHP-EJ model might in practise not actually be possible. The authors of the paper were contacted but no contact could be established, so their exact model could not be obtained. It was therefore decided to construct an own model based on the model description in the paper. Thereby, all values used in the paper were adapted such as the efficiencies of the different parts of the ejector and observed limitations in terms of the entrainment ratio. The model itself was also based on a few simplifying assumptions as discussed in Section 3.1.2. Logically, the incorporation of these assumptions decreased the resemblance what could be expected in real-life operation. Nevertheless, besides these assumptions the theoretical model was based on energy and mass balances and the continuity equation increasing its accuracy. It was furthermore unfortunate that the Mach number approach presented very different ejector output pressures and that no pattern could be observed in the differences. On the other hand, the fact that Padilla et al.(2016) did not adapt this Mach number approach in their model might have been due to this reason.

A validation of the ejector model was given in the paper. However, it was mentioned that no experimental data was available for an ejector with a gas-gas mixing flow of CO_2. Therefore, the validation was done with experimental data for R141b (gas phase only). The validation produced results within a 15 % error margin, and it was noted that "the results show that the simplicity of the ejector model used by this paper leads to some discrepancies with experimental results since geometrical parameters were not taken into account." (Padilla et al., 2016). Therefore, the relevance of the validation was somewhat questionable but as no experimental data was present it was the best that could be obtained. In conclusion, it was evident that for the ejector modelling a lot of assumptions needed to be done. The presented results of the HTHP-EJ model should therefore be considered with caution. Nevertheless, it was the most accurate result that could be obtained within this study and was done with the goal to assess the feasibility of an ejector-assisted sCO_2 reversed Brayton HTHP. It would have been interesting to develop a more detailed ejector model, but this would be a thesis/research project on its own. Future research will have to verify how an ejector would perform under the proposed operating conditions. Experimental validation of real-life ejector performance under comparable operation conditions would provide especially interesting insights.

In the cost calculations a larger uncertainty was present, mainly for the turbomachinery. As already mentioned, the compressor could not be simulated in APEA for the exact operating conditions from the model due to the restriction in compressor inlet temperature. This translated in different temperature levels and a slightly different sCO_2 mass flow hence decreasing the accuracy of the cost estimation. For the turbine cost estimation this was even more significant as the pressure cost scaling and power scaling had to be introduced as explained in Section 3.3.1. The heat exchangers could be modelled quite accurately with Aspen EDR. Therefore, the only uncertainty in the cost estimations of the heat exchangers was the accuracy in the prediction of Aspen EDR which were unknown. Finally, the estimation of the ejector costs involved the largest uncertainty as Aspen Plus could not be used and no sCO_2 ejector technology exists for the presented operating conditions. Equation 3.45 provided a ballpark estimate of the costs that could be expected, and actual ejector costs are expected to be lower. This is since the provided estimate the ejector costs were similar to the costs of a heat exchanger which Professor Hooman fairly pointed out is not to be expected. It would therefore be interesting to obtain more detailed cost estimations for the ejector in future research. Nonetheless, the goal of the cost estimation was to get a general idea on the cost that could be expected for the HTHP designs. Therefore, the incorporated methods were deemed accurate enough and no more accurate method was identified during the study.

It is also of interest to briefly reflect on the design choices made for the (ejector-assisted) sCO_2 reversed Brayton HTHP in this study. Moreover, discuss what could be done to further improve the basic sCO_2 reversed Brayton HTHP cycle. First of all, it became evident during the parametric analysis that a lot of factors had an impact on the performance of the HTHP. It was therefore challenging to obtain an ideal combination of optimal values for every parameter and create the most-optimal HTHP design. Nonetheless, the proposed designs were the best guess of an optimal HTHP(-EJ) design. Moreover, it was observed that especially the chosen output temperature of 280 °C limited the presented designs in Section 3.3. This was mainly the case for the designs with lower turbomachinery efficiencies that could reach higher output temperatures with a similar COP as briefly discussed in Section 3.3.1. The fact that this is possible was in principle a positive observation. It indicates that it would be of interest to investigate in future research what output temperatures could be realized within the current equipment limitations. On the other hand, if the COP remains limited to the values presented in this study it remains to be seen if the financial feasibility is strong enough to be competitive with other technologies such as E-heater technology. It is expected that this would also be very application specific. In terms of the selected equipment the use of a radial turbine and centrifugal compressor seems undisputed. However, the choice to go with shell-and-tube heat exchangers instead of for example printed-circuit heat exchangers as proposed in other studies was well-substantiated but could prove to be non-optimal in future studies. In terms of cycle optimization, the ejector provided itself as interesting option, but more options are available. In the paper by Zühlsdorf et al. (2019) and Huang et al. (2022) the addition of an IHX/recuperator was for example proposed. After discussions with Professor Hooman it seemed that the addition of an IHX is not worth the effort. The idea sounds interesting especially for the large temperature lift cases, but it does not necessarily result in a better COP. An IHX also adds extra complexity and costs to the system so the advantage observed in the paper by Zühlsdorf et al. (2019) that a relative lower pressure ratio could be used is not necessarily worth it. Nevertheless, it might be interesting in further research to verify if the addition of an IHX/recuperator could be a way to improve the COP.

On a final note, the potential to combine HTHP technology with (thermal) energy storage in the future was explored in Chapter 4. As this was purely meant as an indication of what opportunities and challenges were connected to this it had an inherent uncertainty. Technological advancements in the renewable energy industry have seen an enormous surge in recent years and it remains to be seen what the future brings. Nevertheless, it is certain that to deal with the intermittency of supply from VRES also HTHP technology needs to be combined with some form of energy storage. Either before the (electrical) energy is delivered to the HTHP technology, through for example hydrogen- or battery storage, or after the process heat is generated in the form of thermal energy storage.

6

Conclusions and recommendations

In conclusion, in Section 1.2 a two-folded goal was set for the thesis project. The first goal was formulated as: ”identify what is based on commercially available technologies currently the most viable way to electrify the production of medium-temperature process heat for industrial players like Teijin Aramid. Thereby considering optimal use of energy storage technologies to deal with intermittency of electricity production through VRE sources and also what role DSR can play”. It can be concluded that currently the most viable way to electrify the production of medium-temperature process heat for industrial players like Teijin Aramid is the combination of an industrial E-heater with a solid-state or molten-salt sensible TES system. Thereby, it is most realistic to focus on intraday storage with ideally a maximum of 6 hours of charging per period of 24 hours. This would be optimal both from a technical and economical viewpoint. Unfortunately, this would currently result only in partial decarbonization. The effective use of DSR could enable a higher percentage of decarbonization and further improve the proposed electrification.

There are multiple interesting suppliers of TES systems present like Kraftblock, EnergyNest and Kyoto. Moreover, for the case study of the electrification of the Plinke process in the Emmen plant of Teijin Aramid the E-heater + TES solution is in terms of technical feasibility well suited. Only some minor modifications to the current thermal oil system would be required. Moreover, in order to realize the partial decarbonization the current gas heater could also be kept and combined with the E-heater + TES system to be able to switch between natural gas and electricity based on the availability of renewable energy. Technical challenges involved are mainly connected to realizing the required grid connection and adaption of the current thermal oil system. This is something that has to be further investigated by Teijin Aramid. In terms of economical feasibility of the E-heater + TES system there is still a significant challenge to tackle, especially in the OPEX costs. This as it was found that on average the day-ahead natural gas price is about 2.5 times lower than the electricity price without considering additional fees. Through government grants, on both the CAPEX and OPEX, and higher carbon tax the economic feasibility could be improved especially when only aiming for 75% electrification/decarbonization. It was analyzed that applying DSR in the production process of Teijin Aramid could, in combination with the E-heater + TES system, play a role in a higher decarbonization percentage. As the Dutch energy system becomes was expected to become more renewable in the future the shift could then be made to full decarbonization in a later stage. Nevertheless, it is still expected that it will be very difficult to obtain a comparable business-case to natural gas heating in the near future. Therefore, it is currently mainly the question what price an industrial player like Teijin Aramid is willing to pay to decarbonize. Moreover, technological advancements in heat pump technology, alternative carbon-free technologies like combustion of green hydrogen and new (thermal) storage technologies could prove to be more attractive in the future. However, this study concluded that currently the most viable way to electrify and decarbonize the demand of medium-temperature process heat is through the proposed E-heater + TES system.

The following recommendations were devised for Teijin Aramid regarding the electrification of their medium-temperature process heat demand with the E-heater + TES solution:

- Based on the results from the techno-economic analysis select one or two proposed TES suppliers and let these suppliers execute a detailed analysis on feasibility to electrify the medium-temperature process heat supply for the second stage of the Plinke.
- Further investigate the exact technical and financial possibilities to maximize the options DSR to enable further decarbonization combined with the intraday storage from the TES.
- Verify that the required grid connection can be realized as this is of vital importance for the implementation of the E-heater + TES solution.

The second goal of the thesis project was formulated as: ”explore the potential of a sCO_2 reversed Brayton HTHP that could alternatively provide the medium-temperature process heat for industrial players like Teijin Aramid in the future. Thereby also taking into consideration to combine this new kind of HTHP with the energy storage technologies investigated in the other part of the project to still be able to deal with the intermittency in electricity production through VRE sources”. The numerical study on the sCO_2 reversed Brayton HTHP showed that there was definitely potential in providing medium-temperature process heat for temperatures of around 280 °C and beyond. The most interesting finding was that the properties of sCO_2 would in principle also enable supply of high-temperature process heat. The large pressures required to reach these high temperatures proved to be the largest limitation in terms of equipment compatibility. Nevertheless, future improvements in turbomachinery equipment could make this possible. However, to reach these high output temperatures while also achieving a reasonable COP would require a combination of high turbomachinery efficiencies, a high-temperature heat source and further improvement of the sCO_2 reversed Brayton cycle configuration. The use of Aspen Plus enabled the construction of a numerical model that seemed to present a good reflection of what real-life operation could like. With an estimated equipment cost of around 4 million euros to deliver heat at an output temperature of 280 °C the HTHP design seemed plausible from a CAPEX cost point of view. However, the estimated CAPEX is significantly higher than the CAPEX of an commercially available E-heater or natural gas heater. Moreover. as the price of electricity is on average about 2.5 times higher than the natural gas price a reasonable COP of in the range of 2.5 would be required. Unfortunately, it had to be concluded that only for an isentropic compressor efficiency of >80% and an isentropic turbine efficiency of >90% a COP of 2.5 or higher could be achieved with the proposed HTHP design. Where also a (waste) heat source inlet temperature of 150 °C or higher was required. This could be either obtained from an external source or through a cascaded heat pump system which would result in a lower combined COP.

To potentially improve the COP of the HTHP design the addition of a sCO_2 ejector was investigated in an ejector-assisted sCO_2 reversed Brayton HTHP design. A sCO_2 ejector for this application does not exist yet. However, a numerical model was constructed based on the general theoretical equations behind the ejector operation principle as proposed by Padilla et al. (2016) and a numerical HTHP-EJ design was constructed (Padilla et al., 2016). It was found that the mechanical ”pre-compression” of the ejector incorporated in the HTHP-EJ design for some cases showed significant COP improvements compared to the standard HTHP design. This was mainly caused by the improvement in turbine regeneration due to the addition of the ejector. It was difficult to validate if the obtained results where a realistic reflection of reality but the results were definitely promising. The COP of 2.5 was with the HTHP-EJ design well-attainable. This was even the case for lower isentropic turbomachinery efficiencies and lower (waste) heat source inlet temperatures. It would have to be investigated in further research if the predicted COP improvement presented in this study would indeed be possible in real-life operation. To electrify and decarbonize medium-temperature industrial process heat demand through heat pump technology seems unrealistic at this point time. However through alternative improvements of the sCO_2 reversed Brayton HTHP configuration or developments in other novel HTHP technologies it might become possible to electrify and decarbonize medium-temperature industrial process heat demand through heat pump technology in the future.

The following recommendations were devised regarding further research on the sCO_2 reversed Brayton HTHP:

- Further investigate what would be possible for the sCO_2 reversed Brayton HTHP in terms of output temperatures within the current equipment limitations and what COP could be achieved if not limited by the scope of this research.
- Build a prototype of sCO_2 reversed Brayton HTHP in order to find out what COP could be realized in practise and obtain experimental results that can be used for validation.
- Develop a more numerical model of the sCO_2 ejector where the required geometry is also investigated. This to be able to simulate the actual performance of the ejector in this application in more detail and validate the results from this study to see what COP improvements could actually be obtained.
- Construct a prototype of the ejector to gather experimental data.e Alternatively a dynamic numerical model including computational fluid dynamics could be developed to provide more accurate numerical data.
- Investigate alternative configurations for the sCO_2 reversed Brayton HTHP cycle, such as with the addition of an IHX/recuperator, to see what effect this would have on the achieved COP.

On a final note, it was found that the combination of HTHP technology with TES is something that could definitely possible but also has some significant challenges. To deal with the intermittency of supply of VRES energy storage is vital also for HTHP technology both in terms of decarbonization as well as to make it more financially feasible. However, due to the characteristics of heat pump technology it is not evident that thermal energy storage is the best and most suitable way to realize this. The main challenge lies in the optimal temperature levels required for the current technology of sensible TES and the output produced with HTHP technology. Future developments in TES technologies as well as novel HTHP designs might make this combination more feasible in the future. Where also the concept of directly combining HTHP and TES technology though PTES or ETES might prove to be a viable solution. Otherwise battery storage or other storage technologies could provide a good alternative to be combined with HTHP technology for the electrification of medium-temperature industrial process heat.

References

Adams II, T. (2022). *Learn aspen plus in 24 hours, 2nd edition*. McGraw Hill.

Adamson, K.-M., Walmsley, T. G., Carson, J. K., Chen, Q., Schlosser, F., Kong, L., & Cleland, D. J. (2022). High-temperature and transcritical heat pump cycles and advancements: A review. *Renewable and Sustainable Energy Reviews*, *167*, 112798. https://doi.org/10.1016/j.rser.2022.112798

Aga, V., Conte, E., Carroni, R., Burcker, B., & Ramond, M. (2016). *Supercritical co2-based heat pump cycle for electrical energy storage for utility scale dispatchable renewable energy power plants*. https://www.nrel.gov/docs/fy21osti/77955.pdf

Ahn, Y., Bae, S. J., Kim, M., Cho, S. K., Baik, S., Lee, J. I., & Cha, J. E. (2015). Review of supercritical co2 power cycle technology and current status of research and development. *Nuclear Engineering and Technology*, *47*, 647–661. https://doi.org/10.1016/J.NET.2015.06.009

Aly, N. H., Karameldin, A., & Shamloul, M. (1999). Modelling and simulation of steam jet ejectors. *Desalination*, *123*(1), 1–8. https://doi.org/https://doi.org/10.1016/S0011-9164(99)00053-3

Angelino, G., & Invernizzi, C. (1995). Prospects for real-gas reversed brayton cycle heat pumps. *International Journal of Refrigeration*, *18*(4), 272–280. https://doi.org/10.1016/0140-7007(95)00005-V

Arpagaus, C., Bless, F., Uhlmann, M., Schiffmann, J., & Bertsch, S. S. (2018). High temperature heat pumps: Market overview, state of the art, research status, refrigerants, and application potentials. *Energy*, *152*, 985–1010. https://doi.org/10.1016/J.ENERGY.2018.03.166

Aviles, D., Sabri, F., & Hooman, K. (2021). Techno□economic analysis of a hybrid solar□geothermal power plant integrated with a desalination system. *International Journal of Energy Research*, *45*. https://doi.org/10.1002/er.6948

Bell, I. H., Wronski, J., Quoilin, S., & Lemort, V. (2014). Pure and pseudo-pure fluid thermophysical property evaluation and the open-source thermophysical property library coolprop [CoolProp version 6.5.0]. *Industrial & Engineering Chemistry Research*, *53*(6), 2498–2508. https://doi.org/10.1021/ie4033999

Bergman, T., Lavine, A., Incropera, F., & DeWitt, D. (2011). *Fundamentals of heat and mass transfer, 7th edition*. John Wiley & Sons, Incorporated.

BloombergNEF. (2022). *Global energy storage market to grow 15-fold by 2030*. https://about.bnef.com/blog/global-energy-storage-market-to-grow-15-fold-by-2030/

Cabeza, L. F., de Gracia, A., Fernández, A. I., & Farid, M. M. (2017). Supercritical co2 as heat transfer fluid: A review. *Applied Thermal Engineering*, *125*, 799–810. https://doi.org/10.1016/J.APPLTHERMALENG.2017.07.049

CNESA, C. E. S. A. (2021). Energy storage industry white paper 2022 (summary version). *EB/OL*, 06–29.

Danfoss. (2018). *The danfoss multi ejector range for co2 refrigeration: Design, applications and benefits*. https://www.danfoss.com/en/service-and-support/case-stories/dcs/the-danfoss-multi-ejector-range-for-co2-refrigeration/

de Gracia, A., & Cabeza, L. F. (2015). Phase change materials and thermal energy storage for buildings. *Energy and Buildings*, *103*, 414–419. https://doi.org/https://doi.org/10.1016/j.enbuild.2015.06.007

De Kleijn Energy Consultants & Engineers. (n.d.). *Operating principle - transcritical co2 heat pump*. https://industrialheatpumps.nl/english/operating_principle/transcritical_co2_heat_pump/

de Boer, R., Marina, A., Zühlsdorf, B., Arpagaus, C., Bantle, M., Wik, V., Elmegaard, B., Corberan, J. M., & Benson, J. (2020). Strengthening industrial heat pump innovation: Decarbonizing industrial heat. https://www.sintef.no/globalassets/sintef-energi/industrial-heat-pump-whitepaper/2020-07-10-whitepaper-ihp-a4.pdf

DLR. (n.d.). *High-temperature heat pump cobra*. https://event.dlr.de/en/hmi2022-energie/hochtemperatur-waermepumpe-cobra/

Dostal, V., Hejzlar, P., & Driscoll, M. J. (2006). The supercritical carbon dioxide power cycle: Comparison to other advanced power cycles. *Nuclear Technology*, *154*(3), 283–301. http://dx.doi.org/10.13182/NT06-A3734

Eames, I., Aphornratana, S., & Haider, H. (1995). A theoretical and experimental study of a small-scale steam jet refrigerator. *International Journal of Refrigeration*, *18*, 378–386. https://doi.org/10.1016/0140-7007(95)98160-M

EC. (n.d.). *Climate strategies targets - 2050 long-term strategy*. https://climate.ec.europa.eu/eu-action/climate-strategies-targets/2050-long-term-strategy_en

Eggers, J. R., von der Heyde, M., Thaele, S. H., Niemeyer, H., & Borowitz, T. (2022). Design and performance of a long duration electric thermal energy storage demonstration plant at megawatt-scale. *Journal of Energy Storage*, *55*, 105780. https://doi.org/https://doi.org/10.1016/j.est.2022.105780

El-Dessouky, H., Ettouney, H., Alatiqi, I., & Al-Nuwaibit, G. (2002). Evaluation of steam jet ejectors. *Chemical Engineering and Processing: Process Intensification*, *41*(6), 551–561. https://doi.org/https://doi.org/10.1016/S0255-2701(01)00176-3

El-Sayed, Y. (2001). Designing desalination systems for higher productivity. *Desalination*, *134*(1), 129–158. https://doi.org/https://doi.org/10.1016/S0011-9164(01)00122-9

Energy.at-site.be. (2023). *Energy storage - a capacity cost, size and efficiency comparison*. https://energy.at-site.be/storage/

Engineers Edge. (n.d.). *Overall heat transfer coefficient table charts and equation*. https://www.engineersedge.com/thermodynamics/overall_heat_transfer-table.htm

Finger, S., & Khass, O. A. The dlr high temperature heat pump pilot plants. In: European Heat Pump Summit. 2021, October. https://elib.dlr.de/145429/1/DLR_EHPS.pdf

Finney, B., & Jacobs, M. (2010). *File:carbon dioxide pressure-temperature phase diagram.svg*. https://bit.ly/3N1OfWK

Garg, P., Kumar, P., & Srinivasan, K. (2013). Supercritical carbon dioxide brayton cycle for concentrated solar power. *Journal of Supercritical Fluids*, *76*, 54–60. https://doi.org/10.1016/j.supflu.2013.01.010

Heating group. (2023). *Circulation heaters*. https://www.heatinggroup.com/electric-heating/process-heating-en/circulation-heaters-en/

Hołyst, R., & Poniewierski, A. (2012). *Thermodynamics for chemists, physicists and engineers*. Springer Netherlands.

IEA. (2020). *Renewables 2020*. https://www.iea.org/reports/renewables-2020

IEA. (2022). *Renewables 2022*. https://www.iea.org/reports/renewables-2022

IEA. (2023). Global heat pump sales continue double-digit growth. https://www.iea.org/commentaries/global-heat-pump-sales-continue-double-digit-growth

IEA HPT. (n.d.). *Annex 58 task 1: Technologies – state of the art and ongoing developments for systems and components*. https://heatpumpingtechnologies.org/annex58/task1/

IEA HPT TCP. (2023). *Annex 58 high-temperature heat pumps task 1 - technologies task report*. https://heatpumpingtechnologies.org/annex58/wp-content/uploads/sites/70/2023/09/annex-58-task-1-technologies-task-report.pdf

Invertwell. (2023). *032f5674 danfoss co2 multi ejector hp 3875, ctm 6*. https://www.invertwell.com/032f5674-danfoss-co2-multi-ejector-hp-3875-ctm-6/

IRENA. (2020). *Innovation outlook: Thermal energy storage*. https://www.irena.org/-/media/Files/IRENA/Agency/Publication/2020/Nov/IRENA_Innovation_Outlook_TES_2020.pdf

Karakurt, A. S., Bashan, V., & Ust, Y. (2020). *Comparative maximum power density analysis of a supercritical co2 brayton power cycle* (1). Yildiz Technical University Press. https://dx.doi.org/10.18186/thermal.671148

Linares, J. I., Martín-Colino, A., Arenas, E., Montes, M. J., Cantizano, A., & Pérez-Domínguez, J. R. (2023). Carnot battery based on brayton supercritical co2 thermal machines using concentrated solar thermal energy as a low-temperature source. *Energies*, *16*(9). https://doi.org/10.3390/en16093871

Lumenion. (2023). *Power-to-heat: Converting renewable electricity into green heat*. https://lumenion.com/en/

Maruf, M. N. I., Morales-España, G., Sijm, J., Helistö, N., & Kiviluoma, J. (2022). Classification, potential role, and modeling of power-to-heat and thermal energy storage in energy systems: A review. *Sustainable Energy Technologies and Assessments*, *53*, 102553. https://doi.org/https://doi.org/10.1016/j.seta.2022.102553

Mecholic. (n.d.). *Air refrigerator working on bell-coleman cycle with pv and ts diagram (reversed brayton or joule cycle)*. https://www.mecholic.com/2017/12/bell-coleman-refrigeration-cycle.html

MGA Thermal. (n.d.). *Mga thermal || thermal energy storage*. https://www.mgathermal.com/

Mitali, J., Dhinakaran, S., & Mohamad, A. (2022). Energy storage systems: A review. *Energy Storage and Saving*, *1*, 166–216. https://doi.org/10.1016/j.enss.2022.07.002

Moen, O. M., & Heggset, T. (2021). Initial heat pump concepts and integration principles for SHIP200 targeting heat delivery up to 200 °C (steam cycle) and 250 °C (e.g. CO2 cycle). *Forthcoming Research and Industry for European and National Development of SHIP*. https://friendship-project.eu/wp-content/uploads/2021/11/D31INI1.pdf

Netbeheer Nederland. (2023). *Het energiesysteem van de toekomst: De ii3050-scenario's*. https://open.overheid.nl/documenten/ronl-7219ac2558977a6050ac4db764d2ddebb156df32/pdf

Nuclear Power. (n.d.-a). *Brayton cycle – gas turbine engine*. https://www.nuclear-power.com/nuclear-engineering/thermodynamics/thermodynamic-cycles/brayton-cycle-gas-turbine-engine/

Nuclear Power. (n.d.-b). *Isentropic efficiency – turbine/compressor/nozzle*. https://www.nuclear-power.com/nuclear-engineering/thermodynamics/thermodynamic-processes/isentropic-process/isentropic-efficiency-turbinecompressornozzle/

Oehler, J., Gollasch, J. O., Tran, A. P., & Nicke, E. (2021). Part load capability of a high temperature heat pump with reversed brayton cycle. *13th IEA Heat Pump Conference 2021 (HPC2020) Conference Proceedings*. https://elib.dlr.de/145225/1/HPC2020final_DLR_Oehler_20210114.pdf

Padilla, R. V., Too, Y. C. S., Benito, R., McNaughton, R., & Stein, W. (2016). Thermodynamic feasibility of alternative supercritical co2 brayton cycles integrated with an ejector. *Applied Energy*, *169*, 49–62. https://doi.org/https://doi.org/10.1016/j.apenergy.2016.02.029

Patel, S. (n.d.). *What are supercritical co2 power cycles?* https://www.powermag.com/what-are-supercritical-co2-power-cycles/

PBL. (2022). *Klimaat- en energieverkenning 2022*. https://www.pbl.nl/sites/default/files/downloads/pbl-2022-klimaat-en-energieverkenning-4838.pdf

Pelay, U., Luo, L., Fan, Y., Stitou, D., & Rood, M. (2017). Thermal energy storage systems for concentrated solar power plants. *Renewable and Sustainable Energy Reviews*, *79*, 82–100. https://doi.org/https://doi.org/10.1016/j.rser.2017.03.139

Persichilli, M., Kacludis, A., Zdankiewicz, E., & Held, T. (2012). Supercritical co2 power cycle developments and commercialization: Why sco2 can displace steam. *Power-Gen India Central Asia*. https://www.echogen.com/documents/why-sco2-can-displace-steam.pdf

Powell, K. M., Rashid, K., Ellingwood, K., Tuttle, J., & Iverson, B. D. (2017). Hybrid concentrated solar thermal power systems: A review. *Renewable and Sustainable Energy Reviews*, *80*, 215–237. https://doi.org/https://doi.org/10.1016/j.rser.2017.05.067

Python Core Team. (2019). *Python: A dynamic, open source programming language* [Python version 3.8.10]. Python Software Foundation. https://www.python.org/

Rokni, M. (2016). *Introduction to pinch technology*. Technical University of Denmark. https://backend.orbit.dtu.dk/ws/portalfiles/portal/123620478/Pinch_Tech_1.pdf

Sarbu, I., & Sebarchievici, C. (2018). A comprehensive review of thermal energy storage. *Sustainability*, *10*(1). https://doi.org/10.3390/su10010191

Sarkar, J., Bhattacharyya, S., & Gopal, M. R. (2007). Natural refrigerant-based subcritical and transcritical cycles for high temperature heating. *International Journal of Refrigeration*, *30*, 3–10. https://doi.org/10.1016/j.ijrefrig.2006.03.008

Span, R., & Wagner, W. (1996). A New Equation of State for Carbon Dioxide Covering the Fluid Region from the Triple□Point Temperature to 1100 K at Pressures up to 800 MPa. *Journal of Physical and Chemical Reference Data*, *25*(6), 1509–1596. https://doi.org/10.1063/1.555991

Tafur-Escanta, P., Valencia-Chapi, R., López-Guillem, M., Fierros-Peraza, O., & Muñoz-Antón, J. (2022). Electrical energy storage using a supercritical co2 heat pump. *Energy Reports*, *8*, 502–507. https://doi.org/10.1016/j.egyr.2022.01.073

The Engineering Toolbox. (n.d.). *Carbon dioxide - thermophysical properties*. https://www.engineeringtoolbox.com/CO2-carbon-dioxide-properties-d_2017.html

Turton, R., Shaeiwitz, J. A., Bhattacharyya, D., & Whiting, W. B. (2018). *Analysis, synthesis and design of chemical processes* (5th edition). Pearson Education International.

UNILAB SRL. (2019). *What happens to fluid properties near the critical point? - the case of co2*. https://www.unilab.eu/articles/fluid-properties-near-critical-point/

Wang, S. (2018). Air cycle heat pumps. In R. Wang & X. Zhai (Eds.), *Handbook of energy systems in green buildings* (pp. 1–28). Springer Berlin Heidelberg. https://doi.org/10.1007/978-3-662-49088-4_5-1

White, M. T., Bianchi, G., Chai, L., Tassou, S. A., & Sayma, A. I. (2021). Review of supercritical co2 technologies and systems for power generation. *Applied Thermal Engineering*, *185*, 116447. https://doi.org/https://doi.org/10.1016/j.applthermaleng.2020.116447

Zühlsdorf, B., Bühler, F., Bantle, M., & Elmegaard, B. (2019). Analysis of technologies and potentials for heat pump-based process heat supply above 150 °c. *Energy Conversion and Management: X*, *2*. https://doi.org/10.1016/j.ecmx.2019.100011

Appendix-a: Model validation results

In this appendix the validation of the HTHP and HTHP-EJ model are discussed in more detail. It was chosen to add this as an appendix to improve the readability of the report as the validation was quite extensive. The validation provided some insights but it was not the essence of the study. This was mainly due to the fact that no experimental data was available to perform an accurate validation. Moreover, the validation just confirmed that the numerical HTHP model matched well with comparable numerical studies and Aspen Plus. The application of Aspen Plus to enable realistic modelling of the final HTHP designs was of more significant importance.

Paper by Zuhlsdorf et al. (2019)
As briefly discussed in Section 1.3.3 in the paper by Zuhlsdorf et al. (2019) two HTHP configurations were investigated. One of which was a HTHP based on the reversed Brayton cycle configuration including an IHX. The refrigerant used was sCO_2. As the cycle was operated with pressures between 40.7 bar and 140 bar the sCO_2 was partly in (subcritical) gas phase and partly in supercritical phase. In the paper no description was given of the way the HTHP was modelled but two case studies were mentioned. For the first case study of alumina production enough input parameters were given, including the assumed isentropic efficiencies of the turbomachinery. Additionally, a T-s diagram was provided which was enough to validate the HTHP model. The choice to insert an IHX was not further motivated. However, with a COP of 1.72 the HTHP cycle did not perform very well.

As the HTHP model did not include a IHX the model was adapted slightly and the output parameters needed to include the IHX were adopted from the paper. Moreover, it was mentioned that the source and sink stream had a constant heat capacity but the streams were not further specified (Zühlsdorf et al., 2019). The required mass flow of the source stream could be obtained through the given sCO_2 mass flow. It was provided in the paper that the delivered output power should be 50 MW and the input power could be estimated from the provided temperature-heat diagram at +- 24 MW. Finally, the paper mentioned that the COP was calculated assuming a motor and gear efficiency both of 95% so this was also included in the calculations. The rest of the cycle was modelled as described in Section 3.1. The input parameters used for the validation are summarized in Table 6.1. In Figure 6.1a the T-s diagram as presented in the paper can be found. Additionally, the T-s diagram from the HTHP model is shown with the inputs from Table 6.1 in Figure 6.1b. Dashed lines are used for the streams inside the heat exchangers to indicate that the change in the thermodynamic properties of CO_2 is not actually linear. In practise they follow the shown pressure isobars that represent the actual change in temperature and specific entropy.

Parameter	Value	Unit	Parameter	Value	Unit
$T_{cs,in}$	110	°C	P_{low}	40.7	bar
$T_{cs,out}$	60	°C	P_{high}	140	bar
$T_{hs,in}$	140	°C	$\Delta T_{1,cold}$	7.5	°C
$T_{hs,out}$	280	°C	$\Delta T_{1,hot}$	7.5	°C
T_1	139.9	°C	$\dot{m}_{sCO2}$	278.7	kg/s
T_3	147.5	°C	η_{compr}	75	%
T_6	102.5	°C	η_{turb}	75	%
Q_{in}	+- 24	MW	η_{motor}	95	%
Q_{out}	50	MW	η_{gear}	95	%

Table 6.1: Input parameters for the validation with the paper by Zühlsdorf et al. (2019).

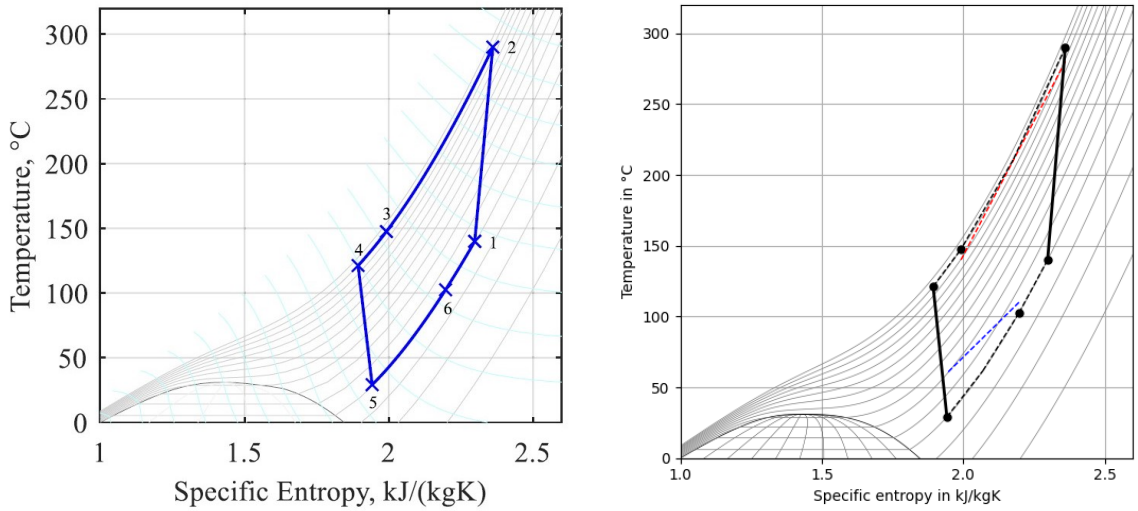

(a) (b)

Figure 6.1: T-s diagram of the $(s)CO_2$ reversed Brayton cycle from the paper by Zühlsdorf et al. (2019) (a) and T-s diagram of the $(s)CO_2$ reversed Brayton cycle HTHP model with the same input parameters (b).

As can be see in Figure 6.1 the T-s diagrams match well. This indicated that the HTHP model was able to successfully reproduce the model from the paper. More detailed output parameters from the HTHP model using these input parameters are given in Table 6.2 below and compared to the values from the paper. The minor differences in output values of all less than 0.5% further confirm that the HTHP model was able to successfully re-generate the values from the paper of Zühlsdorf et al. (2019). The largest deviation of about 0.5 % was observed in the value of Q_{in}. This could be explained by the fact that no exact value was mentioned in the paper. The value of +- 24 MW had to be read-off from a temperature-heat diagram as mentioned earlier. Therefore, it could be concluded that the obtained results served as a good validation of the HTHP model.

Parameter	Value paper	Value HTHP model	Difference	Unit
T_2	290.0	289.93	0.07	°C
T_4	121.2	121.12	0.08	°C
T_5	29.1	29.04	0.06	°C
$\dot{m}_{sCO2}$	278.7	278.72	0.02	kg/s
$\dot{m}_{cs}$	-	267.20	-	kg/s
$\dot{m}_{hs}$	-	159.95	-	kg/s
Q_{in}	+- 24	23.87	+-0.13	MW
Q_{out}	50	49.99	0.01	MW
COP	1.72	1.724	0.004	-
η_{Lorenz}	44	43.91	0.09	%

Table 6.2: Resulting output parameters of the validation with the paper by Zühlsdorf et al. (2019).

On a final note, a few things were observed during the validation that are worth mentioning. First of all, it is illustrated in Figure 6.1b that the heat sink stream is very close to the $(s)CO_2$ stream. This was required to meet the input parameters described in the papers, especially the described inlet- and outlet temperature of the heat sink stream. The detailed calculations even showed that in the middle

of the HEX the temperature difference between the two streams almost reached 0 K while the pinch was 7.5 K. This indicated nonphysical behaviour. Moreover, due to the large required output power of 50 MW the mass flows were substantial as can be seen in Table 6.2. For the heat sink HEX this resulted in a very UA value of 5,774,700 W/K and a NTU of 16.75 despite the large mass flows. This was on the high side and would result in significant costs. In the case of the heat source HEX an UA value of 1,443,900 and a NTU of 4.54 were obtained which was reasonable. Nonetheless, the high UA value indicated an expensive heat exchanger. As the source and sink streams were not further specified in the paper it is not clear if this was something the authors took into account in their design. Moreover, also the interaction of the source and sink streams with the $(s)CO_2$ cycle was unfortunately not further discussed in the paper. In practise this could limit the (cost-)effectiveness of the proposed $(s)CO_2$ reversed Brayton HTHP in the paper.

Paper by Moen and Heggset (2021)
The other paper identified during the literature study that was comparable enough to use for validation was the study done by Moen and Heggset (2021). In this paper a sCO_2 reversed Brayton HTHP was modelled in the program "Modelica". In this paper they specified quite clearly how they modelled the HTHP and the kind of equipment used: a turbocompressor, a gas cooler & gas heater, and an expander (Moen and Heggset, 2021). The gas cooler & gas heater were both modelled as printed-circuit heat exchangers. The design matched well with the HTHP model and no significant adaptions to the model as described in Section 3.1 were required. Moreover, the use of Therminol-66 as HTF for both the source and sink stream was mentioned which also matched well with the HTHP model.

In the paper they presented results based on different source stream inlet temperatures and output powers. A heat source stream inlet temperature of 160 °C and an output power of 12 MW was named as the optimal case. Therefore, it was decided to do the validation with this configuration. Not all parameters were explicitly given. Nevertheless, in combination with the presented T-s diagram all parameters could be estimated accurately enough to use the paper as validation of the HTHP model. The input parameters are presented in Table 6.3. In Figure 6.2a the T-s diagram as presented in the paper is depicted. Additionally, the T-s diagram from the HTHP model using the inputs from Table 6.3 is shown in Figure 6.2b. As mentioned above only the HTHP with a source stream inlet temperature of 160 °C was modelled with the HTHP model. This case is indicated in red in in Figure 6.2a as the legend indicates.

Parameter	Value	Unit	Parameter	Value	Unit
$T_{cs,in}$	160	°C	P_{low}	150	bar
$T_{hs,out}$	240	°C	P_{high}	355.068	bar
T_1	150	°C	P_{cs}	10	bar
$\Delta T_{1,cold}$	10	°C	ΔP_{cs}	6.036	kpa
$\Delta T_{1,hot}$	10	°C	P_{hs}	5	bar
η_{compr}	75	%	ΔP_{hs}	14.465	kpa
η_{turb}	75	%	Q_{out}	12	MW
$\dot{m}_{sCO2}$	97.765	kg/s			
$\dot{m}_{cs}$	146.046	kg/s			

Table 6.3: Input parameters for the validation with the paper by Moen and Heggset (2021).

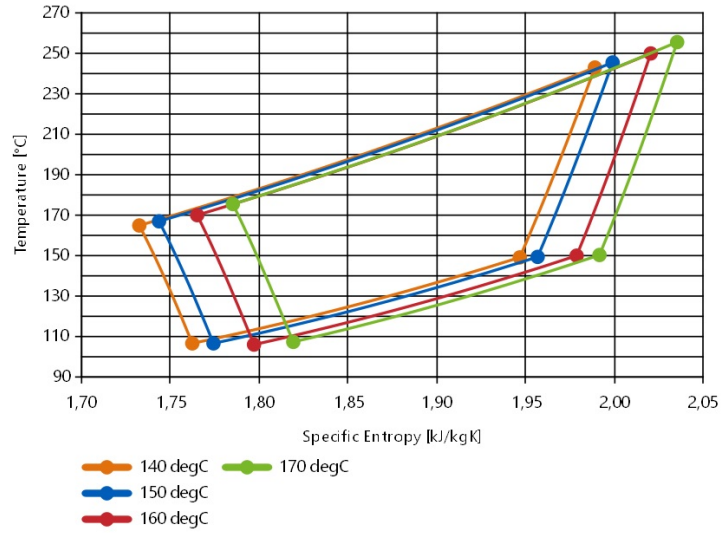

(a)

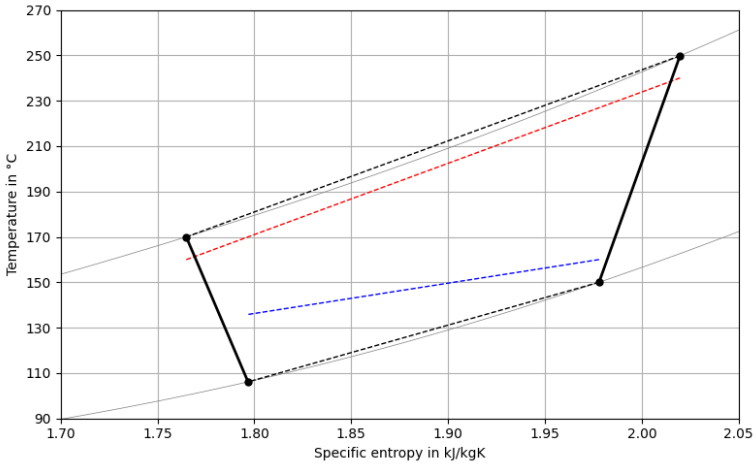

(b)

Figure 6.2: T-s diagram of the sCO_2 reversed Brayton cycle from the paper by Moen and Heggset (2021) (a) and T-s diagram of the sCO_2 reversed Brayton cycle HTHP model with the same input parameters (b).

Similar as with the validation of the Zühlsdorf et al. (2019) paper it can be observed in Figure 6.2 that the T-s diagrams match well. The more detailed outputs as shown in Table 6.4 support the successful validation with only minor differences in the outputs, all less than 0.2 %. The absolute largest differences were observed in the cycle temperatures. For T_3 and T_4 this is explained by the fact that the values from the paper were read-off from the T-s diagram which created a small inaccuracy. The difference observed for T_2 (compressor outlet) was more remarkable as the value of T_1 (compressor inlet) was exactly the same and the same isentropic efficiency was used. This could probably be explained by the way the compressor was modelled in Modelica.

Some concluding remarks on the validation with the paper by Moen and Heggset are mainly related to the heat exchangers interacting with the external HTF streams. The T-s diagram of the HTHP cycle presented in the paper seemed to follow a straight line between state 2 and 3 and state 4 and 1 instead of following the isobar. It was therefore decided to adapt this in the HTHP model but as can be seen in Figure 6.2b this caused quite a significant deviation. It was observed that with the modelling based on the inputs as given in Table 6.3 the value of $\Delta T_{2,hot}$ is with 9.8 °C just below the pinch temperature of 10 °C. In the middle of the HEX the temperature difference between the two streams even reached 6.6 °C if the isobar was followed. As both these temperatures were below the pinch temperature of

Parameter	Value paper	Value HTHP model	Difference	Unit
$T_{cs,out}$	-	135.83	-	°C
$T_{hs,in}$	160	159.974	0.026	°C
T_2	249.948	249.767	0.181	°C
T_3	+-170	169.97	0.026	°C
T_4	+-106	106.12	0.123	°C
$\dot{m}_{sCO2}$	97.765	97.769	0.004	kg/s
$\dot{m}_{cs}$	146.046	146.041	0.005	kg/s
$\dot{m}_{hs}$	68.335	68.242	0.093	kg/s
Q_{in}	7.092	7.082	0.010	MW
Q_{out}	12	11.982	0.018	MW
W_{compr}	8.434	8.420	0.014	MW
W_{turb}	3.526	3.520	0.006	MW
COP	2.44	2.445	0.005	-
COP_{Lorenz}	5.95	5.942	0.008	-

Table 6.4: Resulting output parameters of the validation with the paper by Moen and Heggset (2021).

10 °C this would indicate non-physical behaviour. On the other hand were the HEX modelled in detail in Modelica based on PCME models. Therefore, the general LMTD method as applied in the HTHP model might not provide correct results in this case.

Aspen Plus

The Aspen Plus validation was conducted with the Aspen Plus model as described in Section 3.1.3. All required input parameters were taken from the HTHP model and can be found in Table 6.5 below.

Parameter	Value	Unit	Parameter	Value	Unit
$T_{cs,in}$	150	°C	P_2	320	bar
$T_{hs,in}$	150.2416	°C	P_4	80	bar
T_1	140	°C	$P_{cs,in}$	5	bar
T_{4B}	55.2178	°C	$P_{hs,in}$	5	bar
$\Delta T_{1,cold}$	10	°C	$\dot{m}_{sCO2}$	14.8015	kg/s
$\Delta T_{1,hot}$	15	°C	$\dot{m}_{cs}$	25.0683	kg/s
$\Delta T_{pinch,cold}$	10	°C	$\dot{m}_{hs}$	10.2688	kg/s
$\Delta T_{pinch,hot}$	10	°C			
η_{compr}	80	%			
η_{turb}	90	%			

Table 6.5: Input parameters for the validation of the HTHP model with Aspen Plus.

The final results of the validation of the HTHP model with Aspen Plus are shown in Table 6.6. It could be concluded that the results obtained from the Aspen Plus design match well with the results from the HTHP model and that the Aspen Plus design serves as a good final validation. A few no-

Parameter	Value Aspen Plus model	Value HTHP model	Difference	Unit
$T_{cs,out}$	113.1268	113.1371	0.0103	°C
$T_{hs,out}$	280.0916	280.1028	0.0112	°C
T_2	303.8807	303.8809	0.0002	°C
T_3	165.2416	165.2416	-	°C
T_{4A}	55.2177	55.2178	0.0001	°C
P_1	79.9732	79.9732	-	bar
P_3	319.8964	319.8964	-	bar
$P_{cs,out}$	4.9478	4.9478	-	bar
$P_{hs,out}$	4.6471	4.6471	-	bar
Q_{in}	1.8006	1.8006	-	MW
Q_{out}	3.0009	3.0009	-	MW
W_{compr}	2.1071	2.1071	-	MW
W_{turb}	0.9068	0.9068	-	MW
COP	2.5001	2.5001	-	-
UA_{cold}	58,834	66,000	+7166	W/K
U_{cold}	123.119	300	176.881	W/m^2K
A_{cold}	480.021	220	260.021	m^2
UA_{hot}	221,308	157500	-63808	W/K
U_{hot}	347.711	300	47.711	W/m^2K
A_{hot}	638.424	525	113.424	m^2

Table 6.6: Resulting output parameters for the validation of the HTHP model with Aspen Plus.

table differences were observed which are interesting to discuss briefly. First of all, there was a small difference of less than 0.01 % observed in the heat source and heat sink stream outlet temperatures. The reason for this was not exactly certain but all temperatures of the sCO_2 showed little to no difference. Therefore, the best guess was that the use of the NRTL property method for the Therminol-66 compared to the use of CoolProp in the HTHP model was responsible for this. The small mismatch in $T_{4A}$was caused by the earlier explained iteration process of the pressure drops in the HTHP model but with a difference of less than 0.0002 % this can be considered insignificant.

What was however most interesting to observe were the differences in the outputs of the heat exchangers, which was quite significant. It was found that the cause for the difference in the UA values lay in the fact that the LMTD method in the HTHP model did not consider any correction factors while the Aspen EDR model did. This correction factor was given by Aspen Plus and if the UA value from the Aspen Plus model was multiplied with this value it produces the UA value from the HTHP model. The result of this was that, depending on if this correction factor was larger or smaller than 1, the HTHP model either over- or underestimated the actual UA value. In this case the UA value for the heat source (cold) HEX was slightly underestimated while the UA value for the heat sink (hot) HEX was largely underestimated. This shows the relevance of designing the heat exchangers with Aspen EDR to obtain realistic HEX designs compared to the very general design in the HTHP model.

As already indicated in Section 3.1.3 the value of U was initially estimated in the range of 200-400 W/m^2K and set at 300 W/m^2K in the HTHP model. Hence the difference with the Aspen Plus design was not surprising although it can be seen that for the heat sink (hot) HEX the actual U value was close. For the heat source (cold) HEX the value of 123.119 W/m^2K is on the low side compared to the range of 200-400 W/m^2K. As it is not exactly known how Aspen Plus calculates this value it was difficult to have a definitive explanation. However, in the book by Sinnott & Towler it is indicated that hot

heat transfer oil combined with gas at high pressure is able to result in U values of around 300 W/m^2K. On the other hand, hot heat transfer oil combined with gas at low pressure should result in U values of around 100-150 W/m^2K. It could well be that sCO_2 at pressures close or below the critical point is considered a low pressure gas and that only at pressures far above the critical pressure sCO_2 can be considered a high pressure gas.

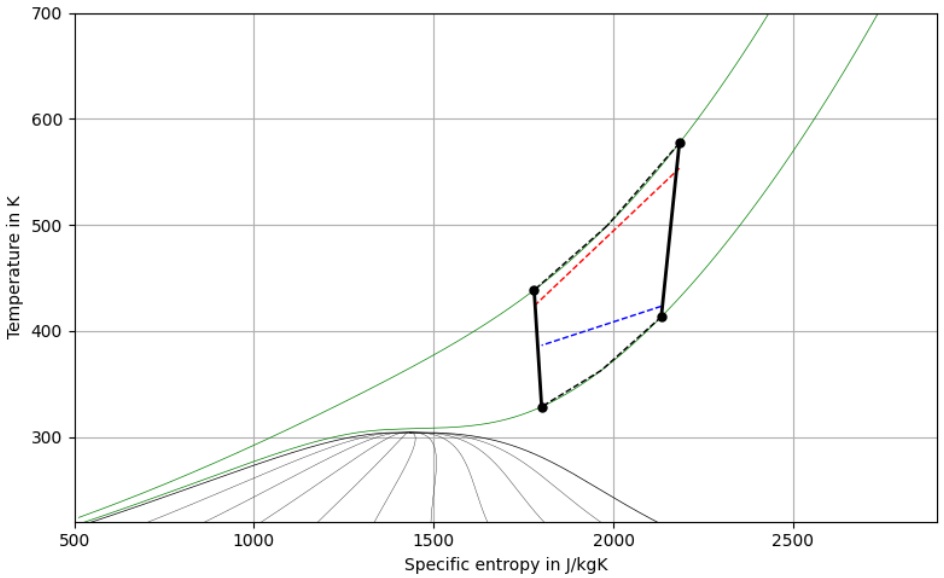

Figure 6.3: T-s plot of the HTHP cycle used for the Aspen validation.

To conclude the validation of the HTHP model with Aspen Plus the temperature profiles inside the heat exchangers also showed good resemblance. This is illustrated through the T-s diagram of the HTHP model including the heat source stream (blue) and heat sink stream (red) in Figure 6.3 and the T-Q diagrams of the heat source (cold) HEX in Figure 6.4(a) and the heat sink (hot) HEX in Figure 6.4(b). Aspen EDR also gave no warnings or errors as can be seen in Figure 6.5.

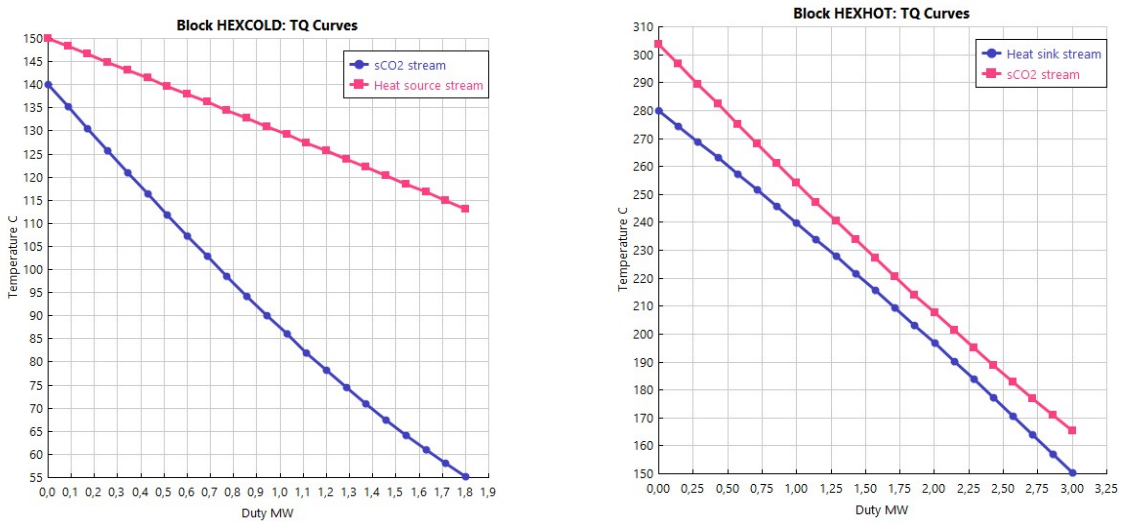

(a) **(b)**

Figure 6.4: T-Q plots for the temperature profile inside the heat source HEX (a) and the heat sink HEX (b) for the HTHP cycle.

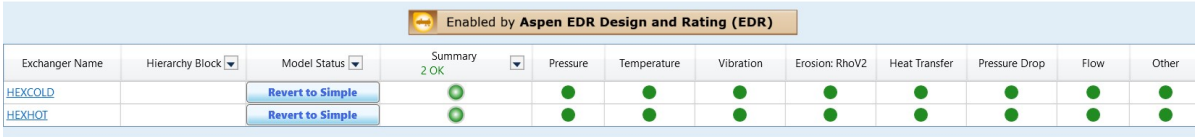

Figure 6.5: Aspen EDR exchanger summary table for the two heat exchangers in the HTHP cycle for the Aspen validation

The validation of the HTHP-EJ model with Aspen Plus was done with the same steps as for the HTHP model with the exception that also inputs from the HTHP model were given to the Splitter (entrainment ratio) and the Mixer (ejector outlet pressure) and that the properties of the sCO_2 stream were given at the compressor inlet ("CO2-EB") due to the split at that location. Again, all required input parameters were taken from the HTHP-EJ model and can be found in Table 6.7 below.

Parameter	Value	Unit	Parameter	Value	Unit
$T_{cs,in}$	150	°C	P_2	345	bar
$T_{hs,in}$	184.9944	°C	P_4	71	bar
T_1	140	°C	$P_{cs,in}$	5	bar
T_{EB}	165.7753	°C	$P_{hs,in}$	5	bar
$\Delta T_{1,cold}$	10	°C	P_{EB}	116.9085	bar
$\Delta T_{1,hot}$	15	°C	$\dot{m}_{sCO2,tot}$	21.8968	kg/s
$\Delta T_{pinch,cold}$	10	°C	$\dot{m}_{cs}$	23.1363	kg/s
$\Delta T_{pinch,hot}$	10	°C	$\dot{m}_{hs}$	13.6122	kg/s
η_{compr}	80	%	ω	5	-
η_{turb}	90	%			

Table 6.7: Input parameters for the validation of the HTHP-EJ model with Aspen Plus.

To match the pressures in the HTHP-EJ model and the Aspen Plus design was unfortunately more difficult due to the inherent difference before and after the split. This caused some larger deviations between the HTHP-EJ model and the Aspen Plus design as can be seen along with the other outputs in Table 6.8.
The obtained outputs from the Aspen Plus HTHP-EJ design show largely the same differences as were observed in the validation of of the HTHP model. Such as the differences in the outlet temperatures of the heat source stream and heat sink stream. The main difference with the validation of the HTHP model are the differences in the pressures. As said earlier this was due the fact that it was more difficult to match this in the HTHP-EJ model and the Aspen Plus design than it was for the HTHP model. Nonetheless, the differences were all within a margin of 0.5% so the outputs still match relatively well, especially looking at the import output parameters like the output power and COP. It can clearly be seen that although the Mixer component is able to realize the output pressure from the HTHP-EJ model, the output temperature differs significantly.

With regard to the heat exchangers two interesting observations were done. Firstly, while the operating conditions of the sCO_2 stream are largely similar and the pressure is even below the critical pressure in the HTHP-EJ model the U value of the heat source (cold) HEX is significantly higher. Both for the heat source (cold) HEX and the heat sink (hot) HEX the U value is above the estimated range of 200-400 W/m^2K resulting in smaller heat exchange surface areas than estimated HTHP-EJ model. It was not certain what caused these higher U values compared to the validation of the HTHP model as the heat exchangers were modelled exactly the same.

Parameter	Value Aspen Plus model	Value HTHP-EJ model	Difference	Unit
$T_{cs,out}$	110.9424	110.9009	0.042	°C
$T_{hs,out}$	280.2041	280.2295	0.0254	°C
T_2	295.5320	295.5320	-	°C
T_3	199.9944	199.9944	-	°C
T_4	65.3229	65.3126	0.010	°C
T_{EA}	157.0955	165.7753	8.6798	°C
P_1	70.5519	70.3023	0.2496	bar
P_3	344.7732	344.830	0.0568	bar
P_{EA}	116.9085	116.9085	-	bar
$P_{cs,out}$	4.7815	4.75702	0.0245	bar
$P_{hs,out}$	4.5401	4.60572	0.0656	bar
Q_{in}	1.7568	1.7594	0.0026	MW
Q_{out}	2.9996	2.9998	0.0027	MW
W_{compr}	2.4951	2.4951	-	MW
W_{turb}	1.4965	1.4965	-	MW
COP	3.0035	3.0040	0.0005	-
UA_{cold}	93,841	75,000	-18,841	W/K
U_{cold}	450.594	300	150.594	W/m^2K
A_{cold}	210.590	250	39.410	m^2
UA_{hot}	235,260	198,000	-37,260	W/K
U_{hot}	504.896	300	204.896	W/m^2K
A_{hot}	472.846	660	187.154	m^2

Table 6.8: Resulting output parameters for the validation of the HTHP-EJ model with Aspen Plus.

The only noticeable difference was the temperature difference of the sCO_2 stream inside the heat source (cold) HEX (84.78 °C in the HTHP model versus 74.58 °C in the HTHP-EJ model) and inside the heat sink (hot) HEX (138.64 °C in the HTHP model versus 95.54 °C in the HTHP-EJ model). Also the mass flow of the sCO_2 stream was is significantly higher for the HTHP-EJ cycle. It could be well be that this enhances the heat transfer hence increase the overall heat transfer coefficient U.
Secondly, in this case the HTHP-EJ model underestimated the UA value for both heat exchangers. This shows that there is not necessarily a pattern in over- or underestimation of the UA value but that it fully depends on the exact operating conditions of the HEX and the stream properties and it is very useful that Aspen EDR is able to make accurate predictions for this. Also for the HTHP-EJ model the temperature profiles inside the heat exchangers match well with the Aspen Plus design as illustrated in Figure 6.6 and Figure 6.4.

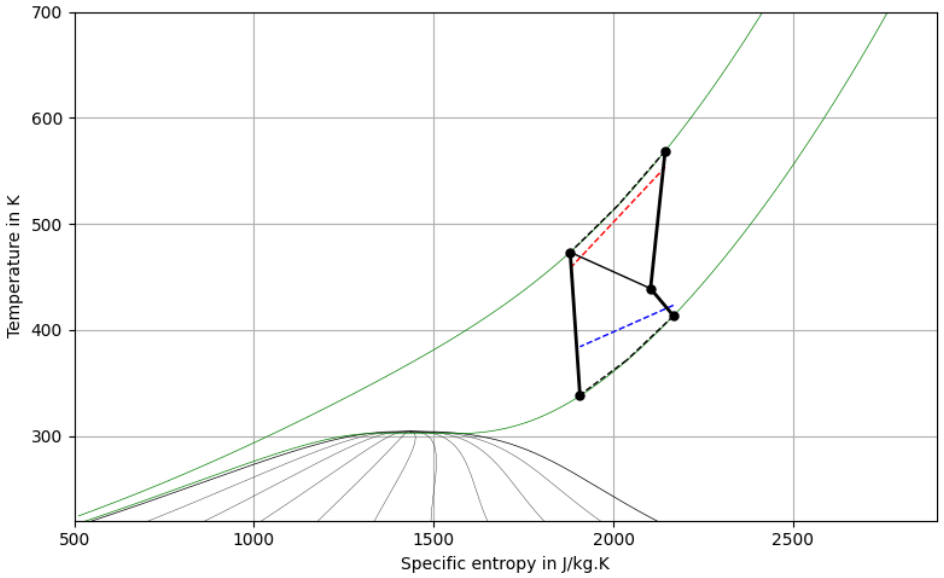

Figure 6.6: T-s plot of the HTHP-EJ cycle used for the Aspen validation

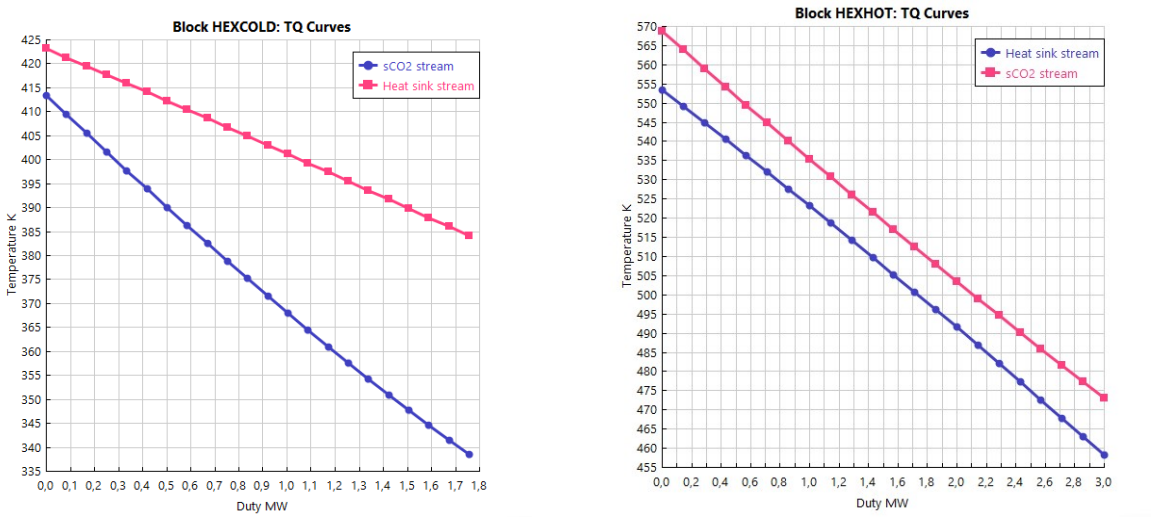

(a) **(b)**

Figure 6.7: T-Q plots for the temperature profile inside the heat source HEX (a) and the heat sink HEX (b) for the HTHP-EJ cycle

In conclusion, it was seen that for the HTHP model the validation with Aspen Plus showed satisfactory results with only very minor differences in terms of output parameters. On the other hand, it had to be concluded that for the validation of the HTHP-EJ model Aspen Plus was less useful. This was mainly due to not being able to validate the ejector, being the most important component of the HTHP-EJ cycle. It could still be used to validate the other components in the cycle but as these were largely similar to the components used in the HTHP cycle did not provide a lot of additional information.

Appendix-b: Python codes

HTHP model Python code

```
"""

@author: Koen Verloop

"""
import CoolProp.CoolProp as CP
from CoolProp.Plots import PropertyPlot
import numpy as np
from scipy.optimize import root_scalar
import matplotlib.pyplot as plt

##Define pressure isobars -> the compressor and turbine pressure ratio used
P1 = 85.4114*1e5   #Pressure at state 1 (compressor inlet) in Pa
P2 = 342*1e5  #Pressure at state 2 (compressor outlet) in Pa
P3 = 341.901*1e5  #Pressure at state 3 (turbine inlet) in Pa
P4 = 86*1e5   #Pressure at state 4 (turbine outlet) in Pa

#%% 1st loop based on ideal turbomachinery (i is for ideal and used to store certain values of the ideal cycle)

##Heat source counter-current HEX (cold HEX)
U_HEX_coldi = 300   #Overall heat transfer coefficient of the cold HEX in W/m2.K
A_HEX_coldi = 320   #Heat transfer area of cold HEX in m2
UA_HEX_coldi = U_HEX_coldi*A_HEX_coldi #Heat transfer coefficient of the cold HEX in W/K
m_csi = 16.70            #Mass flow of the heat source/cold stream (cs) in kg/s
T_cs_ini = 273.15+150   #Inlet temperature of the heat source/cold stream (cs) into cold HEX in K
T_cs_outi = T_cs_ini-60 #Outlet temperature of the heat source/cold stream (cs) leaving cold HEX in K
P_cs_in = 5*1e5         #Inlet pressure of the heat source/cold stream (cs) into cold HEX in Pa
P_cs_out = 4.75678*1e5        #Outlet pressure of the heat source/cold stream (cs) leaving cold HEX in Pa
h_cs_in = CP.PropsSI('H','P',P_cs_in,'T',T_cs_ini,'INCOMP::T66')    #Specific enthalpy of heat source/cold stream (cs) into cold HEX in J/kg
h_cs_out = CP.PropsSI('H','P',P_cs_out,'T',T_cs_outi,'INCOMP::T66') #Specific enthalpy of the heat source/cold stream (cs) leaving cold HEX in J/kg
cp_oil_csi = CP.PropsSI('C','P',(P_cs_in+P_cs_out)/2,'T',(T_cs_ini + T_cs_outi)/2,'INCOMP::T66') #Constant pressure specific heat capacity of the heat source/cold stream (cs) in cold HEX in J/kg.K
Q_HEX_coldi = m_csi*(h_cs_in-h_cs_out) #Heat rejected by the heat source/cold stream (cs) in the cold HEX in W

#LMTD method to find T1 and T4 with set pinch temperature -> dT1 chosen as pinch to minimize the required temperature lift
dT_m_coldi = Q_HEX_coldi/(UA_HEX_coldi) #Mean temperature difference in cold HEX in K
dT1_coldi = 10            #Terminal temperature difference 1 of cold HEX (pinch) in K
T1i = T_cs_ini-dT1_coldi  #Temperature at state 1 (compressor inlet) in K
def equation(dT2_coldi):
    return (dT1_coldi - dT2_coldi)/np.log(dT1_coldi/dT2_coldi)-dT_m_coldi
result = root_scalar(equation, bracket=[0.1, 1000])
dT2_coldi = result.root     #Terminal temperature difference 2 of cold HEX in K
T4i = T_cs_outi - dT2_coldi #Temperature at state 4 (compressor outlet) in K


##Thermodynamic properties at state 1 (compressor inlet) -> part of cold HEX so calculate first
s1i = CP.PropsSI('S','P',P1,'T',T1i,'CO2') #Specific entropy of sCO2 at state 1 in J/kg.K
h1i = CP.PropsSI('H','P',P1,'T',T1i,'CO2') #Specific enthalpy of sCO2 at state 1 in J/kg

##Thermodynamic properties at state 4 (turbine outlet) -> part of cold HEX so calculate first
```

```
s4i = CP.PropsSI('S','P',P4,'T',T4i,'CO2') #Specific entropy of sCO2 at state 4 in J/kg.K
h4i = CP.PropsSI('H','P',P4,'T',T4i,'CO2') #Specific enthalpy of sCO2 at state 4 in J/kg

##Thermodynamic properties at state 2 (compressor outlet)
s2i = s1i #Specific entropy of sCO2 at state 2 in J/kg.K
T2i = CP.PropsSI('T','P',P2,'S',s2i,'CO2') #Temperature of sCO2 at state 2 in K
h2i = CP.PropsSI('H','P',P2,'S',s2i,'CO2') #Specific enthalpy of sCO2 at state 2 in J/kg

##Thermodynamic properties at state 3 (turbine inlet)
s3i = s4i #Specific entropy of sCO2 at state 3 in J/kg.K
T3i = CP.PropsSI('T','P',P3,'S',s3i,'CO2') #Temperature of sCO2 at state 3 in K
h3i = CP.PropsSI('H','P',P3,'S',s3i,'CO2') #Specific enthalpy of sCO2 at state 3 in J/kg

##Mass flow of sCO2 -> assumed to stay constant throughout the HP cycle
m_sCO2i = Q_HEX_coldi /(h1i-h4i) #Mass flow of sCO2 inside the ideal HP cycle in kg/s

##Compressor with isentropic efficiency
eta_compr = 0.8 #Isentropic efficiency of the compressor, value ranges between 0.6 and 0.8
h2_r = h1i + (h2i-h1i)/eta_compr #Real specific enthalpy of sCO2 at state 2 in J/kg
T2_r = CP.PropsSI('T','P',P2,'H',h2_r,'CO2') #Real temperature of sCO2 at state 2 in K
s2_r = CP.PropsSI('S','P',P2,'T',T2_r,'CO2') #Real specific entropy of sCO2 at state 2 in J/
    kg.K

##Turbine with isentropic efficiency
eta_turb = 0.9 #Isentropic efficiency of the turbine, value ranges between 0.7 and 0.9
h4_r = h3i - eta_turb*(h3i-h4i) #Real specific enthalpy of sCO2 at state 4 in J/kg
T4_r = CP.PropsSI('T','P',P4,'H',h4_r,'CO2') #Real temperature of sCO2 at state 4 in K
s4_r = CP.PropsSI('S','P',P4,'T',T4_r,'CO2') #Real specific entropy of sCO2 at state 4 in J/
    kg.K


##NTU effectiveness method check cold HEX
cp_sCO2_41i = CP.PropsSI('C','P',(P1+P4)/2,'T',((T1i+T4i)/2),'CO2') #Average constant
    pressure specific heat capacity of the sCO2 inside the cold HEX in J/kgK
mcp_csi = m_csi*cp_oil_csi           #Heat capacity flow rate of the heat source/cold stream
    (cs) in the cold HEX in W.K
mcp_sCO2_coldi = m_sCO2i*cp_sCO2_41i #Heat capacity flow rate of the sCO2 in the cold HEX in
    W.K
C_min_coldi = min(mcp_csi,mcp_sCO2_coldi) #Minimum heat capacity flow rate in the cold HEX in
     W.K
C_max_coldi = max(mcp_csi,mcp_sCO2_coldi) #Maximum heat capacity flow rate in the cold HEX in
     W.K
Cr_coldi = C_min_coldi/C_max_coldi       #Ratio between min and max heat capacity flow rate
    in the cold HEX
q_max_coldi = C_min_coldi*(T_cs_ini-T4i) #Maximum heat transferred between heat source/cold
    stream (cs) and sCO2 in the cold HEX in W
q_coldi = mcp_csi*(T_cs_ini-T_cs_outi)   #Heat rejected by heat source/cold stream (cs) in
    the cold HEX in W
epsilon_coldi = q_coldi/q_max_coldi      #Effectiveness of the cold HEX
NTU_coldi = UA_HEX_coldi/C_min_coldi     #Number of transfer units (NTU) of the cold HEX,
    ideally between 3-4

#Extra check for pinch temperature in the middle of the cold HEX
s41_mid = (s1i+s4i)/2 #Specific entropy of sCO2 in the middle of the cold HEX in J/kg.K
T41_mid = CP.PropsSI('T','P',(P1+P4)/2,'S',s41_mid,'CO2') #Temperature of sCO2 in the middle
    of the cold HEX in K
T_cs_mid = (T_cs_ini+T_cs_outi)/2 #Temperature of the heat source/cold stream (cs) in the
    middle of the cold HEX in K
dTmid_coldi = T_cs_mid-T41_mid    #Temperature difference in the middle of the cold HEX


#%% 2nd loop based on real turbomachinery (isentropic efficiencies taken into account)

##Updated temperatures for the 2nd loop
T1 = T1i  #Temperature of sCO2 at state 1 in K
T2 = T2_r #Temperature of sCO2 at state 2 in K
T3 = T3i  #Temperature of sCO2 at state 3 in K
T4 = T4_r #Temperature of sCO2 at state 4 in K

#Thermodynamic properties at state 1 (compressor inlet)
s1 = CP.PropsSI('S','P',P1,'T',T1,'CO2') #Specific entropy of sCO2 at state 1 in J/kg.K
```

```
h1 = CP.PropsSI('H','P',P1,'T',T1,'CO2') #Specific enthalpy of sCO2 at state 1 in J/kg
cp_sCO2_1 = CP.PropsSI('C','P',P1,'T',T1,'CO2') #Constant pressure specific heat capacity of sCO2 at state 1 in J/kg.K
cv_sCO2_1 = CP.PropsSI('O','P',P1,'T',T1,'CO2') #Constant volume specific heat capacity of sCO2 at state 1 in J/kg.K
kappa_1 = cp_sCO2_1/cv_sCO2_1  #Heat capacity ratio of sCO2 at state 1
rho_sCO2_1 = CP.PropsSI('D','P',P1,'T',T1,'CO2') #Density of sCO2 at state 1 in kg/m3

#Thermodynamic properties at state 2 (compressor outlet)
h2 = CP.PropsSI('H','P',P2,'T',T2,'CO2') #Specific enthalpy of sCO2 at state 2 in J/kg
s2 = CP.PropsSI('S','P',P2,'T',T2,'CO2') #Specific entropy of sCO2 at state 2 in J/kg.K
cp_sCO2_2 = CP.PropsSI('C','P',P2,'T',T2,'CO2') #Constant pressure specific heat capacity of sCO2 at state 2 in J/kg.K
cv_sCO2_2 = CP.PropsSI('O','P',P2,'T',T2,'CO2') #Constant volume specific heat capacity of sCO2 at state 2 in J/kg.K
kappa_2 = cp_sCO2_2/cv_sCO2_2  #Heat capacity ratio of sCO2 at state 2
rho_sCO2_2 = CP.PropsSI('D','P',P2,'T',T2,'CO2') #Density of sCO2 at state 2 in kg/m3

#Thermodynamic properties at state 3 (turbine inlet)
h3 = CP.PropsSI('H','P',P3,'T',T3,'CO2') #Specific enthalpy of sCO2 at state 3 in J/kg
s3 = CP.PropsSI('S','P',P3,'T',T3,'CO2') #Specific entropy of sCO2 at state 3 in J/kg.K
cp_sCO2_3 = CP.PropsSI('C','P',P3,'T',T3,'CO2') #Constant pressure specific heat capacity of sCO2 at state 3 in J/kg.K
cv_sCO2_3 = CP.PropsSI('O','P',P3,'T',T3,'CO2') #Constant volume specific heat capacity of sCO2 at state 3 in J/kg.K
kappa_3 = cp_sCO2_3/cv_sCO2_3  #Heat capacity ratio of sCO2 at state 3
rho_sCO2_3 = CP.PropsSI('D','P',P3,'T',T3,'CO2') #Density of sCO2 at state 3 in kg/m3

#Thermodynamic properties at state 4 (turbine outlet)
s4 = CP.PropsSI('S','P',P4,'T',T4,'CO2') #Specific entropy of sCO2 at state 4 in J/kg.K
h4 = CP.PropsSI('H','P',P4,'T',T4,'CO2') #Specific enthalpy of sCO2 at state 4 in J/kg
cp_sCO2_4 = CP.PropsSI('C','P',P4,'T',T4,'CO2') #Constant pressure specific heat capacity of sCO2 at state 4 in J/kg.K
cv_sCO2_4 = CP.PropsSI('O','P',P4,'T',T4,'CO2') #Constant volume specific heat capacity of sCO2 at state 4 in J/kg.K
kappa_4 = cp_sCO2_4/cv_sCO2_4  #Heat capacity ratio of sCO2 at state 4
rho_sCO2_4 = CP.PropsSI('D','P',P4,'T',T4,'CO2') #Density of sCO2 at state 4 in kg/m3


##Mass flow of sCO2 -> assumed to stay constant throughout the HP cycle
m_sCO2 = m_sCO2i #Mass flow of sCO2 inside the real HP cycle (same as in the ideal HP cycle) in kg/s

#Updated exchange of energy with the heat source
Q_HEX_cold = m_sCO2*(h1-h4) #Heat absorbed from the heat source/cold stream (cs) in the cold HEX in W


##Energy in and out the HP system
Q_in = m_sCO2*(h1-h4)    #Heat absorbed from the heat source/cold stream (cs) in W
Q_out = m_sCO2*(h2-h3)   #Heat rejected to the heat sink/hot stream (hs) in W
W_compr = m_sCO2*(h2-h1) #Energy (work) needed to compress the sCO2 in W
W_turb = m_sCO2*(h3-h4)  #Energy (work) obtained by expanding the sCO2 in W


##Heat source counter-current HEX (cold HEX)
U_HEX_cold = 611 #Overall heat transfer coefficient of the cold HEX in W/m2.K
A_HEX_cold = 157 #Heat transfer area of cold HEX in m2
UA_HEX_cold = U_HEX_cold*A_HEX_cold #Heat transfer coefficient of the cold HEX in W/K

#LMTD method to find heat source/cold stream (cs) properties with set pinch temperature -> dT1 chosen as pinch to minimize the required temperature lift
dT_m_cold = Q_HEX_cold/(UA_HEX_cold) #Mean temperature difference in cold HEX in K
dT1_cold = 10          #Terminal temperature difference 1 of cold HEX (pinch) in K
T_cs_in = T1+dT1_cold  #Inlet temperature of the heat source/cold stream (cs) into cold HEX in K
def equation(dT2_cold):
    return (dT1_cold - dT2_cold)/np.log(dT1_cold/dT2_cold)-dT_m_cold
result = root_scalar(equation, bracket=[0.1, 1000])
dT2_cold = result.root   #Terminal temperature difference 2 of cold HEX in K
```

```
T_cs_out = T4 + dT2_cold #Outlet temperature of the heat source/cold stream (cs) leaving cold HEX in K

#Updated mass flow of the heat source/cold stream (cs)
cp_oil_cs = CP.PropsSI('C','P',(P_cs_in+P_cs_out)/2,'T',(T_cs_in + T_cs_out)/2,'INCOMP::T66') #Constant pressure specific heat capacity of the heat source/cold stream (cs) inside cold HEX in J/kg.K
h_cs_in = CP.PropsSI('H','P',P_cs_in,'T',T_cs_in,'INCOMP::T66')    #Specific enthalpy of the heat source/cold stream (cs) into cold HEX in J/kg
h_cs_out = CP.PropsSI('H','P',P_cs_out,'T',T_cs_out,'INCOMP::T66') #Specific enthalpy of the heat source/cold stream (cs) leaving cold HEX in J/kg
m_cs = Q_HEX_cold/(h_cs_in-h_cs_out) #Mass flow of the heat source/cold stream (cs) in kg/s


##Heat sink counter-current HEX (hot HEX)
U_HEX_hot = 347 #Overall heat transfer coefficient of the hot HEX in W/m2.K
A_HEX_hot = 465 #Heat transfer area of hot HEX in m2
UA_HEX_hot = U_HEX_hot*A_HEX_hot #Heat transfer coefficient of the hot HEX in W/K

#LMTD method to find hot stream inlet and outlet temperature with set pinch temperature -> dT2 chosen as pinch to allow optimization of the HEX in terms of NTU and effectiveness
dT_m_hot = Q_out/(UA_HEX_hot) #Mean temperature difference in hot HEX in K
dT2_hot = 15          #Terminal temperature difference 2 of hot HEX (pinch) in K
T_hs_in  = T3-dT2_hot #Inlet temperature of the heat sink/hot stream (hs) into hot HEX in K
def equation(dT1_hot):
    return (dT1_hot - dT2_hot)/np.log(dT1_hot/dT2_hot) - dT_m_hot
result = root_scalar(equation, bracket=[0.1, 1000])
dT1_hot = result.root #Terminal temperature difference 1 of hot HEX in K
T_hs_out = T2-dT1_hot #Outlet temperature of the heat sink/hot stream (hs) leaving hot HEX in K
P_hs_in = 5*1e5  #Pressure of the heat sink/hot stream (hs) into hot HEX in Pa
P_hs_out = 4.65341*1e5 #Pressure of the heat sink/hot stream (hs) leaving hot HEX in Pa
h_hs_in = CP.PropsSI('H','P',P_hs_in,'T',T_hs_in,'INCOMP::T66')   #Specific enthalpy of the heat sink/hot stream (hs) into hot HEX in J/kg
h_hs_out = CP.PropsSI('H','P',P_hs_out,'T',T_hs_out,'INCOMP::T66') #Specific enthalpy of the heat sink/hot stream (hs) leaving hot HEX in J/kg
cp_oil_hs = CP.PropsSI('C','P',(P_hs_in+P_hs_out)/2,'T',(T_hs_in + T_hs_out)/2,'INCOMP::T66') #Constant pressure specific heat capacity of the heat sink/hot stream (hs) in hot HEX in J/kg.K
m_hs = Q_out/(h_hs_out-h_hs_in)    #Mass flow of the heat sink/hot stream (hs) in kg/s
Q_HEX_hs = m_hs*(h_hs_out-h_hs_in) #Heat absorbed by the heat sink/hot stream (hs) inside the hot HEX in W


##NTU effectiveness method check cold HEX
cp_sCO2_41 = CP.PropsSI('C','P',(P1+P4)/2,'T',((T1+T4)/2),'CO2') #Average constant pressure specific heat capacity of the sCO2 inside the cold HEX in J/kgK
mcp_cs = m_cs*cp_oil_cs           #Heat capacity flow rate of the heat source/cold stream (cs) in the cold HEX in W.K
mcp_sCO2_cold = m_sCO2*cp_sCO2_41 #Heat capacity flow rate of the sCO2 in the cold HEX in W.K
C_min_cold = min(mcp_cs,mcp_sCO2_cold) #Minimum heat capacity flow rate in the cold HEX in W.K
C_max_cold = max(mcp_cs,mcp_sCO2_cold) #Maximum heat capacity flow rate in the cold HEX in W.K
Cr_cold = C_min_cold/C_max_cold       #Ratio between min and max heat capacity flow rate in the cold HEX
q_max_cold = C_min_cold*(T_cs_in-T4) #Maximum heat transferred between heat source/cold stream (cs) and sCO2 in the cold HEX in W
q_cold = mcp_cs*(T_cs_in-T_cs_out)   #Heat rejected by heat source/cold stream (cs) in the cold HEX in W
epsilon_cold = q_cold/q_max_cold     #Effectiveness of the cold HEX
NTU_cold = UA_HEX_cold/C_min_cold    #Number of transfer units (NTU) of the cold HEX, ideally between 3-4

#Extra check for pinch temperature in the middle of the cold HEX
s41_mid = (s1+s4)/2 #Specific entropy of sCO2 in the middle of the cold HEX in J/kg.K
T41_mid = CP.PropsSI('T','P',(P1+P4)/2,'S',s41_mid,'CO2') #Temperature of sCO2 in the middle of the cold HEX in K
T_cs_mid = (T_cs_in+T_cs_out)/2 #Temperature of the heat source/cold stream (cs) in the middle of the cold HEX in K
dTmid_cold = T_cs_mid-T41_mid   #Temperature difference in the middle of the cold HEX
```

```
215
216
217 ##NTU effectiveness method check hot HEX
218 cp_sCO2_23 = CP.PropsSI('C','P',(P2+P3)/2,'T',((T2+T3)/2),'CO2') #Average constant pressure
    specific heat capacity of the sCO2 inside the hot HEX in J/kg.K
219 mcp_hs  = m_hs*cp_oil_hs         #Heat capacity flow rate of the heat sink/hot stream (hs) in
     the hot HEX in W.K
220 mcp_sCO2_hot = m_sCO2*cp_sCO2_23 #Heat capacity flow rate of the sCO2 in the hot HEX in W.K
221 C_min_hot = min(mcp_hs,mcp_sCO2_hot) #Minimum heat capacity flow rate in the hot HEX in W.K
222 C_max_hot = max(mcp_hs,mcp_sCO2_hot) #Maximum heat capacity flow rate in the hot HEX in W.K
223 Cr_hot = C_min_hot/C_max_hot       #Ratio between min and max heat capacity flow rate in the
    hot HEX
224 q_max_hot = C_min_hot*(T2-T_hs_in) #Maximum heat transferred between heat sink/hot stream (hs
    ) and sCO2 in the hot HEX in W
225 q_hot = mcp_hs*(T_hs_out-T_hs_in)  #Heat rejected by heat sink/hot stream (hs) in the hot HEX
     in W
226 epsilon_hot = q_hot/q_max_hot      #Effectiveness of the hot HEX
227 NTU_hot = UA_HEX_hot/C_min_hot     #Number of transfer units (NTU) of the hot HEX, ideally
    between 3-4
228
229 #Extra check for pinch temperature inside the heat sink (hot) HEX
230 s23_mid = s3+(s2-s3)/2 #Specific entropy of sCO2 in the middle of the hot HEX in J/kg.K
231 T23_mid = CP.PropsSI('T','P',(P2+P3)/2,'S',s23_mid,'CO2') #Temperature of sCO2 in the middle
    of the hot HEX in K
232 T_hs_mid = T_hs_in+(T_hs_out-T_hs_in)/2 #Temperature of the heat sink/hot stream (hs) in the
    middle of the hot HEX in K
233 dTmid_hot = T23_mid-T_hs_mid    #Temperature difference in the middle of the hot HEX
234
235 s23_quarter = s3+(s2-s3)/4 #Specific entropy of sCO2 at 1/4th of the hot HEX in J/kg.K
236 T23_quarter = CP.PropsSI('T','P',(P2+P3)/2,'S',s23_quarter,'CO2') #Temperature of sCO2 at 1/4
    th of the hot HEX in K
237 T_hs_quarter = T_hs_in+(T_hs_out-T_hs_in)/4 #Temperature of the heat sink/hot stream (hs) at
    1/4th of the hot HEX in K
238 dTquarter_hot = T23_quarter-T_hs_quarter    #Temperature difference at 1/4th of the hot HEX
239
240 #%% Final outputs HTHP model
241
242 ##Some general output variables
243 dT12 = T2-T1; #Temperature increase over the compressor in K
244 dT34 = T4-T3; #Temperature decrease over the turbine in K
245 Pressure_ratio = P2/P1  #Pressure ratio in the compressor (same for the turbine)
246 T_HP_output = T_hs_out-273.15 #HTHP output temperature in degrees Celsius
247 Q_output = Q_HEX_hs/1e6 #Total heat delivered to the heat sink/hot stream (hs) in MW
248
249 ##Calculate efficiencies & COP
250 COP = Q_HEX_hs/(W_compr-W_turb)  #COP of the HTHP, wher the turbine is used to power the
    compressor so Wcompr-Wturb
251 COP_Carnot = ((T_hs_out-T_hs_in)/2)/(((T_hs_out-T_hs_in)/2)-((T_cs_in-T_cs_out)/2)) #Carnot
    COP
252 eta_Carnot = COP/COP_Carnot  #Carnot efficiency
253 T_Lor_H = (T_hs_out-T_hs_in)/np.log(T_hs_out/T_hs_in) #Average temperature (glide) of the
    heat sink/hot stream (hs) in the hot HEX in K
254 T_Lor_C = (T_cs_in-T_cs_out)/np.log(T_cs_in/T_cs_out) #Average temperature (glide) of the
    heat source/cold stream (cs) in the cold HEX in K
255 COP_Lorenz  = T_Lor_H/(T_Lor_H-T_Lor_C) #Lorenz COP
256 eta_Lorenz = COP/COP_Lorenz  #Lorenz efficiency
257
258
259 #Delivering required Qin / pre-heating the heat source stream with a regular HP to see what
    total COP would be achieved
260 Q_HP = m_cs*(h_cs_in-h_cs_out)  #Energy delivered if a regular HP is used to generate the
    heat source stream
261 COP_HP = 3                      #Assuming the regular HP can reach a COP of 3
262 W_HP = Q_HP/3                   #Energy required assuming a COP of 3 for the regular HP
263 Combined_COP_HP = (Q_HEX_hs)/(W_compr-W_turb+W_HP) #Combined COP of pre-heating with HP and
    the HTHP
264
265
266 #%% Plots
267
268 ##Temperature-entropy diagram of the HTHP including isobars
```

```
plt.figure(1, dpi=1080)
plot = PropertyPlot('CO2','TS',unit_system = 'SI', tp_limits = 'ACHP')
plot.calc_isolines(CP.iQ, num =11)
#plot.calc_isolines(CP.iHmass, num = 15)
plot.calc_isolines(CP.iP,iso_range=[P1,P2,CP.PropsSI("Pcrit","CO2")], num=3)
plot.draw()
plot.isolines.clear()
plot.props[CP.iP]['color'] = 'green'
plot.props[CP.iP]['lw'] = '0.5'
plot.set_axis_limits([500,2900,220,700])
plot.grid()
plt.axhline(y=CP.PropsSI("Tcrit","CO2"), color='k', linestyle='--',linewidth=1)
plt.plot(s1,T1, color='k',marker=".", markersize=10)
plt.plot(s2,T2, color='k',marker=".", markersize=10)
plt.plot(s3,T3, color='k',marker=".", markersize=10)
plt.plot(s4,T4, color='k',marker=".", markersize=10)
plt.plot([s1,s4],[T_cs_in, T_cs_out],color='b', linestyle='--',linewidth=1)
plt.plot([s3,s2],[T_hs_in, T_hs_out],color='r', linestyle='--',linewidth=1)
plt.plot([s1,s2],[T1,T2],color='k', linestyle='-',linewidth=2)
plt.plot([s3,s4],[T3,T4],color='k', linestyle='-',linewidth=2)
plt.plot([s2,s23_mid],[T2,T23_mid],color='k', linestyle='--',linewidth=1)
plt.plot([s23_mid,s3],[T23_mid,T3],color='k', linestyle='--',linewidth=1)
plt.plot([s1,s41_mid],[T1,T41_mid],color='k', linestyle='--',linewidth=1)
plt.plot([s41_mid,s4],[T41_mid,T4],color='k', linestyle='--',linewidth=1)

plot.xlabel("Specific entropy in J/kgK")
plot.ylabel("Temperature in K")
plot.title ("T-s diagram of the HTHP")
plot.show()
#plot.savefig('HTHP.png', format='png')


##Printed output variables
print('UA_HEX_cold =',UA_HEX_cold, 'W/K')
print('UA_HEX_hot =',UA_HEX_hot, 'W/K')
print('dT2_cold =',dT2_cold, 'K')
print('dTmid_cold =',dTmid_cold, 'K')
print('dT1_hot =',dT1_hot, 'K')
print('dTquarter_hot =',dTquarter_hot, 'K')
print('dTmid_hot =',dTmid_hot, 'K')
print('m_cs =',m_cs, 'kg/s')
print('m_sCO2 =',m_sCO2, 'kg/s')
print('m_hs =',m_hs, 'kg/s')
print('NTU_cold =',NTU_cold)
print('NTU_hot =',NTU_hot)
print('effectiveness_cold =',epsilon_cold)
print('effectiveness_hot =',epsilon_hot)
print('Input (heat) power =',Q_in/1e6, 'MW')
print('Output (heat) power =',Q_output, 'MW')
print('Generated turbine power =',W_turb/1e6, 'MW')
print('Needed compressor power =',W_compr/1e6, 'MW')
print('Net power needed =',(W_compr-W_turb)/1e6, 'MW')
print('Output temperature =',T_HP_output, '°C')
print('Pressure ratio =',Pressure_ratio)
print('Temperature lift HP =',(T2-T1), '°C')
print('Temperature lift full cycle =',(T_hs_out-T_cs_in), '°C')
print('COP =',COP)
print('Lorenz eff =',eta_Lorenz*100, '%')
print('Combined COP with regular HP =',Combined_COP_HP)
print('T1 =',(T1-273.15), '°C')
print('T2 =',(T2-273.15), '°C')
print('T3 =',(T3-273.15), '°C')
print('T4 =',(T4-273.15), '°C')
print('T_cs_in =',(T_cs_in-273.15), '°C')
print('T_cs_out =',(T_cs_out-273.15), '°C')
print('T_hs_in =',(T_hs_in-273.15), '°C')
print('T_hs_out =',(T_hs_out-273.15), '°C')
```

HTHP-EJ model Python code

```
"""

@author: Koen Verloop

"""
import CoolProp.CoolProp as CP
from CoolProp.Plots import PropertyPlot
import numpy as np
from scipy.optimize import root_scalar
import matplotlib.pyplot as plt
import math

##Define pressure isobars -> the compressor and turbine pressure ratio used
P1 = 70.555*1e5   #Pressure at state 1 (compressor inlet) in Pa
P2 = 345*1e5  #Pressure at state 2 (compressor outlet) in Pa
P3 = 344.77*1e5  #Pressure at state 3 (turbine inlet) in Pa
P4 = 71*1e5   #Pressure at state 4 (turbine outlet) in Pa

#%% 1st loop based on ideal turbomachinery (i is for ideal and used to store certain values of the ideal cycle)

##Heat source counter-current HEX (cold HEX)
U_HEX_coldi = 300   #Overall heat transfer coefficient of the cold HEX in W/m2.K
A_HEX_coldi = 297   #Heat transfer area of cold HEX in m2
UA_HEX_coldi = U_HEX_coldi*A_HEX_coldi #Heat transfer coefficient of the cold HEX in W/K
m_csi = 20.05        #Mass flow of the heat source/cold stream (cs) in kg/s
T_cs_ini = 273.15+150   #Inlet temperature of the heat source/cold stream (cs) into cold HEX in K
T_cs_outi = T_cs_ini-50 #Outlet temperature of the heat source/cold stream (cs) leaving cold HEX in K
P_cs_in = 5*1e5         #Inlet pressure of the heat source/cold stream (cs) into cold HEX in Pa
P_cs_out = 4.77052*1e5        #Outlet pressure of the heat source/cold stream (cs) leaving cold HEX in Pa
h_cs_in = CP.PropsSI('H','P',P_cs_in,'T',T_cs_ini,'INCOMP::T66')    #Specific enthalpy of heat source/cold stream (cs) into cold HEX in J/kg
h_cs_out = CP.PropsSI('H','P',P_cs_out,'T',T_cs_outi,'INCOMP::T66') #Specific enthalpy of the heat source/cold stream (cs) leaving cold HEX in J/kg
cp_oil_csi = CP.PropsSI('C','P',(P_cs_in+P_cs_out)/2,'T',(T_cs_ini + T_cs_outi)/2,'INCOMP::T66') #Constant pressure specific heat capacity of the heat source/cold stream (cs) in cold HEX in J/kg.K
Q_HEX_coldi = m_csi*(h_cs_in-h_cs_out) #Heat rejected by the heat source/cold stream (cs) in the cold HEX in W

#LMTD method to find T1 and T4 with set pinch temperature -> dT1 chosen as pinch to minimize the required temperature lift
dT_m_coldi = Q_HEX_coldi/(UA_HEX_coldi) #Mean temperature difference in cold HEX in K
dT1_coldi = 10            #Terminal temperature difference 1 of cold HEX (pinch) in K
T1i = T_cs_ini-dT1_coldi  #Temperature at state 1 (compressor inlet) in K
def equation(dT2_coldi):
    return (dT1_coldi - dT2_coldi)/np.log(dT1_coldi/dT2_coldi)-dT_m_coldi
result = root_scalar(equation, bracket=[0.1, 1000])
dT2_coldi = result.root     #Terminal temperature difference 2 of cold HEX in K
T4i = T_cs_outi - dT2_coldi #Temperature at state 4 (compressor outlet) in K


##Thermodynamic properties at state 1 (compressor inlet) -> part of cold HEX so calculate first
s1i = CP.PropsSI('S','P',P1,'T',T1i,'CO2') #Specific entropy of sCO2 at state 1 in J/kg.K
h1i = CP.PropsSI('H','P',P1,'T',T1i,'CO2') #Specific enthalpy of sCO2 at state 1 in J/kg

##Thermodynamic properties at state 4 (turbine outlet) -> part of cold HEX so calculate first
s4i = CP.PropsSI('S','P',P4,'T',T4i,'CO2') #Specific entropy of sCO2 at state 4 in J/kg.K
h4i = CP.PropsSI('H','P',P4,'T',T4i,'CO2') #Specific enthalpy of sCO2 at state 4 in J/kg

##Thermodynamic properties at state 2 (compressor outlet)
s2i = s1i #Specific entropy of sCO2 at state 2 in J/kg.K
T2i = CP.PropsSI('T','P',P2,'S',s2i,'CO2') #Temperature of sCO2 at state 2 in K
h2i = CP.PropsSI('H','P',P2,'S',s2i,'CO2') #Specific enthalpy of sCO2 at state 2 in J/kg
```

```
58
59 ##Thermodynamic properties at state 3 (turbine inlet)
60 s3i = s4i #Specific entropy of sCO2 at state 3 in J/kg.K
61 T3i = CP.PropsSI('T','P',P3,'S',s3i,'CO2') #Temperature of sCO2 at state 3 in K
62 h3i = CP.PropsSI('H','P',P3,'S',s3i,'CO2') #Specific enthalpy of sCO2 at state 3 in J/kg
63
64
65 ##Incorporation of theoretical ejector model
66
67 #Nozzle section
68 Pp = P3 #Pressure of the primary (p) flow at nozzle inlet in Pa
69 P1ej = 60.9*1e5 #Estimate of pressure at nozzle outlet to realize maximum ejector outlet
       pressure
70 sp = s3i #Specific entropy of the primary (p) flow at nozzle inlet in J/kg.K
71 Tp = T3i #Temperature of the primary (p) flow at nozzle inlet in K
72 eta_n = 0.9 #Isentropic nozzle efficiency, value from paper by Padilla et al.
73 hp = CP.PropsSI('H','P',Pp,'T',Tp,'CO2')    #Specific enthalpy of the primary (p) flow at
       nozzle inlet in J/kg
74 hp1s = CP.PropsSI('H','P',P1ej,'S',sp,'CO2') #Specific enthalpy of the primary (p) flow at
       mixing inlet in J/kg
75 up1 = math.sqrt(2*eta_n*(hp-hp1s)) #Velocity of the primary (p) flow at mixing inlet in m/s
76
77 Ps = P1 #Pressure of the secondary (s) flow at suction inlet in Pa
78 ss = s1i #Specific entropy of the secondary (s) flow at suction inlet in J/kgK
79 Ts = T1i #Temperature of the secondary (s) flow at suction inlet in K
80 hs = CP.PropsSI('H','P',Ps,'T',Ts,'CO2')    #Specific enthalpy of the secondary (s) flow at
       suction inlet in J/kg
81 hs1s = CP.PropsSI('H','P',P1ej,'S',ss,'CO2') #Specific enthalpy of the secondary (s) flow at
       mixing inlet in J/kg
82 us1 = math.sqrt(2*(hs-hs1s)) #Velocity of the secondary (s) flow at mixing inlet in m/s
83
84 cp1_p = CP.PropsSI('C','P',Pp,'T',Tp,'CO2')  #Specific heat capacity at constant pressure of
       the primary (p) flow at mixing outlet in J/kg.K
85 cv1_p = CP.PropsSI('O','P',Pp,'T',Tp,'CO2')  #Specific heat capacity at constant volume of
       the primary (p) flow at mixing outlet in J/kg.K
86 gamma_p = cp1_p/cv1_p                        #Ratio of specific heats at mixing outlet
87 cp1_s = CP.PropsSI('C','P',Ps,'T',Ts,'CO2')  #Specific heat capacity at constant pressure of
       the secondary (s) flow at mixing outlet in J/kg.K
88 cv1_s = CP.PropsSI('O','P',Pp,'T',Ts,'CO2')  #Specific heat capacity at constant volume of
       the secondary (s) flow at mixing outlet in J/kg.K
89 gamma_s = cp1_s/cv1_s                        #Ratio of specific heats at mixing outlet
90
91 #Mach number approach in nozzle section
92 M1_p = math.sqrt(eta_n*(2/(gamma_p-1))*((Pp/P1ej)**((gamma_p-1)/gamma_p)-1)) #Mach number of
       the primary (p) flow at mixing inlet
93 M1_s = math.sqrt((2/(gamma_s-1))*((Ps/P1ej)**((gamma_s-1)/gamma_s)-1)) #Mach number of the
       secondary (s) flow at mixing inlet
94 M1_crit_p = math.sqrt((M1_p**2*(gamma_p+1))/(M1_p**2*(gamma_p-1)+2))  #Critical mach number
       of the primary (p) flow at mixing inlet
95 M1_crit_s = math.sqrt((M1_s**2*(gamma_s+1))/(M1_s**2*(gamma_s-1)+2))  #Critical mach number
       of the secondary (s) flow at mixing inlet
96
97
98 #Mixing section
99 P2ej = P1ej    #Constant pressure approach that the pressure does not change during mixing
100 omega = 5    #Entrainment ratio, ratio of m_s/m_p
101 eta_m = 0.95 #Isentropic mixing efficiency, value from paper by Padilla et al.
102
103 u2 = eta_m*((up1+omega*us1)/(1+omega))     #Velocity of the combined flow at mixing outlet in
        m/s
104 h2ej = (omega*hs+hp)/(1+omega)-(u2**2)/2     #Specific enthalpy of the combined flow at
       mixing outlet in J/kg
105 T2ej = CP.PropsSI('T','P',P2ej,'H',h2ej,'CO2') #Temperature of the combined flow at mixing
       outlet in K
106 c2 = CP.PropsSI('A','P',P2ej,'H',h2ej,'CO2')  #Local speed of sound at mixing outlet in m/s
107 rho2 = CP.PropsSI('D','P',P2ej,'T',T2ej,'CO2') #Density of the combined flow at mixing outlet
        in kg/m3
108
109 cp2 = CP.PropsSI('C','P',P2ej,'T',T2ej,'CO2')  #Specific heat capacity at constant pressure
       at mixing outlet in J/kg.K
110 cv2 = CP.PropsSI('O','P',P2ej,'T',T2ej,'CO2')  #Specific heat capacity at constant volume at
```

```
    mixing outlet in J/kg.K
gamma2 = cp2/cv2                                #Ratio of specific heats at mixing outlet

#Mach number approach in mixing section
M2_crit = (M1_crit_p+omega*M1_crit_s*math.sqrt(Ts/Tp))/(math.sqrt((1+omega)*(1+omega*Ts/Tp)))
     #Critical mach number of the combined flow at mixing outlet

def equation(M2):
    return  math.sqrt((M2**2*(gamma2+1))/(M2**2*(gamma2-1)+2))-M2_crit
result = root_scalar(equation, bracket=[0.1, 1000])

M2 = result.root #Mach number of the combined flow at mixing outlet


#Constant area section (downstream of the shock)
#Initially calculate u3(i) with c2 to estimate constant area outlet conditions
u3i = c2*math.sqrt(((u2/c2)**2+(2/(gamma2-1)))/((u2/c2)**2*((2*gamma2)/(gamma2-1))-1)) #First
     estimate of the velocity at constant area outlet in m/s
h3ej = h2ej+(u2**2)/2-(u3i**2)/2 #First estimate of specific enthalpy at constant area outlet
     in J/kg
rho3 = rho2*(u2/u3i)   #First estimate of density at constant area outlet in kg/m3
P3ej = CP.PropsSI('P','D',rho3,'H',h3ej,'CO2') #First estimate of pressure at constant area
    outlet in Pa
s3ej = CP.PropsSI('S','D',rho3,'H',h3ej,'CO2')  #First estimate of specific entropy at
    constant area outlet in J/kg.K

c3i = CP.PropsSI('A','P',P3ej,'H',h3ej,'CO2')  #First estimate of local speed of sound at
    constant area outlet in m/s
cp3 = CP.PropsSI('C','P',P3ej,'H',h3ej,'CO2')  #First estimate of specific heat capacity at
    constant pressure at constant area outlet in J/kg.K
cv3 = CP.PropsSI('O','P',P3ej,'H',h3ej,'CO2')  #First estimate of specific heat capacity at
    constant volume at constant area outlet in J/kg.K
gamma_c = ((cp2/cv2)+(cp3/cv3))/2              #First estimate of average ratio of specific
    heats at constant area outlet

#Now calculate u3 with c3i to find a better estimate of c3
u3 = c3i*math.sqrt(((u2/c2)**2+(2/(gamma_c-1)))/((u2/c2)**2*((2*gamma_c)/(gamma_c-1))-1)) #
    Velocity at constant area outlet in m/s
h3ej = h2ej+(u2**2)/2-(u3**2)/2  #Specific enthalpy at constant area outlet in J/kg
rho3 = rho2*(u2/u3) #Density at constant area outlet in kg/m3
P3ej = CP.PropsSI('P','D',rho3,'H',h3ej,'CO2') #Pressure at constant area outlet in Pa
s3ej = CP.PropsSI('S','D',rho3,'H',h3ej,'CO2')  #Specific entropy at constant area outlet in
    J/kg.K

c3 = CP.PropsSI('A','P',P3ej,'H',h3ej,'CO2')   #Local speed of sound at constant area outlet
    in m/s
cp3 = CP.PropsSI('C','P',P3ej,'H',h3ej,'CO2')  #Specific heat capacity at constant pressure
    at constant area outlet in J/kg.K
cv3 = CP.PropsSI('O','P',P3ej,'H',h3ej,'CO2')  #Specific heat capacity at constant volume at
    constant area outlet in J/kg.K
gamma_c = ((cp2/cv2)+(cp3/cv3))/2           #Average ratio of specific heats at constant area
     outlet

#Compare c3i with c3 and iterate to the final (correct) value of c3
while abs(c3-c3i) > 0.0000001:

    c3i = CP.PropsSI('A','P',P3ej,'H',h3ej,'CO2')  #First estimate of local speed of sound at
         constant area outlet in m/s
    cp3 = CP.PropsSI('C','P',P3ej,'H',h3ej,'CO2')  #First estimate of specific heat capacity
        at constant pressure at constant area outlet in J/kg.K
    cv3 = CP.PropsSI('O','P',P3ej,'H',h3ej,'CO2')  #First estimate of specific heat capacity
        at constant volume at constant area outlet in J/kg.K
    gamma_c = ((cp2/cv2)+(cp3/cv3))/2           #First estimate of average ratio of specific
        heats at constant area outlet

    u3 = c3i*math.sqrt(((u2/c2)**2+(2/(gamma_c-1)))/((u2/c2)**2*((2*gamma_c)/(gamma_c-1))-1))
         #Velocity at constant area outlet in m/s
    h3ej = h2ej+(u2**2)/2-(u3**2)/2  #Specific enthalpy at constant area outlet in J/kg
    rho3 = rho2*(u2/u3) #Density at constant area outlet in kg/m3
    P3e = CP.PropsSI('P','D',rho3,'H',h3ej,'CO2') #Pressure at constant area outlet in Pa
    s3e = CP.PropsSI('S','D',rho3,'H',h3ej,'CO2')  #Specific entropy at constant area outlet
```

```
        in J/kg.K
161
162     c3 = CP.PropsSI('A','P',P3ej,'H',h3ej,'CO2')   #Local speed of sound at constant area
            outlet in m/s
163     cp3 = CP.PropsSI('C','P',P3ej,'H',h3ej,'CO2')  #Specific heat capacity at constant
            pressure at constant area outlet in J/kg.K
164     cv3 = CP.PropsSI('O','P',P3ej,'H',h3ej,'CO2')  #Specific heat capacity at constant volume
             at constant area outlet in J/kg.K
165     gamma_c = ((cp2/cv2)+(cp3/cv3))/2           #Average ratio of specific heats at constant
            area outlet
166
167     if abs(c3-c3i) < 0.0000001:
168         break
169
170 #With final (correct) value of c3 calculate the final (correct) value of u3
171 gamma_c = ((cp2/cv2)+(cp3/cv3))/2  #Average ratio of specific heats at constant area outlet
172 u3 = c3*math.sqrt(((u2/c2)**2+(2/(gamma_c-1)))/((u2/c2)**2*((2*gamma_c)/(gamma_c-1))-1)) #
        Velocity at constant area outlet in m/s
173 h3ej = h2ej+(u2**2)/2-(u3**2)/2  #Specific enthalpy at constant area outlet in J/kg
174 rho3 = rho2*(u2/u3) #Density at constant area outlet in kg/m3
175 P3ej = CP.PropsSI('P','D',rho3,'H',h3ej,'CO2') #Pressure at constant area outlet in Pa
176 s3ej = CP.PropsSI('S','D',rho3,'H',h3ej,'CO2')  #Specific entropy at constant area outlet in
        J/kg.K
177
178 #Mach number approach in constant area section (downstream of the shock)
179 M3 = (M2**2+(2/(gamma_c-1)))/(((2*gamma_c)/(gamma_c-1))*M2**2-1) #Mach number in constant
        area section downstream of the shock
180 P3ej_2 = P2ej*((1+gamma_c*M2**2)/(1+gamma_c*M3**2)) #Pressure in constant area section
        downstream of the shock in Pa
181
182
183 #Diffuser section
184 eta_d = 0.9 #Isentropic diffuser efficiency, value from paper by Padilla et al.
185 h4sej = h3ej+(u3**2)/(2*eta_d) #Specific isentropic enthalpy at diffuser outlet in J/kg
186 h4ej = h3ej+(u3**2)/2          #Specific enthalpy at diffuser outlet in J/kg
187 s4ej = s3ej                    #Specific entropy at diffuser outlet in J/kg.K
188 P4ej = CP.PropsSI('P','H',h4sej,'S',s4ej,'CO2') #Pressure at diffuser outlet in Pa
189 cp4 = CP.PropsSI('C','S',s4ej,'H',h4ej,'CO2')  #Specific heat capacity at constant pressure
        at diffuser outlet in J/kg.K
190 cv4 = CP.PropsSI('O','S',s4ej,'H',h4ej,'CO2')  #Specific heat capacity at constant volume at
        diffuser area outlet in J/kg.K
191 gamma_d = ((cp3/cv3)+(cp4/cv4))/2          #Average ratio of specific heats in diffuser
192 gamma4 = (cp4/cv4)                         #Average ratio of specific heats at diffuser
        outlet
193
194 #Mach number approach in diffuser section
195 P4ej_2 = P3ej_2*(eta_d*((gamma_d-1)/2)*M3**2+1)**(gamma_d/(gamma_d-1)) #Pressure at diffuser
        outlet in Pa
196
197 #Properties at ejector outlet
198 Pej = P4ej #Pressure at ejector outlet in Pa
199 hej = h4sej #Specific enthalpy at ejector outlet in J/kg
200 sej = s4ej  #Specific entropy at ejector outlet in J/kg.K
201 Tej = CP.PropsSI('T','P',Pej,'H',hej,'CO2') #Temperature at ejector outlet in K
202
203 #Updated state 2 (compressor outlet) as the outlet of the ejector now becomes the inlet of
        the compressor
204 s2i = sej #Specific entropy of sCO2 at state 2 in J/kg.K
205 T2i = CP.PropsSI('T','P',P2,'S',s2i,'CO2') #Temperature of sCO2 at state 2 in K
206 h2i = CP.PropsSI('H','P',P2,'S',s2i,'CO2') #Specific enthalpy of sCO2 at state 2 in J/kg
207
208
209 ##Mass flow of sCO2 -> assumed to stay constant throughout the HP cycle
210 m_sCO2_si = Q_HEX_coldi /(h1i-h4i)  #Mass flow of the secondary flow of sCO2 inside the ideal
         HP cycle in kg/s
211 m_sCO2_pi = m_sCO2_si/omega         #Mass flow of the primary flow of sCO2 inside the ideal
        HP cycle in kg/s
212 m_sCO2_toti = m_sCO2_pi + m_sCO2_si #Mass flow of the combined flow of sCO2 inside the ideal
        HP cycle in kg/s
213
214
```

```
##Compressor with isentropic efficiency
eta_compr = 0.8 #Isentropic efficiency of the compressor, value ranges between 0.6 and 0.8
h2_r = hej + (h2i-hej)/eta_compr #Real specific enthalpy of sCO2 at state 2 in J/kg
T2_r = CP.PropsSI('T','P',P2,'H',h2_r,'CO2') #Real temperature of sCO2 at state 2 in K
s2_r = CP.PropsSI('S','P',P2,'T',T2_r,'CO2') #Real specific entropy of sCO2 at state 2 in J/kg.K

##Turbine with isentropic efficiency
eta_turb = 0.9 #Isentropic efficiency of the turbine, value ranges between 0.7 and 0.9
h4_r = h3i - eta_turb*(h3i-h4i) #Real specific enthalpy of sCO2 at state 4 in J/kg
T4_r = CP.PropsSI('T','P',P4,'H',h4_r,'CO2') #Real temperature of sCO2 at state 4 in K
s4_r = CP.PropsSI('S','P',P4,'T',T4_r,'CO2') #Real specific entropy of sCO2 at state 4 in J/kg.K


##NTU effectiveness method check cold HEX
cp_sCO2_41i = CP.PropsSI('C','P',(P1+P4)/2,'T',((T1i+T4i)/2),'CO2') #Average constant pressure specific heat capacity of the sCO2 inside the cold HEX in J/kgK
mcp_csi = m_csi*cp_oil_csi           #Heat capacity flow rate of the heat source/cold stream (cs) in the cold HEX in W.K
mcp_sCO2_coldi = m_sCO2_si*cp_sCO2_41i #Heat capacity flow rate of the sCO2 in the cold HEX in W.K
C_min_coldi = min(mcp_csi,mcp_sCO2_coldi) #Minimum heat capacity flow rate in the cold HEX in W.K
C_max_coldi = max(mcp_csi,mcp_sCO2_coldi) #Maximum heat capacity flow rate in the cold HEX in W.K
Cr_coldi = C_min_coldi/C_max_coldi       #Ratio between min and max heat capacity flow rate in the cold HEX
q_max_coldi = C_min_coldi*(T_cs_ini-T4i) #Maximum heat transferred between heat source/cold stream (cs) and sCO2 in the cold HEX in W
q_coldi = mcp_csi*(T_cs_ini-T_cs_outi)   #Heat rejected by heat source/cold stream (cs) in the cold HEX in W
epsilon_coldi = q_coldi/q_max_coldi      #Effectiveness of the cold HEX
NTU_coldi = UA_HEX_coldi/C_min_coldi     #Number of transfer units (NTU) of the cold HEX, ideally between 3-4

#Extra check for pinch temperature in the middle of the cold HEX
s41_mid = (s1i+s4i)/2 #Specific entropy of sCO2 in the middle of the cold HEX in J/kg.K
T41_mid = CP.PropsSI('T','P',(P1+P4)/2,'S',s41_mid,'CO2') #Temperature of sCO2 in the middle of the cold HEX in K
T_cs_mid = (T_cs_ini+T_cs_outi)/2 #Temperature of the heat source/cold stream (cs) in the middle of the cold HEX in K
dTmid_coldi = T_cs_mid-T41_mid    #Temperature difference in the middle of the cold HEX


#%% 2nd loop based on real turbomachinery (isentropic efficiencies taken into account)

##Updated temperatures for the 2nd loop
T1 = T1i  #Temperature of sCO2 at state 1 in K
T2 = T2_r #Temperature of sCO2 at state 2 in K
T3 = T3i  #Temperature of sCO2 at state 3 in K
T4 = T4_r #Temperature of sCO2 at state 4 in K

#Thermodynamic properties at state 1 (compressor inlet)
s1 = CP.PropsSI('S','P',P1,'T',T1,'CO2') #Specific entropy of sCO2 at state 1 in J/kg.K
h1 = CP.PropsSI('H','P',P1,'T',T1,'CO2') #Specific enthalpy of sCO2 at state 1 in J/kg
cp_sCO2_1 = CP.PropsSI('C','P',P1,'T',T1,'CO2') #Constant pressure specific heat capacity of sCO2 at state 1 in J/kg.K
cv_sCO2_1 = CP.PropsSI('O','P',P1,'T',T1,'CO2') #Constant volume specific heat capacity of sCO2 at state 1 in J/kg.K
kappa_1 = cp_sCO2_1/cv_sCO2_1  #Heat capacity ratio of sCO2 at state 1
rho_sCO2_1 = CP.PropsSI('D','P',P1,'T',T1,'CO2') #Density of sCO2 at state 1 in kg/m3

#Thermodynamic properties at state 2 (compressor outlet)
h2 = CP.PropsSI('H','P',P2,'T',T2,'CO2') #Specific enthalpy of sCO2 at state 2 in J/kg
s2 = CP.PropsSI('S','P',P2,'T',T2,'CO2') #Specific entropy of sCO2 at state 2 in J/kg.K
cp_sCO2_2 = CP.PropsSI('C','P',P2,'T',T2,'CO2') #Constant pressure specific heat capacity of sCO2 at state 2 in J/kg.K
cv_sCO2_2 = CP.PropsSI('O','P',P2,'T',T2,'CO2') #Constant volume specific heat capacity of sCO2 at state 2 in J/kg.K
kappa_2 = cp_sCO2_2/cv_sCO2_2  #Heat capacity ratio of sCO2 at state 2
```

```
rho_sCO2_2 = CP.PropsSI('D','P',P2,'T',T2,'CO2') #Density of sCO2 at state 2 in kg/m3

#Thermodynamic properties at state 3 (turbine inlet)
h3 = CP.PropsSI('H','P',P3,'T',T3,'CO2') #Specific enthalpy of sCO2 at state 3 in J/kg
s3 = CP.PropsSI('S','P',P3,'T',T3,'CO2') #Specific entropy of sCO2 at state 3 in J/kg.K
cp_sCO2_3 = CP.PropsSI('C','P',P3,'T',T3,'CO2') #Constant pressure specific heat capacity of sCO2 at state 3 in J/kg.K
cv_sCO2_3 = CP.PropsSI('O','P',P3,'T',T3,'CO2') #Constant volume specific heat capacity of sCO2 at state 3 in J/kg.K
kappa_3 = cp_sCO2_3/cv_sCO2_3  #Heat capacity ratio of sCO2 at state 3
rho_sCO2_3 = CP.PropsSI('D','P',P3,'T',T3,'CO2') #Density of sCO2 at state 3 in kg/m3

#Thermodynamic properties at state 4 (turbine outlet)
s4 = CP.PropsSI('S','P',P4,'T',T4,'CO2') #Specific entropy of sCO2 at state 4 in J/kg.K
h4 = CP.PropsSI('H','P',P4,'T',T4,'CO2') #Specific enthalpy of sCO2 at state 4 in J/kg
cp_sCO2_4 = CP.PropsSI('C','P',P4,'T',T4,'CO2') #Constant pressure specific heat capacity of sCO2 at state 4 in J/kg.K
cv_sCO2_4 = CP.PropsSI('O','P',P4,'T',T4,'CO2') #Constant volume specific heat capacity of sCO2 at state 4 in J/kg.K
kappa_4 = cp_sCO2_4/cv_sCO2_4  #Heat capacity ratio of sCO2 at state 4
rho_sCO2_4 = CP.PropsSI('D','P',P4,'T',T4,'CO2') #Density of sCO2 at state 4 in kg/m3


##Mass flow of sCO2 -> assumed to stay constant throughout the HP cycle
m_sCO2_s = m_sCO2_si   #Mass flow of the secondary flow of sCO2 inside the real HP cycle (same as in the ideal HP cycle) in kg/s
m_sCO2_p = m_sCO2_pi   #Mass flow of the primary flow of sCO2 inside the real HP cycle (same as in the ideal HP cycle) in kg/s
m_sCO2_tot = m_sCO2_toti #Mass flow of the combined flow of sCO2 inside the real HP cycle (same as in the ideal HP cycle) in kg/s

#Update energy exchanged with heat source
Q_HEX_cold = m_sCO2_s*(h1-h4) #Heat absorbed from the heat source/cold stream (cs) in the cold HEX in W

##Energy in and out the HP system
Q_in = m_sCO2_s*(h1-h4)    #Heat absorbed from the heat source/cold stream (cs) in W
Q_out = m_sCO2_tot*(h2-h3)   #Heat rejected to the heat sink/hot stream (hs) in W
W_compr = m_sCO2_tot*(h2-hej) #Energy (work) needed to compress the sCO2 in W
W_turb = m_sCO2_s*(h3-h4)  #Energy (work) obtained by expanding the sCO2 in W


##Heat source counter-current HEX (cold HEX)
U_HEX_cold = 457 #Overall heat transfer coefficient of the cold HEX in W/m2.K
A_HEX_cold = 165 #Heat transfer area of cold HEX in m2
UA_HEX_cold = U_HEX_cold*A_HEX_cold #Heat transfer coefficient of the cold HEX in W/K

#LMTD method to find heat source/cold stream (cs) properties with set pinch temperature -> dT1 chosen as pinch to minimize the required temperature lift
dT_m_cold = Q_HEX_cold/(UA_HEX_cold) #Mean temperature difference in cold HEX in K
dT1_cold = 10          #Terminal temperature difference 1 of cold HEX (pinch) in K
T_cs_in = T1+dT1_cold  #Inlet temperature of the heat source/cold stream (cs) into cold HEX in K
def equation(dT2_cold):
    return (dT1_cold - dT2_cold)/np.log(dT1_cold/dT2_cold)-dT_m_cold
result = root_scalar(equation, bracket=[0.1, 1000])
dT2_cold = result.root   #Terminal temperature difference 2 of cold HEX in K
T_cs_out = T4 + dT2_cold #Outlet temperature of the heat source/cold stream (cs) leaving cold HEX in K

#Updated mass flow of the heat source/cold stream (cs)
cp_oil_cs = CP.PropsSI('C','P',(P_cs_in+P_cs_out)/2,'T',(T_cs_in + T_cs_out)/2,'INCOMP::T66') #Constant pressure specific heat capacity of the heat source/cold stream (cs) inside cold HEX in J/kg.K
h_cs_in = CP.PropsSI('H','P',P_cs_in,'T',T_cs_in,'INCOMP::T66')    #Specific enthalpy of the heat source/cold stream (cs) into cold HEX in J/kg
h_cs_out = CP.PropsSI('H','P',P_cs_out,'T',T_cs_out,'INCOMP::T66') #Specific enthalpy of the heat source/cold stream (cs) leaving cold HEX in J/kg
m_cs = Q_HEX_cold/(h_cs_in-h_cs_out) #Mass flow of the heat source/cold stream (cs) in kg/s


```

```
##Heat sink counter-current HEX (hot HEX)
U_HEX_hot = 507 #Overall heat transfer coefficient of the hot HEX in W/m2.K
A_HEX_hot = 394 #Heat transfer area of hot HEX in m2
UA_HEX_hot = U_HEX_hot*A_HEX_hot #Heat transfer coefficient of the hot HEX in W/K

#LMTD method to find hot stream inlet and outlet temperature with set pinch temperature -> dT2 chosen as pinch to allow optimization of the HEX in terms of NTU and effectiveness
dT_m_hot = Q_out/(UA_HEX_hot) #Mean temperature difference in hot HEX in K
dT2_hot = 15          #Terminal temperature difference 2 of hot HEX (pinch) in K
T_hs_in  = T3-dT2_hot #Inlet temperature of the heat sink/hot stream (hs) into hot HEX in K
def equation(dT1_hot):
    return (dT1_hot - dT2_hot)/np.log(dT1_hot/dT2_hot) - dT_m_hot
result = root_scalar(equation, bracket=[0.1, 1000])
dT1_hot = result.root #Terminal temperature difference 1 of hot HEX in K
T_hs_out = T2-dT1_hot #Outlet temperature of the heat sink/hot stream (hs) leaving hot HEX in K
P_hs_in = 5*1e5  #Pressure of the heat sink/hot stream (hs) into hot HEX in Pa
P_hs_out = 4.53666*1e5 #Pressure of the heat sink/hot stream (hs) leaving hot HEX in Pa
h_hs_in = CP.PropsSI('H','P',P_hs_in,'T',T_hs_in,'INCOMP::T66')   #Specific enthalpy of the heat sink/hot stream (hs) into hot HEX in J/kg
h_hs_out = CP.PropsSI('H','P',P_hs_out,'T',T_hs_out,'INCOMP::T66') #Specific enthalpy of the heat sink/hot stream (hs) leaving hot HEX in J/kg
cp_oil_hs = CP.PropsSI('C','P',(P_hs_in+P_hs_out)/2,'T',(T_hs_in + T_hs_out)/2,'INCOMP::T66') #Constant pressure specific heat capacity of the heat sink/hot stream (hs) in hot HEX in J/kg.K
m_hs = Q_out/(h_hs_out-h_hs_in)    #Mass flow of the heat sink/hot stream (hs) in kg/s
Q_HEX_hs = m_hs*(h_hs_out-h_hs_in) #Heat absorbed by the heat sink/hot stream (hs) inside the hot HEX in W


##NTU effectiveness method check cold HEX
cp_sCO2_41 = CP.PropsSI('C','P',(P1+P4)/2,'T',((T1+T4)/2),'CO2') #Average constant pressure specific heat capacity of the sCO2 inside the cold HEX in J/kgK
mcp_cs = m_cs*cp_oil_cs           #Heat capacity flow rate of the heat source/cold stream (cs) in the cold HEX in W.K
mcp_sCO2_cold = m_sCO2_s*cp_sCO2_41 #Heat capacity flow rate of the sCO2 in the cold HEX in W.K
C_min_cold = min(mcp_cs,mcp_sCO2_cold) #Minimum heat capacity flow rate in the cold HEX in W.K
C_max_cold = max(mcp_cs,mcp_sCO2_cold) #Maximum heat capacity flow rate in the cold HEX in W.K
Cr_cold = C_min_cold/C_max_cold       #Ratio between min and max heat capacity flow rate in the cold HEX
q_max_cold = C_min_cold*(T_cs_in-T4) #Maximum heat transferred between heat source/cold stream (cs) and sCO2 in the cold HEX in W
q_cold = mcp_cs*(T_cs_in-T_cs_out)   #Heat rejected by heat source/cold stream (cs) in the cold HEX in W
epsilon_cold = q_cold/q_max_cold     #Effectiveness of the cold HEX
NTU_cold = UA_HEX_cold/C_min_cold    #Number of transfer units (NTU) of the cold HEX, ideally between 3-4

#Extra check for pinch temperature in the middle of the cold HEX
s41_mid = (s1+s4)/2 #Specific entropy of sCO2 in the middle of the cold HEX in J/kg.K
T41_mid = CP.PropsSI('T','P',(P1+P4)/2,'S',s41_mid,'CO2') #Temperature of sCO2 in the middle of the cold HEX in K
T_cs_mid = (T_cs_in+T_cs_out)/2 #Temperature of the heat source/cold stream (cs) in the middle of the cold HEX in K
dTmid_cold = T_cs_mid-T41_mid   #Temperature difference in the middle of the cold HEX


##NTU effectiveness method check hot HEX
cp_sCO2_23 = CP.PropsSI('C','P',(P2+P3)/2,'T',((T2+T3)/2),'CO2') #Average constant pressure specific heat capacity of the sCO2 inside the hot HEX in J/kg.K
mcp_hs  = m_hs*cp_oil_hs         #Heat capacity flow rate of the heat sink/hot stream (hs) in the hot HEX in W.K
mcp_sCO2_hot = m_sCO2_tot*cp_sCO2_23 #Heat capacity flow rate of the sCO2 in the hot HEX in W.K
C_min_hot = min(mcp_hs,mcp_sCO2_hot) #Minimum heat capacity flow rate in the hot HEX in W.K
C_max_hot = max(mcp_hs,mcp_sCO2_hot) #Maximum heat capacity flow rate in the hot HEX in W.K
Cr_hot = C_min_hot/C_max_hot       #Ratio between min and max heat capacity flow rate in the hot HEX
```

```
q_max_hot = C_min_hot*(T2-T_hs_in) #Maximum heat transferred between heat sink/hot stream (hs) and sCO2 in the hot HEX in W
q_hot = mcp_hs*(T_hs_out-T_hs_in)  #Heat rejected by heat sink/hot stream (hs) in the hot HEX in W
epsilon_hot = q_hot/q_max_hot      #Effectiveness of the hot HEX
NTU_hot = UA_HEX_hot/C_min_hot     #Number of transfer units (NTU) of the hot HEX, ideally between 3-4

#Extra check for pinch temperature in the middle of the hot HEX
s23_mid = (s2+s3)/2 #Specific entropy of sCO2 in the middle of the hot HEX in J/kg.K
T23_mid = CP.PropsSI('T','P',(P2+P3)/2,'S',s23_mid,'CO2') #Temperature of sCO2 in the middle of the hot HEX in K
T_hs_mid = (T_hs_in+T_hs_out)/2 #Temperature of the heat sink/hot stream (hs) in the middle of the hot HEX in K
dTmid_hot = T23_mid-T_hs_mid    #Temperature difference in the middle of the hot HEX

#%% Final output HTHP model

##Some general output variables
dT12 = T2-T1; #Temperature increase over the compressor in K
dT34 = T4-T3; #Temperature decrease over the turbine in K
Pressure_ratio_compr = P2/Pej  #Pressure ratio in the compressor
Pressure_ratio_turb = P3/P4  #Pressure ratio in the turbine
T_HP_output = T_hs_out-273.15 #HTHP output temperature in degrees Celsius
Q_output = Q_HEX_hs/1e6 #Total heat delivered to the heat sink/hot stream (hs) in MW

##Calculate efficiencies & COP
COP = Q_HEX_hs/(W_compr-W_turb)     #COP of the HTHP, wher the turbine is used to power the compressor so Wcompr-Wturb
COP_Carnot = ((T_hs_out-T_hs_in)/2)/(((T_hs_out-T_hs_in)/2)-((T_cs_in-T_cs_out)/2)) #Carnot COP
eta_Carnot = COP/COP_Carnot #Carnot efficiency
T_Lor_H = (T_hs_out-T_hs_in)/np.log(T_hs_out/T_hs_in) #Average temperature (glide) of the heat sink/hot stream (hs) in the hot HEX in K
T_Lor_C = (T_cs_in-T_cs_out)/np.log(T_cs_in/T_cs_out) #Average temperature (glide) of the heat source/cold stream (cs) in the cold HEX in K
COP_Lorenz  = T_Lor_H/(T_Lor_H-T_Lor_C) #Lorenz COP
eta_Lorenz = COP/COP_Lorenz #Lorenz efficiency

#Delivering required Qin / pre-heating the heat source stream with a regular HP to see what total COP would be achieved
Q_HP = m_cs*(h_cs_in-h_cs_out)  #Energy delivered if a regular HP is used to generate the heat source stream
COP_HP = 3                      #Assuming the regular HP can reach a COP of 3
W_HP = Q_HP/3                   #Energy required assuming a COP of 3 for the regular HP
Combined_COP_HP = (Q_HEX_hs)/(W_compr-W_turb+W_HP) #Combined COP of pre-heating with HP and the HTHP


COP_HTHP = 2.522163773341272
COP_improvement = ((COP-COP_HTHP)/COP_HTHP)*100

#%% Plots and prints

##Temperature-entropy diagram of the HTHP including isobars
plt.figure(1, dpi=1080)
plot = PropertyPlot('CO2','TS',unit_system = 'SI', tp_limits = 'ACHP')
plot.calc_isolines(CP.iQ, num =11)
#plot.calc_isolines(CP.iHmass, num = 15)
plot.calc_isolines(CP.iP,iso_range=[P1,P2,CP.PropsSI("Pcrit","CO2")], num=3)
plot.draw()
plot.isolines.clear()
plot.props[CP.iP]['color'] = 'green'
plot.props[CP.iP]['lw'] = '0.5'
plot.set_axis_limits([500,2900,220,700])
plot.grid()
plt.plot(s1,T1, color='k',marker=".", markersize=10)
plt.plot(sej,Tej, color='k',marker=".", markersize=10)
plt.plot(s2,T2, color='k',marker=".", markersize=10)
plt.plot(s3,T3, color='k',marker=".", markersize=10)
plt.plot(s4,T4, color='k',marker=".", markersize=10)
```

```
plt.plot([s1,s4],[T_cs_in, T_cs_out],color='b', linestyle='--',linewidth=1)
plt.plot([s3,s2],[T_hs_in, T_hs_out],color='r', linestyle='--',linewidth=1)
plt.plot([s1,sej],[T1,Tej],color='k', linestyle='-',linewidth=2)
plt.plot([sej,s2],[Tej,T2],color='k', linestyle='-',linewidth=2)
plt.plot([s2,s3],[T2,T3],color='k', linestyle='--',linewidth=1)
plt.plot([s3,s4],[T3,T4],color='k', linestyle='-',linewidth=2)
plt.plot([s3,sej],[T3,Tej],color='k', linestyle='-',linewidth=0.75)
plt.plot([s1,s4],[T1,T4],color='k', linestyle='--',linewidth=1)
plot.xlabel("Specific entropy in J/kg.K")
plot.ylabel("Temperature in K")
plot.title ("T-s diagram of the HTHP-EJ")
plot.show()
#plot.savefig('HTHP-EJ.png', format='png')


##Printed output variables
print('UA_HEX_cold =',UA_HEX_cold, 'W/K')
print('UA_HEX_hot =',UA_HEX_hot, 'W/K')
print('dT2_cold =',dT2_cold, 'K')
print('dTmid_cold =',dTmid_cold, 'K')
print('dT1_hot =',dT1_hot, 'K')
print('dTmid_hot =',dTmid_hot, 'K')
print('m_cs =',m_cs, 'kg/s')
print('m_hs =',m_hs, 'kg/s')
print('m_sCO2_p =',m_sCO2_p, 'kg/s')
print('m_sCO2_s =',m_sCO2_s, 'kg/s')
print('m_sCO2_tot =',m_sCO2_tot, 'kg/s')
print('NTU_coldi =',NTU_coldi)
print('NTU_cold =',NTU_cold)
print('NTU_hot =',NTU_hot)
print('effectiveness_cold =',epsilon_cold)
print('effectiveness_hot =',epsilon_hot)
print('Input (heat) power =',Q_in/1e6, 'MW')
print('Output (heat) power =',Q_output, 'MW')
print('Generated turbine power =',W_turb/1e6, 'MW')
print('Needed compressor power =',W_compr/1e6, 'MW')
print('Net power needed =',(W_compr-W_turb)/1e6, 'MW')
print('Output temperature =',T_HP_output, '°C')
print('Pressure ratio compressor =',Pressure_ratio_compr)
print('Pressure ratio turbine =',Pressure_ratio_turb)
print('Temperature lift HP =',(T2-T1), '°C')
print('Temperature lift full cycle =',(T_hs_out-T_cs_in), '°C')
print('COP =',COP)
print('COP improvement w ejector =',round(COP_improvement,2), '%')
print('Combined COP with regular HP =',Combined_COP_HP)
print('T1 =',(T1-273.15), '°C')
print('T2 =',(T2-273.15), '°C')
print('T3 =',(T3-273.15), '°C')
print('T4 =',(T4-273.15), '°C')
print('T_cs_in =',(T_cs_in-273.15), '°C')
print('T_cs_out =',(T_cs_out-273.15), '°C')
print('T_hs_in =',(T_hs_in-273.15), '°C')
print('T_hs_out =',(T_hs_out-273.15), '°C')
print('Pej =',Pej/1e5, 'bar')
print('Difference in Pej =',abs(P4ej_2/P4ej-1)*100, '%')
print('Tej =',(Tej-273.15), '°C')
print('Sej =',sej, 'J/kg/K')
print('Hej =',hej, 'J/kg')
```